Brillouin scattering in photonic crystal fiber : from fundamentals to fiber optic sensors

Birgit Stiller

Université de Franche-Comté

École Doctorale SPIM

Thèse de Doctorat

Spécialité Optique Photonique

présentée par

Birgit Stiller

Brillouin scattering in photonic crystal fiber: from fundamentals to fiber optic sensors

Thèse dirigée par T. Sylvestre et H. Maillotte

soutenue le 12 décembre 2011

Jury :

Rapporteurs :	Prof. Gerd LEUCHS, Université Erlangen-Nuremberg, Allemagne
	Prof. Luc THEVENAZ, Ecole Polytechnique Fédérale de Lausanne, Suisse
Examinateurs :	Dr. Francesco POLETTI, Université de Southampton, Royaume-Uni
	Dr. Alexandre KUDLINSKI, Université Lille 1, France
	Prof. John M. DUDLEY, Université de Franche-Comté, France
	Dr. Vincent LAUDE, Directeur de Recherche CNRS, France
	Dr. Thibaut SYLVESTRE, Chargé de Recherche CNRS, France
	Dr. Hervé MAILLOTTE, Directeur de Recherche CNRS, France
Invité :	Dr. Min Won LEE, Université Paris 13, France

Le renard se tut et regarda longuement le petit prince :
- S'il te plaît... apprivoise-moi! dit-il.

- Je veux bien, répondit le petit prince,
mais je n'ai pas beaucoup de temps.
J'ai des amis à découvrir et beaucoup de choses à connaître.

- On ne connaît que les choses que l'on apprivoise, dit le renard.
Les hommes n'ont plus le temps de rien connaître.
Ils achètent des choses toutes faites chez les marchands.
Mais comme il n'existe point de marchands d'amis,
les hommes n'ont plus d'amis.
Si tu veux un ami, apprivoise-moi !

- Que faut-il faire ? dit le petit prince.

- Il faut être très patient, répondit le renard.
Tu t'assoiras d'abord un peu loin de moi, comme ça, dans l'herbe.
Je te regarderai du coin de l'œil et tu ne diras rien.
Le langage est source de malentendus.
Mais, chaque jour, tu pourras t'asseoir un peu plus près ...

Antoine de Saint-Exupéry, *Le petit prince*
What the little prince knows about how to start writing a thesis manuscript ...

Abstract

Brillouin scattering is a fundamental nonlinear opto-acoustic interaction present in optical fibers with important implications in fields ranging from modern telecommunication networks to smart optical fiber sensors. This thesis is aimed at providing a comprehensive theoretical and experimental investigation of both forward and backward Brillouin scattering in next generation photonic crystal fibers in view of potential applications to above mentioned fields. We show in particular that these micro-structured optical fibers have the remarkable ability to either suppress or enhance photon-phonon interactions compared to what is commonly observed in conventional fibers.

Firstly, this thesis provides a complete experimental characterization of several photonic crystal fibers using a novel highly-resolved distributed sensing technique based on Brillouin echoes. We perform distributed measurements that show both short-scale and long-scale longitudinal fluctuations of the periodic wavelength-scale air-hole microstructure along the fibers. Our mapping technique is very sensitive to structural irregularities and thus interesting for fiber manufacturers to characterize and improve the fiber uniformity during the drawing process. With this technique, we also report the first experimental observation of the acoustic decay time and the Brillouin linewidth broadening in both standard and photonic crystal fibers. Furthermore, we experimentally demonstrate a simplified architecture of our Brillouin echoes-based distributed optical fiber sensor with centimeter spatial resolution. It is based on differential phase-shift keying technique using a single Mach-Zehnder modulator to generate a pump pulse and a π-phase-shifted pulse with an easy and accurate adjustment of delay. These sensing techniques are also applied to distributed strain measurement.

Another aspect of this thesis is the investigation of a novel method for suppressing stimulated Brillouin scattering that is detrimental to optical fiber transmissions and fiber lasers. We experimentally study several fibers and a demonstrate 4 dB increase of the Brillouin threshold in a photonic crystal fiber by varying periodically the core diameter by only 7%. The efficiency of this passive technique is verified by use of our distributed sensing technique where the oscillating Brillouin frequency shift is clearly observed.

Lastly, we present experimental and numerical results demonstrating the simultaneous

frequency-selective excitation of several guided acoustic Brillouin modes in a photonic crystal fiber with a multi-scale structure design. These guided acoustic modes are identified by using a full vector finite-element model to result from elastic radial vibrations confined by the air-silica microstructure. We further show the strong impact of structural irregularities of the fiber on the frequency and modal shape of these acoustic resonances.

Keywords : Nonlinear optics, stimulated Brillouin scattering, guided acoustic wave Brillouin scattering, photonic crystal fiber, Brillouin threshold, optical fiber sensors.

Résumé

Le cadre général dans lequel s'insère ce travail de thèse est celui de l'étude de la diffusion Brillouin dans une nouvelle génération de fibres optiques à cristaux photoniques (PCFs). Ces fibres, qui présentent un arrangement périodique de micro-canaux d'air parallèles le long de la fibre, possèdent en effet des propriétés optiques et acoustiques remarquables et inédites par rapport aux fibres conventionnelles. De façon plus précise, nous montrons dans ce travail, par le biais de simulations numériques et de données expérimentales, que les fibres à cristaux photoniques offrent la possibilité de supprimer ou, à contrario, augmenter les interactions entre les photons et les phonons.

Dans une première partie, nous présentons une méthode de cartographie des fluctuations longitudinales de la microstructure des fibres PCFs à l'aide d'un capteur distribué basé sur une méthode innovante d'écho Brillouin. Cette méthode, très sensible et à haute résolution, est directement intéressante pour caractériser et améliorer l'uniformité des PCFs lors de leur fabrication et également pour la détection des différentes contraintes de témperature et étirement induites le long des fibres. Sur le plan fondamental, notre système de mesure distribuée à haute résolution nous a également permis d'observer, pour la première fois à notre connaissance, le temps de vie des ondes acoustiques dans les fibres à cristaux photoniques et les fibres standard. Par ailleurs, sur le plan technique, nous avons développé une architecture simplifiée de capteur distribué combinant la technique des échos Brillouin et celle de la modulation différentielle par déplacement de phase avec un seul modulateur d'intensité. Nos résultats montrent une résolution centimétrique dans la zone de soudure entre deux fibres optiques à l'aide d'une impulsion de phase de 500 ps.

Nous démontrons dans une deuxième partie la suppression directe et passive de la rétrodiffusion Brillouin stimulée dans une fibre optique microstructurée en faisant varier périodiquement le diamètre de la microstructure. Une augmentation de 4 dB du seuil de puissance Brillouin a été obtenue avec une variation de seulement 7 % sur une période de 30 m. Ce résultat est très intéressant car la diffusion Brillouin est un facteur limitant dans les systèmes de télécommunications par fibre optique et les laser à fibre.

La troisième et dernière partie est consacrée à l'étude numérique et expérimentale de la diffusion Brillouin en avant dans les fibres à cristaux photoniques. En plus de la suppres-

sion de la plupart des modes acoustiques transverses, nous montrons que cette diffusion Brillouin est fortement augmentée pour certains modes acoustiques à haute fréquence qui sont piégés au coeur de la microstructure. Nous avons également étudié une fibre à structure multi-échelle qui révèle l'excitation sélective de plusieurs phonons acoustiques à des fréquences allant jusqu'a 2 GHz. Ces mesures ont étés confirmées par des simulations numériques basées sur une méthode vectorielle aux éléments finis. L'impact des irrégularitées de la microstructure a aussi été mise en évidence.

Mots clés : optique non linéaire, diffusion Brillouin, fibres optiques microstructurées, seuil Brillouin, capteurs Brillouin distribués.

Acknowledgements

First of all, I would like to thank Dr. Hervé Maillotte and Dr. Thibaut Sylvestre for having given me the possibility to make my PhD at the optics department at the FEMTO-ST institute in Besançon. I never regretted that quite spontaneous decision in July 2008 to start this adventure in France. I appreciated a lot your comments and critics on my work, your ideas and the privileged situation in terms of lab equipment and conferences funding, thanks to the INTERREG-VIA project (CD-FOM - capteurs distribués à fibres optiques microstructurées). I would also like to express my gratitude to the CNRS and the Franche-Comté region for the funding of this 3-years PhD-position. Moreover, funding from the COST 299 action permitted me amongst others a spring school participation and a research stay at the EPFL in Lausanne.
Especially to Thibaut I would like to say "merci" for taking the time to guide me when I made my first steps in the lab, in paper writing, in practising oral presentations (thank you for nodding every time so friendly encouraging in the audience when I was giving a talk), ... You motivated and challenged me so much! I appreciated a lot our discussions and the liberty and trust you have given me during my PhD.

My thanks also go to the committee of my PhD defence: Prof. Gerd Leuchs, Prof. Luc Thévenaz, Dr. Francesco Poletti, Dr. Alexandre Kudlinski, Prof. John M. Dudley, Dr. Vincent Laude and Dr. Min Won Lee. Thank you for having accepted to evaluate my PhD manuscript, for making the effort to come to Besançon for my defence and for all your helpful comments and corrections on my manuscript.

Next, I would like to thank my colleagues on the Brillouin-project: Dr. Michaël Delqué and Dr. Min W. Lee in the optics department and Dr. Jean-Charles Beugnot and Dr. Vincent Laude in the micro nano sciences department. Advancing so fast in terms of simulations and experiments was only possible because of your help, with your expertise and knowledge! I appreciated to work with you and I could really learn a lot thanks to you.
My thanks also go to Prof. Luc Thévenaz at the EPFL in whose group I could spend a research stay in 2009 to make my first experimental experiences with Brillouin sensors. Thank you, not only for the collaborative work in Lausanne, but also for all critical comments and helpful discussions via email. Especially, I would like to thank Dr. Stella

Foaleng Mafang for having made the experiments with me and for every conversation we had.
I also wish to thank Dr. Alexandre Kudlinski for the collaboration and all the photonic crystal fibers we could obtain from the institute IRCICA in Lille. Also thank you for helpful discussions and I was always impressed about your very fast and precise answers concerning every information I needed.
Thanks are also due to Dr. Jerôme Hauden from Photline for the collaborative work in terms of modulators for our Brillouin sensor setup.

I am very grateful having had the possibility to work in the optics department in Besançon, especially the nonlinear optics group (ONL Dream Team). I could always count on interesting and helpful discussions and short-term material borrowing :-). Thank you, les optos, for your rich experimental treasure chest. Thank you for Matlab help, Michaël Delqué and Eric Lantz (merci pour l'initiation à l'escalade et nos discussions). Thank you to Gil Fanjoux, Fabrice Devaux and Mathieu Chauvet, the other permanent stuff of the ONL Dream Team. Thank you to Maxime Jacquot, Jean-Marc Merolla, Laurent Larger, Remo Giust, Pierre-Ambroise Lacourt, Philippe Boyer, for giving me (the Not-French) the possibility to give student courses. Thank you, Kien Phan Huy, for your endless enthusiasm for physics and for the help during my first months of my PhD (bisou à Ulrike). Thank you, John Dudley ("Turbocharge your writing today!"), Belinda Lafon and a couple of others, for the motivation during the thesis writing in the summer. Merci à Valérie, Belinda, Cindy, Brigitte et Joëlle pour tout votre aide, votre patience et votre bonne humeur !

Very special thanks go to all the current and former PhD students (+Ludo) I met at the institute. Without you, these three years would have been far away from what it was. Thank you for every help, every discussion and every funny action. I think about (in a random order):
- the oldies: Jassem, Jean, Abdou, Rémy, Jérémy, Armand (Patsy's Inn rules), Jean-Luc (merci pour l'oeuf et pour ton caractère jurassien, kleine Schnecke;-)...), Anne (merci pour ton aide tout au début de ma thèse et d'être venue à ma soutenance), Seb (je n'oublierai jamais ton acceuil en juin 2011 chez toi à Puimichel), Mika (tu étais l'âme de ma thèse (c'est volé) qui a donné poésie et sens à tout sujet (c'est pas volé), merci pour chaque discussion, encouragement, chanson et ton "être Mika")
- the Eric apostles: Joé (toujours souriant) et Paul-Antoine (je vous souhaite : [Bobby 1:2 vous], du courage !), Mischa (un, dos, tres, la salsa !)
- Benattou (pour toi, il faudrait tout un chapitre, merci pour tout: commençant par le déménagement, les amis de la radio, ... jusqu'au voyage en Provence avec Seb)
- Ludo (merci pour a) les fibres polies, b) les mardis au PPG, c) que tu sois toujours là pour nous, d) tes blagues de tout genre :-P)
- "my" former Master students and friends: Batiste (merci pour chaque anectode de notre

vie quotidienne au bureau et pour les 50% de filles en -115B :-P), Antoine (good luck for your PhD in New Zealand!), Jacques Calin, Eric, Rémi, Arnaud, Anouck, Diane, Aude :-) et Nathapon (Wie geht's?)
- the soirée-connection: Mathieu et Benj (merci pour tout ce temps passé ensemble et chaque verre de vin du Jura), Caro (merci pour ton rire, ton orginalité et ce super chapeau), Clément (j'ai l'impression que tu as toujours été chez nous, merci, tu es un enrichissement), Simon (hello to Copenhagen)
- the Belgium guys: Adrien et Laurent (merci à vous pour le ping pong et l'ambiance)
- and not to forget: Elsie, Abdoulaye (tu as encore ma cliveuse, non ?), Amaury (Guten Tag), Romain (tu nous fais des surprises...), Huihui, Ismael, Luai, Nour (merci pour les gâteaux syriens), Yvan
- Bob (comme synonyme pour toutes vos sottises, mes très chèrs collègues thésards).
Thank you also to all the other people of the optics department (le fameux Johan, le fameux John, Luca, Nadège Coinche, Luc, Hervé T, Maria, Patrick, Manu, Nadège, Poppey and many many more) because there are actually more than one anecdote with almost everybody of you which made work and life in the lab nicer.

Personally, I wish to thank some friends in Besançon because these three years in France have not only been a professional experience but also a personal adventure. Merci à tous les gens de Radio Etna (les loups -garous : Benattou, Dejan, Emilie, Edin, Mous, Den, Deniz, Damir, Angela, Daniel, Galois ...), de la Salsa et de Salsamoondo (Aline et Antoine, Roméo, JJ, Christophe, Olivier, Adeline, Jérémy, Régis, Pierre et Marianne...), d'Escale Jeunes (Nathalie, Claire (avec s), Claire (sans s), Alex, Clémence, Tony, Aurore, François, Guillaume, Micky, Christophe, Gilles ...) et tous les autres (Patrick du PPG, Emmanuelle et Michelle, ...).

At last, I would like to say thank you to my family and friends in Germany and elsewhere who believed in me and helped me where they could. Special thanks go to: Betti (my homebase:-), danke an euch alle vier, dass ihr zu meiner Verteidigung gekommen seid!), Linda (my almost sister), Matthias (danke für so viele Gespräche, Garfield-Comics, das PhD-Comic-Autogramm, deine Musik und geduldiges Korrekturlesen), Tobi (danke für deinen Mut in den ersten Monaten hier und deine Musik) and Alessio (the world is ours!).

Danke, Mama, Papa und Florian, weil ihr immer für mich da seid und mich unterstützt, was auch immer ich entscheide.

Contents

Introduction

In October 2009 the Nobel Prize in Physics was awarded to Willard Boyle, Georg Smith and Charles Kao, pleasant news for a first-year Ph.D. student in fiber optics. Thanks to Charles Kao who proposed in 1966 [1] optical fibers as a transmission medium for communication technology, the high technology standard in ultra-broadband internet and telecommunications today is possible. Optical fibers were then further extensively developed to reach a low loss level compatible with long-haul communications systems [2]. Thirty years later, a novel type of optical fibers, called *photonic crystal fibers (PCFs)*, has been proposed and demonstrated by P. St. J. Russell and co-workers [3, 4]. These periodic wavelength-scale air-hole micro-structured optical fibers has opened the way for new fundamental and applied achievements in nonlinear optics and acoustics.

An important physical effect combining optics and acoustics is Brillouin scattering which was first theoretically predicted by Léon Brillouin in 1922 [5] in his famous publication "Diffusion de la lumière et des rayons X par un corps transparent homogène". Brillouin scattering is an inelastic scattering that results from the interaction of optical waves with acoustic phonons in contrast to Raman scattering [6] where the light is scattered by optical phonons. Due to the guiding nature of the fiber, only two scattering directions are possible: backward scattering that results from longitudinal acoustic waves and forward scattering which relies on transverse acoustic modes. Forward Brillouin scattering or guided acoustic wave Brillouin scattering (GAWBS) has first been investigated by Shelby *et al.* [7]. In the backward direction, the scattered waves can reach high optical power since the process gets exponentially amplified, i.e. stimulated, above a critical or threshold power. In optical fibers, stimulated Brillouin scattering was first investigated in 1972 by Ippen and Stolen [8].

Stimulated Brillouin scattering (SBS) has recently been studied in photonic crystal fibers because of their remarkable ability to guide both acoustic and optical modes within their air-silica microstructure [9–12]. The first experiment of SBS in PCF was carried out at in 1999 [13] where a multi-peak backscattered Brillouin spectrum instead of a single narrow peak in conventional fibers has been observed. GAWBS was experimentally investigated

in PCF by Elser *et al.* and Beugnot *et al.* [14, 15]. They both showed the performance of PCFs to reduce noise induced by thermal vibrations with help of the micro-structure.

In addition, acoustic waves involved in SBS are sensitive to temperature and strain and so the idea was soon arriving to use them for distributed sensing applications. The most popular system is Brillouin optical time-domain analysis (BOTDA), and it has been proposed for the first time in 1989 by Horiguchi *et al.* [16] in conventional fibers. Since then, the spatial resolution of distributed sensors has continuously been increased, for example by using new optical pulse formats [17–19]. PCFs have attracted some interest for Brillouin sensors and only the dependency of temperature and strain on the Brillouin frequency shift in a PCF has been measured in 2004 by Zou *et al.* [20] for the first time.

As far as Brillouin scattering is useful for sensing applications, the more it is detrimental for fiber-based optical transmissions and fiber lasers. As mentioned before, above a threshold power the back-reflected power significantly increases which severely limits the transmitted power through the fiber. For this purpose, PCFs attract much interest because they can be used for Brillouin scattering suppression. A few techniques have been proposed such as using a phononic bandgap nanostructure within the fiber core to inhibit Brillouin acoustic modes [10] or through longitudinal variations of the structural parameters to increase the Brillouin threshold [21].

The focus of this dissertation is to provide a comprehensive theoretical and experimental investigation of both backward and forward Brillouin scattering in photonic crystal fibers both for fundamental aspects and for applications to fiber optic technologies. We show in general that these micro-structured optical fibers have the remarkable ability to harness the photon-phonon interaction compared to what is commonly observed in conventional fibers, leading to new characteristics for both forward and backward Brillouin scattering.

This dissertation is divided in five chapters. The first chapter is aimed at giving an overview and understanding of optical fibers and their optical properties. A short historical overview is then given and general fiber parameters are defined both for conventional and micro-structured optical fibers. The second part of this chapter deals with nonlinear optical effects present in optical fibers.

The second chapter is devoted to light scattering and will be distinguished in linear and nonlinear scattering, respectively, with a special attention to the general principle and theory of both backward and forward Brillouin scattering. We also give an overview of the state of current knowledge on these specific topics and we introduce distributed fiber optic sensors based on Brillouin scattering.

We will provide a complete experimental characterization of Brillouin backscattering in

various photonic crystal fibers in chapter 3. This encompasses Brillouin threshold and gain spectrum measurements using the self-heterodyne measurement technique, as well as distributed measurements based on different techniques. First the conventional Brillouin optical time domain analysis (BOTDA) is described in detail. Further developments providing much higher spatial resolution with the Brillouin echoes distributed sensing (BEDS) technique are shown. Then we experimentally demonstrate a simplified architecture of our Brillouin echoes distributed sensor with centimeter spatial resolution. It is based on differential phase-shift keying technique using a single Mach-Zehnder modulator to generate a pump pulse and a π-phase-shifted pulse with an easy and accurate adjustment of delay. These techniques help for a further investigation of the fine features of SBS in PCFs. Using these techniques, we further perform distributed strain measurements in both photonic crystal and conventional fibers. Moreover, we realize a longitudinal mapping of PCFs which reveals the impact of fiber inhomogeneities on Brillouin scattering by comparing two fibers with nearly the same air-silica micro-structure but different drawing processes. This technique is directly interesting for PCF manufacturers in order to improve the regularity of fiber drawing. With the BEDS technique, we also report the observation of the decay time of the acoustic waves in both standard and photonic crystal fibers. Due to the high resolution, it was possible to reveal that the Brillouin signal decays faster in PCF than in standard fibers. We provide a theoretical model based on a multiple-Lorentzian fit of the corresponding Brillouin linewidth broadening observed in PCF to explain the origin of the shorter acoustic decay time.

The fourth chapter of this thesis investigates a novel method for suppressing stimulated Brillouin scattering that is detrimental to all-optical processing fiber technologies and fiber lasers. First an overview about SBS suppressing methods will be given and a theoretical approach to calculate the critical pump power for the Brillouin threshold is introduced. We then experimentally study several fibers and demonstrate a 4 dB increase of the Brillouin threshold in a photonic crystal fiber by varying periodically the core diameter by only 7%. The measured SBS threshold is compared to theory and to experimental values in uniform photonic crystal fibers with nearly the same air-silica micro-structure. The efficiency of this passive technique is verified by use of our distributed sensing technique where the oscillating Brillouin frequency shift is clearly observed.

Forward Brillouin scattering in photonic crystal fibers is studied both theoretically and experimentally in chapter 5. In addition to the suppression of most of the low-frequency acoustic modes, we report in particular the simultaneous efficient frequency-selective excitation of several guided acoustic Brillouin modes in a photonic crystal fiber with a multi-scale, µm- and sub-µm-structure design. These guided acoustic modes have been identified by using a full vector finite-element model to result from elastic radial vibrations trapped by the air-silica microstructure. We further show the strong impact of structural irregularities of the fiber on the frequency and modal shape of these acoustic resonances

by comparison with a perfectly symmetric fiber structure. Finally the relationship between core diameter and acoustic resonance frequency is carefully examined.

All this work has been done in the framework of the European Programme INTERREG-IVA, in particular the project "CD-FOM - capteurs distribués à fibres optiques microstructurées", in collaboration with the Ecole Polytechnique Fédérale de Lausanne (EPFL), the IRICICA institute at the University of Lille 1 and Photline Technologies. Its main objective is the investigation and development of distributed photonic crystal fiber-based sensors. Moreover, financial support from the COST 299 action permitted amongst others a research stay at the EPFL in Lausanne and a spring school participation. Furthermore, fiber samples have been provided by Draka and PERFOS.

Finally, the research in this dissertation has been presented at a number of national and international conferences and has been subject to publications in several scientific journals :

Journal publications:

B. Stiller, S. Foaleng-Mafang, J.-C. Beugnot, M.W. Lee, M. Delqué, A. Kudlinski, L. Thévenaz, H. Maillotte, and T. Sylvestre, "Photonic crystal fiber mapping using Brillouin echoes distributed sensing", *Optics Express*, vol. 18, no. 19, 20136-20142 (2010)

B. Stiller, M. Delqué, J.-C. Beugnot, M. W. Lee, G. Mélin, H. Maillotte, V. Laude, and T. Sylvestre, "Frequency-selective excitation of guided acoustic modes in a photonic crystal fiber", *Optics Express*, vol. 19, no. 8, 7689-7694 (2011)

E. Carry, J.-C. Beugnot, B. Stiller, M. W. Lee, H. Maillotte, and T. Sylvestre, "Temperature Coefficient of High-Frequency Guided Acoustic Modes in Photonic Crystal Fiber", *Applied Optics*, vol. 50, no. 35, 6543-6547 (2011)

M. W. Lee, B. Stiller, J. Hauden, H. Maillotte, C. Roch, L. Thévenaz, and T. Sylvestre, "Differential phase-shift keying technique-based Brillouin echo-distributed sensing", *IEEE Photonics Technology Letters*, vol. 24, no. 1, 79-81 (2012)

B. Stiller, A. Kudlinski, M. W. Lee, G. Bouwmans, M. Delqué, J.-C. Beugnot, H. Maillotte, and T. Sylvestre, "SBS mitigation in a microstructured optical fiber by periodically varying the core diameter", accepted for publication in *IEEE Photonics Technology Letters*, 10.1109/LPT.2012.2186286

Other publication:

B. Stiller, "Son et lumière dans les fibres optiques microstructurées", in *Prix A'Doc 2011*, Presses universitaires de Franche Comté, 2011, Best Ph.D. Student Award.

International conferences:

B. Stiller, M. Delqué, M.W. Lee, S. Foaleng Mafang, J.C. Beugnot, A. Kudlinski, L. Thevenaz, H. Maillotte, and T. Sylvestre, "Effect of inhomogeneities on backward and forward Brillouin scattering in photonic crystal fibers", *SPIE Photonics Europe*, Bruxelles, Belgium, 12-16 April 2010. Proceedings SPIE "Photonic Crystal Fibers IV", **771406**, 1-12 (2010).

J.-C. Beugnot, M. Delqué, B. Stiller, M. W. Lee, H. Maillotte, V. Laude, G. Mélin, and T. Sylvestre, "Guided Acoustic Wave Brillouin Scattering in a Nanostructure Core Fiber", *OSA Nonlinear Photonics*, Karlsruhe, Germany, 21-24 June 2010. Proceedings OSA Nonlinear Photonics 2010, **NMC3**.

B. Stiller, J.-C. Beugnot, S. Foaleng Mafang, M. W. Lee, M. Delqué, A. Kudlinski, H. Maillotte, V. Laude, L. Thévenaz, and T.Sylvestre, "Observation of Brillouin Linewidth Broadening and Decay Time in Photonic Crystal Fiber", *IEEE Photonics Summer Topicals Meeting*, Playa del Carmen, Mexico, 19-21 July 2010. Proceedings Photonics Society Summer Topical Meeting Series, 2010 IEEE, 168-169 (2010).

J.-C. Beugnot, B. Stiller, S. Foaleng Mafang, M. W. Lee, M. Delqué, A. Kudlinski, H. Maillotte, V. Laude, L. Thévenaz, and T. Sylvestre, "Experimental Observation of Brillouin Linewidth Broadening and Decay Time in Photonic Crystal Fiber", *European Conference on Optical Communications ECOC*, Turin, Italy, 19-23 Sept 2010.

B. Stiller, M. W. Lee, M. Delqué, G. Bouwmans, A. Kudlinski, J.C. Beugnot, H. Maillotte, and T. Sylvestre, "Suppression of SBS in a photonic crystal fiber with periodically-varied core diameter", *Optical Fiber Communication Conference*, Los Angeles, USA, 6-10 March 2011 Proceedings OFC 2011, **OMO5**.

H. Maillotte, J.C. Beugnot, B. Stiller, M. W. Lee, M. Delqué, S. Benchabane, V. Laude, S. Foaleng Mafang, L. Thevenaz, G. Bouwmans, A. Kudlinski, G. Mélin, and T. Sylvestre, "Opto-acoustic coupling and Brillouin phenomena in microstructure optical fibers" (invited conference), *International Conference on Micro/Nano Optical Engineering* (ICOME 2011), Changchun, China, 12-16 June 2011

M. W. Lee, B. Stiller, J. Hauden, H. Maillotte, L. Thévenaz, and T. Sylvestre, "Brillouin echo-distributed sensing based on differential phase-shift keying technique", *European Conference on Optical Communications ECOC*, Geneva, Switzerland, 18-22 Sept 2011, **Tu.6.LeCervin.2**

Workshops and national conferences:

B. Stiller, T. Sylvestre, H. Maillotte, J.C. Beugnot, and A. Kudlinski, "Characterization of backward and forward Brillouin Scattering in a photonic crystal fiber", Eigth Technical Meeting *"European COST Workshop 299 FIDES"*, Wroclaw, Poland, 9-11 Sept 2009.

B. Stiller, S. Foaleng Mafang, J.C. Beugnot, M. Delqué, M.W. Lee, A. Kudlinski, L. Thévenaz, H. Maillotte, and T. Sylvestre, "Cartographie des fibres optiques microstructurées par détection des échos Brillouin", *JNOG 2010*, Besançon, France, 20-22 Oct 2010.

J.-C. Beugnot, B. Stiller, S. Foaleng, M. W. Lee, M. Delqué, A. Kudlinski, H. Maillotte, V. Laude , L. Thévenaz, and T. Sylvestre, "Mesure de l'élargissement du spectre Brillouin et du temps d'amortissement acoustique dans les fibres optiques", *JNOG 2010*, Besançon, France, 20-22 Oct 2010

B. Stiller, M. W. Lee, M. Delqué, A. Kudlinski, H. Maillotte, and T. Sylvestre, "Suppression of SBS in a photonic crystal fiber with periodically-varied core diameter", *Tagung der Deutschen Physikalischen Gesellschaft 2011*, Dresden, Germany, 14-18 March 2011, contribution **Q 6.4**.

M. W. Lee, B. Stiller, J. Hauden, H. Maillotte, L. Thévenaz and T. Sylvestre, "Capteur distribué à fibre optique à haute résolution utilisant l'effet Brillouin et la technique DPSK", *JNOG 2011*, Marseille, France, 4-7 July 2011

B. Stiller, M. W. Lee, M. Delqué, G. Bouwmans, A. Kudlinski, J.-C. Beugnot, H. Maillotte, and T. Sylvestre, "Suppression de l'effet Brillouin dans une fibre optique microstructurée", *JNOG 2011*, Marseille, France, 4-7 July 2011

Bibliography

[1] K. C. Kao and G. A. Hockham, "Dielectric-fibre surface waveguides for optical frequencies", *IEE Proceedings J Optoelectronics*, vol. 133, no. 3, pp. 1151–1158, 1966.

[2] F. P. Kapron, D. B. Keck, and R. D. Maurer, "Radiation losses in glass optical waveguides", *Applied Physics Letters*, vol. 17, no. 10, pp. 423–425, 1970.

[3] J. C. Knight, T. A. Birks, P. St. J. Russell, and D. M. Atkin, "All-silica single-mode optical fiber with photonic crystal cladding", *Optics Letters*, vol. 21, no. 19, pp. 1547–1549, 1996.

[4] P. St.J. Russell, "Photonic crystal fibers", *Science*, vol. 299, pp. 358–362, 2003.

[5] L. Brillouin, "Diffusion de la lumière et des rayons x par un corps transparent homogéne", *Ann. Physique*, vol. 17, pp. 88–122, 1922.

[6] C V. Raman and K. S. Krishnan, "A new type of secondary radiation", *Nature*, vol. 121, pp. 501–502, 1928.

[7] R. M. Shelby, M.D. Levenson, and P.W. Bayer, "Guided acoustic-wave Brillouin scattering", *Physical Review B*, vol. 31, pp. 5244–5252, April 1985.

[8] E. P. Ippen and R. H. Stolen, "Stimulated Brillouin scattering in optical fibers", *Applied Physics Letters*, vol. 21, no. 11, pp. 539–541, 1972.

[9] P. St. J. Russell, E. Martin, A. Diez, S. Guenneau, and A. B. Movchan, "Sonic band gaps in PCF preforms: enhancing the interaction of sound and light", *Optics Express*, vol. 11, no. 20, pp. 2555, 2003.

[10] V. Laude, A. Khelif, S. Benchabane, M. Wilm, T. Sylvestre, B. Kibler, A. Mussot, J. M. Dudley, and H. Maillotte, "Phononic band-gap guidance of acoustic modes in photonic crystal fibers", *Physical Review B*, vol. 71, no. 4, pp. 045107, 2005.

[11] P. Dainese, P. St. J. Russell, N. Joly, J. C. Knight, G. S. Wiederhecker, H. L. Fragnito, V. Laude, and A. Khelif, "Stimulated Brillouin scattering from multi-GHz-guided acoustic phonons in nanostructured photonic crystal fibres", *Nature Physics*, vol. 2, no. 6, pp. 388–392, 2006.

[12] P. Dainese, P. St. J. Russell, G. S. Wiederhecker, N. Joly, H. L. Fragnito, V. Laude, and A. Khelif, "Raman-like light scattering from acoustic phonons in photonic crystal fiber", *Optics Express*, vol. 14, no. 9, pp. 4141–4150, 2006.

[13] N. G. R. Broderick, T. M. Monro, P. J. Bennett, and D. J. Richardson, "Nonlinearity in holey optical fibers: measurement and future opportunities", *Optics Letters*, vol. 24, no. 20, pp. 1395–1397, 1999.

[14] D. Elser, U. L. Andersen, A. Korn, O. Glockl, S. Lorenz, Ch. Marquardt, and G. Leuchs, "Reduction of guided acoustic wave Brillouin scattering in photonic crystal fibers", *Physical Review Letters*, vol. 97, pp. 133901, 2006.

[15] J.-C. Beugnot, T. Sylvestre, H. Maillotte, G. Mélin, and V. Laude, "Guided acoustic wave Brillouin scattering in photonic crystal fibers", *Optics Letters*, vol. 32, no. 1, pp. 17–19, 2007.

[16] T. Horiguchi and M. Tateda, "Optical-fiber-attenuation investigation using stimulated brillouin scattering between a pulse and a continuous wave", *Optics Letters*, vol. 14, no. 8, pp. 408–410, 1989.

[17] X. Bao, A. Brown, M. DeMerchant, and J. Smith, "Characterization of the Brillouin loss spectrum of single-mode fibres by use of very short (10-ns) pulses", *Optics Letters*, vol. 24, no. 8, pp. 510–512, 1999.

[18] A. W. Brown and B. G. Colpitts, "Dark-pulse Brillouin optical time-domain sensor with 20-mm spatial resolution", *Journal of Lightwave Technology*, vol. 25, no. 1, pp. 381–386, 2007.

[19] S. M. Foaleng, M. Tur, J.-C. Beugnot, and L. Thévenaz, "High spatial and spectral resolution long-range sensing using Brillouin echoes", *Journal of Lightwave Technology*, vol. 28, no. 20, pp. 2993–3003, 2010.

[20] L. Zou, X. Bao, S. Afshar V., and L. Chen, "Dependence of the Brillouin frequency shift on strain and temperature in photonic crystal fiber", *Optics Letters*, vol. 29, no. 13, pp. 1485, 2004.

[21] F. Poletti, K. Furusawa, Z. Yusoff, N. G. Broderick, and D. J. Richardson, "Nonlinear tapered holey fibers with high stimulated Brillouin scattering threshold and controlled dispersion", *J. Opt. Soc. Am. B*, vol. 24, no. 9, pp. 2185–2194, 2007.

Chapter 1

Optical fibers and their nonlinearities

The first chapter is aimed at providing a comprehensive overview of silica optical fibers and their properties and nonlinear effects. In a first short paragraph the development of optical fibers up to now is outlined. Then fiber parameters are defined for conventional and photonic crystal fibers (PCFs) and the guidance mechanisms of hollow core and solid core PCF are briefly explained. The second part of this chapter deals with nonlinear optical effects.

1.1 Optical fibers

Optical fibers are nowadays widely used in manifold fields. The most known domain is telecommunications where high transmission rates up 69.1 Tb/s [1] (OFC 2010) and 101.7 Tb/s [2] (OFC 2011) have recently been reached over several hundreds of kilometres. Another industrial sector, where optical fibers play an important role, is civil engineering, where they are used for several types of optical fibers sensors as point sensors, such as interferometers, fiber gratings and distributed fiber sensors. A deeper insight into optical fiber sensors will be given in chapters 2.4.3.3 and 3.2. Here, we start with a short retrospect to the starting point of optical fibers.

1.1.1 Short historical overview

It was in 1966 that Charles Kao proposed [3] optical fibers as a transmission medium for communication technology. At that time optical fibers exceeded 1000 dB/km in terms of optical losses [4] and were still far away from a high-data-rate transmission. With the invention of the laser, reported in 1960 by Maiman [5] and the reduction of the fiber losses to 20 dB/km at about 1 µm [6] in 1970, optical fibers got also into the center of interest of nonlinear optics community since now high optical intensity in a rather small fiber core could be reached. In 1981 the use of single mode fibers (SMF) over 44 km was reported [7] and the fiber loss was reduced to 0.2 dB/km at 1.55 µm [8]. At around 1.55 µm a loss minimum window in silica fibers is found. Therefore the standard wavelength for telecommunication systems was chosen at that wavelength and most of the devices for the experiments in this thesis are adapted to 1.55 µm. Since then, many different types of optical fibers have been developed, starting from the conventional step-index-fiber: graded index fibers, dispersion shifted fibers (DSF), dispersion compensating fibers (DCF), polarization maintaining fibers (PMF), highly nonlinear fibers (HNLF), highly birefringent fibers (Hibi fiber), fibers with different dopant, polymer optical fibers (POF) and more. An important new generation of fibers was developed in the 1990ies: *Photonic crystal fibers* (PCFs) [9, 10]. The cross-section of these fibers exhibit a periodic microstructure consisting of air holes and solid material. Two types of PCFs can be distinguished: *hollow core PCFs* and *solid core PCFs*. Hollow core PCFs are based on *photonic bandgap guiding* which has been theoretically shown in [11] for air-silica fibers. The other guidance form is *modified internal total reflection* for solid core PCFs [12] and is basically the same as in conventional fibers because the mean refractive index around the solid core is lower than in the fiber core. The first realisation of a PCF, a solid core fiber, has been presented in 1996 [9] and is depicted in Fig.(1.1a) whereas the first hollow core PCF has been drawn in 1999 [13] and can be found in Fig.(1.1b,c). Both fibers were

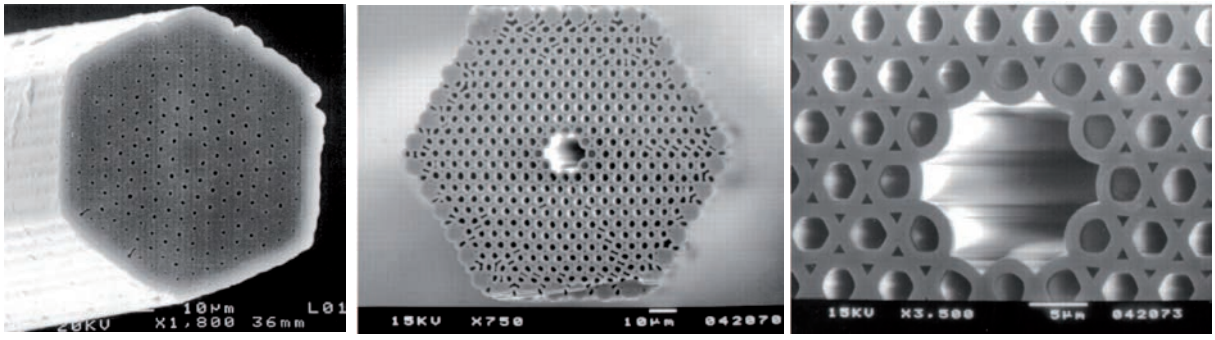

(a) **(b)** **(c)**

Figure 1.1: (a) SEM image of the first solid core PCF [9], (b,c) SEM images of the first hollow core PCF [13].

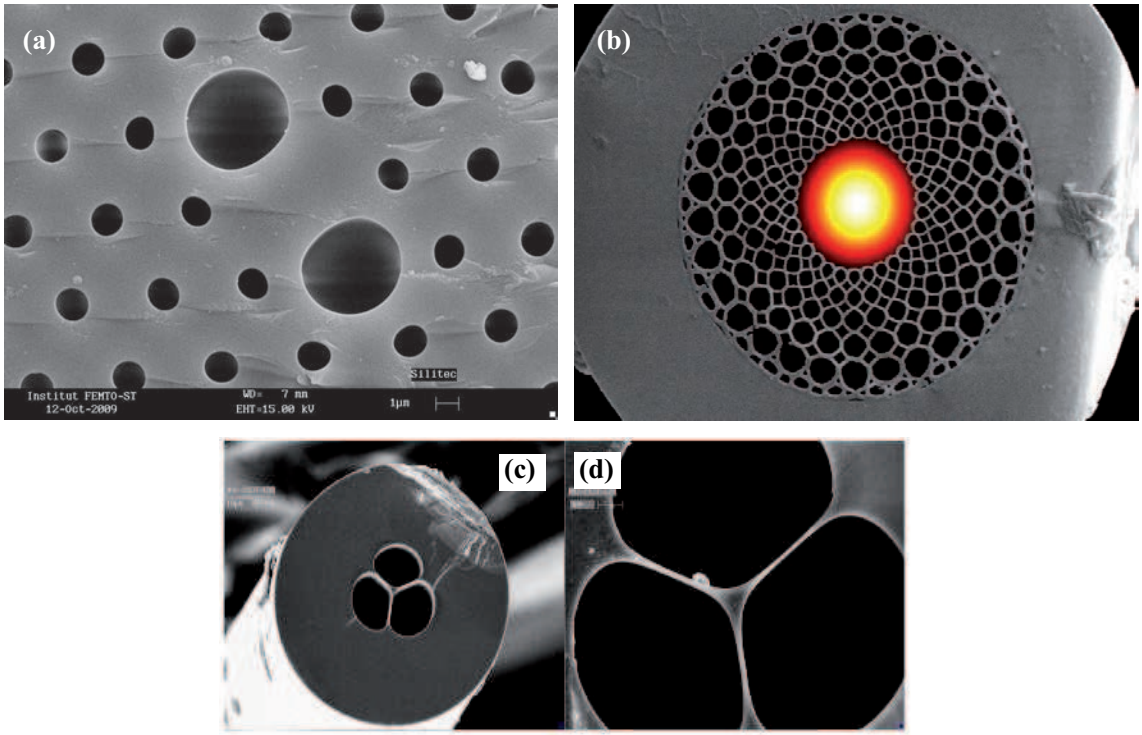

Figure 1.2: SEM images of (a) a birefringent PCF with two larger air holes (image realized at the institut FEMTO-ST), (b) a *chirped* PCF which is a low dispersion PCF [30, 31], (c,d) a suspended core fiber with 2.6 µm core diameter.

drawn at the University of Bath. PCFs have several remarkable characteristics which have been investigated in the subsequent two decades. *Endlessly single mode* guidance in PCF has been discovered in 1997 [14] from 450 nm up to 1.55 µm. Large effective areas in PCF [15, 16] can also be obtained by designing the air-hole structure. The group velocity dispersion and higher order dispersion can be widely tunable [17, 18] and ultra high nonlinear coefficients have been achieved [19]. They are advantageously used for supercontinuum generation [20, 21] and have remarkable acoustic properties since the periodic structure acts like an acoustic filter [22–25]. This is interesting for quantum experiments because they allow for a measurement below the shot noise level [26]. Some PCFs are depicted in Fig.(1.2): birefringent fibers (Fig.(1.2a)), multi-scale structures like a *chirped* PCF (Fig.(1.2b)) and suspended core fibers (Fig.(1.2c,d)), used for example for gas sensing [27]. They are not only realized in pure silica, but also in composition with doping [28] or in completely other material like polymer fibers [29].

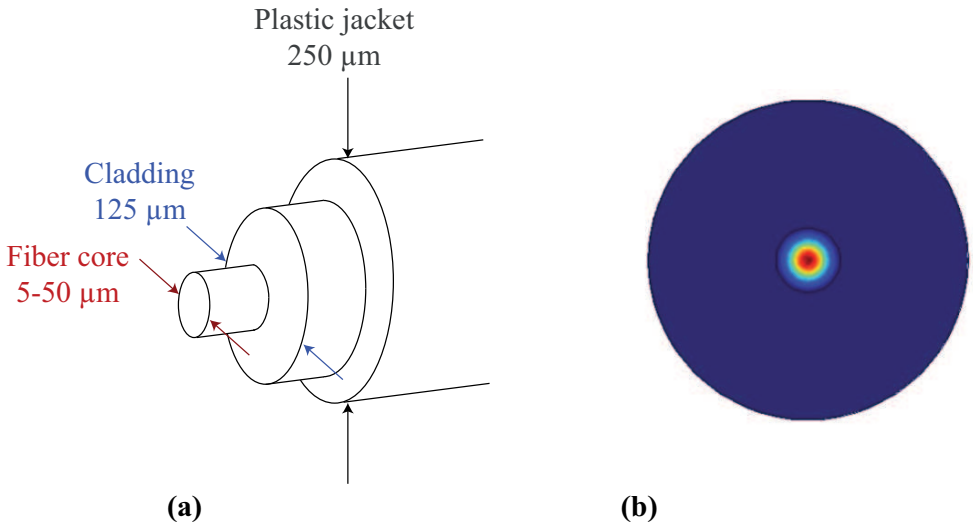

Figure 1.3: (a) Structure of a conventional step-index fiber, (b) fundamental optical mode in a step-index fiber.

1.1.2 Fiber parameters

The underlying physics of conventional optical fibers is based on the well known internal total reflection, where no light escape the fiber core below a certain critical angle $\theta_c = \cos^{-1}(n_{\text{clad}}/n_{\text{core}})$ where n_{clad} and n_{core} are the refractive indices of the fiber cladding and core, respectively [12]. Fig.(1.3) shows a simplified view of a conventional step-index fiber that consists of three main components :

- SiO_2 fiber core (about 5-50 µm diameter), doped with GeO_2 to obtain a slightly higher refractive index
- SiO_2 fiber cladding (125 µm diameter) with a lower refractive index as the fiber core
- Plastic protecting jacket to absorb light that is not properly guided in the fiber core but mainly to protect the glass from mechanical strengths.

As previously shown, the configuration of a PCF is completely different. Here we find two general types of compositions: an air-hole structure with a solid core (Fig.(1.1a)) and a hollow core (Fig.(1.1b)). Solid core fibers follow the same physics as step index fibers since the refractive index around the fiber core is lower than in the fiber core itself. As a consequence, doping the fiber core is no more needed which was the first idea of Kaiser *et al.* in Ref. [32] for a single-material fiber which resulted later in the invention of PCFs. The mechanism of the guiding in hollow core fibers, so-called photonic bandgap guidance, is a bit harder to understand since the fiber core has a refractive index of n=1

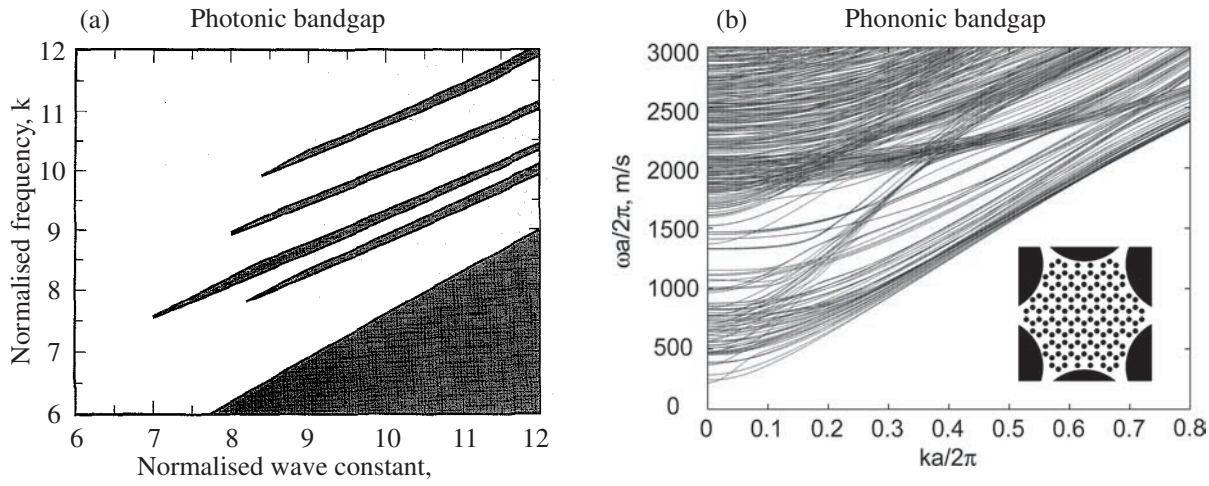

Figure 1.4: (a) Full 2-D optical bandgaps (shaded) of silica/air structure in Ref. [11], (b) acoustic bandgap diagramm of a nanostructured fiber, shown in the inset from Ref. [24].

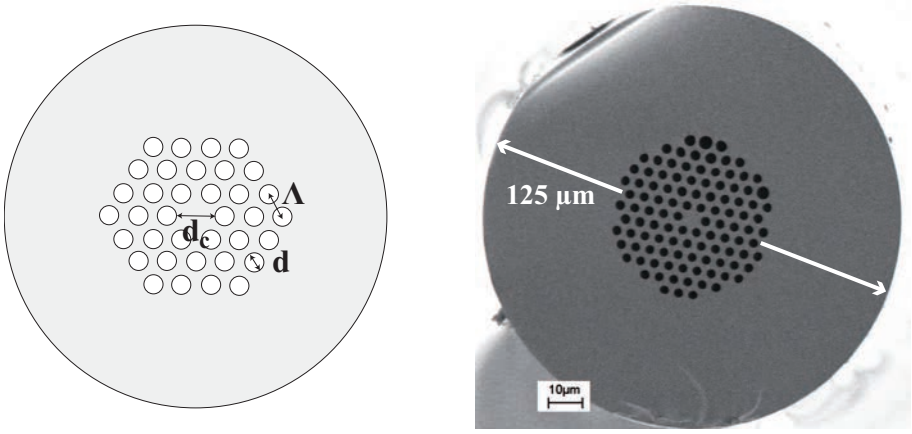

Figure 1.5: Cross-section of a PCF with hexagonal structure: d_c is the core diameter , Λ the pitch and d the air-hole diameter.

(air) which is lower than in the air-hole structure around the fiber core. Light propagation in this kind of PCF is based on the coherent reflection of light in the micro structured periodic cladding around the fiber core [12]. The air-hole structure gives rise to *photonic bandgaps*, as shown in Fig.(1.4a). If light is injected on a mode which is forbidden in the band diagram of the air-hole structure, the light is trapped in the fiber core and hence, is guided in air. This is also valid for acoustic waves as can be seen in Fig.(1.4b) that shows a *phononic bandgap* in a nano-structured PCF. In Fig.(1.5) we find the typical structural parameters: the core diameter d_c, the distance between two air holes centers (the pitch) Λ and the hole diameter d. After this short explanation of the respective guidance mechanism we define some important parameters for conventional fibers as well as for PCF.

1.1.2.1 Fiber loss

The most basic fiber parameter is the linear attenuation which is due to absorption abilities of every material and linear Rayleigh scattering. In silica the linear loss developed from 1000 dB/km [4] over a breakthrough in 1970 to 20 dB/km [6] to about 0.17 dB/km nowadays [33]. For a fiber with length L the output power P_{out} versus the input one P_{in} can be written as:

$$P_{out} = P_{in} \exp(-\alpha_{lin} L) \tag{1.1}$$

Here α is the absorption coefficient on a linear scale. However, in fiber optics the attenuation is often given in dB. The linear loss coefficient α_{dB} in dB and on a linear scale is related as [34]:

$$\alpha_{dB} = -\frac{10}{L} \log\left(\frac{P_{out}}{P_{in}}\right) = 4.343\, \alpha_{lin} \tag{1.2}$$

An effective length for fibers can be defined as follows [34]:

$$L_{\text{eff}} = \frac{(1 - \exp(-\alpha_{lin} L))}{\alpha_{lin}} \tag{1.3}$$

For nonlinear effects, the effective length is a more meaningful parameter as the linear loss or the fiber length, because former are dependent of the intensity of the launched optical wave. Concerning nonlinear effects, the fiber can be seen as a loss-less fiber with length L_{eff} instead of taking into account loss and real fiber length (Fig.(1.6)). For very long fibers ($\alpha L < 10$), the effective length tends to $1/\alpha_{lin}$.

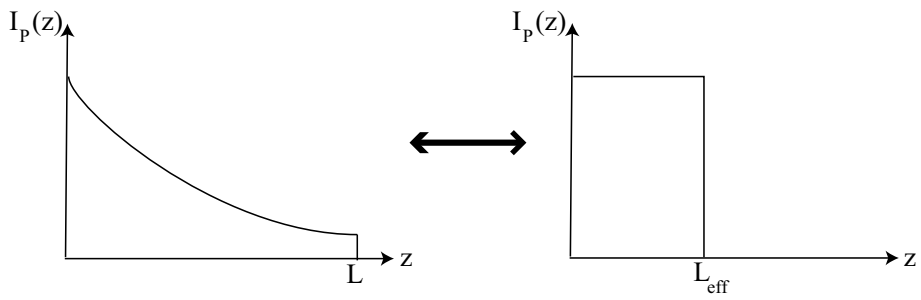

Figure 1.6: Distributed pump power due to fiber loss in the fiber with its real length and equivalent fictive loss-less fiber with effective length L_{eff} [35].

1.1.2.2 Effective mode area

The effective mode area (EMA) of fibers can be derived from the modal distribution $F(x, y)$ of the fundamental fiber mode and writes as [34]:

$$A_{\text{eff}} = \frac{\left(\int\int_{-\infty}^{\infty} |F(x,y)|^2 \, dxdy\right)^2}{\int\int_{-\infty}^{\infty} |F(x,y)|^4 \, dxdy} \tag{1.4}$$

where $F(x, y)$ is the transverse distribution of the optical mode, for SMF the fundamental mode. The EMA of a fiber is important because nonlinear effects are rising with higher intensity density. Since PCFs often have small fiber cores, their EMA is small as well and nonlinear effects get more important. The other way around, large mode area fibers are especially made to avoid high nonlinear effects such as Brillouin and Raman Scattering. Later we will see that the EMA plays a role for the critical power for stimulated Brillouin scattering.

1.1.2.3 Numerical aperture

The numerical aperture (NA) of a fiber is one of the parameters that are always provided by fiber manufacturers because it is related to the maximum angle θ_c^{air} under which light can be injected into the fiber core [12]:

$$NA = sin(\theta_c^{\text{air}}) = \sqrt{n_{\text{core}}^2 - n_{\text{clad}}^2} = n_{\text{core}} sin(\theta_c) \tag{1.5}$$

The NA is normally measured at the output of the fiber and defined at 1% of the Gaussian intensity profile. Since in a multimode fiber the higher modes are more diffracted at the

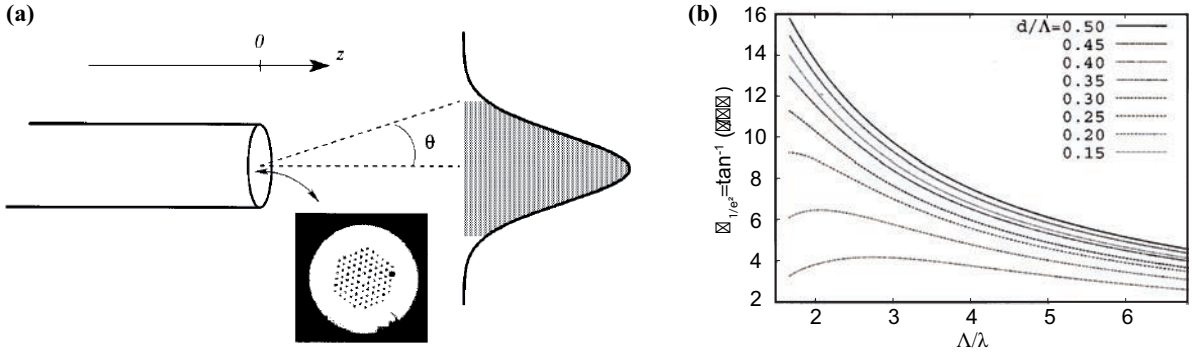

Figure 1.7: (a) Coupling of light from the output of the fiber into free space with half-divergence angle θ [36]; (b) Half-divergence angle of a PCF for different hole sizes [36].

fiber output the Gaussian profile gets broader and the NA is higher. This factor is important if working with free space optics and can be calculated for PCFs [37]:

$$NA \approx \left(1 + \frac{\pi A_{\text{eff}}}{\lambda^2}\right)^{-1/2} \tag{1.6}$$

with A_{eff} the EMA and λ the wavelength of the incident light. This approximation has been made for a Gaussian field of width ω since there is the standard approximate expression $\tan\theta = \lambda/\pi\omega$ for the half-divergence angle θ (Fig.(1.7a)) of the light diffracted at the output of the fiber [37, 38]. In [36] we find a study of the NA in dependence of the air filling fraction d/Λ (Fig.(1.7b)) where it can be seen that for larger air holes, the numerical aperture rises independently from the core diameter which has been fixed in this study.

1.1.2.4 Cutoff wavelength

For conventional fibers the following cutoff wavelength can be calculated to know above which wavelength the fiber is a single mode fiber [34]:

$$\lambda = \frac{2\pi a}{V}\sqrt{n_{\text{core}}^2 - n_{\text{clad}}^2} \tag{1.7}$$

where V=2.405 is the normalized frequency and the first zero of the Bessel function J_0 [12] and a the radius of the fiber core. This means that single mode propagation for a short wavelength of 500 nm requires a small fiber core. Increasing then the launched wavelength in such a small core fiber causes that the fundamental mode spreads further into the cladding, which ends up in a high sensitivity to fiber bending [12].
As already mentioned, it has been shown in [14] that PCFs have a large range of single mode guidance and can even be endlessly single mode. For PCFs, Eq.(1.7) has to be

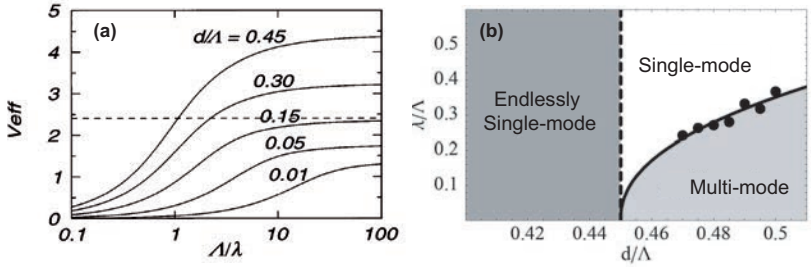

Figure 1.8: (a) Variation of V_{eff} with Λ/λ for various air filling fractions d/Λ, dashed line: V=2.405, cutoff value for a step-index fiber [14]; (b) Cutoff wavelength over air filling fraction in which three different regimes are shown: single mode, multi mode and endlessly single mode [37].

modified because there is no refractive index n_{clad} but rather an effective index $n_{clad,eff}$ for the air hole cladding structure [14]:

$$\lambda = \frac{2\pi a_{\text{eff}}}{V_{\text{eff}}} \sqrt{n_{\text{core}}^2 - n_{\text{clad,eff}}^2} \tag{1.8}$$

where a_{eff} is the diameter of a circle that is embedded into the hexagonally symmetric fiber core and V_{eff} depends on the air filling fraction, as shown in Fig.(1.8a). For certain values of d/Λ, V_{eff} is always below the critical value V=2.405, which means that the fiber is single-mode for all wavelengths. Another study has been done in Ref. [37] where the same results has been obtained, presented in Fig.(1.8b). We obtain an endlessly single mode fiber under a certain value of the air filling fraction d/Λ and the typical behaviour of a cutoff wavelength above this value. An empirical formula for this cutoff wavelength in function of d and Λ is given by [37]:

$$\lambda \approx 1.34\,\Lambda \left(\frac{d}{\Lambda} - 0.45\right)^{0.45} \tag{1.9}$$

1.1.2.5 Birefringence

The so-called single-mode fibers guide actually two optical modes simultaneously. They are orthogonally polarized and the two will propagate with the same velocity in perfectly radial-symmetric fibers. In birefringent fibers, i.e. fibers that are not completely radial symmetric, these two modes have a different phase and group velocity because the refractive index is different for the different modes, propagating according to an x-axis and orthogonal y-axis. The phase modal birefringence is given by:

$$B_m = \frac{|\beta_x - \beta_y|}{k_0} = |n_x - n_y| = \Delta n \tag{1.10}$$

with β_i the mode propagation constant, k_0 the wave vector in vacuum and n_i the refractive index according to the axis. The group modal birefringence can then be written as:

$$\Delta N = \Delta n - \lambda \frac{d\Delta n}{d\lambda} \tag{1.11}$$

Conventional fibers are theoretically not birefringent but material and geometrical inhomogeneities can induce a low birefringence in the order of 10^{-6}. As one may think that PCFs with a hexagonal structure may be birefringent since they have not the same air-material distribution in x- and y-axis, it should be emphasized here, that this is not the case. As explained in [39] the hexagonal symmetry of a perfect micro structured fiber leads to no birefringence. Nevertheless, PCFs are more sensitive to irregularities, since small variations of the hole diameter lead to a different refractive index. Besides the drawing process of PCFs is more complicated and induces more fiber irregularities [40, 41]. On

the other hand PCFs with asymmetrical air hole structure like two big air holes, as shown in Fig.(1.2), can reach ultra-high birefringence up to 10^{-2}, as presented in Refs. [42, 43].

1.1.2.6 Dispersion

Dispersion describes the effect that the refractive index n is dependent on the light frequency. The parameter $\beta(\omega)$ is the mode propagation constant of the optical mode and can be developed as follows by Taylor expansion:

$$\beta(\omega) = n(\omega)\frac{\omega}{c} = \beta_0 + \beta_1(\omega - \omega_0) + 1/2\beta_2(\omega - \omega_0)^2 + ... \tag{1.12}$$

with

$$\beta_m = \left(\frac{d^m\beta}{d\omega^m}\right)_{\omega=\omega_0} \tag{1.13}$$

$m = 0...n$ and

$$\beta = \frac{n_{\text{eff}}\omega}{c} \tag{1.14}$$

We can calculate β_1 and β_2:

$$\beta_1 = 1/V_G = n_G/c = 1/c \cdot \left(n_{\text{eff}} + \omega\frac{dn_{\text{eff}}}{d\omega}\right) \tag{1.15}$$

$$\beta_2 = 1/c(2\frac{dn_{\text{eff}}}{d\omega}) + \omega\frac{dn_{\text{eff}}^2}{d\omega^2}) \tag{1.16}$$

where V_G is the group velocity and n_G the group refractive index. The group velocity dispersion (GVD) can be derived:

$$D(\lambda) = \frac{d\beta_1}{d\lambda} = -\frac{2\pi c}{\lambda^2}\beta_2 = -\frac{\lambda}{c}\frac{d^2n_{\text{eff}}}{d\lambda^2} \tag{1.17}$$

given in $ps \cdot nm^{-1} \cdot km^{-1}$. The zero-dispersion wave length (ZDW) is defined at D=0 and is important for pulse propagation and for nonlinear processes as for example those that lead to supercontinuum generation. PCFs have the particularity that the ZDW can be adjusted by the micro structure and even two or three dispersion wavelengths can be obtained [44].

1.1.2.7 Fabrication and splicing

Micro structured optical fibers need a more specific drawing process than conventional fibers because of their tiny air-hole micro-structure. Here, the procedure for the most common PCFs with a hexagonal structure is shortly sketched in Fig.(1.9). In a first step

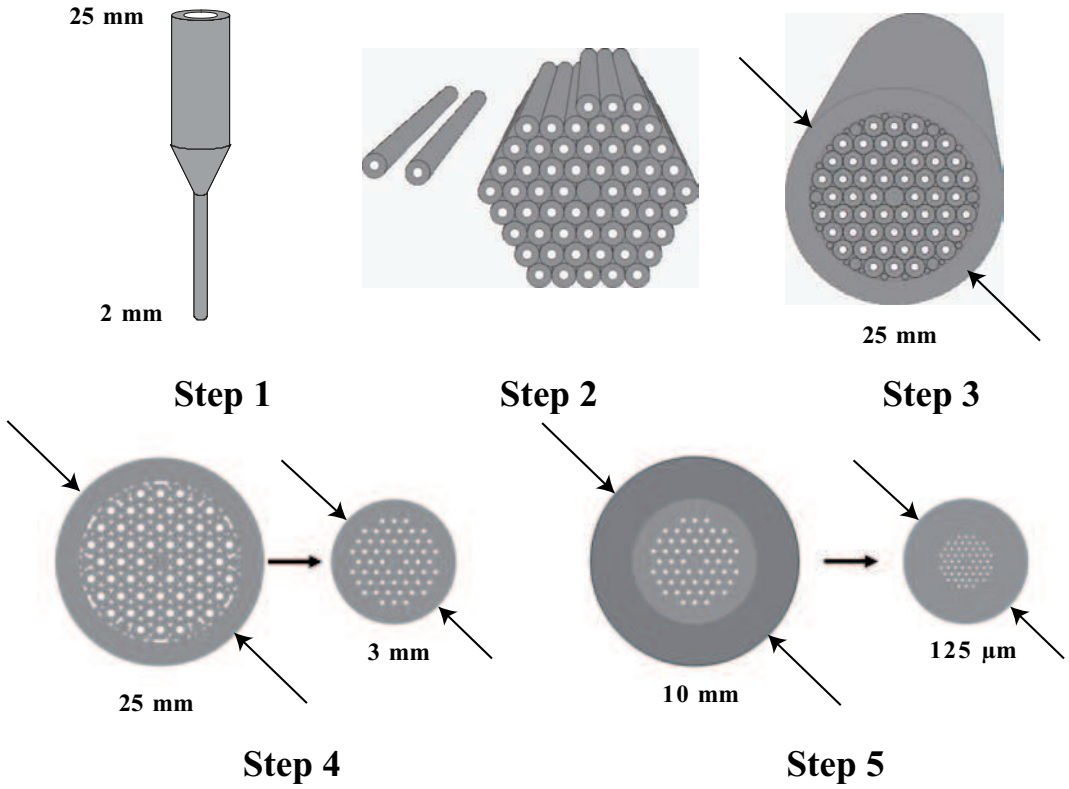

Figure 1.9: Example of a PCF drawing process for a PCF with hexagonal structure, schemes courtesy of A. Kudlinski, Ircica Lille

.

capillary-shaped rods are drawn down to 2 mm diameter. Then they are hexagonally arranged with a solid rod (solid core fiber) or also capillary rod (hollow core) in the middle to build the fiber core (step 2). The third step is inserting this structure in a jacketing tube which is the primary PCF preform, the *stack* (25 mm diameter). This stack is then drawn down to 3 mm, to a so-called *cane*, in step 4. In a last step a second jacketing tube surrounds the cane and will finally be drawn down to the PCF with a 125 µm outer diameter. During this last step the temperature, pressure and drawing velocity is precisely controlled because it is crucial in order to obtain the same air hole size and a uniform longitudinal structure. In paragraph 3.4 two PCFs with different drawing processes will be compared with respect to their longitudinal uniformity. It is also possible to insert purposely micro structure variations by sinusoidally changing the outer diameter. These fibers are investigated in chapter 4 by different Brillouin scattering measurements.

Splicing PCF to conventional SMF has attracted much interest because the connection between them is challenging. The different mode field diameter and the sensitive air hole structure of the PCF need a specific splicing process. In our experiments two different fiber splicers were used: arc fusing splicer (with Ericsson FSU 995 PM) and filament

fusing splicer (Vytran FFS-2000). In general the two fiber ends that should be spliced are cleaned and cleaved carefully, so that their end facet are perfectly plane. Then they are aligned by help of high precision micro controllers. In case of arc fusing splicing an electric spark is generated that rises the temperature up to the melting point of silica and melts both fiber ends together. In contrast filament fusing uses a tungsten filament that allows for a slower splicing and thus for a more homogeneous splicing point and lower splicing losses. Moreover, the fiber is heated over a longer length of the fiber which can be used for taper drawing. For a deeper insight and an overview about some interesting papers about PCF splicing the reader is referred to Ref. [45] and for fusing splicing to Ref. [46].

1.2 Nonlinear effects in optical fibers

In order to describe light propagating through a material, we have to consider how the polarization (the dipole moment per unit volume) changes with an applied electric field. The induced polarization $\mathbf{P}$ for a dielectric material, that is exposed to an electric field $\mathbf{E}$, can be written as [47]:

$$\mathbf{P} = \epsilon_0 \, \chi \, \mathbf{E} \tag{1.18}$$

where χ is the susceptibility, dependant on the material. For intense electric fields, the response of the material gets nonlinear which is expressed in the following extended form where the susceptibility χ developed in higher orders:

$$\begin{aligned} \mathbf{P} &= \epsilon_0 \left(\chi^{(1)} \cdot \mathbf{E} + \chi^{(2)} : \mathbf{EE} + \chi^{(3)} \vdots \mathbf{EEE} + ... \right) = \\ &= \mathbf{P}_{\mathrm{L}}^{(1)} + \mathbf{P}_{\mathrm{NL}}^{(2)} + \mathbf{P}_{\mathrm{NL}}^{(3)} + ... \end{aligned} \tag{1.19}$$

where ϵ_0 is the vacuum permittivity and $\chi^{(j)}$ the jth order susceptibility.

1.2.1 Second-order susceptibility

The second-order susceptibility $\chi^{(2)}$ is responsible for nonlinear effects like second harmonic generation (SHG), sum-frequency generation (SFG), difference-frequency generation (DFG), optical parametric amplification (OPA), optical rectification and the Pockels effect. But the second-order susceptibility has only an important contribution in crystals with no inversion symmetry at a molecular level. A widely used material that is not inversion symmetric is $LiNbO_3$ because it exhibits one high nonlinear coefficient in the susceptibility matrix $\chi^{(2)}$. A lot of research has been made for example about photonic

crystals and periodically poled $LiNbO_3$, but also for applications like electro-optics modulators it is an important material. Nevertheless, the second-order susceptibility disappears in materials with inversion symmetry like silica which is mostly used for optical fibers. Here, the most important nonlinear effects results from the third-order susceptibility $\chi^{(3)}$.

1.2.2 Third-order susceptibility

From $\chi^{(3)}$ the refractive index can be rewritten in dependence of the intensity $I = |\mathbf{E}|^2$ of the optical field such as:

$$n(I) = n_0 + n_2 |\mathbf{E}|^2 \tag{1.20}$$

where n_0 is due to the linear susceptibility and n_2 can be calculated as:

$$n_2 = \frac{3}{8n} \mathrm{Re}[\chi^3_{xxxx}]. \tag{1.21}$$

The nonlinear attenuation is given by:

$$\alpha_2 = \frac{3\omega_0}{4nc} \mathrm{Im}[\chi^3_{xxxx}]. \tag{1.22}$$

The intensity-dependent refractive index is known as the optical Kerr-effect. In optical fibers where the fiber core is doped with GeO_2, n_2 is about $2.6{\cdot}10^{-20}\,\mathrm{m^2W^{-1}}$ [34] and in pure silica $2.2{\cdot}10^{-20}\,\mathrm{m^2W^{-1}}$ [48]. By help of the nonlinear refractive index, the nonlinear coefficient is defined as:

$$\gamma = \frac{2\pi n_2}{\lambda A_{\mathrm{eff}}} \tag{1.23}$$

given in $W^{-1}km^{-1}$, where A_{eff} is the EMA and λ the wavelength of the incident wave. The nonlinear coefficient γ in silica is small compared to other nonlinear materials but the fact that the light is confined in a small fiber core is responsible that γ still plays an important role in silica fibers.
Some important nonlinear effects resulting from the third-order susceptibility $\chi^{(3)}$ are: third-harmonic generation (THG), four wave mixing (FWM), parametric amplification, stimulated Raman scattering (SRS), cross-phase modulation (XPM), self-phase modulation (SPM) and modulation instability (MI):

- SRS is an inelastic scattering effect and will be further explained in chapter 2.
- THG and FWM are considered as elastic phenomena where THG results in the generation of one photon with angular frequency $3{\cdot}\omega$ out of three photons with angular frequency ω. FWM results in the generation of two photons with angular frequency ω_3 and ω_4 out of two photons ω_1 and ω_2 such as:

$$\omega_1 + \omega_2 = \omega_3 + \omega_4 \tag{1.24}$$

- SPM occurs when an optical wave experiences a self-induced phase shift due to the optical Kerr-effect:

$$\Phi_{\mathrm{SPM}} = (n_0 + n_2 \left|\mathbf{E}\right|^2) k_0 L \tag{1.25}$$

  where k_0 is the wavevector and L the fiber length. SPM is the reason for soliton generation and for spectral broadening of the Brillouin gain in optical fibers if the pump pulse gets too short.

- XPM causes a phase shift to an optical wave with angular frequency ω_1 by another co-propagating wave with angular frequency ω_2:

$$\Phi_{\mathrm{XPM}} = n_2 k_0 L(\left|\mathbf{E}_1\right|^2 + 2\left|\mathbf{E}_2\right|^2) \tag{1.26}$$

  or between two orthogonally polarized angular frequencies:

$$\Phi_{\mathrm{XPM}} = n_2 k_0 L(\left|\mathbf{E}_x\right|^2 + 2/3\left|\mathbf{E}_y\right|^2) \tag{1.27}$$

- MI is the result from the interaction between nonlinearities and dispersion. It is observed at high optical intensity as two broad side-bands symmetrical around the pump wave and can be interpreted as a degenerated FWM process where energy is transferred from the pump wave to both side-bands.

After this short overview about third-order nonlinear effects, an introduction into linear and nonlinear, elastic and inelastic scattering with a focus on Brillouin scattering will be given in the next chapter.

Bibliography

[1] A. Sano, H. Masuda, T. Kobayashi, M. Fujiwara, K. Horikoshi, E. Yoshida, Y. Miyamoto, M. Matsui, M. Mizoguchi, H. Yamazaki, Y. Sakamaki, and H. Ishii, "69.1-Tb/s (432 x 171-Gb/s) C- and extended L-band transmission over 240 km using PDM-16-QAM modulation and digital coherent detection", in *Optical Fiber Communication Conference, OFC*, 2010, PDPB7.

[2] D. Qian, M. Huang, E. Ip, Y. Huang, Y. Shao, and T. Wang J. Hu, "101.7-Tb/s (370x294-Gb/s) PDM-128QAM-OFDM transmission over 3x55-km SSMF using pilot-based phase noise mitigation", in *Optical Fiber Communication Conference, OFC*, 2011, PDPB5.

[3] K. C. Kao and G. A. Hockham, "Dielectric-fibre surface waveguides for optical frequencies", *IEE Proceedings J Optoelectronics*, vol. 133, no. 3, pp. 1151–1158, 1966.

[4] G. P. Agrawal, *Fiber-Optic Communication Systems*, John Wiley & Sons, inc, 2nd edition, 1997.

[5] T. H. Maiman, "Stimulated optical radiation in ruby", *Nature*, vol. 187, pp. 493–494, 1960.

[6] F. P. Kapron, D. B. Keck, and R. D. Maurer, "Radiation losses in glass optical waveguides", *Applied Physics Letters*, vol. 17, no. 10, pp. 423–425, 1970.

[7] J. I. Yamada, S. Machida, and T. Kimura, "2 Gbit/s optical transmission experiments at 1.3 μm with 44 km single-mode fibre", *Electronics Letters*, vol. 17, no. 13, pp. 479 – 480, 1981.

[8] T. Miya, Y. Terunuma, T. Hosaka, and T. Miyashita, "Ultimate low-loss single-mode fibre at 1.55 μm", *Electronics Letters*, vol. 15, no. 4, pp. 106–108, 1979.

[9] J. C. Knight, T. A. Birks, P. St. J. Russell, and D. M. Atkin, "All-silica single-mode optical fiber with photonic crystal cladding", *Optics Letters*, vol. 21, no. 19, pp. 1547–1549, 1996.

[10] P. St.J. Russell, "Photonic crystal fibers", *Science*, vol. 299, pp. 358–362, 2003.

[11] T. A. Birks, P. J. Roberts, P. St. J. Russell, D. M. Atkin, and T. J. Shepherd, "Full 2-d photonic bandgaps in silica/air structures", *Electronics Letters*, vol. 31, no. 22, pp. 1941–1943, 1995.

[12] L. Thévénaz, Ed., *Advanced Fiber Optics, Concepts and Technology*, EPFL Press, 2011.

[13] R. F. Cregan, B. J. Mangan, J. C. Knight, T. A. Birks, P. St. J. Russell, P. J. Roberts, and D. C. Allan, "Single-mode photonic band gap guidance of light in air", *Science*, vol. 285, no. 5433, pp. 1537–1539, 1999.

[14] T. A. Birks, J. C. Knight, and P. St. J. Russel, "Endlessly single-mode photonic crystal fibers", *Optics Letters*, vol. 22, no. 13, pp. 961–963, 1997.

[15] J. C. Knight, T. A. Birks, R. F. Cregan, P. St.J. Russell, and J-P. de Sandro, "Large mode area photonic crystal fiber", *Electronics Letters*, vol. 34, no. 13, pp. 1347–1348, 1998.

[16] W. J. Wadsworth, R. M. Percival, G. Bouwmans, J. C. Knight, and P. St. J. Russell, "High power air-clad photonic crystal fiber laser", *Optics Express*, vol. 11, no. 1, pp. 48–53, 2003.

[17] A. Ferrando, E. Silvestre, P. Andrés, J. J. Miret, and M. V. Andrés, "Designing the properties of dispersion-flattened photonic crystal fibers", *Optics Express*, vol. 9, no. 13, pp. 687–697, 2001.

[18] T. A. Birks, D. Mogilevtsev, J. C. Knight, and P. St. J. Russell, "Dispersion compensation using single-material fibers", *Journal of Lightwave Technology*, vol. 11, no. 6, pp. 674–676, 1999.

[19] J. Y. Y. Leong, P. Petropoulos, J. H. V. Price, H. Heidepriem, S. Asimakis, R. C. Moore, K. E. Frampton, V. Finazzi, X. Feng, T. M. Monro, and D. J. Richardson, "High-nonlinearity dispersion-shifted lead-silicate holey fibers for efficient 1 μm pumped supercontinuum generation", *Journal of Lightwave Technology*, vol. 24, no. 1, pp. 183–190, 2006.

[20] J. K. Ranka, R. S. Windeler, and A. J. Stentz, "Optical properties of high-delta air silica microstructure optical fibers", *Optics Letters*, vol. 25, no. 11, pp. 796–798, 2000.

[21] J. M. Dudley, G. Genty, and S. Coen, "Supercontinuum generation in photonic crystal fiber", *Physical Review Letters B*, vol. 78, no. 4, pp. 1135–1184, 2006.

[22] M. W. Haakestad and H. E. Engan, "Acoustooptic properties of a weakly multimode solid core photonic crystal fiber", *Journal of Lightwave Technology*, vol. 24, no. 2, pp. 838–845, 2006.

[23] P. St. J. Russell, E. Martin, A. Diez, S. Guenneau, and A. B. Movchan, "Sonic band gaps in PCF preforms: enhancing the interaction of sound and light", *Optics Express*, vol. 11, no. 20, pp. 2555, 2003.

[24] V. Laude, A. Khelif, S. Benchabane, M. Wilm, T. Sylvestre, B. Kibler, A. Mussot, J. M. Dudley, and H. Maillotte, "Phononic band-gap guidance of acoustic modes in photonic crystal fibers", *Physical Review B*, vol. 71, no. 4, pp. 045107, 2005.

[25] J.-C. Beugnot, T. Sylvestre, H. Maillotte, G. Mélin, and V. Laude, "Guided acoustic wave Brillouin scattering in photonic crystal fibers", *Optics Letters*, vol. 32, no. 1, pp. 17–19, 2007.

[26] D. Elser, U. L. Andersen, A. Korn, O. Glockl, S. Lorenz, Ch. Marquardt, and G. Leuchs, "Reduction of guided acoustic wave Brillouin scattering in photonic crystal fibers", *Physical Review Letters*, vol. 97, pp. 133901, 2006.

[27] T. Ritari, J. Tuominen, H. Ludvigsen, J. Petersen, T. Sørensen, T. Hansen, and H. Simonsen, "Gas sensing using air-guiding photonic bandgap fibers", *Optics Express*, vol. 12, no. 17, pp. 4080–4087, 2004.

[28] W. J. Wadsworth, J. C. Knight, W. H. Reeves, P. St. J. Russel, and J. Arriaga, "Yb -doped photonic crystal fiber laser", *Electronics Letters*, vol. 36, no. 17, pp. 1452–1454, 2000.

[29] M. van Eijkelenborg, M. Large, A. Argyros, J. Zagari, S. Manos, N. Issa, I. Bassett, S. Fleming, R. McPhedran, C. Martijn de Sterke, and N. A. Nicorovici, "Microstructured polymer optical fibre", *Optics Express*, vol. 9, no. 7, pp. 319–327, 2001.

[30] J. S. Skibina, R. Iliew, J. Bethge, M. Bock, D. Fischer, V. I. Beloglasov, R. Wedell, and G. Steinmeyer, "A chirped photonic-crystal fibre", *Nature Photonics*, vol. 2, pp. 679–683, 2008.

[31] J. Bethge, G. Steinmeyer, S. Burger, F. Lederer, and R. Iliew, "Guiding properties of chirped photonic crystal fibers", *Journal of Lightwave Technology*, vol. 27, no. 11, pp. 1698–1706, 2009.

[32] P. V. Kaiser and H. W. Astle, "Low-loss single-material fibers made from pure fused silica", *The Bell System Technical Journal*, vol. 53, pp. 1021–1039, 1974.

[33] *Corning, SMF 28*, http://www.corning.com.

[34] G. P. Agrawal, *NonLinear Fiber Optics*, Academic Press, third edition, 2001.

[35] M. Niklès, *La Diffusion Brillouin dans les fibres optiques : étude et application aux capteurs distribués*, PhD thesis, Ecole Polytechnique Fédérale de Lausanne, 1997.

[36] N. A. Mortensen, J. R. Folken, P. M. W. Skovagaard, and J. Broeng, "Numerical aperture of single-mode photonic crystal fibers", *IEEE Photonics Technology Letters*, vol. 14, no. 8, pp. 1094, 2002.

[37] N. A. Mortensen, "Effective area of photonic crystal fibers", *Optics Express*, vol. 10, no. 7, pp. 341–348, 2002.

[38] A. K. Ghatak and K. Thyagarajan, *Introduction to Fiber Optics*, Cambridge University Press, 1998.

[39] M. J. Steel, T. P. White, C. Martijn de Sterke, R. C. McPhedran, and L. C. Botten, "Symmetry and degeneracy in microstructured optical fibers", *Optics Letters*, vol. 26, no. 8, pp. 488–490, 2001.

[40] I. K. Hwang, Y. J. Lee, and Y. H. Lee, "Birefringence induced by irregular structure in photonic crystal fibers", *Optics Express*, vol. 11, no. 22, pp. 2799, 2003.

[41] K. S. Hong, K. J. Lee, D.-I. Yeom, and B. Y. Kim, "Characterization of structural irregularities in highly birefringent photonic crystal fiber using torsional acoustic polarization coupling", *Optics Communications*, vol. 283, no. 20, pp. 4094–4098, 2010.

[42] H. Ademgil and S. Haxha, "Highly nonlinear birefringent photonic crystal fiber", *Optics Communications*, vol. 282, pp. 2831–2835, 2009.

[43] J. Olszewski, "Birefringence analysis in photonic crystal fibers with germanium-doped core", *J. Opt. A: Pure Appl. Opt.*, vol. 11, no. 4, pp. 045101, 2009.

[44] A. Boucon, D. Alasia, J. Beugnot, G. Mélin, S. Lempereur, A. Fleureau, H. Maillotte, J. M. Dudley, and T. Sylvestre, "Supercontinuum generation from 1.35 to 1.7 μm by nanosecond pumping near the second zerodispersion wavelength of a microstructured fiber", *IEEE Photonics Technology Letters*, vol. 20, no. 10, pp. 842 – 844, 2008.

[45] J.-C. Beugnot, *La diffusion Brillouin dans les fibres optiques microstructurées*, PhD thesis, Université de Franche-Comté, 2007.

[46] *Vytran*, http://www.vytran.com/.

[47] R. W. Boyd, *Nonlinear Optics*, Academic Press, third edition, 2001.

[48] L. D. Landau and E. M. Lifshitz, *Statistical Physics*, Butterworth-Heinemann, 3rd edition, 1984.

Chapter 2

Light Scattering

In any material, that is not completely homogeneous, light waves are scattered due to density fluctuations, impurities or thermal particles motion [1]. Different types of scattering occur:

- Linear scattering, where the incident optical waves do not modify the optical properties of the material which is the case below a certain threshold for each type of scattering. Linear scattering can be distinguished in elastic and inelastic scattering. Photons in an elastic scattering process keep their energy, hence no frequency shift of the scattered photons is observed, which is the case for Rayleigh scattering. Inelastic scattering results from an energy exchange with the material and thus leads to a frequency shift for the scattered optical wave, like spontaneous Raman scattering and spontaneous Brillouin scattering.
- Nonlinear scattering modifies the optical medium by electrostriction in case of stimulated Brillouin scattering (SBS) and initiation of molecular vibrational and rotational states for stimulated Raman scattering (SRS).

In this chapter an overview about these light scattering types will be given with a special emphasis on Brillouin scattering, both spontaneous and stimulated scattering.

2.1 Linear Scattering

The term *linear* scattering comes from the fact that the susceptibility of the material is independent from the propagating electric field if the optical intensity remains under a

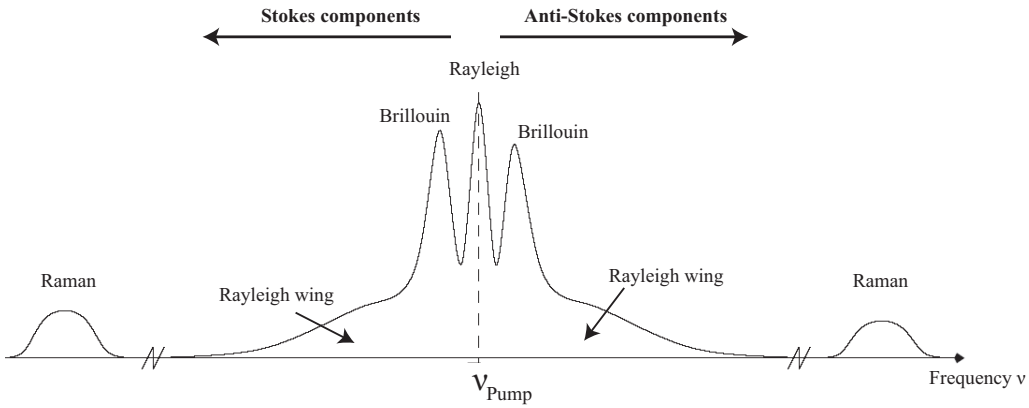

Figure 2.1: Typical linear scattering spectrum with Stokes and Anti-Stokes components of Raman, Brillouin and Rayleigh scattering.

certain limit. Then the polarization in Eq.(1.19) is only *linearly* dependent on the electrical field. A typical optical spectrum of linearly scattered light is depicted in Fig.(2.1). The scattered waves with a higher frequency compared to the pump frequency are called Anti-Stokes components, the lower frequency waves are the Stokes components. The Anti-Stokes components arise when the optical wave absorbs already existing phonons, the Stokes-components originate from the optical wave dispensing energy on phonons. The four different types of linear scattering can be distinguished by their frequency shift, intensity and the form and full width at half maximum (FWHM) of the spectrum as it will be explained in the next paragraphs.

2.1.1 Elastic Scattering: Spontaneous Rayleigh and Rayleigh-wing scattering

Rayleigh scattering results from the interaction of light with non-propagating density fluctuations and leads to spectral broadening (15 MHz) without any frequency shift [2]. It has been observed in 1871 by Lord John William Strutt Rayleigh and is the origin for the blue color of the sky. Light excites the dipole molecules which by themselves emit the same wavelength where the deviation angle depends on the incident wavelength. Rayleigh scattering is in addition to infra-red absorption responsible for linear loss in optical fibers. Rayleigh-wing scattering originates from fluctuations in the orientation of anisotropic molecules [2] and is spectrally broad with a FWHM of 150 GHz because of the fast molecular reorientation response.

2.1.2 Inelastic Scattering: Spontaneous Raman and Brillouin scattering

When light exchanges energy with the optical medium, as it is the case for inelastic scattering, the frequency of the scattered photons changes. Here, the interaction with optical and acoustic phonons is described: spontaneous Raman and Brillouin scattering.

2.1.2.1 Spontaneous Raman Scattering

Raman scattering is based on the interaction of optical waves with optical phonons. Spontaneous Raman scattering is weak, the scattering cross section per unit volume is only $10^{-6}\,\mathrm{cm}^{-1}$ [2]. These high frequency phonons are present as vibrational modes in the molecules of the medium. Thus, the frequency shift is as high as 13.2 THz due to a response time of 75 fs, hence a lot more shifted from the pump wave as Brillouin scattering. The FWHM of spontaneous Raman scattering is about 40 THz and the decay time of the optical phonons is 150 fs. Spontaneous Raman scattering can be seen as a more local effect due to its molecular origin whereas Brillouin scattering concerns larger areas of the material, since it is due to acoustic waves in the material.

2.1.2.2 Spontaneous Brillouin scattering

Brillouin scattering originates from acoustic phonons in contrast to the optical phonons that cause Raman scattering. Acoustic phonons are acoustic waves or elastic waves. At a temperature $\mathrm{T} > 0\,\mathrm{K}$ these acoustic vibrations are present everywhere in the optical fiber and the phonon number is distributed following the Bose-Einstein distribution:

$$N = \frac{1}{\exp\left(\frac{hf}{kT}\right) - 1} + \frac{1}{2}. \tag{2.1}$$

where f is the frequency of the phonon, h is the Planck constant and k the Boltzmann constant. These acoustic phonons can be expressed as a density variation [2]:

$$\Delta\rho = \left(\frac{\partial\rho}{\partial p}\right)_s \Delta p + \left(\frac{\partial\rho}{\partial s}\right)_p \Delta s \tag{2.2}$$

where ρ is the density, p the pressure and s entropy. The first term is due to acoustic waves (adiabatic density fluctuations) and is important for the description of Brillouin scattering. The second term comes from isobaric density fluctuations and is responsible for Rayleigh scattering. The change of the density in Eq.(2.2) involves a variation of the

dielectric constant ϵ as:

$$\Delta\epsilon = \left(\frac{\partial\epsilon}{\partial\rho}\right)_T \Delta\rho + \left(\frac{\partial\epsilon}{\partial T}\right)_\rho \Delta T \tag{2.3}$$

with the temperature T. The second term can be neglected because the density variation influences stronger than temperature variations [1]. Introducing the first term of Eq.(2.2), which is crucial for Brillouin scattering, into Eq.(2.3) leads to:

$$\Delta\epsilon = \left(\frac{\partial\epsilon}{\partial\rho}\right)_T \left(\frac{\partial\rho}{\partial p}\right)_s \Delta p = \frac{\gamma_e}{\rho_0}\left(\frac{\partial\rho}{\partial p}\right)_s \Delta p \tag{2.4}$$

where the electrostrictive coefficient γ_e is defined as:

$$\gamma_e = \rho_0 \left(\frac{\partial\epsilon}{\partial\rho}\right)_T . \tag{2.5}$$

By help of Eq.(2.4) we can calculate an additional contribution P_{add} to the polarization according to Eq.(1.18):

$$\mathbf{P} = \epsilon_0\chi\cdot\mathbf{E} + \Delta\epsilon\cdot\mathbf{E} = \epsilon_0\chi\cdot\mathbf{E} + \mathbf{P}_{\text{add}} \tag{2.6}$$

with

$$\mathbf{P}_{\text{add}} = \frac{\gamma_e}{\rho_0}\left(\frac{\partial\rho}{\partial p}\right)_s \Delta p\cdot\mathbf{E} = \frac{\gamma_e}{\rho_0}\Delta\rho\cdot\mathbf{E} \tag{2.7}$$

From an acoustic point of view the density fluctuations in Eq.(2.2) have to full-fill the following wave equation for the acoustic propagation[1] [2]:

$$\frac{\partial^2\rho}{\partial t^2} - \Gamma'\nabla^2\frac{\partial\rho}{\partial t} - V_A^2\nabla^2\rho = 0 \tag{2.8}$$

with V_A the acoustic velocity and Γ' the damping parameter given by:

$$\Gamma' = \frac{1}{\rho}\left[4/3\eta_s + \eta_b + \kappa/C_p(\gamma-1)\right]. \tag{2.9}$$

Here, η_s and η_s are the shear and the bulk viscosity, κ the thermal conductivity, γ the adiabatic index and C_P the compressibility for constant pressure.
For Eq.(2.8) a general solution can be found as [2, 4]:

$$\Delta\rho = 1/2\, Q(z,t)\, exp(i(\Omega t - \mathbf{qr})) + c.c. \tag{2.10}$$

In the same way the optical waves have to comply the optical wave equation [2]:

$$\frac{\partial^2}{\partial z^2}\mathbf{E} - \frac{1}{(c/n)^2}\frac{\partial^2}{\partial t^2}\mathbf{E} = \frac{1}{\epsilon_0 c^2}\frac{\partial^2}{\partial t^2}\mathbf{P}_{\text{add}} \tag{2.11}$$

[1] Derived from the Navier-Stokes equations for the case of a viscous and compressible fluid [3]

where P_{add} can be found in Eq.(2.1.2.2). The optical wave equation has solutions of the form

$$\mathbf{E} = 1/2\ A(z,t)\ exp(i(\omega t - \mathbf{kr})) + c.c. \tag{2.12}$$

well-known as electromagnetic waves.
Bringing acoustics and optics together, we can introduce Eqs.(2.10) and (2.1.2.2) into Eq.(2.11) and obtain a description for Brillouin scattering [2, 5]:

$$\begin{aligned}\frac{\partial^2}{\partial z^2}\mathbf{E} - \frac{1}{(c/n)^2}\frac{\partial^2}{\partial t^2}\mathbf{E} = \\ = \frac{\gamma_e}{4\epsilon_0 c^2}\left[(\omega+\Omega)^2 Q(z,t)A(z,t)\exp(i((\Omega+\omega)t-(q+k)r))\right] + \\ + \frac{\gamma_e}{4\epsilon_0 c^2}\left[(\omega-\Omega)^2 Q(z,t)A(z,t)\exp(i((\Omega-\omega)t-(q+k)r))\right]\end{aligned} \tag{2.13}$$

in which two spectral components, the Stokes component with frequency $\omega - \Omega$ and the Anti-Stokes component with frequency $\omega + \Omega$, can be identified. Fig.(2.2) shows schematically the Stokes process for spontaneous Brillouin scattering with the different wave vectors and pulsations. The energy and momentum conservation for the Stokes wave are given by:

$$\omega_P = \omega_S + \Omega \tag{2.14a}$$

$$\mathbf{k}_P = \mathbf{k}_S + \mathbf{q} \tag{2.14b}$$

where $\mathbf{k_i}$, ω_{i} (i = P, S) are the wave vectors and frequencies of the pump and Stokes wave and $\mathbf{q}$, Ω for the acoustic wave, respectively. The respective wavelengths are obtained by:

$$|\mathbf{k}_{\text{P}}| = \frac{2\,\pi\,\text{n}}{\lambda_{\text{P}}}, \qquad |\mathbf{k}_{\text{S}}| = \frac{2\,\pi\,\text{n}}{\lambda_{\text{S}}}, \qquad |\mathbf{q}| = \frac{2\,\pi}{\lambda_{\text{B}}} = \frac{\Omega}{V_A} \tag{2.15}$$

As shown in Fig.(2.2) the conservation of momentum with angle θ between the pump

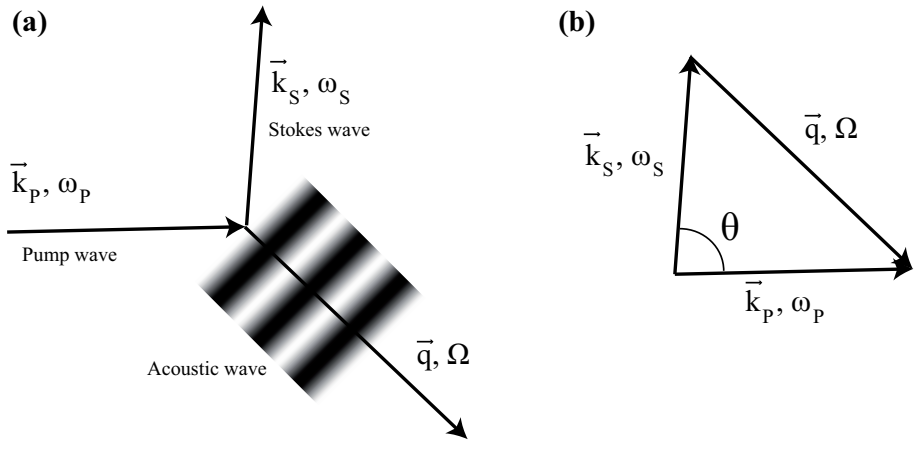

Figure 2.2: Stokes process of spontaneous Brillouin scattering

and the Stokes wave writes:

$$|\mathbf{q}| = |\mathbf{k}_\mathrm{P}| \; + \; |\mathbf{k}_\mathrm{S}| \; - \; 2\,|\mathbf{k}_\mathrm{P}||\mathbf{k}_\mathrm{S}|\cos\theta \tag{2.16}$$

From Eq.(2.15) and Eq.(2.16) we can derive the relationship for the Brillouin frequency shift:

$$\Omega = \frac{2\,n\,V_A}{\lambda_P}\,\sin(\theta/2) \tag{2.17}$$

Since in optical fibers there are only two possibilities, forward and backward, that the scattered light is guided, one can see for the maximum of the backscattered Brillouin gain spectrum (BGS) that the Brillouin frequency shift (BFS) ν_B is reached for $\theta = 180^\circ$:

$$\nu_B = \frac{2n_\mathrm{eff}V_L}{\lambda_P} \tag{2.18}$$

with V_L the longitudinal acoustic velocity and $\mathrm{n_{eff}}$ the effective refractive index for the optical wave. In silica fibers this frequency shift ν_B of the backscattered light is about 11 GHz. For the Anti-Stokes component the same considerations can be made and we obtain the same frequency shift ν_B but on the other side of the pump wave. Clearly spoken, the Stokes wave has the frequency $\nu_P - \nu_B$ and the Anti-Stokes wave $\nu_P + \nu_B$.
As mentioned, the density fluctuations in case of Brillouin scattering are moving, because they are acoustic waves. From this point of view the Brillouin scattering process can also be explained with the Doppler effect because the optical wave is reflected at a moving grating, in one or the other direction in the fiber. Rayleigh scattering however results from not moving density fluctuations and thus is not frequency shifted.

2.2 Nonlinear Scattering

In comparison to linear or spontaneous scattering, where light is deviated in the material by existing density fluctuations or other inhomogeneities, nonlinear light scattering modifies the optical properties of the material. We will first give a detailed description of stimulated Brillouin scattering (SBS) and then a short insight into stimulated Raman scattering.

2.2.1 Stimulated Brillouin scattering

As we have seen in the previous paragraph, spontaneous Brillouin scattering results from the interaction between optical pump wave and acoustic phonons which number is determined by the Bose-Einstein-distribution in Eq.(2.1), thus originates from thermal background. A small fraction of the pump power is backscattered and shifted by the Brillouin frequency shift (BFS, Eq.(2.18)), to both sides to the pump wave, the Stokes and

Anti-Stokes components. When the optical pump power increases the scattering process becomes stimulated or nonlinear because the scattered optical waves generate additional acoustic phonons. In silica fibers the physical mechanism that generates acoustic waves out of optical intensity lattices is electrostriction which will be explained in the following paragraph.

2.2.1.1 Electrostriction

Electrostriction is the physical phenomenon whereby materials as silica become compressed under the effect of applied electric fields [2]. The origin for this effect is to minimize the potential energy of the material by molecules moving to intense areas of the optical field. The molecules "escape from the dark" and the material density rises where an intensity maximum of the optical field is. The force that attracts the molecules to high optical intensities can be written as [2, 6]:

$$\mathbf{F} = (p\nabla)\mathbf{E} \tag{2.19}$$

where $p = \alpha E$ is the dipole moment (α polarizability) and E the electric field. This can be explained on the molecular level where a molecule develops a dipole moment p in the presence of an electric field. The force in Eq.(2.19) attracts molecules to regions with higher optical intensity and accordingly changes the density in this part of the material. The difference in density induces a change for the dielectric constant:

$$\Delta\epsilon = \frac{\partial\epsilon}{\partial\rho}\Delta\rho \tag{2.20}$$

with ρ the density of the material. The increase in potential energy that is added by the polarization of the molecule can then be written as:

$$\Delta u = 1/2\epsilon_0 \left|\mathbf{E}\right|^2 \Delta\epsilon = 1/2\epsilon_0 \left|\mathbf{E}\right|^2 \frac{\partial\epsilon}{\partial\rho}\Delta\rho. \tag{2.21}$$

According to the first law of thermodynamics, the change of energy has to be equal to the work of compressing the material:

$$\Delta W = -p_{st}\frac{\Delta\rho}{\rho_0} \tag{2.22}$$

where p_{st} is the electrostrictive pressure resulting from the electrical field induce compression. From Eqs.(2.21) and (2.22) we can derive:

$$p_{st} = -1/2\rho_0\epsilon_0\frac{\partial\epsilon}{\partial\rho}\left|\mathbf{E}\right|^2 = -1/2\gamma_e\epsilon_0\left|\mathbf{E}\right|^2. \tag{2.23}$$

where the electrostrictive constant γ_e has already been defined in Eq.(2.5). Since the change in density is $\Delta\rho = -\rho C p_{st}$ with C the compressibility, we find the change in material density induced by an applied electric field of strength $\mathbf{E}$ [2]:

$$\Delta\rho = 1/2\epsilon_0\rho C\gamma_e\mathbf{E}^2. \tag{2.24}$$

In these considerations E is a static field, which is not the case for the interferences of the pump and Stokes waves in SBS. Here, E^2 has to be replaced by the mean value of several optical periods $\langle E \cdot E\rangle$ because high frequencies do not contribute to the electrostrictive pressure by reason of the slow molecule displacement compared to the optical wave. Thus, only the minima and maxima of the electric field of the beating between pump and Stokes wave play a role for electrostriction.

2.2.1.2 Classical Theory

Now that we know the physical background of electrostriction we can explain the mechanism of SBS in a figurative scheme, shown in Fig.(2.3). The pump wave is scattered by thermally excited acoustic waves in the optical fiber because they present not only a moving density grating but also a refractive index grating. The pump wave and the scattered Stokes wave interfere and create a beating with intensity minima and maxima of light. By electrostriction the density in regions of high and low optical power will change and constructs a moving density grating. With the altered density the refractive index in the optical fiber varies via the electro-optic effect and this results in a moving refractive index grating. The incident pump wave is now again scattered by the refractive index grating and the process starts all over. This reinforces the Stokes wave and then consequently the acoustic wave. Hence, the process can be seen as a feedback loop. As already mentioned, the frequency shift of the scattered wave can be understood as the results from the Doppler-effect: the light is scattered at a moving grating and thus gets a frequency shift. For the three participating waves the following three wave equations must be full-filled [2].

The acoustic wave equation for an acoustic wave ρ is similar to Eq.(2.8):

$$\frac{\partial^2\rho}{\partial t^2} - \Gamma'\nabla^2\frac{\partial\rho}{\partial t} - V_A^2\nabla^2\rho = \nabla\mathbf{f} \tag{2.25}$$

but with an additional term for the electro-strictive force.
The optical wave equations for the pump wave $\mathbf{E}_P$ and the Stokes wave $\mathbf{E}_S$:

$$\frac{\partial^2}{\partial z^2}\mathbf{E}_P - \frac{n^2}{(c^2}\frac{\partial^2}{\partial t^2}\mathbf{E}_P = \frac{1}{\epsilon_0 c^2}\frac{\partial^2}{\partial t^2}\mathbf{P}_P^{\mathrm{NL}} \tag{2.26a}$$

$$\frac{\partial^2}{\partial z^2}\mathbf{E}_S - \frac{n^2}{(c^2}\frac{\partial^2}{\partial t^2}\mathbf{E}_S = \frac{1}{\epsilon_0 c^2}\frac{\partial^2}{\partial t^2}\mathbf{P}_S^{\mathrm{NL}} \tag{2.26b}$$

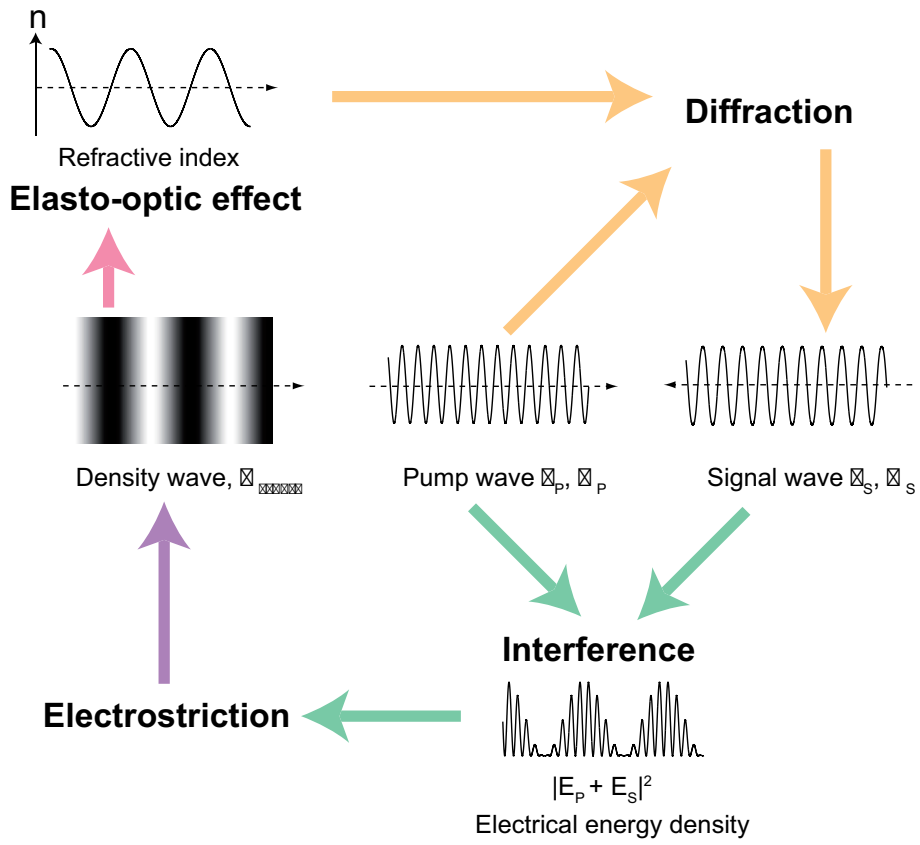

Figure 2.3: Stimulated Brillouin scattering process: a self-sustained loop with different participating physical phenomena: electrostriction (optical intensity lattice to a density wave), elasto-optic effect (density wave to a refractive index grating), diffraction (pump wave is diffracted at the refractive index grating), interference (pump and Stokes wave create an optical intensity pattern).

The solutions for these wave equations have the form:

$$\rho = \mathbf{Q} \cdot \exp(i\mathbf{q}z - i\Omega t) + c.c. \tag{2.27}$$

for the density wave and

$$\mathbf{E}_P = \mathbf{A}_P \cdot \exp(i\mathbf{k}_P\mathbf{z} - i\omega_P t) + c.c. \tag{2.28a}$$

$$\mathbf{E}_S = \mathbf{A}_S \cdot \exp(i\mathbf{k}_S\mathbf{z} - i\omega_S t) + c.c. \tag{2.28b}$$

for the pump and the Stokes wave, respectively. Note that $\omega_P = \omega_S + \Omega$ and $k_P = k_S + q$ as mentioned in paragraph 2.1.2.2. Since we are in an optical fiber where only forward an backward waves are guided we can write the different wave vectors as scalars.
In Eq.(2.25) an additional term $\nabla\mathbf{f}$ for the electrostrictive force coming from the interferences between pump and Stokes waves is added. It can be expressed with help of Eq.(2.23) and considering the form of the optical waves as:

$$\nabla\mathbf{f} = \nabla\nabla p_{st} = \nabla(-1/2\gamma_e\epsilon_0\langle \mathrm{E}^2\rangle) = \gamma_e\epsilon_0(k_P - k_S)^2\left[A_P A_P^{\star}\exp(i(k_P - k_S)z - i\Omega t) + c.c.\right] \tag{2.29}$$

Substituting Eqs.(2.29) and (2.27) in (2.25) results in the following equation for the amplitude Q in Eq.(2.27), assuming that the acoustic amplitude varies slowly in space and time which means amongst others that all the second derivations in time and space can be neglected:

$$-2i\Omega\frac{\partial Q}{\partial t} + \left(\Omega_B^2 - \Omega^2 - i\Omega\Gamma_B\right)Q - 2iqV_A^2\frac{\partial Q}{\partial z} = \epsilon_0\gamma_e q^2 A_P A_S^\star. \tag{2.30}$$

Γ_B is the Brillouin linewidth and replaces: $\Gamma_B = q^2\Gamma'$.
The polarization in Eqs.(2.26) is nonlinear in contrast to spontaneous Brillouin scattering because the polarisation depends on the optical intensity as implicitly claimed in paragraph 2.2.1.1 about electrostriction. Thus, with Eq.(2.1.2.2) $P_{add} = \frac{\gamma_e}{\rho_0}\left(\frac{\partial\rho}{\partial p}\right)_s \Delta p \cdot \mathbf{E}$, the nonlinear polarisation terms in Eqs.(2.26) can be written as

$$P_P^{\mathrm{NL}}(z,t) = \epsilon_0\gamma_e/\rho_0 Q A_S \tag{2.31a}$$
$$P_S^{\mathrm{NL}}(z,t) = \epsilon_0\gamma_e/\rho_0 Q A_P \tag{2.31b}$$

where Q is the amplitude for the acoustic wave, the solution of Eq.(2.30):

$$Q(z,t) = \epsilon_0\gamma_e q^2 \frac{A_P A_S^\star}{\Omega_B^2 - \Omega^2 - i\Omega\Gamma_B}. \tag{2.32}$$

Here steady-state conditions are assumed (the time derivative term vanishes) and the spatial derivation in Eq.(2.30) is neglected. Now we introduce the solutions Eq.(2.28) and the polarisation Eq.(2.31) into the wave equations Eq.(2.26) and we obtain, with the approximation of the slowly varying amplitude, the coupled equations:

$$\frac{\partial A_P}{\partial z} + \frac{1}{c/n}\frac{\partial A_P}{\partial t} = \frac{i\omega\gamma_e}{2nc\rho_0} Q A_S \tag{2.33a}$$
$$-\frac{\partial A_S}{\partial z} + \frac{1}{c/n}\frac{\partial A_S}{\partial t} = \frac{i\omega\gamma_e}{2nc\rho_0} Q^\star A_P \tag{2.33b}$$

Here the approximation has been done that $\omega \approx \omega_P \approx \omega_S$. If we use steady-state conditions, the time derivations can be neglected. With $I_i = 2n\epsilon_0 c A_i A_i^\star$, i=P,S the following differential equations for the intensities are then derived:

$$\frac{dI_P}{dz} = -g_B I_P I_S - \alpha I_P \tag{2.34a}$$
$$\frac{dI_S}{dz} = -g_B I_P I_S + \alpha I_S \tag{2.34b}$$

SBS is a gain process and the Brillouin gain spectrum (BGS) g_B has a Lorentzian shape:

$$g_B(\Omega) = g_B \frac{(\Delta\nu_B/2)^2}{(\Omega_B - \Omega)^2 + (\Delta\nu_B/2)^2} \tag{2.35}$$

with the Brillouin gain factor [7]:

$$g_B = \frac{4\pi n^8 p_{12}^2}{c\lambda_P^2 \rho_0 \nu_B \Delta\nu_B}. \tag{2.36}$$

The different parameters for g_{B0} can be found in table (2.1). In literature values ranging from $1{\cdot}10^{11}\,\mathrm{mW}^{-1}$ to $5{\cdot}10^{11}\,\mathrm{mW}^{-1}$ [11–13] are reported.

Table 2.1: Values to calculate the Brillouin gain g_B

Refractive index silica	n = 1.444 [8]
Elasto-optic constant SO_2	p_{12} = 0.285 [9]
Density	$\rho_0 = 2.21{\cdot}10^3$ kg/m^2 [10]
Pump wave	λ_P = 1.55 µm
Acoustic velocity	ν_A = 5996 m/s [9]
FWHM	$\Delta\nu_B$ = 28 MHz

2.2.1.3 Acoustic decay time

The Brillouin linewidth Ω_B is given as angular frequency and is related as $\Omega_B = 2\pi\Delta\nu_B$ to the measured frequency linewidth $\Delta\nu_B$ in the experiment. The acoustic decay time is inversely linear related to the Brillouin linewidth $\Delta\nu_B$ [14–16]:

$$\tau_A = \frac{1}{\pi\Delta\nu_B} \tag{2.37}$$

when referring to the amplitude of the acoustic wave, as the amplitude and not the intensity of the acoustic wave enters Eq.(2.33). However, the decay time of the acoustic *phonon* is half of τ_A because phonons are energy packages so related to the square of the amplitude $I = \|Q\|^2$. Since it is an exponential decay and the quadrature is found in the exponent, this leads to a phonon life time $\tau_{\mathrm{Ph}} = \tau_A/2$ [2]. Further discussions can be found in [5]. In chapter 3.5, we will present measurements of the acoustic decay time τ_A of the Brillouin Stokes wave which are in good agreement with Eq.(2.37).

2.2.1.4 Brillouin threshold

As we have now discussed spontaneous and stimulated Brillouin scattering, an interesting parameter has to be introduced, the critical pump power for the Brillouin threshold. It defines a kind of threshold between spontaneous and stimulated scattering, where the power of the backscattered wave begins to grow exponentially and is no more weak. Different definitions exist for the threshold, for example when the backscattered power equals the pump power [16] or when the backscattered power is 1% of the pump power [17]. The threshold can then be derived from the previous equations for stimulated Brillouin scattering as [7]:

$$P_{\mathrm{cr}} = \frac{C \cdot K \cdot A_{\mathrm{eff}}}{g_B \cdot L_{\mathrm{eff}}}, \tag{2.38}$$

where A_{eff} is the EMA, L_{eff} the effective length, C a constant and g_B the Brillouin gain. K=3/2 is a factor that accounts for random polarization evolution in the fiber and C depends amongst others on the fiber parameters, the Brillouin frequency shift (BFS), the

Brillouin gain spectrum (BGS) and the definition of the Brillouin threshold [7]. C is often given as 21, according to Smith *et al.* in 1972 [18] but this is an approximation which can be derived more precisely as will be explained in chapter 4.

2.2.2 Stimulated Raman scattering

As mentioned in paragraph 2.1.2.1 spontaneous Raman scattering comes from the interaction of optical waves with molecular vibrations of the medium. It is a weak process where about $10^{-6}\,\mathrm{cm}^{-1}$ of the pump power is converted to the scattered waves. If the pump power is sufficiently high, the interference of the incident optical wave and the Stokes wave is strong enough to stimulate the molecules to vibrate at the Raman frequency Ω_R and the scattering becomes a stimulated process. The pump and signal wave can be expressed as [16]:

$$\frac{\partial P_P}{\partial z} = -\frac{\omega_P}{\omega_S}\frac{g_R}{A_{\text{eff}}}P_P P_S - \alpha_P P_P \tag{2.39a}$$

$$\frac{\partial P_S}{\partial z} = \frac{g_R}{A_{\text{eff}}}P_P P_S - \alpha_S P_S \tag{2.39b}$$

where P_i (i=S,P) is the power of the pump and Stokes waves, α_i the absorption coefficients and g_R the Raman gain which is in the order of $1{\cdot}10^{-13}\,\mathrm{mW}^{-1}$. A critical pump power, a threshold, for SRS can be defined where the Stokes power generated from noise equals the injected pump power [16]:

$$\mathrm{P}^{\text{seuil}}_{\text{Raman}} = \frac{16\mathrm{A}_{\text{eff}}}{\mathrm{g_R L_{eff}}} \tag{2.40}$$

The critical pump power for SRS is higher than for SBS. The factor 16 may eventually have to be recalculated in the same way as the factor C in Eq.(2.38) for the Brillouin threshold power since it originates from the same considerations in Smith *et al.* [18].
At the end of this paragraph about nonlinear light scattering a short comparison between SRS and SBS is summarized in table (2.2).

Table 2.2: Comparison of stimulated Raman and Brillouin scattering [2, 19]

	Raman	Brillouin
Phonon type	Optical phonon	Acoustic phonon
Frequency shift	13.2 THz (independent of λ_{Pump})	11 GHz (dependent of λ_{Pump})
Damping time	≈ 75 fs	≈ 10 ns
Direction	forward & backward	only backward (phase matching)
Gain	$\propto \frac{\rho}{\lambda_{Pump}}$ (ρ density)	$\propto \rho^2$ (ρ density)
Gain (mW^{-1})	$1{\cdot}10^{-13}$	$1\text{-}3{\cdot}10^{-11}$

2.3 Forward Brillouin Scattering

As explained in the previous paragraph Brillouin backscattering results from the interaction of longitudinal acoustic waves and the optical wave. The frequency shift depends on the angle between acoustic and pump wave and has been derived in Eq.(2.18). According to this equation, in forward direction no frequency shift should be observed. But forward Brillouin scattering, also called guided acoustic wave Brillouin scattering (GAWBS), is caused by mostly transversal acoustic modes with a very small component in longitudinal direction. The transverse acoustic modes induce a phase shift to the optical waves which can be measured by an interferometer.
Two types of transverse acoustic modes are crucial for GAWBS: radial modes (Fig.(2.4a)) and torso-radial modes (Fig.(2.4b)). They are density waves that oscillate with a certain frequency. They both cause a periodically in time changing effective refractive index in the fiber core that can be written as:

$$\Delta n_{\text{eff}} = n_{\text{eff}} \cdot \cos(\omega_{\text{GAWBS}} t). \tag{2.41}$$

Imaging the optical waves passing through a local transverse mode (Fig.(2.5)), it leads to a phase shift on the optical wave because the effective refractive index changes as for an acousto-optic modulator. It can be seen as a temporal grating, thus we will be able to observe the vibration as a frequency peak in frequency domain (Fig.(2.5), f_1 and f_2). Of course, these acoustic modes can be found all over the fiber because they originate from acoustic phonons, whose number is given by the Bose-Einstein distribution, Eq.(2.1), comparable to what has been explained for spontaneous Brillouin scattering in paragraph 2.1.2. It must be emphasized that forward Brillouin scattering is also spontaneous scattering caused by acoustic modes that are propagating in all directions in the fiber. A stimulated process with a CW pump as for backward scattering can barely be managed because of the very small wave-vector in longitudinal direction of the transverse acoustic modes. Some experiments to stimulate GAWBS have, however, been performed

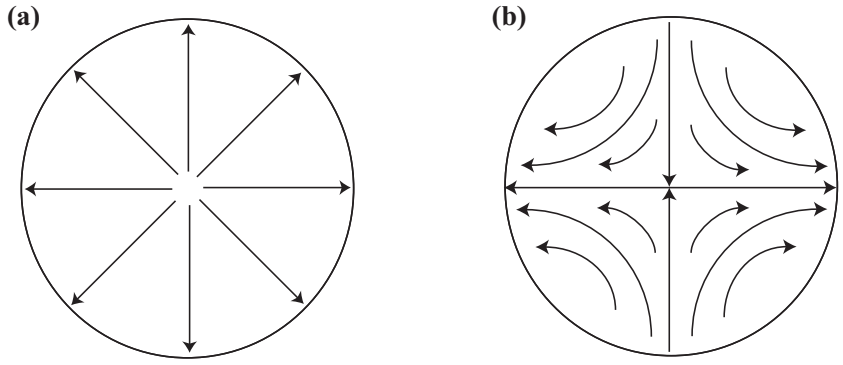

Figure 2.4: Transverse acoustic modes in a glass rod: (a) Radial symmetric acoustic modes R_{0m}, torso-radial acoustic modes TR_{2m}

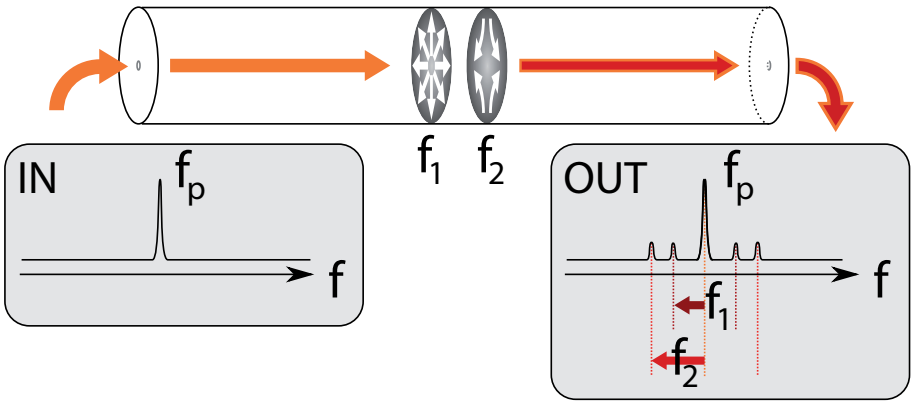

Figure 2.5: Description of forward Brillouin scattering. A pump wave at f_p gets phase shifts passing through transversal acoustic modes which is observed at the output of the fiber in frequency regime

by Prof. Russell's group by using train pulses to increase the optical intensity [20, 21]. Additionally to the phase modulation by both types of acoustic modes, torso-radial modes change the polarization state of the optical wave as they break the radial symmetry of the silica rod. These modes can be observed by choosing the polarization state before injecting into the fiber and measuring in another polarization state at the output of the fiber. The resulting frequency peaks are called depolarized GAWBS in contrast to polarized GAWBS, caused by the polarization preserving radial modes.
Since forward Brillouin scattering is observable through phase modulation induced by both types of transverse modes an interferometer setup must be employed to observe it. This will be further explained in chapter 5. Visualizing GAWBS by an interferometer reveals many frequency peaks up to 1 GHz for an SMF, owing to the interaction of many acoustic modes together with the optical mode. This phenomenon has been presented for the first time by Shelby *et al.* [22]. Fig.(2.6) shows their results for polarized (a) and depolarized (b) GAWBS where plenty of distinct frequency peaks up to 600 MHz (a) and 800 MHz (b) appear. The frequency values depend on the outer diameter of the cladding d_{ext} and the ratio between the transverse and longitudinal acoustic velocity $\alpha = V_L/V_T$. For an SMF, that can be considered as a cylindrical glass rod from an acoustic view point, the frequency values can theoretically be obtained by resolving the following two equations:
For polarized GAWBS (R_{0m}-modes):

$$(1-\alpha^2)J_0(y_m) - \alpha^2 J_2(y_m) = 0 \tag{2.42}$$

For depolarized GAWBS (TR_{2m}-modes):

$$\begin{vmatrix} (3-y_m^2/2J_2(\alpha y_m) & (6-y_m^2/2)J_2(y_m) - 3y_m J_3(y_m) \\ J_2(\alpha y_m) - \alpha y_m J_3(\alpha y_m & (2-y_m^2/2)J_2(y_m) + y_m J_3(y_m) \end{vmatrix} = 0 \tag{2.43}$$

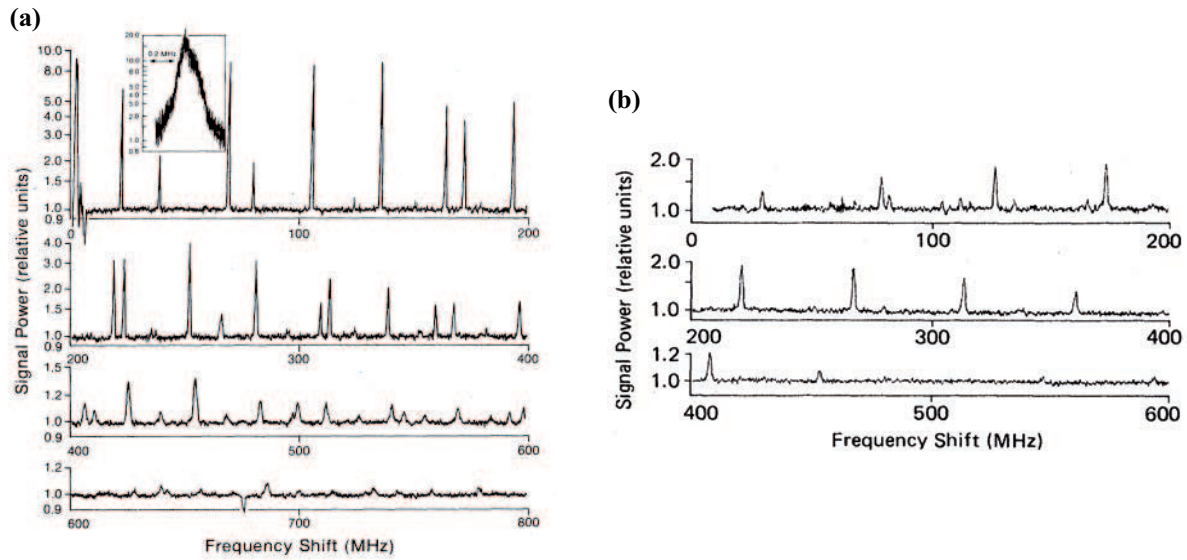

Figure 2.6: (a) Depolarized and (b) polarized GAWBS in an SMF, observed in Ref. [22].

with $J_n(y)$, n=0,2 the nth Bessel functions, y_m the solutions and $\alpha = \mathrm{V_L}/\mathrm{V_T}$. These equations are derived from the boundary conditions in a uniform long cylinder. A detailed description can be found in Ref. [23].
For photonic crystal fibers (PCFs) the analysis is more complicated because of the air-hole micro-structure. Thus, it will be resolved by numerical simulations based on the finite element method (FEM) in chapter 5.

2.4 State of the art

The last paragraph of this chapter is dedicated to a short overview about some milestones in research up to recent publications that deal with Brillouin scattering. The first part is about investigations in stimulated Brillouin scattering in optical fibers from a general view point. In the second part several papers about guided acoustic wave Brillouin scattering will be presented with a special attention to PCFs. Finally we will have an insight into the research of fiber sensors with a focus on distributed Brillouin sensors.

2.4.1 Stimulated Brillouin scattering

For the first time Léon Brillouin predicted in 1922 [24] theoretically the scattering of X-rays and optical waves on thermally excited acoustic waves in crystals. He pointed out that in contrast to Rayleigh-scattering the light-matter interaction induces a frequency

shift to the scattered waves. Another type of inelastic light scattering was discovered in 1928 by Raman and Krishnan [25]. Besides these investigations in India and France, molecular scattering was also studied by Landsberg and Mandelshtam in Russia, Smekal in Austria and Wood in the United States [1, 7]. But not until the achievement of the laser in 1960 [26] these nonlinear phenomena became an important research field and led later to many applications e.g. in telecommunication, spectroscopy and sensor systems for temperature and strain.

The first experimental investigation of SBS in crystals of quartz and sapphire has been realized in 1964 by Chiao *et al.* [27]. An accurate measurement with high resolution interferometers has been made possible and provided further informations about the frequency shift, the linewidth and intensity of the Brillouin gain spectrum. An early paper by Tang *et al.* [28] shows a detailed analysis of the three coupled nonlinear wave equations in order to describe the amplification of the coherent Stokes wave by SBS. Using Brillouin scattering, acoustic properties as the sound velocity have been measured, e.g. in different glasses in Ref. [29].

Stimulated Brillouin scattering was also studied in optical fibers, for the first time in 1972 by Ippen and Stolen [30]. In the same year Smith published a paper about stimulated Brillouin and Raman scattering limitations in low-loss optical fibers. He considered Brillouin scattering as detrimental for fiber-based optical communication and derived a formula for the Brillouin threshold which has been widely used. Other important early publications are about SBS in single mode fibers in 1983 (Cotter [13]) and spontaneous Brillouin scattering for fiber characterization in 1986 (Tkach *et al.* [31]). Later Boyd *et al.* [17] and Gaeta *et al.* [32] explained theoretically how SBS can be derived from thermal acoustical noise and developed a theoretical model based on statistic properties of SBS. In [17] another definition of the Brillouin threshold has been introduced (if the backscattered power equals 1% of the input power) and in [32] we find descriptions about the dynamics of the Brillouin gain spectrum, e.g. that the Lorentzian shape develops to a Gaussian one with increasing input power. In 1997, Niklès *et al.* [33] provided a detailed investigation of the Brillouin gain spectrum in SMF and its dependence of temperature and strain. An overview about different measurement methods of the Brillouin gain spectrum will be given in paragraph 3.1.1.1. Other publications about the Brillouin gain investigate spectra in the depleted pump regime [34], polarization dependency of Brillouin scattering [35–38] and linewidth broadening of the BGS [39, 40]. Kovalev *et al.* [39] claimed that the linewidth broadening is related to the numerical aperture of the fiber and proposed an inhomogeneous model of SBS in Ref. [40]. They assumed that the optical fiber guides a fan of different beam directions within the critical angle of the numerical aperture that leads to inhomogeneous broadening of SBS. This paper, however, leads to controversy because the SBS linewidth broadening can be interpreted by the standard three-wave model without involving inhomogeneous broadening [41]. A new parameter

for the Brillouin gain coefficient has been proposed in Ref. [11]. Instead of using g_B they introduce the parameter C_B that is the value of $C(\nu) = g(\nu)/A_{\text{eff}}^{\text{ao}}$ at the maximum BFS, ν_B, where $A_{\text{eff}}^{\text{ao}}$ is the acousto-optic effective area. C_B is directly measurable and makes a better comparison of fibers with different EMAs. Other work about the magnitude of the Brillouin gain coefficient can be found in [42–45]. On the one hand, Brillouin scattering has led to an amount of interesting phenomena as slow and fast light [46, 47] and applications as Brillouin fiber lasers [48, 49] and Brillouin sensors (see paragraph 2.4.3.3). An extensive overview about applications of Brillouin scattering is listed in [7]. On the other hand it is detrimental for fiber communication systems and fiber lasers and thus many different active and passive techniques have been developed to suppress it. An overview about Brillouin suppression techniques can be found in chapter 4.

Since the discovery of PCFs [50, 51], SBS has also widely been studied in this new type of fibers because the periodic air-hole micro-structure provides unexpected effects on the acoustic modes and their small cores lead to high nonlinearity. The first work about SBS in PCF has been carried out at the University of Southampton [52] where a multi-peak backscattered Brillouin spectrum has been observed. Another publication of this group has also shown a broadened BGS in comparison to standard DSF [53].

Later works reported on the influence of the microstructure on the effective refractive index by cutting a PCF into 2m-long pieces [54] and its impact on the Brillouin threshold [55]. In Refs. [56, 57] PCF with germanium-doped cores and their temperature coefficients have been studied in order to perform simultaneous measurement of strain and temperature. Later publications were dedicated to SBS in ultra-small core PCF. Dainese *et al.* [58] investigated nano-structured PCF and revealed a clearly separated three-peak spectrum with narrow FWHM which increases the Brillouin threshold fivefold. A higher threshold, due to linewidth broadening, has also been reported in 2007 by our research group [59]. A distributed Brillouin gain measurement was also performed that reveals the influence of strain on the BGS. Two other articles by McElhenny *et al.* [60, 61] point out the behaviour of Brillouin gain, shift and threshold for small core PCF from 1.7 µm to 8 µm core diameter in relation to the polarization state. Another article about polarization dependency in highly birefringent microstructure fiber contains an interesting experimental analysis about the distributed BFS with a dual-peaked spectrum [62]. In our laboratory, as a part of this thesis, the influence of inhomogeneities in PCF has been studied in [63, 64] with respect to Brillouin gain and threshold measurement and a distributed characterization of the BGS. A further result of the distributed Brillouin measurement has been obtained by extracting the phonon life time in PCF and comparing it to the Brillouin gain linewidth [65, 66]. These publications will be discussed in detail in paragraph 3.4 and 3.5.

More recently, two research groups have been interested by theoretical modeling of SBS.

In Ref. [67] a detailed implementation of a 2-D finite-element method is proposed to simulate Brillouin gain characteristics of PCF with different refractive index profiles and material composition. Taking into account the effect of electrostriction, Carlson *et al.* [68] presents a full vectorial numerical investigation of Brillouin gain and phonon decay rate. The paper proposes random acoustically micro-structured PCF which results in Brillouin suppression by 8 dB relative to that of homogeneous fused silica fibers.

By this wide variety of publications about SBS in PCF, the high interest in this research field is represented. Nevertheless, forward scattering in PCF has attracted also much attention as we will see in the next chapter.

2.4.2 Guided Acoustic Wave Brillouin Scattering

Guided acoustic wave Brillouin scattering (GAWBS) has been experimentally investigated for the first time in Refs. [22,69]. In Fig.(2.6) the frequency peaks for polarized and depolarized GAWBS are shown that have been obtained up to 800 MHz. These modes, weak in comparison to SBS, can give us informations about the fiber structure because they result from transverse acoustic modes. Articles about the influence of the design of single-mode fibers on GAWBS [70, 71] have been published where they also test the possibility of estimating the fiber core diameter with help of GAWBS [71]. Dynamics of GAWBS in a Brillouin fiber ring laser has been studied [72], i.e. the coupling between longitudinal and transverse modes. Forward Brillouin scattering in dual-mode single-core fibers was shown in [73]. Besides, some work has been done on the dependency of dopant [74] where different acoustic velocity have been measured and the influence of applied strain and temperature [75]. These articles show a strong impact of the fiber microstructure, on forward Brillouin scattering.

Indeed, in 2005, our research group demonstrated in Ref. [76] that a PCF can also be a phononic crystal. The authors investigated theoretically phononic band-gaps in a nanostructured cored PCF which should lead to SBS suppression. Therefore a mixed microstructure-nanostructure PCF has been designed to guide the optical mode on the one hand but on the other hand have a band-gap for SBS phonons. Experimentally, forward Brillouin scattering in PCF has first been observed in Ref. [77]. Since several of their experiments were working at the quantum noise limit, they were interested in these new micro-structured fibers to dispose of the numerous acoustic modes up to 200 MHz. Indeed, they observed a tenfold noise reductions compared to a conventional optical fiber. In our lab, Beugnot *et al.* [78] showed one year later that in PCFs a main mode, related to the fiber core, is enhanced and the frequencies peaks in the lower frequency regime are almost suppressed. They also proposed that the fiber core diameter and the frequency of

the fundamental mode are related by the transverse acoustic velocity in silica.

In Ref. [79], another term for forward Brillouin scattering is proposed: Raman-like light scattering because the frequencies of the peaks are independent from the pump wavelength like for Raman-scattering and the acoustic phonons behave like optical ones, tightly trapped in the small fiber core. Starting with this paper, a lot of publications followed from Russell's group. They reported about the excitation of GAWBS by electrostriction using pulse trains [20, 80] and used this technique for the characterization of acoustic resonances in fiber tapers [21]. They also found a relation between taper diameter and frequency of the acoustic resonance but slightly different to Ref. [78]. This will be more detailed in chapter 5.2. In Ref. [81] several PCFs with different air-filling fractions have been investigated and two types of forward scattering are distinguished: intramodal (frequency shifted within the same optical mode) and intermodal (frequency shifted and in a different optical mode). Recently, Kang *et al.* [82] presented stimulated forward scattering by launching the pump and stokes waves orthogonally in a birefringent PCF. They called this effect forward stimulated inter-polarization scattering (SIPS) and it led to new applications, e.g. a variable-optical attenuator [83] and a light-driven opto-acoustic isolator [84].

Forward Brillouin scattering in a highly nonlinear fiber has also recently been investigated [85]. Due to a large gain, frequencies up to 1 GHz have been observed. The Anti-Stokes side-bands are shown to be slightly asymmetric compared to the Stokes spectrum as resulting from interferences with the optical Kerr-effect. It has also experimentally been shown that the linewidth of the peaks increases linearly with the acoustic frequency. In our lab as a part of this work, the effect of a PCF with multi-scale structure on the forward Brillouin scattering spectrum has been presented in [86]. The strong relation between the different diameters in the micro structure and the GAWBS spectrum is pointed out, experimentally and numerically, and the impact of transverse structural irregularities is clearly shown. A full vector finite-element model reveals the elastic radial vibrations of the real (based on the SEM-image) and the perfect micro-structure. More details will be found in chapter 5.4.

2.4.3 Fiber Sensors

2.4.3.1 Overview

An optical fiber sensor reveals a measurand of interest in one (or more) properties of an optical signal that is guided within an optical fiber [87]. The light guided by the fiber is influenced by the measurand, such that the output-light exiting the optical fiber

sensor can have different output-power, phase, polarization state or different spectral components compared with the incoming-light [87]. Possible measurands are distances and displacements (by reflection or interferometric method), mechanical strain (elasto-optic effect), rotation (Sagnac effect), electric voltages and currents (electro-optic and Faraday effect), temperature (thermo-optic effect, black body radiation, fluorescence) or chemical properties (absorption, luminescence) [87]. The advantages of fiber sensors are manifold: low-cost, low in weight, immune to electromagnetic interference, chemically passive and capable of remote measurement [5]. Fiber sensors can be divided in two categories [87]:

- intrinsic sensors (optical fiber contains the sensing element or is the sensing element) and extrinsic sensors (optical fiber only transports the information from the sensing element)

- point sensors (sense localized points along a fiber) and distributed sensors (deliver a continuous sensor signal along the fiber)

Our field of interest focus on distributed Brillouin fiber sensing where the fiber itself is the sensing element. Consequently, we can categorize them as intrinsic distributed sensors. We will not further deepen the field of point sensors but provide a short overview about the different distributed Brillouin fiber sensors.

2.4.3.2 Distributed fiber sensors

In distributed fiber sensors, information about the measurand is obtained at each point of the fiber with a certain spatial resolution. The principle of distributed fiber sensors is sending an optical pulse through the fiber, observing the backscattered light and measuring the position in the fiber with the time-of-flight of the pulse. The spatial resolution is given by the pulse width of the pump pulse.
Rayleigh scattering was first used for this purpose, which is known as Optical Time-Domain Reflectometry (ODTR). It has been developed in 1976 by Barnoski *et al.* [88] and is mainly used for detecting loss, splices and any other defaults in the fiber. The first distributed sensor using inelastic scattering was developed in 1985 by Dakin *et al.* [89] using Raman backscattered light. The Raman backscattered signal is lower than Rayleigh backscattering but offers a higher sensitivity to temperature. The third category of distributed sensors is based on Brillouin scattering and can be divided into different evaluation techniques: Time domain, frequency domain and correlation based.

2.4.3.3 Distributed Brillouin sensing

Brillouin sensors exploit the sensitivity of the BFS to temperature and strain. Brillouin sensing provides some advantages compared to other distributed techniques [90]. They use low-loss and low cost single-mode optical fibers which offers a long distance range (up to several tens of km) and compatibility with telecommunication components. Besides they are frequency based (Raman sensors are intensity based) which makes them more accurate since they do not suffer from sensitivity drifts and any fiber loss.
In the following the different techniques will shortly be explained. Further insights can be found in some doctoral thesis [3, 5, 6, 91, 92] and review articles [90, 93, 94].

Brillouin optical time-domain reflectometry (BOTDR) Brillouin optical time-domain reflectometry (BOTDR) is based on the OTDR technique but the Brillouin backscattered signal is used instead of Rayleigh scattering. For the first time it has been developed by Kurashima in 1992 [95]. The advantage of this system is that it requires access to only one end of the fiber. Resolutions up to 1 m over 10 km [96] and 2 m over 30 km [97] were reached with this system.

Brillouin optical time-domain analysis (BOTDA) Brillouin optical time-domain analysis (BOTDA) has been proposed for the first time in Ref. [35] with the purpose to investigate local fiber attenuation. The working principle is based on a pump-probe technique where an intense pump pulse is inserted to one end of the fiber and a CW-probe wave to the other input. The signal wave is shifted by the BFS to the pump wave frequency. The pump and the signal waves are counterpropagating, hence the gain experienced by the probe, while the pump pulse is propagating in the fiber, can be analyzed. A detailed explanation will be given in chapter 3.2, here we focus on an short historical overview and the state of the art of this technique.
The temperature and strain dependency of the BFS has been explored in [33, 35, 98] and further development was carried out in [99–101]. Note that using Brillouin loss, hence the Anti-Stokes component, led to a 32-km long sensor with 5 m spatial resolution [100] and using Brillouin gain to a 22-km sensing fiber with 10 m resolution [99]. The authors claim that pump depletion is the reason for this discrepancy whereas normally the Brillouin effect should be symmetrical in Stokes and Anti-Stokes component. In [101] the BOTDA setup has been improved by using only one laser source for both the pump and the probe wave to reduce the effect of frequency drifts of two different lasers. A detailed insight is given in Refs. [5, 6]. The BOTDA technique is limited to 1 m spatial resolution [102] by the long acoustic decay time (about 10 ns). Since Brillouin scattering is a polarization sensitive process, the pump and the probe wave have to be aligned carefully [37]. But the polarization dependency can also be advantageously employed for measuring local

birefringence properties along the fiber [36]. In Ref. [103] a vector BOTDA has been proposed which give access not only to the intensity of the Brillouin gain but also to its phase distribution.
The BOTDA technique is a common monitoring system in civil engineering because of its high performance in detecting temperature and strain. Therefore the data are explored and the BFS is extracted for the whole fiber. To distinguish changes in temperature and strain, two fibers are installed and one fiber is protected against strain by a loose tube and thus senses only temperature. The system is commercialized for example by the company *Omnisens* in Switzerland up to 30 km with less than 2 m spatial resolution [104]. On a research level the limit in length goes up to 100 km with distributed Raman amplification and 2 m spatial resolution [105, 106] and reaches 120 km with 3 m spatial resolution using optical pulse coding technique [107].

Brillouin optical frequency-domain analysis (BOFDA) Brillouin optical frequency-domain analysis (BOFDA) was firstly introduced by Garcus *et al.* [108, 109] and is described in detail in Ref. [91]. Using BOTDA technique, the direct pulse response in time-domain is obtained and analyzed. In a BOFDA system the frequency response of the sensor system is achieved and the spatial resolved information about the BFS is obtained by the inverse Fourier transformation. Two CW-lasers are inserted to different ends of the fiber and in the end a complex transfer function is analyzed which relates the amplitudes of the counter-propagating pump and signal waves. The signal wave is down-shifted as for the BOTDA modulated by different frequencies. Since both the time and frequency domain are intrinsically linked, they also have the same physical limitation, 1 m spatial resolution [91]. A detailed explanation is carried out in Ref. [5]. Latest developments in BOFDA by enhancing the post-processing methods are proposed in Ref. [92] and a detailed theoretical model for an intensity and phase modulated pump has been developed in Ref. [110].

Brillouin optical correlation-domain analysis (BOCDA) The previously mentioned distributed sensor techniques have all the physical limit of 1 m because of the acoustic decay time (10 ns). In 2000, a new method was proposed to overcome this limit, the Brillouin optical correlation-domain analysis (BOCDA) [111, 112]. Here, two synchronous frequency modulated waves are injected into two different ends of the fiber and the Brillouin scattering is generated locally along the fiber. Depending on the correlation of the interacting waves, Brillouin scattering is very sensitive to polarization, phase or frequency mismatch. The principle of BOCDA is based on the fact that the correlation between the two waves are artificially low everywhere in the fiber, except for the location where the Brillouin gain has to be measured [87]. Since a pump pulse is no more needed, which limited the spatial resolution, the resolution can be enhanced up to

1 cm [113]. Based on BOCDA, recently both the BOTDR and BOCDA have been combined to BOCDR-system [114] where they have the advantage of a single-ended sensor, a fast acquirement and a high spatial resolution of 40 cm.

Brillouin echo distributed sensing (BEDS) Another technique to overcome the spatial resolution limit is realized in Brillouin echo distributed sensing (BEDS). The general concept is based on the preceding existence of an acoustic wave in the fiber which is established by a CW signal and CW pump wave. We find again the principal of two CW light waves and thus the Brillouin gain spectrum is not broaden. The acoustic wave, correspondingly the refractive index grating, is "activated" before which gives a constant background amplification on the signal wave [87].
Three different configurations of very short pump pulses have been proposed by several working groups. A detailed description is given in chapter 3.2. First additional bright pulses were sent through the fiber (Fig.(3.14a)) where a high resolution of 15 cm has been shown in [115, 116]. The second type is a dark pulse, applied on the pump wave (Fig.(3.14b)) which results in a "negative" gain in Brillouin backscattering. With this technique 2 cm spatial resolution has been achieved [117]. The third configuration uses a short π-phase shift pulse instead of a dark pulse because it is supposed to yield an even sharper contrast in the Brillouin loss process (Fig.(3.14c)). This leads to a twice higher Brillouin response and hence is the most efficient concept [4]. The latter is called Brillouin echoes distributed sensing [90, 118, 119]. The remarkable advantage of this new distributed measurement technique is the high spatial resolution (up to 5 cm) with high contrast while conserving a narrow Brillouin gain spectrum. This technique has been developed at the EPFL [90, 118] and a deeper inside in theory and evolution of the experiment can be found in Ref. [5]. Further work dealt with the influence of self-phase modulation on Brillouin sensors [120]. We will use this technique for mapping PCFs in terms of inhomogeneities due to the drawing process [63] (see chapter 3.4). With help of this highly resolved system it was also possible to extract the acoustic decay time for the first time in PCF [65, 66] (see chapter 3.5). We further demonstrate a simplified version using DPSK-modulation in order to facilitate the pulse adjustment and decrease the linear loss by replacing components [121, 122], which is explained in detail in chapter 3.2.3.

Brillouin dynamic grating distributed sensing (BDG-DS) A recent technique uses the concept of Brillouin dynamic gratings [123]. The authors use polarization maintaining fibers to insert a pump wave on one axis of the fiber where it generates an index grating. The probe wave is frequency-shifted and injected to the other end of the fiber on the other polarization axis. The frequency-shift is determined by the birefringence of the polarization maintaining fiber. This technique offers a higher sensitivity to temperature and the spatial resolution of a BOTDA system can be enhanced [90, 124]. The high-

est resolution, 1 cm, for a time-domain Brillouin sensor has been obtained in [125, 126]. Another important advantage of this technique is the discrimination of strain and temperature [127, 128]. Measuring the two independent optical parameters birefringence and BFS it is possible to evaluate the influence of temperature or strain because the respective strain- and temperature-dependency of the birefringence and BFS have opposite signs.

2.4.3.4 Photonic crystal fibers for distributed Brillouin sensing

Photonic crystal fibers with their air-hole micro-structure provide new application fields to fiber sensors. They are predestinated for gas and liquid sensing applications since the air holes can be filled by different techniques [129–131]. PCFs are also used for sensing based on fiber Bragg gratings [132, 133] and interferometric configurations [134–136]. More applications can be found in review articles [137, 138].
Due to their air-hole micro-structure the acoustic properties of PCF are quite different in comparison to conventional SMF. Consequently, it suggests itself as interesting for Brillouin sensors since it is based on acoustic waves. Nevertheless, in terms of Brillouin distributed sensing PCFs have not yet been a lot investigated. In 2004, Zou *et al.* [57] measured for the first time the temperature and strain coefficients in a PCF. Two peaks in the SBS spectrum are found and supposed to vary differently with strain and temperature [57, 139, 140]. The investigation was carried out with a 15 cm resolution distributed Brillouin sensing system and they obtain a similar temperature but better strain accuracy as for conventional fibers. This multi-peak Brillouin gain spectra have attracted more attention in Ref. [141, 142]. The authors studied the pump wavelength and temperature dependence of a dual-peaked Brillouin gain in a small-core PCF to find out a different temperature dependence of both peaks. Indeed, slightly different slopes are observed for both peaks, but the more interesting observation is that the height ratio of the two Brillouin peaks is almost linearly decreasing with increasing temperature. In 2009, Dong *et al.* [143] used a polarization maintaining PCF for distributed temperature sensing based on the birefringence effect as previously described in the paragraph about BDG-DS. The polarization maintaining PCF provides a small core area, thus enhances nonlinear effects and so reduces the needed power of pump and probe pulse for distributed Brillouin sensing. The temperature and strain dependence of forward Brillouin scattering has been measured in a conventional SMF in [75, 144]. In our group the temperature coefficient of forward Brillouin scattering in a PCF has been investigated where most of the low-frequency peaks are suppressed and a main acoustic mode is obtained at 1.15 GHz [145]. Experimental results show a temperature coefficient of 106 kHz/°C for this acoustic resonance frequency of 1.15 GHz. This temperature coefficient is more than 10 times larger than that previously measured in conventional single-mode fibers in Ref. [75].

Bibliography

[1] I. L. Fabelinskii, *Molecular Scattering of Light*, Plenum Press, New York, 1968.

[2] R. W. Boyd, *Nonlinear Optics*, Academic Press, third edition, 2001.

[3] D. Alasia, *Advanced trends in nonlinear optics applied to distributed optical-fibre sensors*, PhD thesis, Ecole Polytechnique Fédérale de Lausanne, 2006.

[4] J-C. Beugnot, M. Tur, S. Foaleng Mafang, and L. Thévenaz, "Distributed Brillouin sensing with sub-meter spatial resolution: modeling and processing", *Optics Express*, vol. 19, no. 8, pp. 7381–7397, 2011.

[5] S. M. Foaleng, *Brillouin Echoes for Advanced Distributed Sensing in Optical Fibres*, PhD thesis, Ecole Polytechnique Fédérale de Lausanne, 2011.

[6] M. Niklès, *La Diffusion Brillouin dans les fibres optiques : étude et application aux capteurs distribués*, PhD thesis, Ecole Polytechnique Fédérale de Lausanne, 1997.

[7] A. Kobyakov, M. Sauer, and D. Chowdhury, "Stimulated Brillouin scattering in optical fibers", *Advances in Optics and Photonics*, vol. 2, no. 1, pp. 1–59, 2010.

[8] I. H. Malitson, "Interspecimen comparison of the refractive index of fused silica", *J. Opt. Soc. Am.*, vol. 55, no. 11, pp. 1205–1208, 1965.

[9] D. Royer and E. Dieulesaint, *Ondes Élastiques Dans Les Solides*, Dunod, Paris, 1997.

[10] P. Benassi, V. Mazzacurati, G. Ruocco, and G. Signorelli, "Elasto-optic constants in silicate glasses: Experiment and theory", *Physical Review B*, vol. 48, no. 9, pp. 5987–5996, 1993.

[11] V. Lanticq, S. Jiang, R. Gabet, Y. Jaouën, F. Taillade, G. Moreau, and G. P. Agrawal, "Self-referenced and single-ended method to measure Brillouin gain in monomode optical fibers", *Optics Letters*, vol. 34, no. 7, pp. 1018–1020, 2009.

[12] B. Robert, S. Norcia-Molin, D. Dolfi, S. Tonda, J.-P. Huignard, R. Frey, G. Melin, and L. Gasca, "Optically carried microwave signal modulation depth enhancement by stimulated Brillouin scattering in PCFs", *Electronics Letters*, vol. 42, no. 2, pp. 108–109, 2006.

[13] D. Cotter, "Stimulated Brillouin scattering in monomode optical fiber", *J. Opt. Commun.*, vol. 4, pp. 10–19, 1983.

[14] C. N. Pannell, P. St. J. Russell, and T. P. Newson, "Stimulated Brillouin scattering in optical fibers : the effects of optical amplification", *J. Opt. Soc. Am. B*, vol. 10, no. 4, pp. 684–690, April 1993.

[15] K. Oguso, H. Li, and M. Kitao, "Brillouin coefficients of chalcogenide glasses", *J. Opt. Soc. Am. B*, vol. 21, no. 7, pp. 1302–1304, 2004.

[16] G. P. Agrawal, *NonLinear Fiber Optics*, Academic Press, third edition, 2001.

[17] R. W. Boyd, K. Rzazewski, and P. Narum, "Noise initiation of stimulated Brillouin scattering", *Physical Review A*, vol. 42, no. 9, pp. 5514–5521, 1990.

[18] R. G. Smith, "Optical power handling capacity of low loss optical fibers as determined by stimulated Raman and Brillouin scattering", *Applied Optics*, vol. 11, no. 11, pp. 2489–2494, 1972.

[19] M. Damzen, V. Vlad, A. Mocofanescu, and V. Babin, *Stimulated Brillouin Scattering: Fundamentals and Applications*, Institute of Physics Publishing, Bristol and Philadelphia, third edition, 2003.

[20] M. S. Kang, A. Nazarkin, A. Brenn, and P. St. J. Russell, "Tightly trapped acoustic phonons in photonic crystal fibres as highly nonlinear artificial Raman oscillators", *Nature Physics*, vol. 5, pp. 276–280, 2009.

[21] M. S. Kang, A. Brenn, G. S. Wiederhecker, and P. St. J. Russell, "Optical excitation and characterization of gigahertz acoustic resonances in optical fiber tapers", *Applied Physics Letters*, vol. 93, no. 13, pp. 131110, 2008.

[22] R. M. Shelby, M.D. Levenson, and P.W. Bayer, "Guided acoustic-wave Brillouin scattering", *Physical Review B*, vol. 31, pp. 5244–5252, April 1985.

[23] R. N. Thurston, "Elastic waves in rods and clad rods", *J. Acoust. Soc. Am.*, vol. 64, no. 1, pp. 1–37, 1978.

[24] L. Brillouin, "Diffusion de la lumière et des rayons x par un corps transparent homogéne", *Ann. Physique*, vol. 17, pp. 88–122, 1922.

[25] C V. Raman and K. S. Krishnan, "A new type of secondary radiation", *Nature*, vol. 121, pp. 501–502, 1928.

[26] T. H. Maiman, "Stimulated optical radiation in ruby", *Nature*, vol. 187, pp. 493–494, 1960.

[27] R. Y. Chiao and C. H. Townes, "Stimulated Brillouin scattering and coherent generation of intense hypersonic waves", *Physical Review Letters*, vol. 12, no. 21, pp. 592–595, 1964.

[28] C. L. Tang, "Saturation and spectral characteristics of the Stokes emmision in the stimulated Brillouin process", *Journal of Applied Physics*, vol. 37, no. 6, pp. 2946–2955, 1966.

[29] D. Heiman, D.S. Hamilton, and R.W. Hellwarth, "Brillouin scattering measurements on optical glasses", *Physical Review B*, vol. 19, no. 12, pp. 6583–6592, 1979.

[30] E. P. Ippen and R. H. Stolen, "Stimulated Brillouin scattering in optical fibers", *Applied Physics Letters*, vol. 21, no. 11, pp. 539–541, 1972.

[31] R. W. Tkach, A. R. Chraplyw, and R. M. Derosier, "Spontaneous Brillouin scattering for single-mode optical-fibre characterization", *Electronics Letters*, vol. 22, no. 19, pp. 1011 – 1013, 1986.

[32] A. L. Gaeta and R.W. Boyd, "Stimulated Brillouin scattering in the presence of external feedback", *International Journal of Nonlinear Optics Physics*, vol. 1, no. 3, pp. 581, 1991.

[33] M. Niklès, L. Thévenaz, and P. A. Robert, "Brillouin gain Spectrum Characterization in Single-Mode Optical Fiber", *Journal of Lightwave Technology*, vol. 15, no. 10, pp. 1842–1851, 1997.

[34] A. Yeniay, J. M. Delavaux, and J. Toulouse, "Spontaneous and Stimulated Brillouin Scattering Gain Spectra in Optical Fibers", *Journal of Lightwave Technology*, vol. 20, no. 8, pp. 1425, 2002.

[35] T. Horiguchi and M. Tateda, "Optical-fiber-attenuation investigation using stimulated brillouin scattering between a pulse and a continuous wave", *Optics Letters*, vol. 14, no. 8, pp. 408–410, 1989.

[36] L. Thévenaz, S. M. Foaleng, and M. Niklès, "Fast measurement of local PMD with high spatial resolution using stimulated Brillouin scattering", in *Proceedings of the 33rd European Conference on Optical Communication ECOC'2007, Berlin, Germany*, 2007.

[37] M. O. Van Deventer and A. J. Boot, "Polarisation properties of stimulated Brillouin scattering in single mode fibers", *Journal of Lightwave Technology*, vol. 12, no. 4, pp. 585–590, 1994.

[38] L. Ursini, M. Santagiustina, and L. Palmieri, "Polarization-dependent Brillouin gain in randomly birefringent fibers", *IEEE Photonics Technology Letters*, vol. 22, no. 10, pp. 712–714, 2010.

[39] V. I. Kovalev and R. G. Harrison, "Waveguide-induced inhomogeneous spectral broadening of stimulated Brillouin scattering in optical fiber", *Optics Letters*, vol. 27, no. 22, pp. 1022, 2002.

[40] V. I. Kovalev and R. G. Harrison, "Observation of inhomogeneous spectral broadening of stimulated brillouin scattering in optical fiber", *Physical Review Letters*, vol. 85, no. 9, pp. 1879, 2000.

[41] S. Randoux and J. Zemmouri, "Comment on "observation of inhomogeneous spectral broadening of stimulated Brillouin scattering in an optical fiber"", *Physical Review Letters*, vol. 88, no. 2, pp. 029401, 2002.

[42] S. Le Floch and P. Cambon, "Study of Brillouin gain spectrum in standard single-mode optical fiber at low temperatures (1.4-370 K) and high hydrostatic pressures (1-250 bars)", *Optics Communications*, vol. 219, pp. 395–410, 2003.

[43] S. Afshar, V. P. Kalosha, X. Bao, and L. Chen, "Enhancement of stimulated Brillouin scattering of higher-order acoustic modes in single-mode optical fiber", *Optics Letters*, vol. 30, no. 20, pp. 2685–2687, 2005.

[44] A. B. Ruffin, M.-J. Li, X. Chen, A. Kobyakov, and F. Annunziata, "Brillouin gain analysis for fibers with different refractive indices", *Optics Letters*, vol. 30, no. 23, pp. 3123–3125, 2005.

[45] B. Ward and J. Spring, "Finite element analysis of Brillouin gain in SBS-suppressing optical fibers with non-uniform acoustic velocity profiles", *Optics Express*, vol. 17, no. 18, pp. 15685–15699, 2009.

[46] M. G. Herráez, K. Y. Song, and L. Thévenaz, "Arbitrary-bandwidth Brillouin slow light in optical fibers", *Optics Express*, vol. 14, no. 4, pp. 1395–1400, 2006.

[47] K. Y. Song and K. Hotate, "25 GHz bandwidth Brillouin slow light in optical fibers", *Optics Letters*, vol. 32, no. 3, pp. 217–219, 2007.

[48] S. P. Smith, F. Zarinetchi, and S. Ezekiel, "Narrow-linewidth stimulated Brillouin fiber laser and applications", *Optics Letters*, vol. 16, no. 6, pp. 393–395, 1991.

[49] J. Boschung, L. Thevenaz, and P. A. Robert, "High-accuracy measurements of the linewidth of a Brillouin fiber ring laser", *Electronics Letters*, vol. 30, no. 18, pp. 1488–1489, 1994.

[50] J. C. Knight, T. A. Birks, P. St. J. Russell, and D. M. Atkin, "All-silica single-mode optical fiber with photonic crystal cladding", *Optics Letters*, vol. 21, no. 19, pp. 1547–1549, 1996.

[51] P. St.J. Russell, "Photonic crystal fibers", *Science*, vol. 299, pp. 358–362, 2003.

[52] N. G. R. Broderick, T. M. Monro, P. J. Bennett, and D. J. Richardson, "Nonlinearity in holey optical fibers: measurement and future opportunities", *Optics Letters*, vol. 24, no. 20, pp. 1395–1397, 1999.

[53] J. H. Lee, Z. Yusoff, W. Belardi, M. Ibsen, T. M.Monro, and D. J. Richardson, "Investigation of Brillouin effects in small-core holey optical fiber : lasing and scattering", *Optics Letters*, vol. 28, no. 21, pp. 2022–5521, 2002.

[54] K. Furusawa, Z. Yusoff, F. Poletti, T. M. Monro, N. G. R. Broderick, and D. J. Richardson, "Brillouin characterization of holey optical fibers", *Optics Letters*, vol. 31, no. 17, pp. 2541–2543, 2006.

[55] F. Poletti, K. Furusawa, Z. Yusoff, N. G. Broderick, and D. J. Richardson, "Nonlinear tapered holey fibers with high stimulated Brillouin scattering threshold and controlled dispersion", *J. Opt. Soc. Am. B*, vol. 24, no. 9, pp. 2185–2194, 2007.

[56] L. Zou, X. Bao, and L. Chen, "Brillouin scattering spectrum in photonic crystal fiber with a partially germanium-doped core", *Optics Letters*, vol. 28, no. 21, pp. 2022–5521, 2003.

[57] L. Zou, X. Bao, S. Afshar V., and L. Chen, "Dependence of the Brillouin frequency shift on strain and temperature in photonic crystal fiber", *Optics Letters*, vol. 29, no. 13, pp. 1485, 2004.

[58] P. Dainese, P. St. J. Russell, N. Joly, J. C. Knight, G. S. Wiederhecker, H. L. Fragnito, V. Laude, and A. Khelif, "Stimulated Brillouin scattering from multi-GHz-guided acoustic phonons in nanostructured photonic crystal fibres", *Nature Physics*, vol. 2, no. 6, pp. 388–392, 2006.

[59] J.-C. Beugnot, T. Sylvestre, D. Alasia, H. Maillotte, V. Laude, A. Monteville, L. Provino, N. Traynor, S. Foaleng Mafang, and L. Thévenaz, "Complete experimental characterization of stimulated Brillouin scattering in photonic crystal fiber", *Optics Express*, vol. 15, no. 23, pp. 15517–15522, 2007.

[60] J. E. McElhenny, R. K. Pattnaik, J. Toulouse, K. Saitoh, and M. Koshiba, "Unique characteristic features of stimulated Brillouin scattering in small-core photonic crystal fibers", *J. Opt. Soc. Am. B*, vol. 25, no. 4, pp. 582–593, 2008.

[61] J. E. McElhenny, R. Pattnaik, and J. Toulouse, "Polarization dependence of stimulated Brillouin scattering in small-core photonic crystal fibers", *J. Opt. Soc. Am. B*, vol. 25, no. 12, pp. 2107–2115, 2008.

[62] A. Minardo, R. Bernini, W. Urbanczyk, J. Wojcik, N. Gorbatov, M. Tur, and L. Zeni, "Stimulated Brillouin scattering in highly birefringent microstructure fiber: experimental analysis", *Optics Letters*, vol. 33, no. 20, pp. 2329–2331, 2008.

[63] B. Stiller, S. M. Foaleng, J.-C. Beugnot, M. W. Lee, M. Delqué, G. Bouwmans, A. Kudlinski, L. Thévenaz, H. Maillotte, and T. Sylvestre, "Photonic crystal fiber mapping using Brillouin echoes distributed sensing", *Optics Express*, vol. 18, no. 19, pp. 20136–20142, 2010.

[64] B. Stiller, M. Delqué, M.W. Lee, S. Foaleng Mafang, J.C. Beugnot, A. Kudlinski, L. Thevenaz, H. Maillotte, and T. Sylvestre, "Effect of inhomogeneities on backward and forward Brillouin scattering in photonic crystal fibers", in *Proceedings SPIE Photonics Europe, Photonic Crystal Fibers IV*, 2010, vol. 7714 of *771406*, pp. 1–12.

[65] B. Stiller, J. C. Beugnot, S. Foaleng Mafang, M. W. Lee, M. Delqué, A. Kudlinski, H. Maillotte, V. Laude, L. Thévenaz, and T.Sylvestre, "Observation of Brillouin linewidth broadening and decay time in photonic crystal fiber", in *Proceedings IEEE Photonics Society Summer Topical Meeting Series,*, 2010, pp. 168–169.

[66] J. C. Beugnot, B. Stiller, S. Foaleng Mafang, M. W. Lee, M. Delqué, A. Kudlinski, H. Maillotte, V. Laude, L. Thévenaz, and T. Sylvestre, "Experimental observation of Brillouin linewidth broadening and decay time in photonic crystal fiber", in *European Conference on Optical Communications ECOC, September 21-25, Torino, Italy*, 2010, Tu.4.D.S.

[67] S. Dasgupta, F. Poletti, S. Liu, P. Petropoulos, D. J. Richardson, L. Gruner-Nielsen, and S. Herstrom, "Modeling Brillouin gain spectrum of solid and microstructured optical fibers using a finite element method", *Journal of Lightwave Technology*, vol. 29, no. 1, pp. 22–30, 2011.

[68] C. G. Carlson, R. B. Ross, J. M. Schafer, J. B. Spring, and B. G. Ward, "Full vectorial analysis of Brillouin gain in random acoustically microstructured photonic crystal fibers", *Phys. Rev. B*, vol. 83, pp. 235110, 2011.

[69] R. M. Shelby, M. D. Levenson, and P. W. Bayer, "Resolved forward Brillouin scattering in optical fibers", *Physical Review Letters*, vol. 54, no. 9, pp. 939–942, 1985.

[70] C. K. Jen, J.E.B. Oliveira, N. Goto, and K. Abe, "Role of guided acoustic wave properties in single-mode optical fibre design", *Electronics Letters*, vol. 24, no. 23, pp. 1419–1420, 1988.

[71] M. Oshashi, N. Shibata, and K. Shiraki, "Fiber diameter estimation based on guided acoustic wave Brillouin scaterring", *Electronics Letters*, vol. 28, no. 10, pp. 900–901, 1992.

[72] E. Picholle and A. Picozzi, "Guided-acoustic-wave resonances in the dynamics of a stimulated brillouin fiber ring laser", *Optics Communications*, vol. 125, pp. 327–330, February 1997.

[73] P. St. J. Russell, D. Culverhouse, and F. Farahi, "Theory of forward stimulated Brillouin scattering in dual-mode single-core fibers", *IEEE Journal of Quantum Electronics*, vol. 27, no. 3, pp. 836–842, 1991.

[74] K. Shiraki and M. Ohashi, "Sound velocity measurement based on guided acoustic-wave brillouin scattering", *IEEE Photonics Technology Letters*, vol. 4, no. 4, pp. 1177, 1992.

[75] Y. Tanaka and K. Ogusu, "Temperature coefficient of sideband frequencies produced by depolarized guided acoustic-wave Brillouin scattering", *IEEE Photonics Technology Letters*, vol. 10, no. 12, pp. 1769–1771, 1998.

[76] V. Laude, A. Khelif, S. Benchabane, M. Wilm, T. Sylvestre, B. Kibler, A. Mussot, J. M. Dudley, and H. Maillotte, "Phononic band-gap guidance of acoustic modes in photonic crystal fibers", *Physical Review B*, vol. 71, no. 4, pp. 045107, 2005.

[77] D. Elser, U. L. Andersen, A. Korn, O. Glockl, S. Lorenz, Ch. Marquardt, and G. Leuchs, "Reduction of guided acoustic wave Brillouin scattering in photonic crystal fibers", *Physical Review Letters*, vol. 97, pp. 133901, 2006.

[78] J.-C. Beugnot, T. Sylvestre, H. Maillotte, G. Mélin, and V. Laude, "Guided acoustic wave Brillouin scattering in photonic crystal fibers", *Optics Letters*, vol. 32, no. 1, pp. 17–19, 2007.

[79] P. Dainese, P. St. J. Russell, G. S. Wiederhecker, N. Joly, H. L. Fragnito, V. Laude, and A. Khelif, "Raman-like light scattering from acoustic phonons in photonic crystal fiber", *Optics Express*, vol. 14, no. 9, pp. 4141–4150, 2006.

[80] G. S. Wiederhecker, A. Brenn, H. L. Fragnito, and P. St. J. Russell, "Coherent control of ultrahigh-frequency acoustic resonances in photonic crystal fibers", *Physical Review Letters*, vol. 100, pp. 203903, 2008.

[81] A. Brenn, G. S. Wiederhecker, M. S. Kang, H. Hundertmark, N. Joly, and P. St.J. Russell, "Influence of air-filling fraction on forward Raman-like scattering by transversely trapped acoustic resonances in photonic crystal fibers", *J. Opt. Soc. Am. B*, vol. 26, no. 8, pp. 1641–1648, 2009.

[82] M. S. Kang, A. Brenn, and P. St. J. Russell, "All-optical control of gigahertz acoustic resonances by forward stimulated interpolarization scattering in a photonic crystal fiber", *Physical Review Letters*, vol. 105, pp. 153901, 2010.

[83] M. S. Kang and P. St. J. Russell, "In-fiber unidirectional variable-optical-attenuator controlled by light", in *European Conference on Optical Communication (ECOC), 2010*, 2010.

[84] M. S. Kang, A. Butsch, and P. St. J. Russell, "Reconfigurable light-driven opto-acoustic isolators in photonic crystal fibre", *Nature Photonics*, vol. 5, pp. 549–553, 2011.

[85] J. Wang, Y. Zhu, R. Zhang, and D. J. Gauthier, "FSBS resonances observed in a standard highly nonlinear fiber", *Optics Express*, vol. 19, no. 6, pp. 5339–5349, 2011.

[86] B. Stiller, M. Delqué, J.-C. Beugnot, M. W. Lee, G. Mélin, H. Maillotte, V. Laude, and T. Sylvestre, "Frequency-selective excitation of guided acoustic modes in a photonic crystal fiber", *Optics Express*, vol. 19, no. 8, pp. 7689–7694, 2011.

[87] L. Thévénaz, Ed., *Advanced Fiber Optics, Concepts and Technology*, EPFL Press, 2011.

[88] M. K. Barnoski and S. M. Jensen, "Fiber waveguides: a novel technique for investigating attenuation characteristics", *Applied Optics*, vol. 15, no. 9, pp. 2112–2115, 1976.

[89] J. P. Dakin, D. J. Pratt, G. W. Bibby, and J. N. Ross, "Distributed optical fibre Raman temperature sensor using a semiconductor light source and detector", *Electronics Letters*, vol. 21, no. 13, pp. 569–570, 1985.

[90] L. Thévenaz, "Brillouin distributed time-domain sensing in optical fibers: state of the art and perspectives", *Frontiers in Optoelectronics China*, vol. 3, no. 1, pp. 13–21, 2010.

[91] K. Krebber, *Ortsauflösende Lichtleitfaser-Sensorik für Temperatur und Dehnung unter Nutzung der stimulierten Brillouin-Streuung basierend auf der Frequenzbereichsanalyse*, PhD thesis, Ruhr-Universität Bochum, 2001.

[92] N. Nöther, *Distributed Fiber Sensors in River Embankments: Advancing and Implementing the Brillouin Optical Frequency Domain Analysis*, PhD thesis, BAM Bundesanstalt für Materialforschung und -prüfung, 2010.

[93] Kellie Brown, Anthony W. Brown, and Bruce G. Colpitts, "Characterization of optical fibers for optimization of a brillouin scattering based fiber optic sensor", *Optical Fiber Technology*, vol. 11, no. 2, pp. 131–145, 2005.

[94] X. Bao, "Optical fiber sensors based on Brillouin scattering", *Optics & Photonics News*, vol. 20, no. 9, pp. 40–46, 2009.

[95] T. Kurashima, T. Horiguchi, and Y. Koyamada, "A new technique to shift lightwave frequency for dofs", in *Proc. SPIE 1797*, 1992, pp. 18–30.

[96] K. Shimizu, T. Horiguchi, Y. Koyamada, and T. Kurashima, "Coherent self-heterodyne Brillouin OTDR for measurement of brillouin frequency shift distribution in optical fibers", *Journal of Lightwave Technology*, vol. 12, no. 5, pp. 730 – 736, 1994.

[97] T. Kurashima, M. Tateda, T. Horiguchi, and Y. Koyamada, "Performance improvement of a combined otdr for distributed strain and loss measurement by randomizing the reference light polarization state", *IEEE Photonics Technology Letters*, vol. 9, no. 3, pp. 1041–1135, 1997.

[98] D. Culverhouse, F. Farahi, and C. N. Pannell D.A. Jackson, "Potential of stimulated Brillouin scattering as sensing mechanism for distributed temperature sensors", *Electronics Letters*, vol. 25, no. 4, pp. 913–915, 1989.

[99] X. Bao, D. J. Webb, and D. A. Jackson, "22-km distributed temperature sensor using Brillouin gain in an optical fiber", *Optics Letters*, vol. 18, no. 7, pp. 552–554, 1993.

[100] X. Bao, D. J. Webb, and D. A. Jackson, "32-km distributed temperature sensor based on Brillouin loss in an optical fiber", *Optics Letters*, vol. 18, no. 18, pp. 1561–1563, 1993.

[101] M. Niklès, L. Thévenaz, and P. A. Robert, "Simple distributed fiber sensor based on Brillouin gain spectrum analysis", *Optics Letters*, vol. 21, no. 10, pp. 758–760, 1996.

[102] A. Fellay, L. Thévenaz, M. Facchini, M. Niklès, and P. Robert, "Distributed sensing using stimulated Brillouin scattering : towards ultimate resolution.", in *Optical Fiber Sensors (OFS), Williamsburg, Virginia*, 1997.

[103] M. Dossou, D. Bacquet, and P. Szriftgiser, "Vector Brillouin optical time-domain analyzer for high-order acoustic modes", *Optics Letters*, vol. 35, no. 22, pp. 3850, 2010.

[104] *Omnisens*, http://www.omnisens.ch/.

[105] X. Angulo-Vinuesa, S. Martin-Lopez, J. Nuno, P. Corredera, J.-D. Ania-Castanon, L. Thévenaz, and M. Gonzalez-Herraez, "Hot spot detection over 100 km with 2 meter resolution in a Raman-assisted Brillouin distributed sensor", in *Proc. SPIE*, 2011, vol. 7753, p. 775309.

[106] S. Martin-Lopez, M. Alcon-Camas, F. Rodriguez, P. Corredera, J. D. Ania-Castañon, L. Thévenaz, and M. Gonzalez-Herraez, "Brillouin optical time-domain analysis assisted by second-order Raman amplification", *Optics Express*, vol. 18, no. 18, pp. 18769–18778, 2010.

[107] M. A. Soto, G. Bolognini, and F. Di Pasquale, "Long-range simplex-coded BOTDA sensor over 120km distance employing optical preamplification", *Optics Letters*, vol. 36, no. 2, pp. 232–234, 2011.

[108] D. Garus, K. Krebber, F. Schliep, and T. Gogolla, "Distributed sensing technique based on Brillouin optical-fiber frequency-domain analysis.", *Optics Letters*, vol. 21, no. 17, pp. 1402–1404, 1996.

[109] D. Garcus, T. Gogolla, K.Krebber, and F. Schliep, "Brillouin optical-fiber frequency-domain analysis for distributed temperature and strain measurements", *Journal of Lightwave Technology*, vol. 15, no. 4, pp. 654 – 662, 1997.

[110] A. Minardo, G. Testa, L. Zeni, and R. Bernini, "Theoretical and experimental analysis of Brillouin scattering in single-mode optical fiber excited by an intensity- and phase-modulated pump", *Journal of Lightwave Technology*, vol. 28, no. 2, pp. 193–200, 2010.

[111] K. Hotate and T. Hasegawa, "Measurement of Brillouin gain spectrum distribution along an optical fiber using a correlation-based technique - proposal, experiment and simulation.", *IEICE Trans. Electronics*, vol. E 83-C, no. 3, pp. 405–412, 2000.

[112] K. Hotate and M. Tanaka, "Distributed fiber Brillouin strain sensing with 1-cm spatial resolution by correlation-based continuous-wave technique", *IEEE Photonics Technology Letters*, vol. 14, no. 2, pp. 197–199, 2002.

[113] S. LeFloch and L. Thévenaz, "Correlation-based Brillouin sensing using an injection-locking technique", in *Technical Digest of the 16th Optical Fiber Sensors Conference OFS'2003, Nara Japan*, 2003, vol. We2-2, pp. 286–289.

[114] Y. Mizuno, W. Zou, Z. He, and K. Hotate, "Proposal of Brillouin optical correlation-domain reflectometry (BOCDR)", *Optics Express*, vol. 16, no. 16, pp. 12148–12153, 2008.

[115] X. Bao, A. Brown, M. DeMerchant, and J. Smith, "Characterization of the Brillouin loss spectrum of single-mode fibres by use of very short (10-ns) pulses", *Optics Letters*, vol. 24, no. 8, pp. 510–512, 1999.

[116] L. Zou, X. Bao, Y. Wan, and L. Chen, "Coherent probe-pump-based Brillouin sensor for centimeter-crack detection", *Optics Letters*, vol. 30, no. 4, pp. 370–372, 2005.

[117] A. W. Brown and B. G. Colpitts, "Dark-pulse Brillouin optical time-domain sensor with 20-mm spatial resolution", *Journal of Lightwave Technology*, vol. 25, no. 1, pp. 381–386, 2007.

[118] S. Foaleng Mafang, J.-C. Beugnot, and L. Thévenaz, "Optimized configurarion for high resolution distributed sensing using Brillouin echoes", in *Proceedings SPIE, UK, Edinburgh*, 2009, p. 75032C.

[119] S. M. Foaleng, M. Tur, J.-C. Beugnot, and L. Thévenaz, "High spatial and spectral resolution long-range sensing using Brillouin echoes", *Journal of Lightwave Technology*, vol. 28, no. 20, pp. 2993–3003, 2010.

[120] S. Foaleng Mafang, F. Rodriguez-Barrios, S. Martin-Lopez, M. Gonzalez-Herraez, and L. Thévenaz, "Detrimental effect of self-phase modulation on the performance of Brillouin distributed fiber sensors", *Optics Letters*, vol. 36, no. 2, pp. 97, 2011.

[121] M. W. Lee, B. Stiller, J. Hauden, H. Maillotte, C. Roch, L. Thévenaz, and T. Sylvestre, "Differential phase-shift keying technique-based Brillouin echo-distributed sensing", *IEEE Photonics Technology Letters*, vol. 24, no. 1, pp. 79–81, 2012.

[122] M. W. Lee, B. Stiller, J. Hauden, H. Maillotte, L. Thévenaz, and T. Sylvestre, "Brillouin echo-distributed sensing based on differential phase-shift keying technique", in *European Conference on Optical Communications ECOC, Geneva, Switzerland*, 2011, Tu.6.LeCervin.2.

[123] K. Y. Song, W. Zou, Z. He, and K. Hotate, "All-optical dynamic grating generation based on Brillouin scattering in polarization-maintaining fiber", *Optics Letters*, vol. 33, no. 9, pp. 926–928, 2008.

[124] K. Y. Song, W. Zou, Z. He, and K. Hotate, "Optical time-domain measurement of Brillouin dynamic grating spectrum in a polarization-maintaining fiber", *Optics Letters*, vol. 34, no. 9, pp. 1381–1383, 2009.

[125] K.-Y. Song, S. Chin, N. Primerov, and L. Thevenaz, "Time-domain distributed sensor with 1 cm spatial resolution based on Brillouin dynamic gratings", in *Proceedings of the 20th International Conference on Optical Fibre Sensors*, 2009, Proc. SPIE 7503, pp. 75037V–4.

[126] K. Y. Song, S. Chin, N. Primerov, and L. Thevenaz, "Time-domain distributed fiber sensor with 1 cm spatial resolution based on Brillouin dynamic grating", *Journal of Lightwave Technology*, vol. 28, no. 14, pp. 2062–2067, 2010.

[127] W. Zou, Z. He, and K. Hotate, "Complete discrimination of strain and temperature using Brillouin frequency shift and birefringence in a polarization-maintaining fiber", *Optics Express*, vol. 17, no. 3, pp. 1248–1255, 2009.

[128] W. Zou, Z. He, and K. Hotate, "Demonstration of Brillouin distributed discrimination of strain and temperature using a polarization-maintaining optical fiber", *Journal of Lightwave Technology*, vol. 22, no. 8, pp. 526 – 528, 2010.

[129] T. Ritari, J. Tuominen, H. Ludvigsen, J. Petersen, T. Sørensen, T. Hansen, and H. Simonsen, "Gas sensing using air-guiding photonic bandgap fibers", *Optics Express*, vol. 12, no. 17, pp. 4080–4087, 2004.

[130] F. Benabid, F. Couny, J. C. Knight, T. A. Birks, and P. St J. Russell, "Compact, stable and efficient all-fibre gas cells using hollow-core photonic crystal fibres", *Nature*, vol. 434, pp. 488–491, 2005.

[131] A. van Brakel, C. Grivas, M. N. Petrovich, and D. J. Richardson, "Micro-channels machined in microstructured optical fibers by femtosecond laser", *Optics Express*, vol. 15, no. 14, pp. 8731–8736, 2007.

[132] B. J. Eggleton, P. S. Westbrook, R. S. Windeler, S. Spälter, and T. A. Strasser, "Grating resonances in air-silica microstructured optical fibers", *Optics Letters*, vol. 24, no. 21, pp. 1460–1462, 1999.

[133] N. Groothoff, J. Canning, E. Buckley, K. Lyttikainen, and J. Zagari, "Bragg gratings in air-silica structured fibers", *Optics Letters*, vol. 28, no. 4, pp. 233–235, 2003.

[134] C.-L. Zhao, J. Zhao, W. Jin, J. Ju, L. Cheng, and X. Huang, "Simultaneous strain and temperature measurement using a highly birefringence fiber loop mirror and a long-period grating written in a photonic crystal fiber", *Optics Communications*, vol. 282, no. 20, pp. 4077–4080, 2009.

[135] O. Frazao, S. H. Aref, J. M. Baptista, J. L. Santos, H. Latifi, F. Farahi, J. Kobelke, and K. Schuster, "Fabry-pérot cavity based on a suspended-core fiber for strain and temperature measurement", *IEEE Photonics Technology Letters*, vol. 21, no. 17, pp. 1229–1231, 2009.

[136] H. Gong, C. C. Chan, L. Chen, and X. Dong, "Strain sensor realized by using low-birefringence photonic-crystal-fiber-based sagnac loop", *IEEE Photonics Technology Letters*, vol. 22, no. 16, pp. 1238–1240, 2010.

[137] T. Nasilowski, F. Berghmans, T. Geernaert, K. Chah, J. Van Erps, G. Statkiewicz, M. Szpulak, J. Olszewski, G. Golojuch, T. Martynkien, W. Urbanczyk, P. Mergo, M. Makara, J. Wojcik, C. Chojetzki, and H. Thienpont, "Sensing with photonic crystal fibres", in *IEEE International Symposium on Intelligent Signal Processing*, 2007, pp. 1–6.

[138] O. Frazão, J. L. Santos, and F. M. Araújoand L. A. Ferreira, "Optical sensing with photonic crystal fibers", *Laser & Photonics Reviews*, vol. 2, no. 6, pp. 449–459, 2008.

[139] L. F. Zou, X. Y. Bao, and L. Chen, "Simultaneous distributed Brillouin strain and temperature sensor with photonic crystal fiber", in *Proceedings of the society of photo-optical instrumentation engineers (SPIE)*, 2004, vol. 5384, pp. 13–17.

[140] L. Zou, X. Bao, and L. Chen, "Distributed Brillouin temperature sensing in photonic crystal fiber", *Smart Materials and Structures*, vol. 14, no. 3, pp. S8, 2005.

[141] W. Zhang, Y. Wang, P. Yanyan, Y. Huang, and J. Peng, "Influences of pump wavelength and environment temperature on the dual-peaked Brillouin property of a small-core microstructured fiber", *Optics Letters*, vol. 32, no. 16, 2007.

[142] Y. Pi, W. Zhang, Y. Wang, Y. Huang, and J. Peng, "Temperature dependence of the spontaneous Brillouin scattering spectrum in microstructure fiber with small core", *Tsinghua Science & Technology*, vol. 13, no. 1, pp. 43–46, 2008.

[143] Y. Dong, X. Bao, and L. Chen, "Distributed temperature sensing based on birefringence effect on transient Brillouin grating in a polarization-maintaining photonic crystal fiber", *Optics Letters*, vol. 34, no. 17, pp. 2590–2592, 2009.

[144] Y. Tanaka and K. Ogusu, "Tensile-strain coefficient of resonance frequency of depolarized guided acoustic-wave Brillouin scattering", *IEEE Photonics Technology Letters*, vol. 11, no. 7, pp. 865–867, July 1999.

[145] E. Carry, J.-C. Beugnot, B. Stiller, M. W. Lee, H. Maillotte, and T. Sylvestre, "Temperature coefficient of the high-frequency guided acoustic mode in a photonic crystal fiber", *Applied Optics*, 2011, accepted.

Chapter 3

Experimental investigation of Brillouin backscattering in photonic crystal fibers

The theory of Brillouin scattering has already been introduced in chapter 2 where we have seen that two types of Brillouin scattering can be measured in different ways: forward and backward scattering. Brillouin backscattering results from the interaction of optical waves with longitudinal acoustic waves in contrast to forward Brillouin scattering which comes from transverse acoustic modes. This chapter is dedicated to experiments of Brillouin backscattering in photonic crystal fibers (PCFs). The results of *integrated* and *distributed* measurements will be shown. *Integrated* measurement of Brillouin backscattering means that the signal backscattered from the whole length of the fiber is recorded due to the use of a CW-pump wave: we launch a CW-pump wave into the fiber and obtain the spectrum of the Brillouin gain from the light backscattered in the whole fiber. Distributed measurement, on the other hand, reveals the spectrum of the Brillouin gain for each section of the fiber limited in spatial resolution. This requires a more complicated experimental setup with pump and probe waves that travel counter-propagatively in the fiber.
This chapter begins with two paragraphs on the experimental setups for integrated and distributed measurements as well as the setup to determine the critical pump power for the Brillouin threshold. The term *stimulated Brillouin scattering* attracts attention because it is used in different ways. On the one hand *stimulated* means that the pump stimulates Brillouin backscattering in a fibre and the Brillouin-backscattered power significantly increases, which, per definition, is the case above the critical pump power. On the other hand when the pump and probe waves counter-propagate in a fiber, Brillouin scattering gets *stimulated* by both waves. This is the case for the distributed measurements. Physically, it is the same process because for both cases. The backscattered or

counter-propagation wave interferes with the pump wave and creates an acoustic grating by electrostriction. Nevertheless, when we are talking about *stimulated* in this manuscript we mean Brillouin backscattering from a CW-pump above the critical pump power.
Chapter 3.1 and 3.2 will present these two techniques. We were able to achieve some interesting results, both for studies in fundamental physics and for applications such as the monitoring of fiber homogeneity, that may be interesting for fiber manufacturers. In chapter 3.3 we present the result of distributed measurements with strain applied to a part of the fiber. Different fibers are measured and compared to results in literature. In chapter 3.4 we show the impact of fiber inhomogeneities on Brillouin scattering. We will compare two fibers with nearly the same air-hole micro-structure but fabricated by different drawing processes and fully characterize them in terms of Brillouin frequency shift through the integrated and distributed measurements of Brillouin scattering. The last paragraph 3.5 reports about the observation of the decay time of acoustic waves in PCFs and conventional SMFs. With help of a high-resolved distributed measurement in PCFs we show the possibility to measure the acoustic decay time of different fibres. We will see in particular that the signal of Brillouin backscattering decays faster in a PCF than in a conventional SMF. We also provide a theoretical model based on multiple Lorentzian fits to explain the origin of the acoustic decay time.

3.1 Integrated measurement of Brillouin backscattering

3.1.1 Brillouin gain spectrum

As already mentioned in chapter 2.1.2 the spectrum of Brillouin gain in an optical fiber has a Lorentzian shape and is shifted by about 11 GHz from the pump wave. This is quite close to the pump wave and hence requires an accurate measurement. Different setups have been developed for this purpose since the first measurement of Brillouin scattering in optical fibers by Ippen and Stolen in 1972 [1].

3.1.1.1 Overview about Brillouin gain spectrum measurement methods

In Ref. [1] the authors proposed a method to analyse the backscattered wave and the determination of the Brillouin frequency shift (BFS) of optical fiber using a Fabry-Perot etalon. The advantage of their method is a simple setup but the spectral resolution was not good enough to measure precisely the Brillouin linewidth. This was improved by

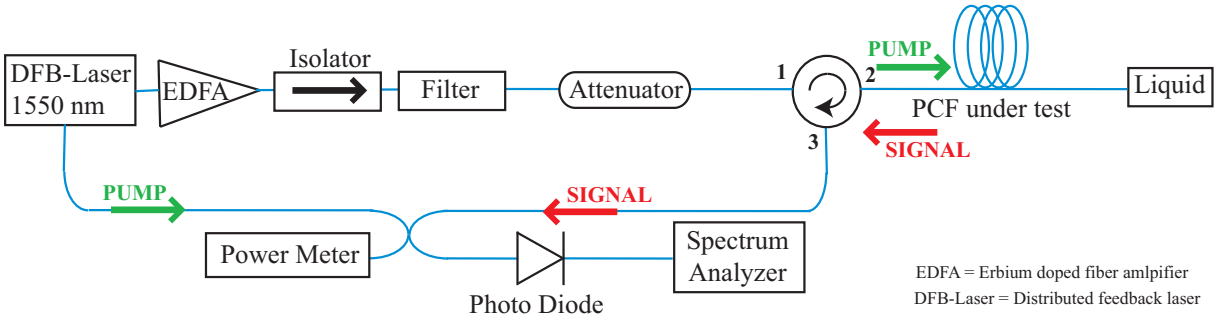

Figure 3.1: Experimental setup for the self-heterodyne measurement of Brillouin gain spectrum.

Gaeta and Boyd in 1991 [2] where they achieved a resolution of 0.6 MHz and measured the FWHM of Brillouin gain spectrum at different pump powers. They also demonstrated that the Brillouin gain spectrum evolves from a Lorentzian shape to a Gaussian one and narrows when increasing the pump power. Other methods are based on the pump-probe configuration which is commonly used for distributed Brillouin sensors. Shibata *et al.* [3] presented a setup where two optical waves, a pump and a probe wave, are launched in a single optical fiber in the opposite direction, respectively. The probe wave is shifted by the BFS of the fiber with respect to the pump wave and amplified along the fiber by the Brillouin gain occured by the pump. The probe wave is scanned in frequency around the BFS to obtain the Brillouin gain spectrum. This setup needs a high frequency stability of the two laser sources and allows a distributed measurement with high spectral resolution when pulses are used. Niklès *et al.* [4] later improved the experiment by using only one laser source. Although it is simplified the setup remains quite complicated to implement compared to other methods. The distributed setups will be discussed further in paragraph 3.2.
Another method to determine the BGS is the self-heterodyne technique, which was introduced by Tkach *et al.* in 1986 [5]. This method is based on the beating of the pump with the backscattered wave and the Brillouin gain sepctrum is measured by a fast photodetector and an RF spectrum analyser which offers very high spectral resolution compared to an optical spectrum analyser (OSA). In this thesis we have used this method for integrated Brillouin measurements and it will be explained in the next paragraph. A more detailed overview about the different measurement techniques can be found in [6].

3.1.1.2 The self-heterodyne technique

The self-heterodyne configuration to measure the backscattered Brillouin spectrum [7,8] is depicted in Fig.(3.1). We used a distributed feedback laser (DFB[1]) at 1550 nm with

[1]RIO 0194-1-34-1, linewidth 20 kHz at 1.55 nm

a linewidth of 30 kHz. The laser is set to a temperature of 27°C and the bias current of 40 mA. The laser emission is amplified by an erbium-doped fiber amplifier (EDFA, Keopsys, 33 dBm) and injected into an isolator. The isolator avoids reflections to protect the EDFA. Then a 5-nm bandpass filter is inserted to remove the amplified spontaneous emission (ASE) coming from the EDFA to ensure accurate measurement. The light passes through the optical circulator from port 1 to port 2. The light enters the PCF whose other end is dipped in a viscous index adaptation liquid to prevent Fresnel reflections. The light backscattered in the PCF passes through the circulator from port 2 to port 3. A 50:50-coupler enables a heterodyne detection using the frequency beating between the Brillouin signal backscattered from the PCFs and the original laser source. This setup allows a very accurate measurement. The interference beating is acquired by a fast photodiode (bandwidth ranging from 30 kHz - 12 GHz) and visualised as Brillouin gain spectrum on the RF spectrum analyser (Anritsu[2]).

3.1.1.3 Experimental results

We first studied a 260 m - long all-silica single-mode fiber (SMF). The experimental result of the Brillouin gain spectrum is shown in Fig.(3.2) where averaging with about 100 data rows and fitting with a Lorentzian shape has been used. First we can see that the FWHM in Fig.(3.2 a) narrows with increasing pump power as it was reported in [3] because the Brillouin gain rises exponentially for all frequencies. In the low-power range we find a FWHM of about 30 MHz which is in good accordance to the measured FWHM in silica [9, 10]. In this region the data is noisy because the scattering process is not yet stimulated but rather caused by thermal vibrations. The evolution of the spectrum can be observed in Fig.(3.2 b-d) for 10 dBm, 20 dBm and 25 dBm pump powers, respectively. In Fig.(3.2 b) we observe one main peak at 10.85 GHz and a smaller second at 10.89 GHz. The power ratio between the two peaks will change with increasing pump power while the data becomes less noisy and the Brillouin gain spectrum more stable. The first peak is the acoustic mode due to the core of the SMF and the second peak is supposed to be a second acoustic mode of the fiber cladding [11, 12]. Since the optical wave is confined in the fiber core, only the main peak can be stimulated at high pump powers. This is the reason for which the second peak remains small compared to the mainpeak in Fig.(3.2 d). We now compare these results for the conventional SMF to our various PCFs. The first PCF we tested has a multiscale structure of which the cross section can be seen in the inset of Fig.(3.3 b). This fiber has two zero-dispersion wavelengths, was drawn for supercontinuum generation [13] and will receive more attention in chapter 5 for its acoustic behaviour. As can be seen in Fig.(3.3 b), the Brillouin gain spectrum measured at a pump power of 12.1 dBm (8 dB below the Brillouin threshold of this fiber) has three peaks at 10.72 GHz,

[2]Anritsu MS2667C Spectrum Analzer 9 kHz-30 GHz

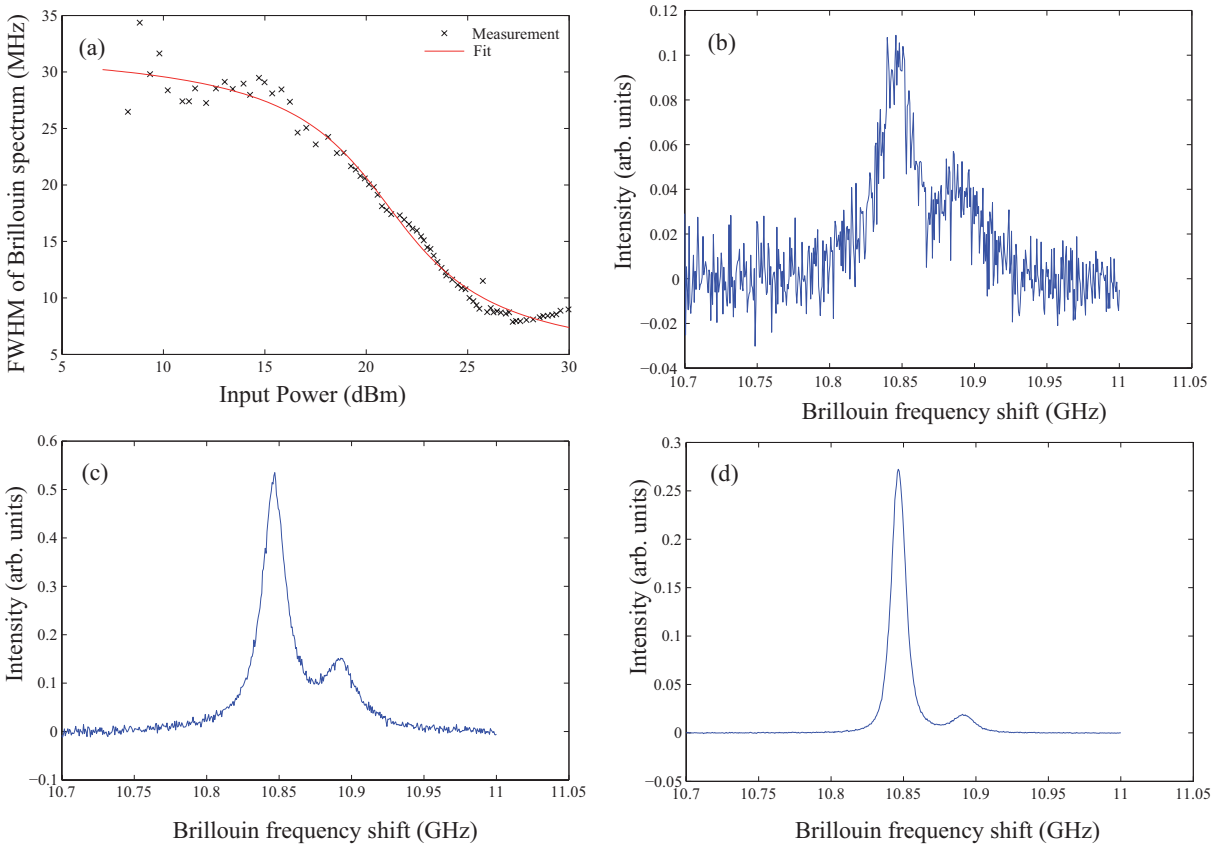

Figure 3.2: (a) Brillouin linewidth (FWHM) versus pump power, Brillouin gain spectrum (maximum: 10.85 GHz) at (b) 10 dBm, (c) 20 dBm and (d) 25 dBm for a 260m-long SMF.

10.92 GHz and 11.11 GHz. The FWHM of the main peak at 10.72 GHz evolves from about 90 MHz to 20 MHz. The larger FWHM in low power range for PCFs in comparison to conventional SMF is probably due to several interacting acoustic modes, which is in good accordance to what has been observed in Refs. [7, 14]. This is also the case for the other PCF, which has a hexagonal structure (inset of Fig.(3.4 b)). Its FWHM is about 80 MHz for low pump power and narrows to 30 MHz while increasing the pump. The Brillouin gain spectrum is single-mode at 11.07 GHz and has a slightly asymmetric bump at the right side. Further integrated measurement of the Brillouin gain will be shown in paragraph 3.4 and 4.3 and a multi-Lorentzian model for several acoustic modes in one Brillouin spectrum will also be discussed in paragraph 3.5.

3.1.2 Critical pump power of the Brillouin threshold

In this paragraph we describe the measurement of the critical pump power for the Brillouin threshold as introduced theoretically in paragraph 2.2.1.4. We use the definition that the

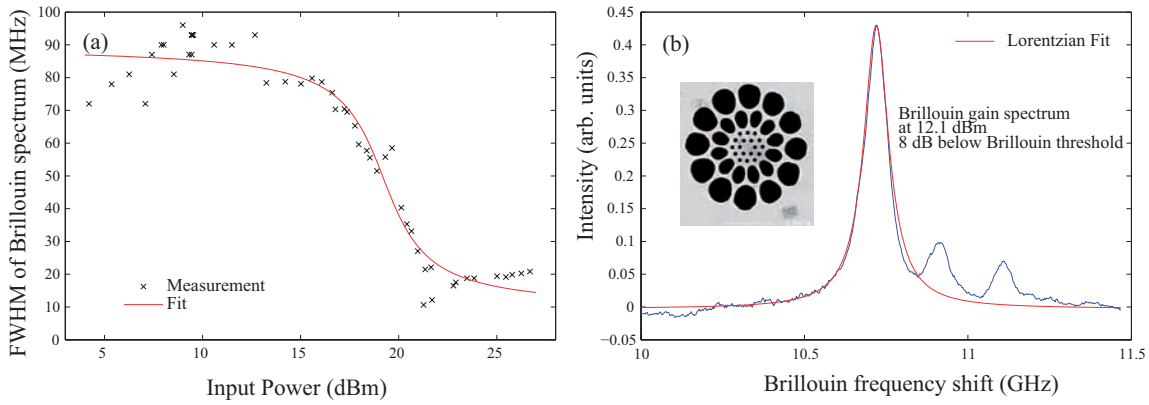

Figure 3.3: (a) Brillouin linewidth (FWHM) versus pump power, (b) Brillouin gain spectrum (maximum: 10.72 GHz) at 12.1 dBm, 8 dB below Brillouin threshold, for a 106m-long multiscale PCF. The SEM image is shown in the inset.

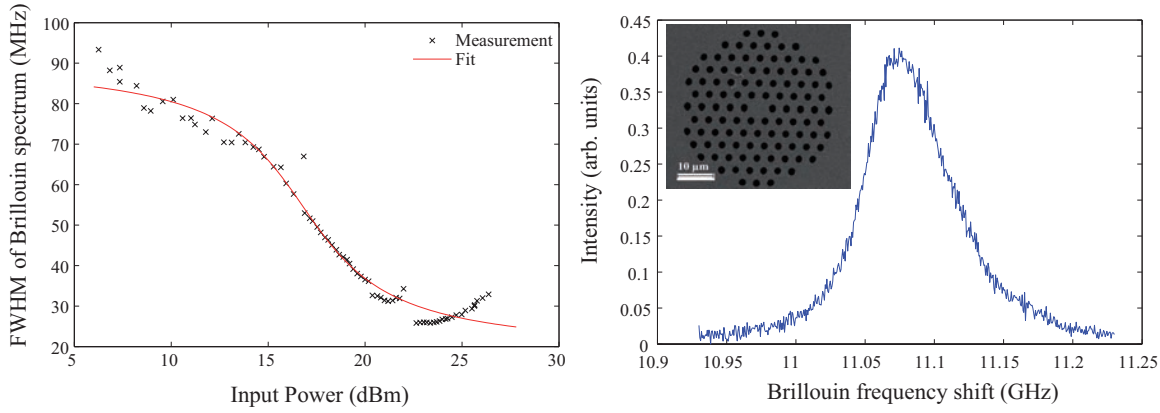

Figure 3.4: (a) Brillouin linewidth (FWHM) versus pump power, (b) Brillouin gain spectrum (maximum: 11.07 GHz) at 15 dBm, 7 dB below Brillouin threshold, for a 380m-long PCF with hexagonal structure. The SEM image is shown in the inset.

critical pump power is reached when the backscattered power is 1% of the pump power [15] but there exists as well the definition that the Brillouin threshold is reached when the backscattered power equals the injected power [16]. We decided to take the 1%-definition because this is the range where Brillouin scattering does not saturate. The setup for the measurement of the Brillouin threshold is schematically sketched in Fig.(3.5). It is a simplified version of the self-heterodyne measurement setup. We just removed the self-heterodyne detection and replaced it by a power meter at port 3 of the circulator. For this measurement it is very important to avoid Fresnel reflections because they are harmful in the low power range for stable measurements. To determine the critical power of the Brillouin threshold of the fiber under test we measure three data-series: the input power, the backscattered power and for reasons of completeness as well the transmitted

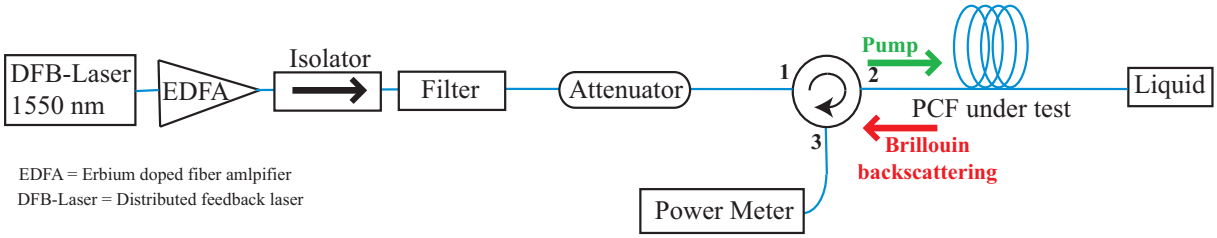

Figure 3.5: Experimental setup for Brillouin threshold measurement.

power. The input power is measured at port 2 of the circulator directly before the pump wave enters the fiber. After that we have to subtract the splicing loss of the fiber input. The backscattered power is measured at port 3 and then the splice losses and circulator linear loss between ports 2 and 3 are removed. The transmitted power is measured at the other end of the fiber and this time we have to sum the splice loss at this fiber output because we want to obtain the output power coming directly from the PCF. Thus it is very important to know the splicing losses as exactly as possible which should precisely be measured during the splicing process. With this setup we can also identify the linear attenuation of optical fibers.

To determine the Brillouin threshold we plot the backscattered power in function of the input power and look for the value of input power for which the backscattered power is 1% of the injected power using a polynomial fit. Figs.(3.6), (3.7) and (3.8) show three examples of Brillouin threshold measurement which correspond to the same fibers as

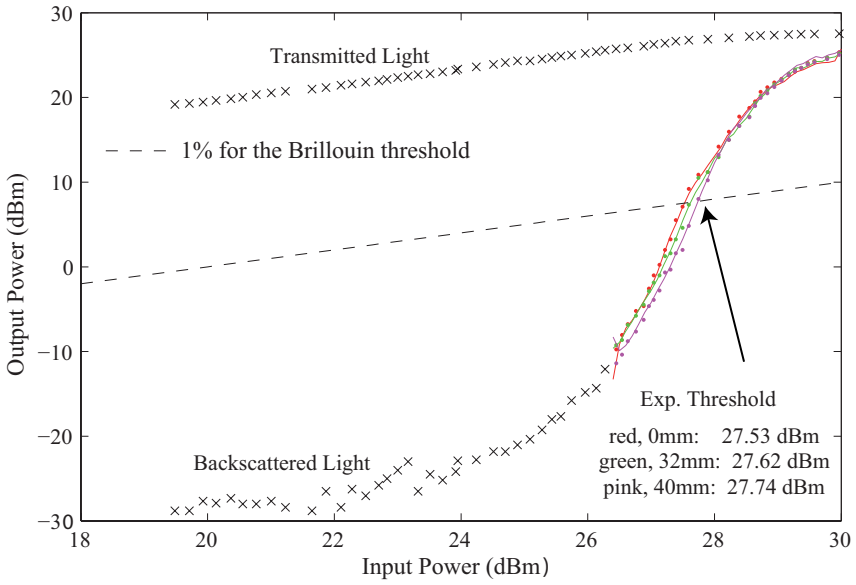

Figure 3.6: Brillouin threshold measurement for a 260m-long SMF, with application of different strain (0 mm, 32 mm and 40 mm over a 12m-section of the fiber).

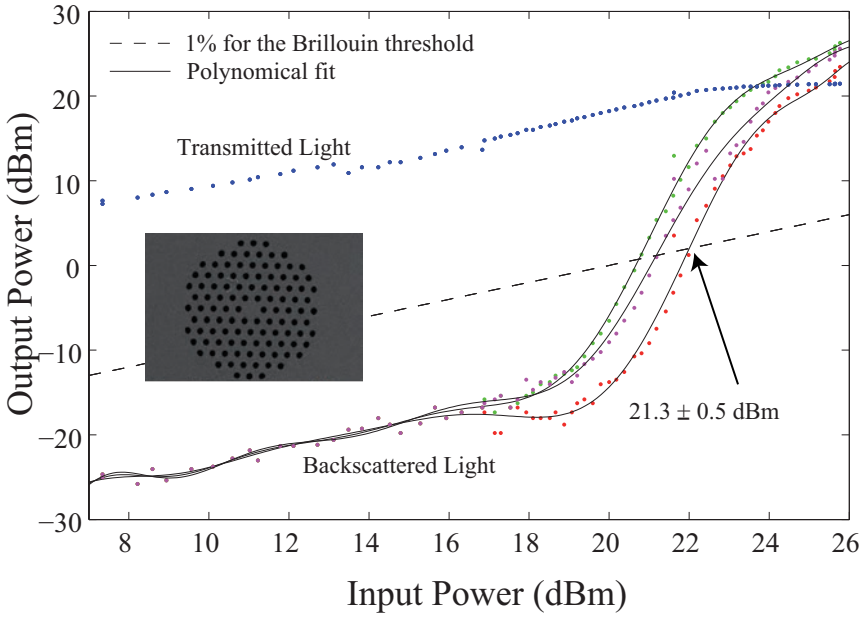

Figure 3.7: Brillouin threshold measurement for a 380m-long PCF, the three measurements have been carried out without applying strain, one by inverting the fiber.

previously presented for the Brillouin gain measurement. The threshold for the 260 m - long SMF was determined for three cases: without applied strain, with an elongation of 32 mm over 12 m (corresponds to 2667 $\mu\epsilon$) and 40 mm over 12 m (corresponds to 3333 $\mu\epsilon$). The strain slightly changes the Brillouin threshold from 27.53 dBm to 27.62 dBm and 27.74 dBm because the Brillouin frequency shift varies for this 12m-section of the fiber. Nevertheless, the difference is tiny and within the uncertainty of the measurement which can be estimated to about 1 dB, taking into account the error for the splicing loss, the loss of the components and accuracy of the power meter. The Brillouin threshold measurement of the 380m-long PCF without applying any strain shows this very clearly because the three different measurements (two times in the same direction, one time while inverting the fiber) vary from 20.8 dBm to 22.0 dBm and give a mean result of 21.3±0.5 dBm. Thus, the effect of the applied strain in Fig.(3.6) is within the measurement uncertainty and can not provide a experimental investigation of the influence of applied strain on the Brillouin threshold. The theoretical threshold of the 380m-long PCF is calculated to 22.3 dBm by Eq.(2.38), taking into account the measurement of the Brillouin gain.

In Fig.(3.8) the threshold for the third fiber is obtained as 19.9 dBm. As this PCF is shorter (106 m) than the previous PCF, one can think that the threshold must be higher than in the 380m-long fiber according to Eq.(2.38), however the critical pump power is lower. The reason is the diameter of the fiber core: 2.4 µm for the multi-scale PCF and 5.7 µm for the classical PCF. As the effective mode area for the multi-scale PCF is small,

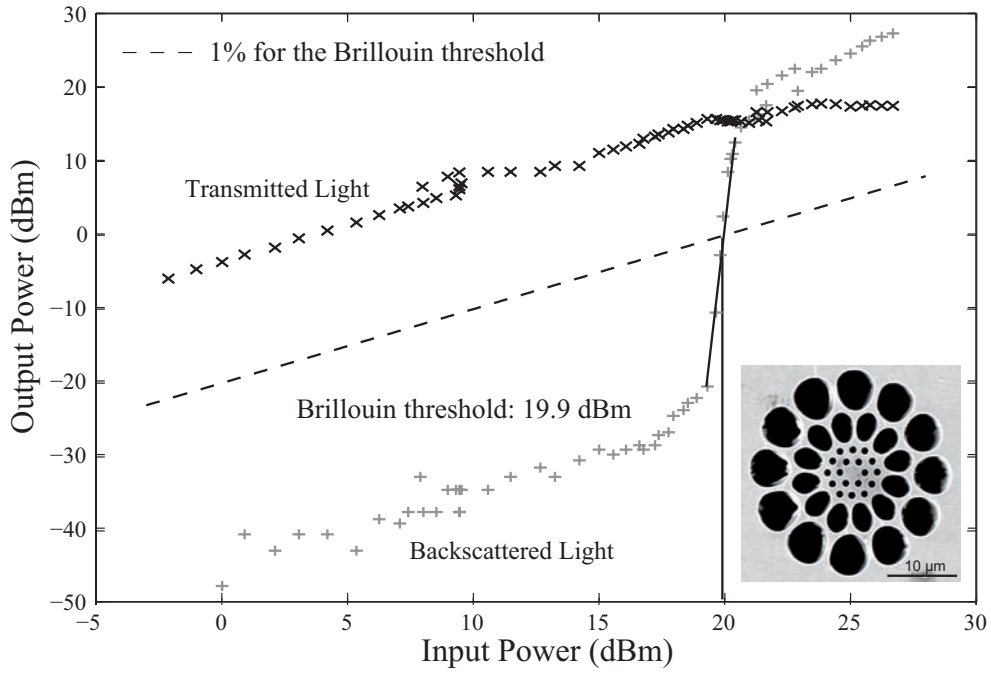

Figure 3.8: Brillouin threshold measurement for a 106m-long multiscale PCF.

the optical power density in the fiber core is high which increases the nonlinear scattering. For the multi-scale PCF a theoretical threshold of 21.0 dBm has been calculated. Further theoretical and experimental results will be discussed in chapter 4 for PCF with varying micro-structure size.

3.2 Distributed measurement of Brillouin backscattering

In addition to the self-heterodyne measurement of the Brillouin gain, the distributed Brillouin scattering experiment allows for the observation of the Brillouin gain spectrum throughout the fiber with a limited spatial resolution. In chapter 2.4 we have already introduced different techniques for distributed Brillouin sensors, namely, the Brillouin Optical Time Domain Analysis (BOTDA), Brillouin Echoes Distributed Sensing (BEDS) and its latest development to Differential Phase Shift Keying - BEDS (DPSK-BEDS). Thereafter, we provide a detailed description and comparison of these techniques.

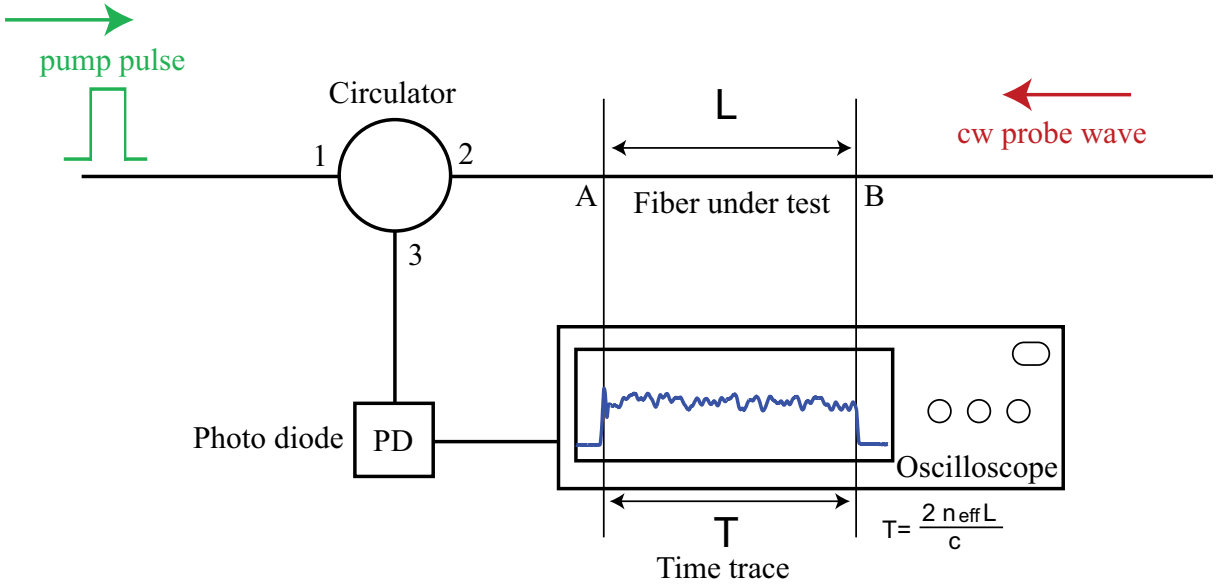

Figure 3.9: General working principle of BOTDA technique.

3.2.1 Brillouin Optical Time Domain Analysis - BOTDA

We will now go further into detail to describe the *Brillouin optical time domain analysis* technique (BOTDA) which is a pump-probe technique, as mentioned in paragraph 3.1, for mapping the Brillouin gain spectrum. The here described concept has been proposed and demonstrated in 1996 by Niklès *et al.* [4]. Fig.(3.9) summarizes the working principle of the BOTDA system. In general, we insert a pulsed pump to one end (A) of the fiber and a CW-probe wave to the other input (B). The CW probe wave is frequency shifted to the pump wave. The intense pump pulse generates backward Brillouin gain and if the frequency shift between pump and probe is equal to the BFS, then the probe wave is amplified by the pump pulse through Brillouin scattering. This can be observed from the backscattered signal at input A. By a circulator we separate the backward travelling light and achieve the signal by a photo diode and an oscilloscope. We will obtain an upward signal on the oscilloscope due to Brillouin backscattering as long as the pump pulse is propagating in the fiber and interacting with the CW probe wave. The time trace T corresponds to the length L of the fiber by

$$T = \frac{2n_{\text{eff}}L}{c} \tag{3.1}$$

with c the speed of light and n_{eff} the effective refractive index of the fiber which is about 1.444 [17]. Thus for a 100 m long fiber we observe a signal during 1 µs. The factor 2 is due to the fact that the pump pulse propagates in the opposite direction of the probe. The BFS is sensitive to temperature, strain, doping and structural irregularities in the fiber. In Fig.(3.10) we see the effect of strain applied on a conventional 260m-long SMF.

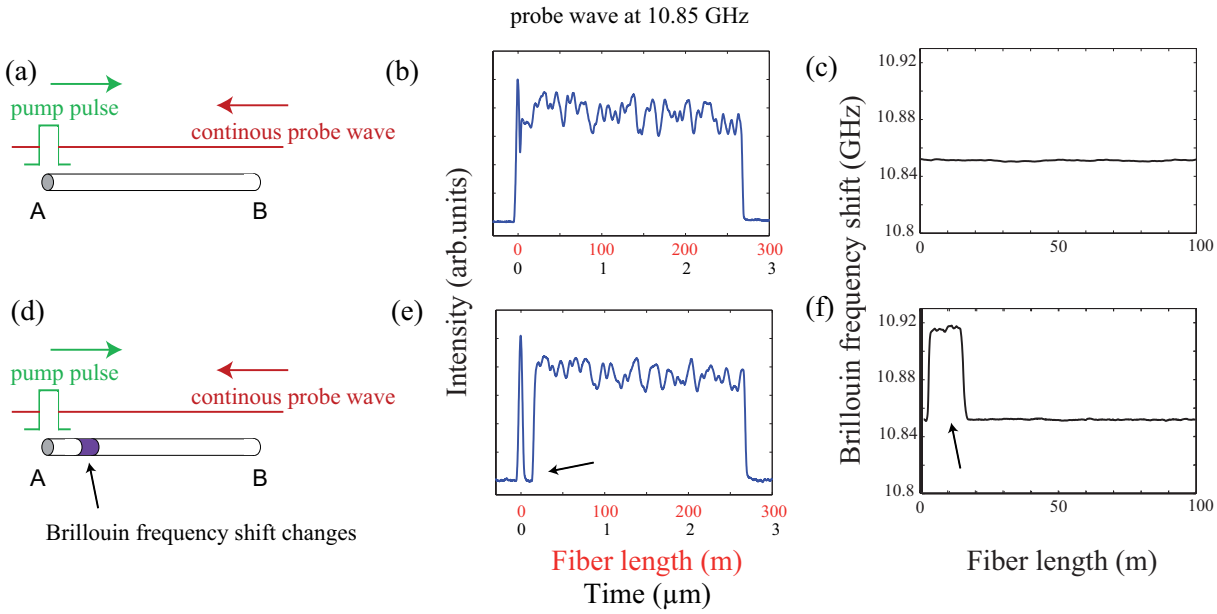

Figure 3.10: BOTDA measurement, times traces and BFS: (a-c) for a fiber with homogeneous BFS, (d-f) for a fiber with a frequency shift due to applied strain. (a,d) pump and probe wave are injected in opposite direction into the fiber, (b,e) time trace on the oscilloscope, the time trace corresponds to the fiber length, when the pulse leaves the fiber, the Brillouin gain decreases; in (e) the frequency shift can be seen by the sharp decrease in Brillouin gain (arrow), (c,f): distributed BFS, nearly constant for (c) and frequency shift in (f) where strain over a 12m-section has been applied.

In Fig.(3.10a-c) no strain is applied, in contrast to Fig.(3.10d-f) where a 12m-section of the fiber is stretched. In the time trace at a probe frequency of 10.85 GHz in Fig.(3.10e), we clearly observe the decrease in Brillouin gain when the pump pulse travels through the stretched 12m-section. Here the BFS is shifted to about 10.9 GHz, thus the probe wave (at 10.85 GHz) is not amplified by the pump pulse. The BFS is depicted in Fig.(3.10c,f), where the influence of strain in the 12m-section is obvious. After this general explanation about the working principle of BOTDA technique we go further into detail with the experimental setup which is schematically depicted in Fig.(3.11). The output of a DFB laser[3] at 1.55 μm is amplified by an erbium doped fiber amplifier (EDFA[4]) and then split into two arms by a 50:50 fiber coupler. One arm serves for the CW probe and the other one for the pump. A $LiNbO_3$ electro-optic intensity modulator (Photline technologies [5]) on the arm of the probe wave, driven by a microwave generator[6], creates two sidebands, Stokes and Anti-Stokes, tuned by the BFS ($\approx$ 11 GHz) with respect to the carrier

[3]RIO 0194-1-34-1, linewidth 20 kHz at 1.55 μm
[4]Keopsys 33 dBm
[5]CDF-X-EP-1550, insertion loss: 5 dB at 1.55 μm, electro-optic bandwidth 15 GHz, extinction ratio 37 dB at 1550 nm, $V_\pi \approx 6$ V
[6]Hittite HMC-T2100, 10 MHz-20 GHz signal generator

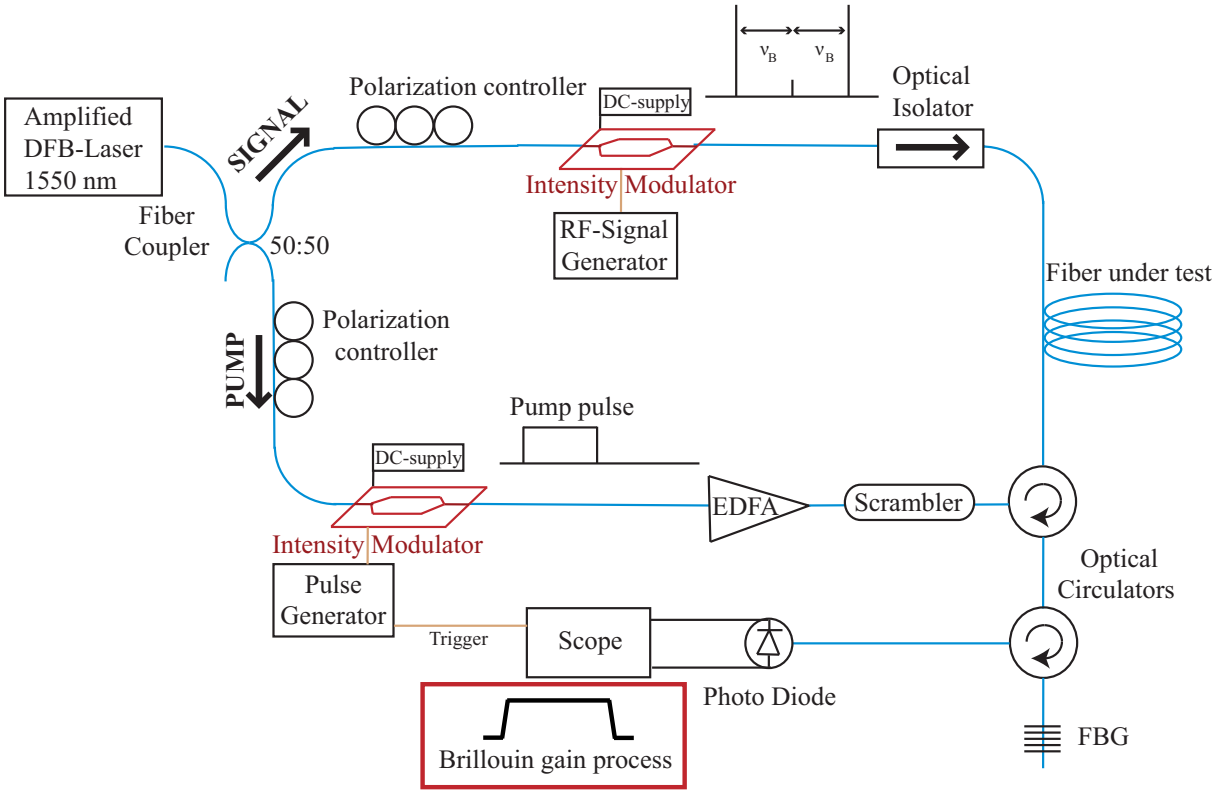

Figure 3.11: Experimental setup of BOTDA technique.

frequency. A DC bias is applied to the modulator to drive it in the minimum of its transfer function. In this way the carrier wave is eliminated as 37 dB and the side-bands are the strongest. After the intensity modulator the probe wave goes through an optical isolator and is injected into the fiber under test. The isolator serves to stop the pump wave which will be injected to the other input of the fiber. The other arm is connected to the opposite end of the PCF through an optical circulator. The pump wave is modulated with a 5 kHz repetition rate via another intensity modulator (Photline Technologies[7]) driven by a pulse generator[8]. An intensity square pulse is applied on the pump with a duration varying from 10 ns to about 30 ns. The pump pulse is then amplified by another EDFA by about 10 dB. The pulse duration for BOTDA measurement is limited to 10 ns from a physical point of view because the acoustic wave decay time is about 10 ns and below this time no more information about the BFS can be obtained. However, we will see in the next paragraph, how to exceed this limit. As amplifier for the pump a 17 dBm - EDFA from Manlight[9] was used. The amplified pump pulse is then polarization scrambled so that the polarization does not play any role in the distributed measurement because Brillouin scattering is a

[7]MXPE LN10, insertion loss: 4.5 dB at 1.55 µm, electro-optic bandwidth 14.8 GHz, extinction ratio 35 dB at 1550 nm, 53 dB at 1535 nm, V_π=6.2 V

[8]HP8131A-020

[9]Manlight 17 dBm-EDFA, Packaging made by M.W.Lee

polarization sensitive process [18] (see Fig.(3.12 a,b) which are explained later). It would have been possible to use the scrambler on the probe wave as well but it turned out that this induces much more instablity in the BOTDA measurement, probably due to the fact that the probe wave is CW-light [9]. The scrambled and amplified pump pulse enters then the fiber so that the reflected Stokes light interferes with the probe. A tunable fiber Bragg grating (FBG, 10 GHz - linewidth[10]) connected to a second optical circulator filters out the Anti-Stokes-wave and residual pump light. The output CW probe is then detected by a 1.2 GHz photodetector and monitored with a real-time oscilloscope[11] (12 GHz bandwidth) while it is scanned around the BFS so that all BFS variations due to inhomogeneities and strain can be readily detected. For the oscilloscope we chose a resolution that is adapted to the physical resolution limit due to the pump pulse duration, which means about at least 3 measurement points per resolution (e.g. for 10 ns pulse duration 3 points every 10 ns). Depending on the stability of the obtained signal, we used either 512 or 1024 data series averaging. For the data acquisition most of the different devices are driven by a Labview and Matlab program. Three data are then saved, namely, a frequency vector in the range where the probe wave was swept, a time date on the oscilloscope and a matrix of the monitored signal for each frequency point. Hereby, the matrix was normalized by taking into account the DC of the signal (at 1/50 at the beginning of the time trace) and by dividing the data by this DC rate.

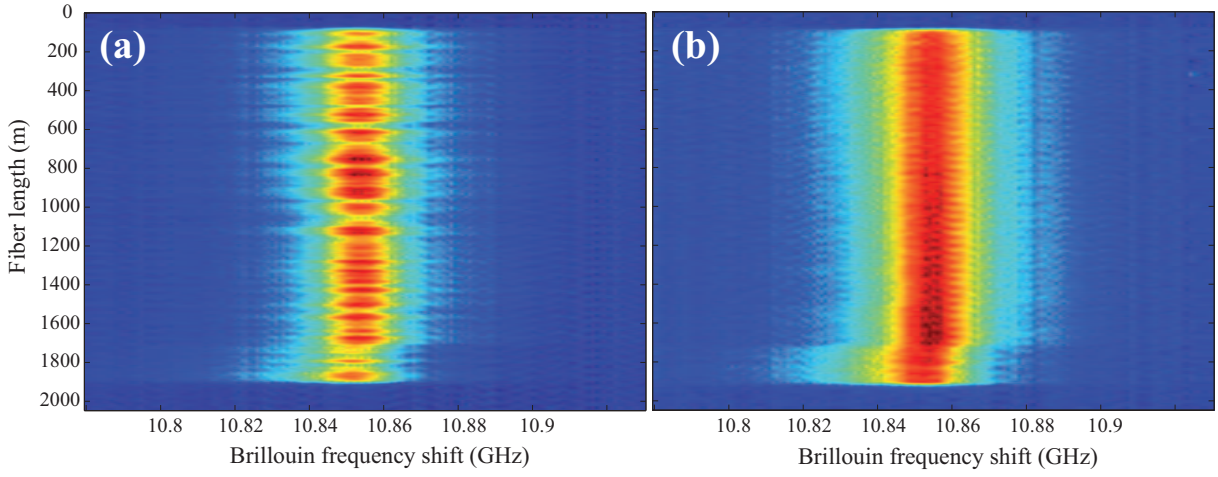

Figure 3.12: Mapping of 1.7km-long SMF with 2 m spatial resolution and 1 MHz frequency resolution, (a) without polarization scrambler and (b) with polarization scrambler.

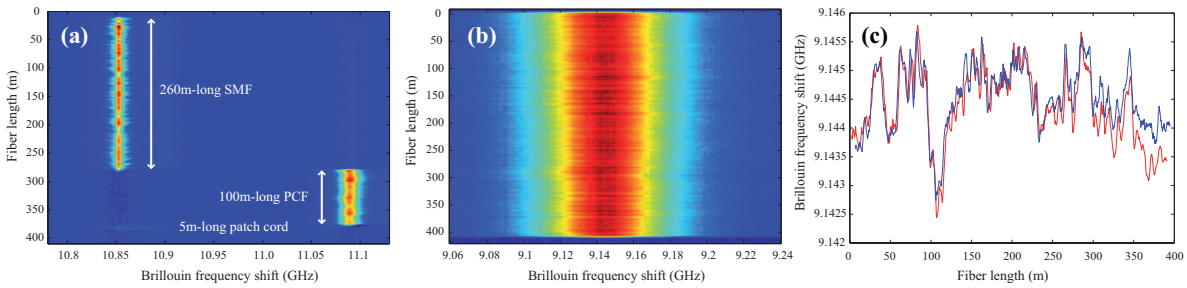

Figure 3.13: (a) Distributed Brillouin gain of three concatenated fibers : a 260 m SMF, a 100 m PCF and a 5 m SMF patch cord, (b) Distributed measurement of a 420 m HNLF at a BFS of 9.145 GHz. (c) Analyzed data for the BFS in (b). The red and blue data correspond were obtained by inverting the fiber. The spatial resolution is 2 m and the frequency resolution 1 MHz.

3.2.1.1 Experimental results

Figs.(3.12 a,b) show a direct comparison of the BOTDA trace when the polarization scrambler is switched off and on. The measurement was carried out with 2 m spatial resolution and 1 MHz frequency resolution. The mean Brillouin frequency shift is about 10.854 GHz. We clearly observe strong intensity fluctuations along the fiber which are due to birefringence [19]. The state of polarization of the probe and pump wave turns randomly and as Brillouin scattering is a polarisation dependent process, their arbitrary variation of polarisation results in intensity fluctuations. When their polarisations are matched, the gain becomes maximal, but when they are orthogonaly polarised, the gain is minimal. In the distributed BGS in Fig.(3.12 b), the frequency is shifted by about 4 MHz for the last 200 m of the fiber. This is due to partially higher strain induced by fiber coiling and the same frequency shift has been observed by inverting the fiber. In Fig.(3.13 a) a series of another SMF, a PCF and an SMF patch cord have been investigated. The SMF is 260 m long and its BFS is 10.85 GHz. The PCF was drawn by the IRCICA institute in Lille and will be studied in detail in paragraph 3.4 of this chapter. We observe the BFS at 11.08 GHz and more fluctuations in BFS as for the SMF which is not surprising because the drawing process for PCFs is more challenging than for conventional SMF. The 5 m patch cord at the end is barely visible which is due to the relatively high loss of the pump in the PCF. The BFS at about 10.85 GHz is similar to that of the 260 m SMF. A highly nonlinear fiber (HNLF) with 400 m length has been analyzed in Fig.(3.13 b,c). Since the fiber core is highly doped with germanium the acoustic velocity and effective refractive index changes which reduces the BFS to 9.145 GHz. For this fiber we now have a look at the analysis of the raw data.
In order to obtain the distributed BFS and the FWHM of the BGS the raw data have

[10] AOS Tunable Grating, 1545-1555 nm
[11] Agilent infiniium DSA 91204A Digital Signal Analyzer 12 GHz, 40 GSa/s

been analyzed by several operations. For each frequency the time trace from the oscilloscope is convolved with a square function. More precisely, each 10 measuring points were convolved with a 10 points long square function to reduce the noise coming from the oscilloscope and the photo diode. After that the Brillouin gain spectrum is fitted for each point along the fiber. Using Lorentzian curve fit, we extract the BFS and the FWHM. For a more precise analysis of the BFS it is possible to fit the data only around its maximum with a polynomial fit. Therefore just the topmost data points are exploited. A comparison of both fitting types will be later presented in Fig.(3.33). For the different fitting curves the function *nlinfit* in *Matlab* has been used.
The result for the BFS of the HNLF is plotted in Fig.(3.13 c). A clear decline in the BFS after 100 m is observed, caused by coiling strain or microstructure inhomogeneities in this part of the fiber. The red curve is the result for injecting the pump pulse into one end of the fiber, the blue one presents the results by inverting the injection direction of the fiber. In that manner, we can see that large peaks in BFS match each other. Hence it confirms our BFS measurement. At the end we qualitatively observe the same tendency but a quantitative difference in BFS. This may be due to pump depletion at the end of the fiber.

3.2.2 Brillouin Echoes Distributed Sensing - BEDS

BEDS technique basically differs from a conventional BOTDA system. Indeed, precise distributed measurements of Brillouin gain spectrum (BGS) can be made with enhanced spatial resolution by applying a short π-phase shift in a CW pump wave instead of using rectangular intensity pulses. Thanks to this phase shift, the spatial resolution down to 1 cm can be obtained in BEDS. In addition to the higher spatial resolution this configuration offers the advantage to measure a gain spectrum unaltered by the pump spectrum and experimentally observe the acoustic lifetime [20, 21]. The basic idea comes from techniques that are based upon the pre-established existence of an acoustical wave in the fiber resulting from the interaction of a CW probe and a CW pump wave. Hence, a refractive index grating is propagating in the fiber, caused by electrostriction (chapter 2.2.1.1). Since the acoustic field originates from two CW waves, the Brillouin gain spectrum is not broadened. The acoustic wave, correspondingly the refractive index grating, is "activated" before which gives a constant background amplification on the probe wave [22]. Three different configurations using very short pump pulses have been developed by several working groups [9]. The pulses (shorter than the acoustic decay time) have been applied to the CW pump wave in order to obtain a temporal resolved response of the Brillouin scattering. Since this change on the pump wave is very fast, the acoustic wave is almost not affected during the pulse. First additional bright pulses are sent through the fiber (Fig.(3.14 a)). This effects an additional amplification of the probe wave and

can be seen as a Brillouin gain process, similar to BOTDA but with an additional continuous wave background. A high resolution of 15 cm has been shown in [23, 24]. The second type is a dark pulse, applied on the pump wave, which means that the pump is turned off for some nanoseconds (Fig.(3.14 b)). The result is a "negative" gain in Brillouin backscattering and corresponds to a Brillouin loss process. In fact it is the absence of the Brillouin gain in comparison to the background amplification. Since the acoustic decay time is about 10 nanoseconds the acoustic wave keeps vibrating during the dark pulse but there is no more amplification of the probe wave. In this method 2 cm spatial resolution sensing has been achieved using a dark pulse of 200 ps [25]. The third configuration uses a short π-shift pulse instead of a dark pulse because it is supposed to yield an even sharper contrast in the Brillouin loss process (Fig.(3.14 c)) by breaking the phase matching between the pump, the probe and the acoustic wave. This means that the π-phase shifted pulse is reflected by the acoustic wave and interferes destructively with the CW-probe wave. This third type of pulses leads to a twice higher Brillouin response and hence is the most efficient concept. This technique is called Brillouin echoes distributed sensing (BEDS) [26]. This name comes on the one hand from the formal analogy with the spin echoes equation for nuclear magnetic resonance [9] and on the other hand from the fact that the reflected π-phase pulse can be viewed as an "echo" on the probe wave. The remarkable advantages of this new distributed measurement technique are its high spatial

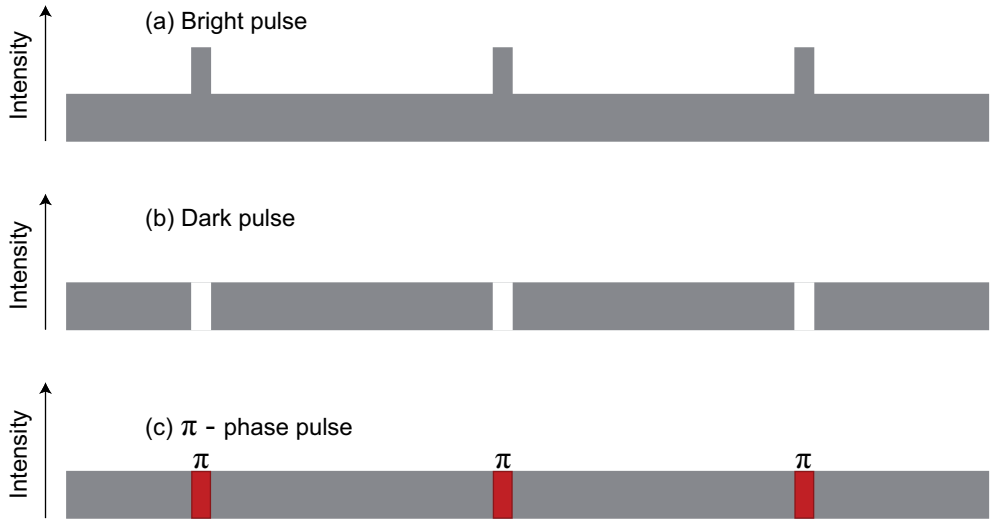

Figure 3.14: Three different methods to make Brillouin echoes [9]: (a) bright pulse: a continuous flow of pump light activates the acoustic wave, giving constant background amplification on the probe. The additional pump light in the pulse is reflected and its effect is observed as an additional amplification. (b) dark pulse: the pump is turned off for a short period of time, so that no light is reflected and the constant background amplification is stopped. (c) π phase-shift pulse: a π phase shift is applied to the pump for a short time, so that the reflected light interferes destructively with the probe, equivalent to a Brillouin loss process.

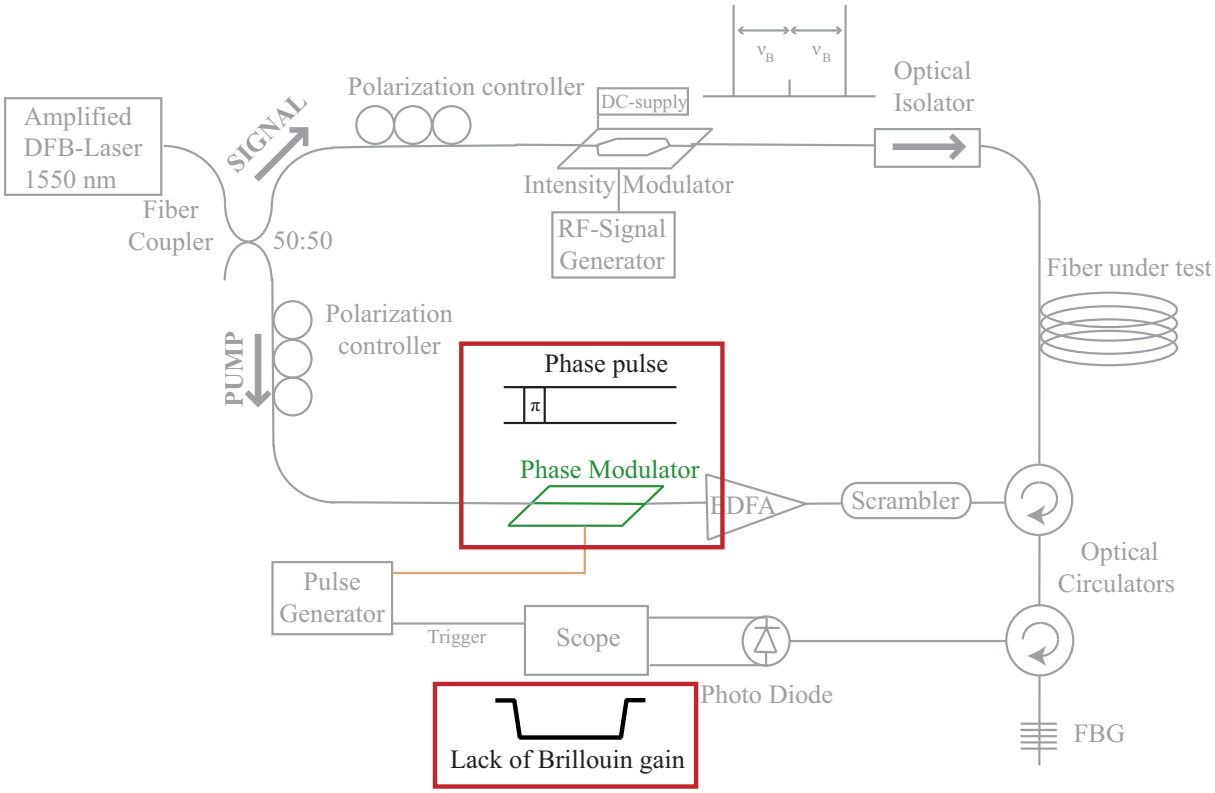

Figure 3.15: Experimental setup of BEDS system: a phase modulator replaces the intensity modulator on the pump wave. On the oscilloscope a downward signal is obtained.

resolution (up to 5 cm) and its large dynamics while conserving a narrow Brillouin gain spectrum at the same time. This technique has been first developed at the EPFL Lausanne [26, 27] and a detailed theory and evolution of the experiment can be found in [9]. The experimental setup is schematically shown in Fig.(3.15). Most of the devices have already been explained in the previous paragraph but the main difference with respect to BOTDA is that the intensity modulator is replaced by a phase modulator (provided by Photline Technologies[12]) to generate very short π-phase shifts on the CW pump wave. A short π-phase shift is applied on the CW pump wave for instance for a duration of 3 ns which corresponds to 30 cm spatial resolution. The pulse length should be compromised with the fiber attenuation. In fact, both the short phase pulse and the attenuation induce low contrast in the time trace of Brillouin response at the oscilloscope. Therefore, when the attenuation is high, the pulse needs to be lengthened in order to achieve proper sensing. The reflected pump light interferes destructively with the probe as mentioned before, so we obtain a downward time signal which corresponds to a Brillouin loss process (Fig.(3.15)).
Two practical issues that occur with the BEDS technique has to be taken into account: detrimental effects of the continuous activation of the acoustic wave and the so-called

[12]MPZ-LN-10, insertion loss: 2.9 dB at 1550 nm, electro-optic bandwidth 15 GHz, V_π=5.9V

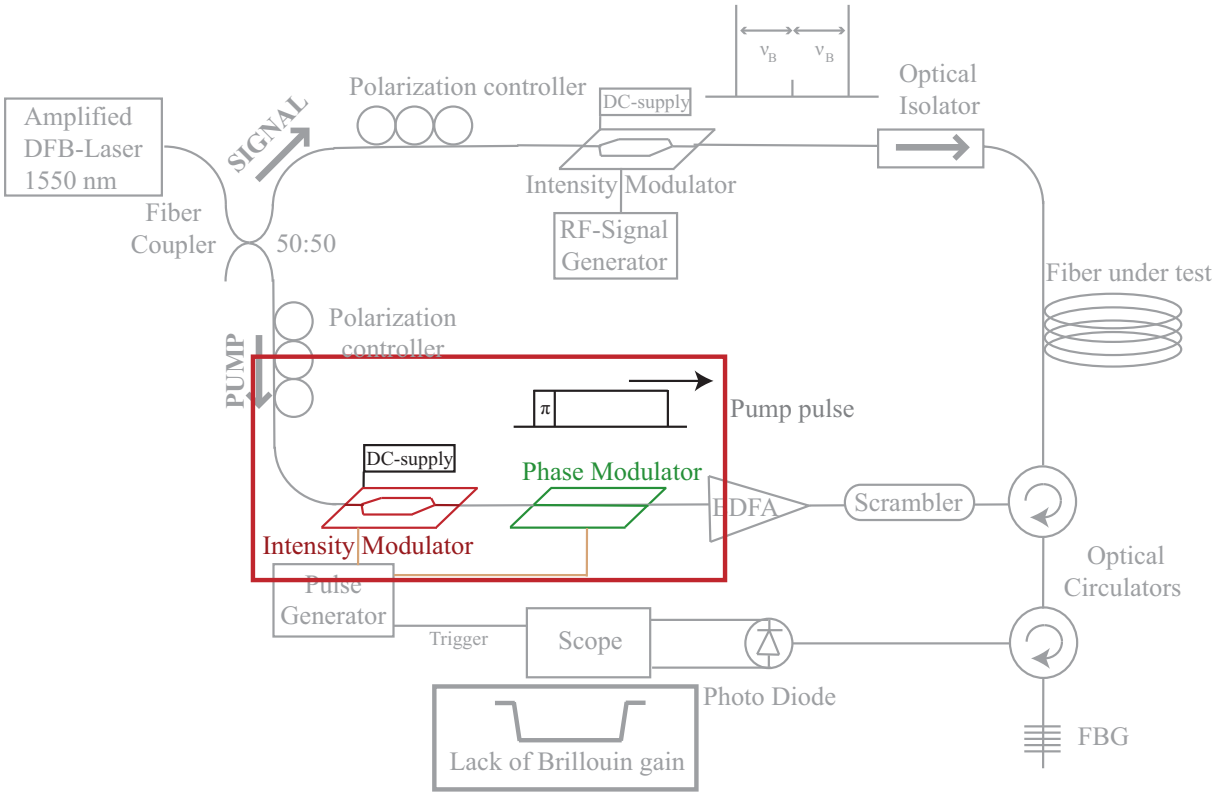

Figure 3.16: Enhanced experimental setup of the BEDS system: an intensity modulator is added before the phase modulator to remove the second echo and to avoid pump depletion.

second echo [9]. When the acoustic field is generated by two continuous waves the sensing range and accuracy is limited by pump depletion and spontaneous Brillouin noise. Both causes additional signal-beat noise at the detector and requires more averaging on the oscilloscope. The so-called second echo emerges from the fact that the acoustic wave has a finite lifetime of ten nanoseconds. Accordingly, the backscattered response of the BEDS system is partially decaying during the phase pulse. This creates a second echo when the pump is restored to its original state after the pulse. The lifetime of acoustic wave is around 10 ns. This means that the acoustic wave exists for 10 ns and during this time the CW pump wave can still interact with the acoustic wave. We will see in paragraph 3.5 that this effect allow to observe the acoustic decay time. To avoid these undesirable effects we can use a long intensity pulse instead of a continuous pump wave. First of all this avoids pump depletion and improves the probe to noise ratio for the Brillouin response. For this purpose a second intensity modulator is added to the experimental setup (Fig.(3.16)) before the phase modulator. A pump intensity pulse of about 30-100 ns is produced and the delay between the two modulators has to be adjusted in order to place the phase pulse somewhere inside the intensity pulse. However, this does not yet help to eliminate the second echo. In order to get rid of the second echo the pump must be turned off immediately after the phase pulse so that no more light can be reflected after the pulse end and no trailing light is present [26]. This is achieved by adjusting the delay

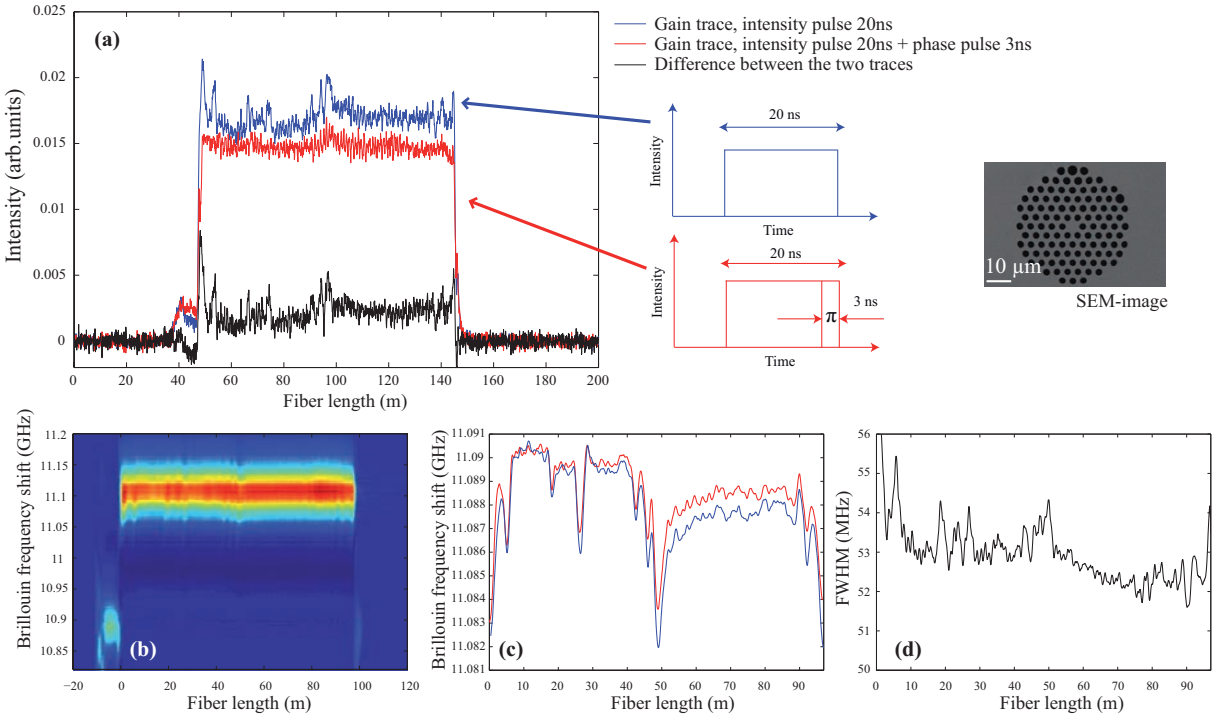

Figure 3.17: Differential BEDS measurement of a 100 m PCF. (a) gain traces to obtain a high resolved Brillouin gain mapping without second echo, (b) Brillouin gain mapping, (c) distributed Brillouin frequency shift (in both directions), (d) distributed FWHM of the Brillouin gain. The spatial resolution is 30 cm and the frequency resolution is 1 MHz.

between the two pulses so that the π-phase pulse is generated at the end of the intensity pulse. Then the interaction between the residual acoustic wave and the pump wave does not occur any more.

3.2.2.1 Experimental results

To get better insight to this technique the BEDS traces of a 100 m PCF is shown in Fig.(3.17 a). The PCF has a hexagonal structure with core, hole diameter and pitch at about 5.5 µm, 2.7 µm and 4.1 µm. This fiber will also be studied in paragraph 3.4 in comparison to a second PCF with a similar structure. Here, the experimental approach and the analysis of the data will be explained with help of this fiber. The setup to avoid the second echo has been used. Thus, for each frequency shift on the probe wave two time traces from the oscilloscope are saved: one with the long intensity pulse (here 20 ns) without the phase shift (Fig.(3.17 a), blue trace) and one with the long intensity pulse including the short phase shift (here 3 ns, Fig.(3.17 a), red trace). After that we calculate the difference of both curves to obtain the highly resolved Brillouin response of the 3ns-long phase pulse only. This is the reason for which this technique is also called *differential*

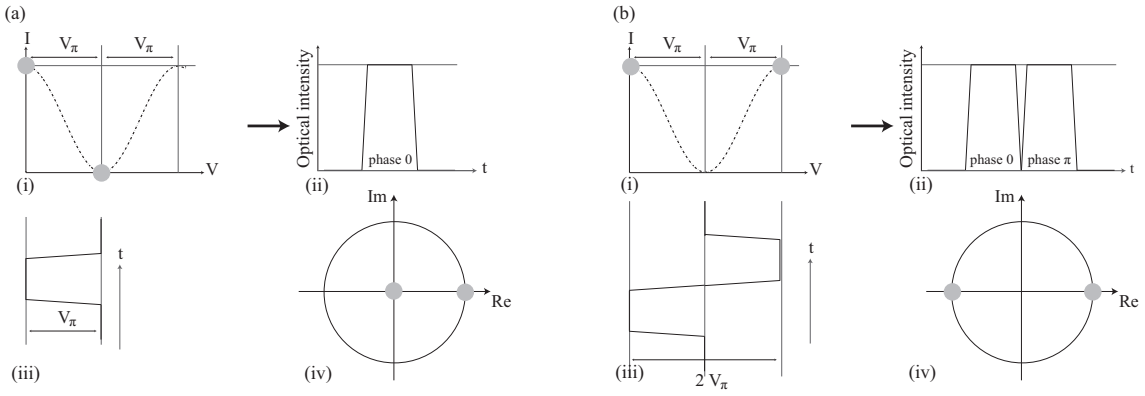

Figure 3.18: Use of a Mach-Zehnder interferometer modulator with (a)On Off keying and (b) Differential Phase Shift Keying. (i) Transfer function, (ii) optical output of modulator, (iii) RF input for bias, (iv) constellation diagram, respectively for (a) and (b).

BEDS. The color map of the BEDS results can be seen in Fig.(3.17 b). SMF patch cords are clearly observed at each side of the PCF. In the middle (at 50 m of the fiber) the BFS slightly drops. This fiber has been coiled on two layers on the fiber spool and the BFS in the middle of fiber comes from local strain at the point where the fiber changed from one layer to another one. By using a Lorentzian fit, as explained in paragraph 3.2.2, it is possible to retrieve the BFS and FWHM at each point of the fiber with a high resolution of 30 cm which corresponds to the 3 ns phase pulse (Fig.(3.17 c,d)). Another possibility to avoid the second echo is the deconvolution method where the data is inversely convolved with the impulse response of the system [9]. The original Brillouin response is then reconstructed numerically. Here we choose the experimental method because of several advantages. The second echo is completely eliminated in comparison to the deconvolution method where it is only strongly suppressed [9]. 5km-fiber sensing with a resolution of 5 cm can be achieved whereas the CW pump measurement is limited to 1 km due to pump depletion [9]. The disadvantage of the experimental technique is the need of two modulators (an intensity and a phase modulators) on the pump wave which means higher loss (more than 5 dB), high cost of the system and a more complicated measurement. Moreover, it is necessary to adjust accurately the π-phase pulse at the end of the intensity pulse and to take two acquisitions for each frequency of the probe wave, one time with the intensity pulse and a second time with both pulses. Then the difference between both measured data has to be made to obtain the original highly resolved Brillouin response without second echo. In the following paragraph, we will demonstrate how to implement BEDS technique using a single modulator.

3.2.3 Differential Phase Shift Keying based BEDS

As previously described the use of two modulators for the pump wave is needed for a distributed BEDS measurement while eliminating the second echo. Moreover, as the phase pulse must be positioned at the end of the intensity pulse, it needs a sophisticate adjustment of the delay between the pulses. In this chapter, we propose and demonstrate a new concept to perform BEDS with only one modulator for the pump [28]. The optical π-phase pulse is directly generated using a single intensity modulator based on differential phase-shift keying (DPSK) technique instead of a phase modulator. A long positive electrical pulse is followed by a short negative pulse and this positive-negative shape pulse is applied to the modulator to generate an optical π-phase shift at the end of the long intensity pulse. This means that the long intensity pulse (30-100 ns) and the short π-phase pulses are generated by the same intensity modulator, a phase modulator is needless. First the principle of DPSK will be explained. DPSK technique is widely used in telecom industry to transmit bit-sequence messages in form of π-phase shift using an intensity modulator, i.e. Mach-Zehnder interferometer modulator (MZI). In the working principle of DPSK, optical phase can be shifted by modulating an MZI with an amplitude of double half-wave voltage ($2 \cdot V_\pi$). The transfer function of an MZI is shown in Fig.(3.18a(i)). When an electrical pulse with amplitude V_π, the bias, is applied on the MZI, as in Fig.(3.18a(iii)), we get from a minimum to a maximum of the transfer function. This induces an intensity pulse to the light wave, as in Fig.(3.18a(ii)). The same intensity pulse would be obtained switching to the other maximum in the transfer function as depicted in Fig.(3.18b(ii)). Nevertheless, there is a difference in optical phase as it can be seen in the constellation diagram in Fig.(3.18a,b(iv)). Thus switching from $-V_\pi$ to V_π induces a phase pulse almost without inducing any difference in optical intensity. But since the "0" is crossed by switching from $-V_\pi$ to V_π, a short decay in intensity can be observe between the 0-phase and π-phase intensity pulse. Also in our case, the MZI is driven at its minimum bias point by a positive voltage $0 < V < V_\pi$ and successively a negative voltage $0 > V > -V_\pi$, the relative phase-shift between the optical fields at the two voltages is π, or vice-versa [29]. Therefore, when a negative pulse of V_π (or a pulse of $-V_\pi$) is applied to the modulator just after a positive pulse of V_π at the minimum bias point as illustrated in Fig.(3.19 a), the output optical intensity remains unchanged whilst the phase of the optical field at the negative pulse part is shifted by π with respect to the positive pulse part. In order to generate such an electrical pulse, the positive and negative electrical pulses are separately generated as shown in Fig.(3.19 b). Their peak-to-peak amplitude is 7.6 V and applied to the MZI used in the work (Photline MXPE series, $V_\pi = 6.2$ V, 20 GHz bandwidth). The pulse durations are set to 30 ns and 500 ps, respectively. In telecom, such pulses are applied to a dual-drive MZI [30]. In our work, these long and short pulses are applied to the DC and RF inputs of the MZI, respectively. An adaptation of 50 Ω is made in the DC port and it provides a sufficient bandwidth for the 30-ns pulse. As the pulses are in form

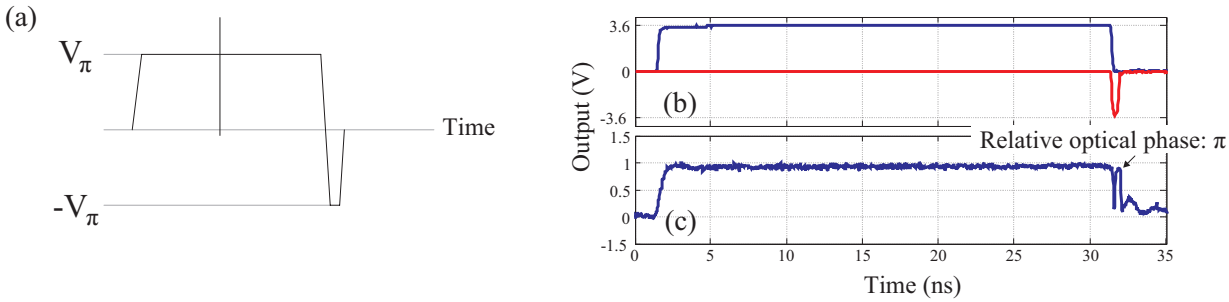

Figure 3.19: (a) Schematic drawing of a positive/negative electrical pulse. (b) A upward (blue trace) and a downward (red trace) electrical pulses are generated separately and applied to the MZI. The durations of the long and short intensity pulses are 30 ns and 500 ps, respectively. (c) The intensity pulses at the MZI output. The phase is shifted by π for 500 ps at the pulse end.

of intensity at the output of the MZI, the delay between the pulses is readily adjusted. Fig.(3.19 c) exhibits two intensity pulses at the modulator output, which are generated by the electrical pulses seen in Fig.(3.19 b). A 30-ns intensity pulse is followed by a 500-ps intensity pulse with π-shifted phase. A short drop between the two pulses is seen due to the fast transition from the positive pulse to the negative pulse. The 500-ps duration of the short pulse defines a spatial resolution of 5 cm in our DPSK-based BEDS system. This dual-phase state intensity pulse is then used as the pump wave in the experimental setup shown in Fig.(3.20) schematically. The setup is nearly the same as BOTDA system as described in paragraph 3.2.1 but different electrical pulses are applied to the MZI of the pump. The CW emission of a distributed feedback (DFB) laser at 1550 nm is split into the pump and probe arms by a 50:50 tap coupler. In the pump side, an RF bias-T is used to combine the positive pulse and DC bias. The DC bias of an MZI (Photline MXPE series) is adjusted to be at the minimum bias point. This creates the long intensity pulse. The short phase pulse at the end of the intensity pulse is generated from the RF-input of the MZI by the same pulse generator as explained before. In order to demonstrate the performance of the concept developed in the work, a 2-m single-mode fiber (SMF) was spliced with a 1-m fiber with a high numerical aperture (HNA). The splice point is protected by a heat-shrinking fiber protective sleeve of 5 cm. For comparison, distributed measurements of the splice segment have been done in two BEDS systems: conventional BEDS system using a phase and an intensity modulators for pump and DPSK-BEDS system using a single intensity modulator. Fig.(3.21 a) shows the distributed measurement obtained in the conventional BEDS system via a π-phase shifted pulse with a pulse width of 500 ps. It clearly reveals the splice segment of 5 cm between the fibers at a frequency shift of 10.55 GHz. The BFS of the HNA and SMF are 10.67 GHz and 10.85 GHz, respectively. Fig.(3.21 b) displays the mapping using DPSK-BEDS developed in the work. It also manifests clearly the 5-cm splice segment and the 10.55 GHz frequency shift. Therefore, it is evident that our system demonstrates performances as good as the standard

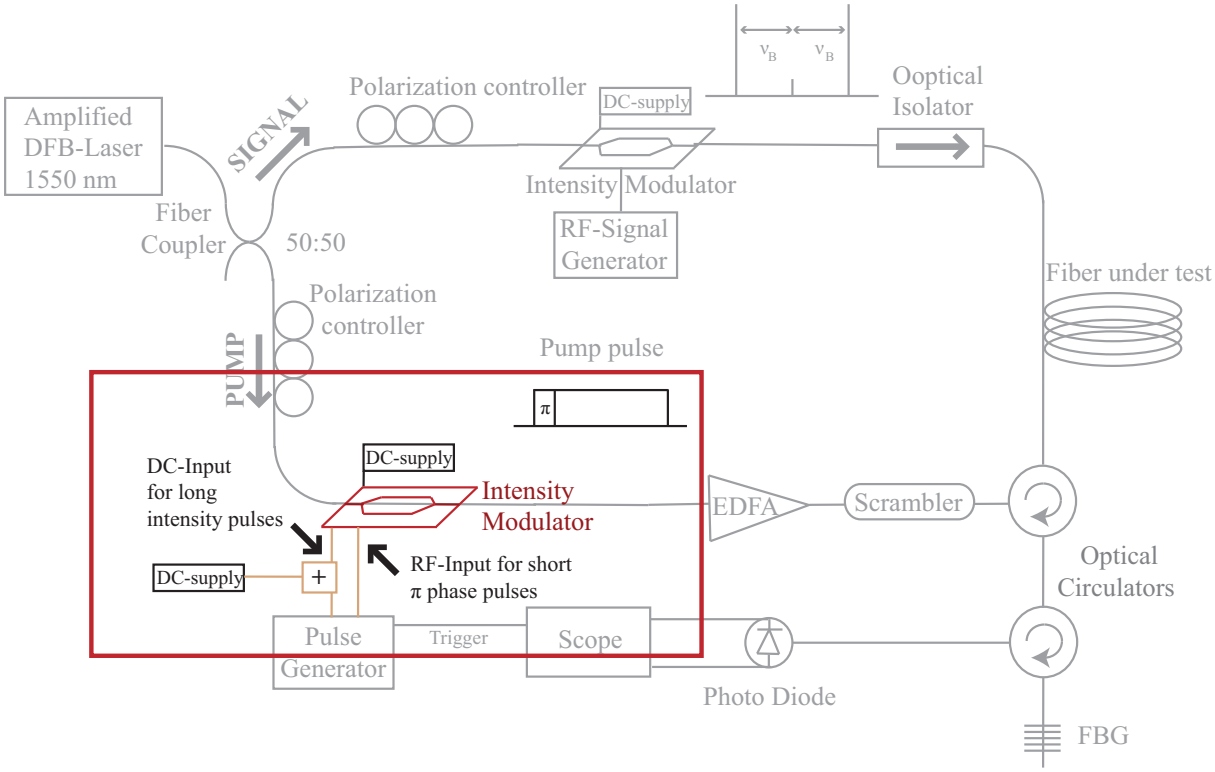

Figure 3.20: Experimental setup of DPSK-BEDS system using a single Mach-Zehnder Interferometer modulator (MZI) for the pump instead of the intensity and phase modulator in Fig.(3.16).

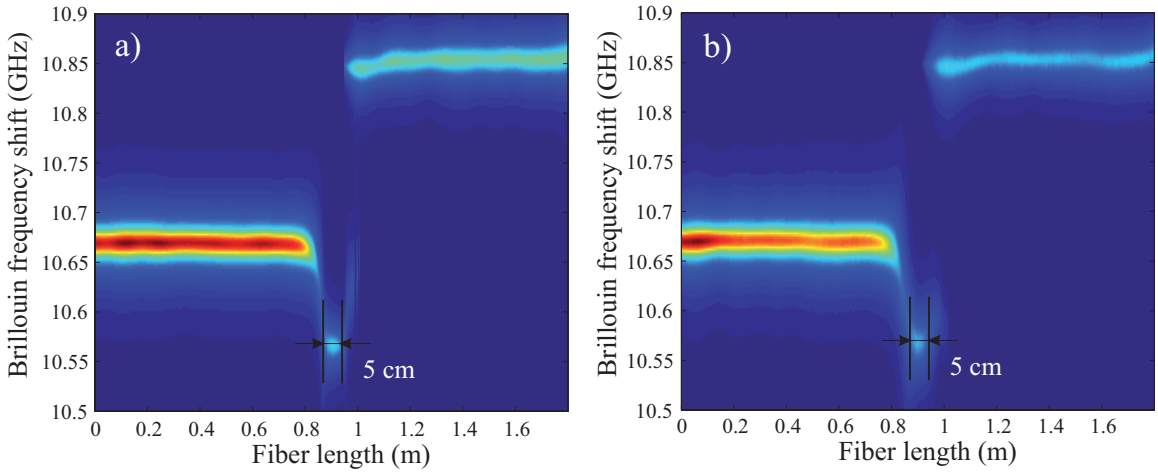

Figure 3.21: Distributed measurements of HNA/SMF fibers showing a splice segment of 5 cm (a) in standard BEDS system using a phase modulator and (b) in our BEDS system based on DPSK technique.

BEDS system. However, the contrast of the measurement in BEDS is slightly better than

that in DPSK-BEDS. This is due to the peak-to-peak amplitude of $7.2\,V$ which is only $1.16 \cdot V_\pi$ in DPSK-BEDS where $2 \cdot V_\pi$ is needed for the best performance. On the other hand, in BEDS a pulse amplitude of 5.1 V is applied to the phase modulator of which the V_π is 5.9 V. In this case, only V_π is required for the best operation and the amplitude meets almost this requirement $(0.87 \cdot V_\pi)$.
We have also tested the DPSK-BEDS system with centimeter resolution for strain monitoring which will be presented in chapter 3.3. We have successfully demonstrated a new concept for BEDS with centimeter resolution based on differential phase-shift keying technique. Our results clearly reveal the 5-cm splice segment between two fibers and its Brillouin frequency shift with a spatial resolution of 5 cm. Our new concept enables distributed measurements with centimetre resolution by simply adding a negative pulse on the pump in a BOTDA system. If a 100 ps-pulse generator and a fast photo-detector are equipped in the setup, the resolution down to 1 cm can be made. Therefore it simplifies conventional BEDS systems by using a single modulator for pump rather than two modulators, and improves the optical loss of the pump. It also allows an easy adjustment of the delay between two pulses.

3.2.4 BOTDA using a QPSK modulator

DPSK-BEDS technique improves the BEDS-setup with respect to optical loss on the pump wave and the adjustment of the delay between intensity and phase pulses. Let us now have a look at the probe wave arm in the setup. Due to the intensity modulator, which is driven by an RF signal generator at about 11 GHz corresponding to the BFS of the fiber, we obtain two sidebands at the output of the modulator: a down- and a up-shifted component corresponding to the Stokes and anti-Stokes components for spontaneous Brillouin scattering. This does not mean that a stimulated anti-Stokes Brillouin process takes place which is not physically correct. Only a Stokes process in stimulated Brillouin scattering is possible which means that either the pump transfers energy to the down-shifted optical wave or the up-shifted wave transfers energy to the pump wave. Both, Stokes and anti-Stokes component (=down-shifted and up-shifted component), are launched into the fiber and interact with the pump pulse. By help of the fiber Bragg grating we chose either the Stokes or anti-Stokes component and filter out residual pump light. The Stokes wave leads to an upward signal at the oscilloscope whilst the Anti-Stokes wave produces a downward signal. The reason is that the anti-Stokes (up-shifted) wave transfers its energy to the pump (Brillouin loss process), whereas the Stokes (down-shifted) wave receive energy from the pump pulse (Brillouin gain process). But the selection takes place after the interaction of both waves in the fiber because Stokes or anti-Stokes component is filtered out by the fiber Bragg grating.

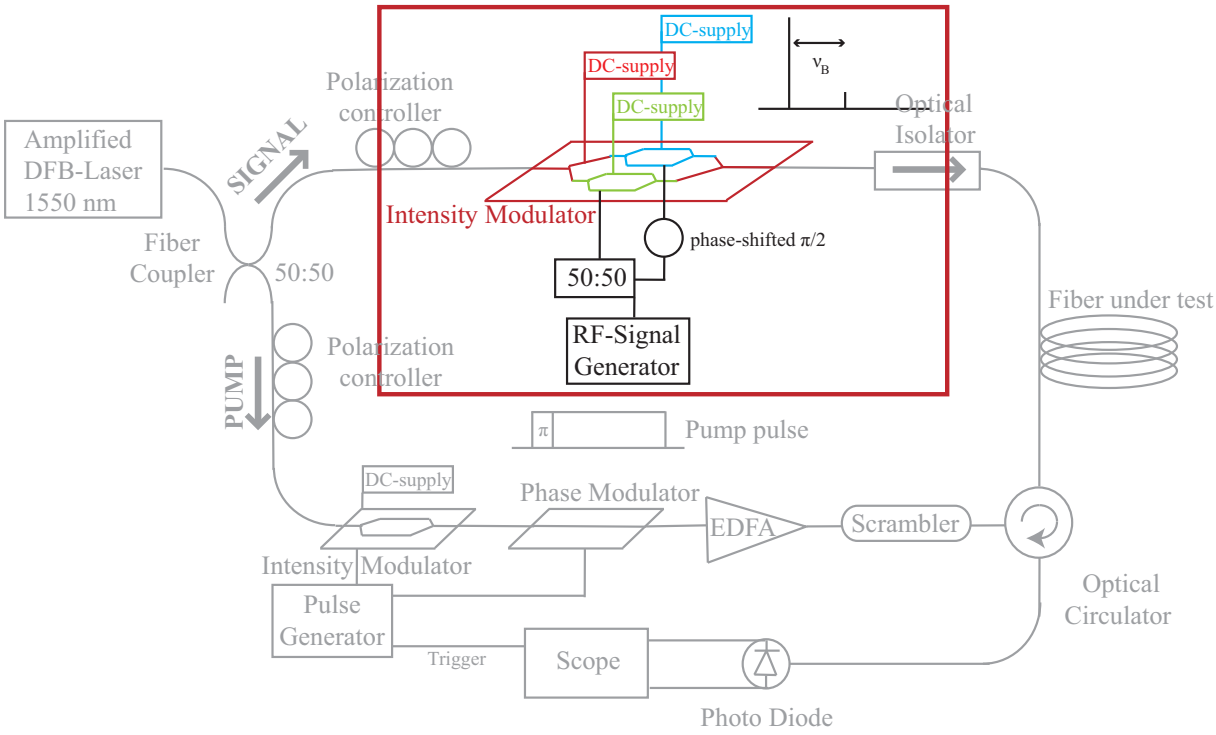

Figure 3.22: BOTDA setup using a QPSK modulator.

The early demonstrations were done with a single frequency using two distinct lasers [31, 32]. Since such configuration induces lots of noises due to the jittering of the two lasers and is expensive, the configuration was modified exploiting an intensity modulator [4]. The advantage of this configuration is that the jittering of the laser does not affect distributed measurements. However, it needs a filter to suppress anti-Stokes signal for distributed measurements. A technique to suppress Stokes or anti-Stokes component was proposed using a single sideband modulator such as dual-drive modulator [33]. Dual-drive modulator is Mach-Zehnder interferometer modulator with 2 RF ports for each interference arm. By applying an RF signal to both ports with a phase shift of $\pi/2$ between the ports, a single side-band can be obtained at the modulator output. This technique was adapted to BOCDA [34] and BOTDA based on Brillouin dynamic grating [35]. In our work, we have adapted the technique to our BOTDA system using an optical QPSK (Quadrature Phase-Shift Keying) modulator (I & Q modulator). Such a modulator is also exploited in BOCDA [36]. QPSK modulation is used to transmit twice more bit sequence messages than conventional PSK. Optical QPSK modulators can perform such a modulation on optical phase. In fact, it is an intensity modulator with two Mach-Zehnder interferometers as shown in Fig.(3.22). A 11 GHz RF signal is injected into two RF ports of the modulator with a $\pi/2$-shifted phase. Three DC bias must be adjusted to obtain a single side-band at the modulator output. The two DC bias for the two interferometers are used to suppress the pump wave and the DC bias at the Y junction at the interferometer outputs is used to unbalance the side bands. By adjusting the last DC bias, either Stokes

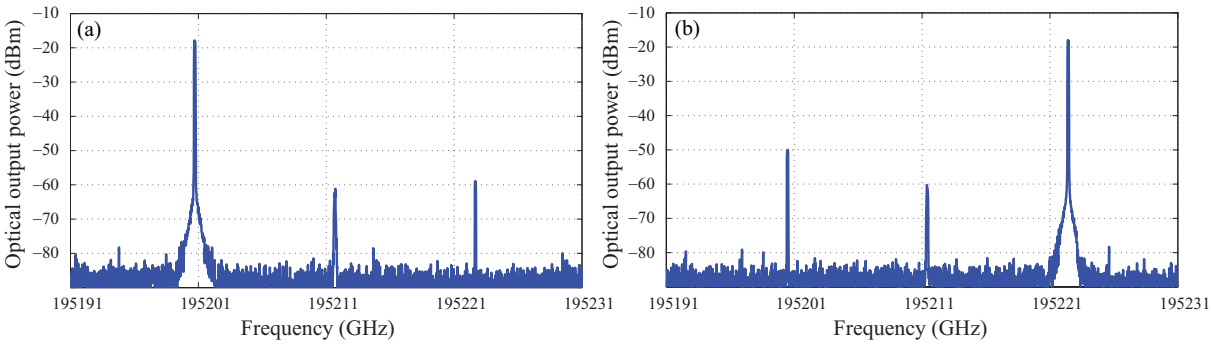

Figure 3.23: Spectra of (a) the Stokes signal and (b) the anti-Stokes signal at the output of the 50 km SMF at 10.94 GHz.

or anti-Stokes signal can be chosen. The advantage of QPSK modulator compared to dual-drive modulator lies on the high performance of carrier suppression as well as side-mode suppression. The modulator used in the setup is provided by Photline Technologies and has a carrier suppression of 55 dB with a side-mode suppression of 40 dB at 1535 nm. Therefore, a centre-wavelength of 1535 nm is used in the setup shown in Fig.(3.22) for the best performance of the modulator. As a single side band is used as the probe, no additional filter is needed before the photo-detector. Although the QPSK modulator has a high optical insertion loss, the distributed measurement signal has a higher contrast than that using a conventional intensity modulator and a fiber Bragg grating. In fact, the signal does not suffer from the optical loss due to the fiber Bragg grating. On the other hand, problems with this technique are the complicated adjustment of three DC-bias and the continuous DC-bias drift of the modulator. Hence, it has to be regulated for each measurement.

3.2.4.1 Experimental results

In the following some results are shown. First, spectra of Stokes and anti-Stokes signals have been observed at the output of the QPSK modulator. Fig.(3.23 a) shows a spectrum of the Stokes signal. The QPSK modulator is tuned to generate the Stokes signal. It is clearly seen that the modulator can suppress the carrier wave by 55 dB and its single side-band suppression ratio is 40 dB at 10.94 GHz from the pump frequency at 195211 GHz (1535 nm). These suppression ratios can ensure a good quality of BOTDA measurements without a filter. A spectrum with the anti-Stokes signal is shown in Fig.(3.23 b). The carrier is suppressed by 55 dB. However the single side-band suppression ratio is 32 dB which is lower than that of the Stokes signal. Nevertheless this suppression ratio is enough to perform a good quality of distributed measurement without filter. After the spectra observation, we have performed a distributed measurement of an SMF with 50 km length using the QPSK modulator as shown in Fig.(3.24). The loss of the SMF is 0.2 dB/km

which is not as high as in a PCF but results in a significant loss for long lengths like 50 km. We have measured distributed the Brillouin gain for the Stokes and anti-Stokes probes with a 3 m-spatial resolution and a 1 MHz-frequency resolution. The distributed measurements using the Stokes and the anti-Stokes probes are shown in Fig.(3.24 a) and (3.24 b), respectively. By comparing the two figures, it is evident that the measurement with the anti-Stokes probe shows a better quality than that with the Stokes probe. Fig.(3.24 b) clearly reveals the 50 km length of the fiber despite of the fiber attenuation. The beginning of the fiber is very similar in both cases. But the contrast at the end of the fiber is remarkably improved using the anti-Stokes signal. Fig.(3.25) shows Brillouin responses recorded

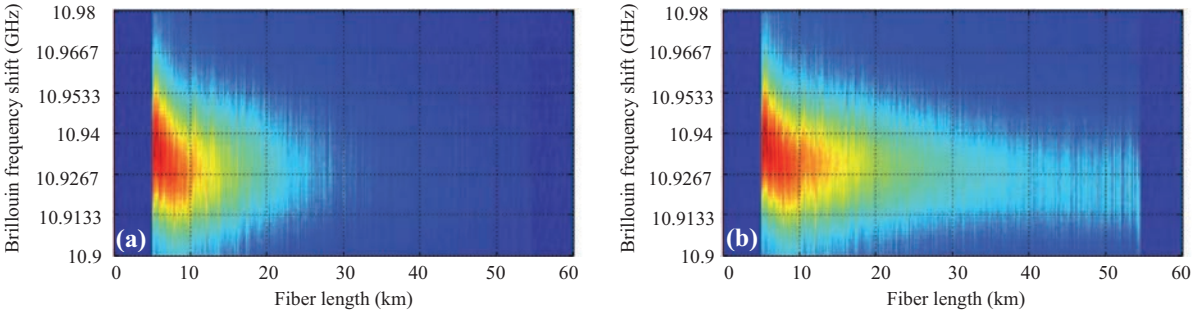

Figure 3.24: Distributed measurements of a 50 km SMF using (a) the Stokes probe and (b) the anti-Stokes probe generated by the QPSK modulator.

by the oscilloscope. The blue trace in Fig.(3.25 a) represents the Brillouin response with the anti-Stokes (loss process), the red one is obtained by use of the Stokes component (gain process). We can observe in the figure the linear loss along the SMF mainly due to the fiber attenuation. In the beginning of the fiber, the gain amplitudes of the Stokes and the anti-Stokes probes are similar. However, at the end of the fiber, the Brillouin gain is merely noticeable for the Stokes wave whilst the gain for the anti-Stokes wave still remains. The origin of this difference may be the pump depletion being higher in the Stokes probe than that in the anti-Stokes probe. Since the anti-Stokes involves Brillouin loss process, the energy of the anti-Stokes wave is transferred to the pump. Therefore it would be expected that the pump bears low depletion thanks to the anti-Stokes wave. Moreover, the Stokes signal is not present and the pump looses its energy mainly by fiber attenuation (10 dB for 50 km), but not much by Brillouin gain. For the Stokes case, the Stokes probe takes Brillouin gain continuously from the pump. This results in high pump depletion. As the anti-Stokes signal is not present, the pump keeps loosing its energy by the fiber attenuation and depletion. The measurements show a high performance of our BOTDA setup using a QPSK modulator because commercial BOTDA sensors work with a 30 km fiber length. We have made a comparison between BOTDA including the QPSK modulator and the classical BOTDA with a filter. The 50 km distributed traces are shown in Fig.(3.25 b) for the Stokes (red trace) and the anti-Stokes probe (blue trace).

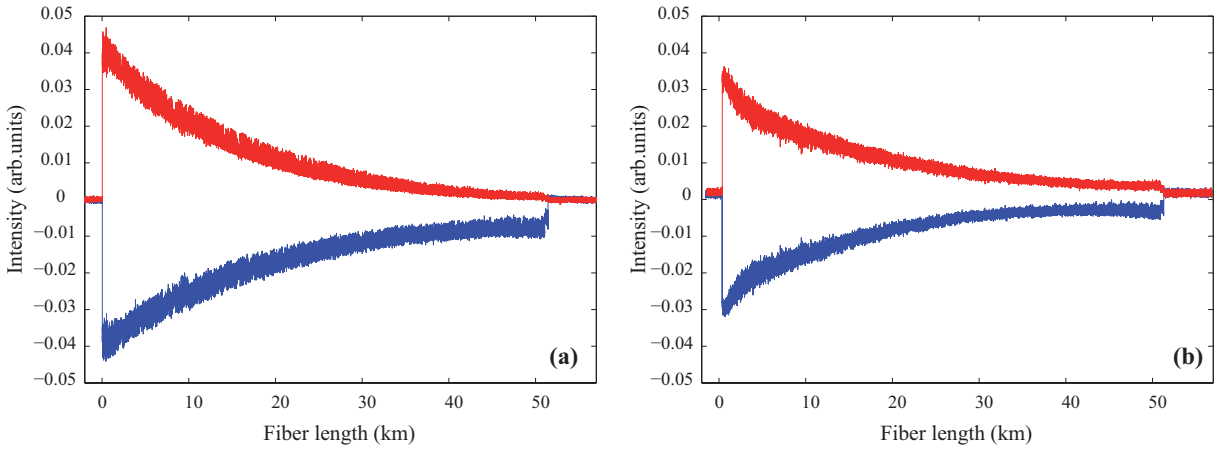

Figure 3.25: (a) Distributed measurements along the 50 km fiber using the Stokes probe (red trace) and anti-Stokes probe (blue trace), (b) distributed measurements along the 50-km fiber using the classical BOTDA setup shown in Fig.(3.11). The double side-band probe is filtered out to select the Stokes signal (red trace) or the anti-Stokes signal (blue trace).

The anti-Stokes traces in Figs.(3.25 a,b) reveals no significant difference in terms of the signal contrast. Besides, the Stokes trace in Fig.(3.25 b) also exhibits gain at the end of the fiber. As both the Stokes and anti-Stokes probes are present in the classical BOTDA system, the pump looses its energy by the Stokes and the anti-Stokes transfers some of its energy to the pump. Therefore, the pump with the Stokes and anti-Stokes would suffer less from depletion than that with the Stokes only in the QPSK BOTDA. The comparison also manifests that anti-Stokes can enhance the sensing range compared to Stokes. From the trace amplitudes, it also reveals that the signal amplitude is twice greater in the QPSK BOTDA setup than that in the classical BOTDA setup. As such, a QPSK modulator provides an improvement of signal-to-noise ratio on distributed measurements.

3.3 Distributed strain measurement

As mentioned in chapter 3.2, an application of Brillouin distributed measurement is temperature and strain monitoring. In this paragraph the measurement of the strain coefficient will be shown.

For strain monitoring we have set up an elongation platform that can be controlled with high precision (10 µm) by Labview. Therefore we fixed the fiber with tape and marked the point where the fiber has been fixed to be sure that the fiber is stretched without slipping under the tape. First we measured the BFS depending on applied strain

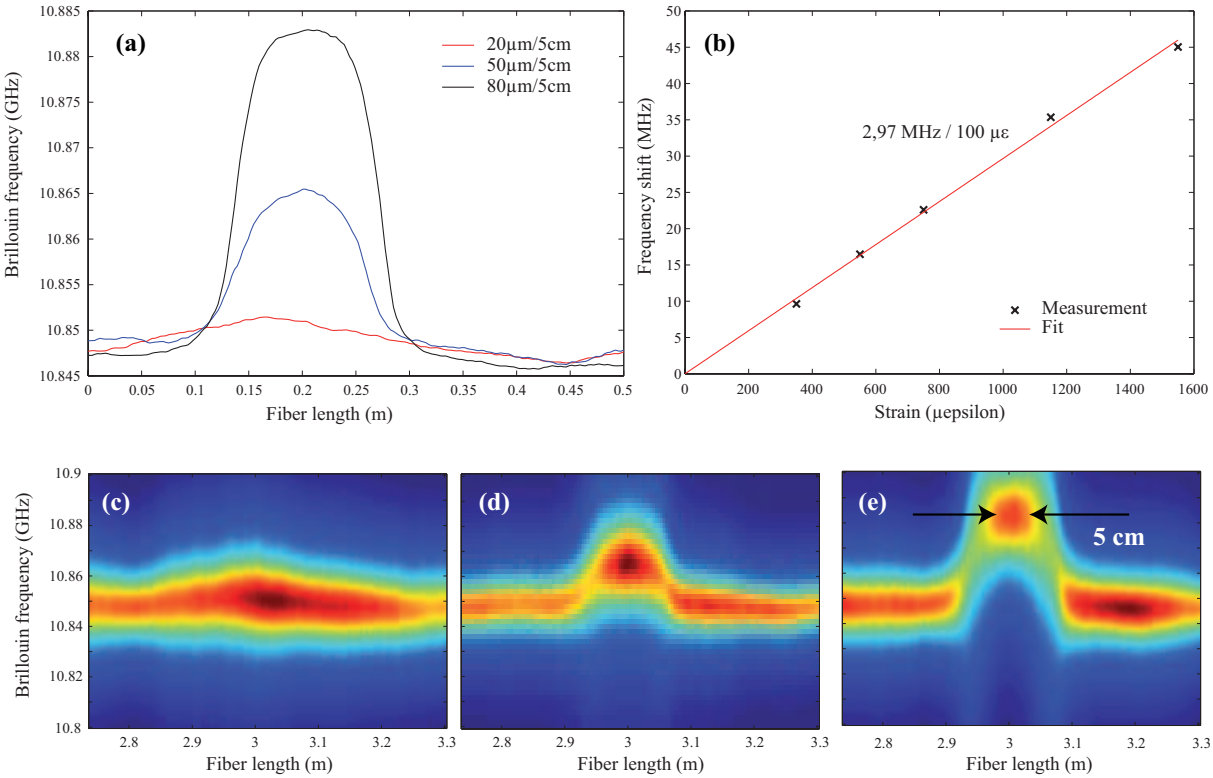

Figure 3.26: (a) Brillouin frequency shift versus fiber length and (c-e) Brillouin gain mapping for three different elongations applied to a 5-cm fiber section. (b) BFS dependent on applied strain

on 5 cm of an SMF. The measurement was obtained by the DPSK-BEDS technique with a spatial resolution of 5 cm. The effect of an elongation of 0 - 80 µm on the BFS can be seen in Fig.(3.26) where (a) shows the analysis of the BFS for three different elongations, (b) fitted data in order to estimate the strain coefficient and (c-e) the mapping of the 5 cm section for 20 µm, 50 µm and 80 µm over 5 cm. Since 5 cm corresponds to the spatial resolution of the system the graphs do not decline sharply at the end of the 5cm-section in Fig.(3.26 a,c-e). Nevertheless, it confirms well the performance of the DPSK-BEDS system. As the elongation length increases, the BFS increases from 10.847 GHz to 10.865 GHz and 10.883 GHz. However, the figure reveals the elongation over more than 5 cm. We speculate that the pure fiber may slightly slip inside the fiber coating by the strain. The BFS is displaced by 18 MHz at 600 $\mu\varepsilon$ and 36 MHz at 1200 $\mu\varepsilon$. It is seen from the elongation measurements that the strain coefficient is obtained as 2.97 MHz per 100 $\mu\varepsilon$, in poor agreement with the value reported in literature which is 5.055 MHz/100 $\mu\varepsilon$ [37]. This is due to the very short length of 5 cm. For a more precise strain measurement we also performed strain monitoring over 12.3 m by comparing an SMF, a PCF and a highly nonlinear fiber (HNLF).

For this measurement the standard BEDS setup has been used and a long stretch

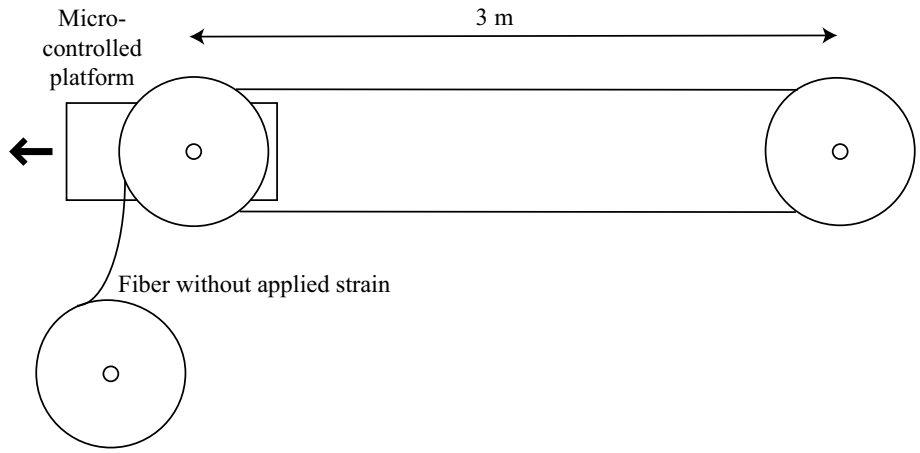

Figure 3.27: Experimental setup to stretch fibers (here 12.3 m).

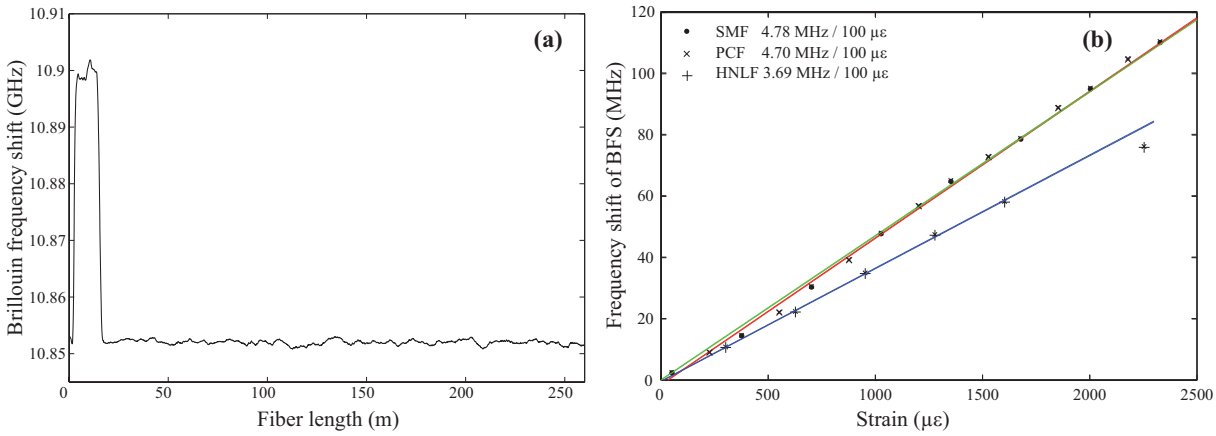

Figure 3.28: Distributed strain measurement over 12.3 m of the fiber. (a) BFS for a 260 m SMF where the first 12.3 m are frequency shifted, (b) Strain coefficients for an SMF (260 m), PCF (100 m, 5.5 μm fiber core diameter) and HNLF (490 m).

bench was realized where 12.3 m of the fiber were coiled up. In Fig.(3.27) the construction is visualized: two fiber coils are needed, one fixed on the movable elongation platform, the second one fixed at 3 m from the first one on the optical table. The second coil is not tighten on the table but can turn so that the strain can be homogeneously distributed on the 12.3 m (about 4 x 3 m) of the fibers. In Fig.(3.28) we see the 260m-long SMF where 12.3 m were stretched by 7 mm. The shift in BFS from 10.85 GHz to about 10.90 GHz can clearly be observed. Figs.(3.29 a-c) show the mapping of a 260m-long SMF, a 100m-long PCF (5.5 μm fiber core) and a 490m-long HNLF with 28 mm elongation over 12.3 m. The BFS is different for each fiber due to their different effective refractive indexes (SMF and PCF) and also different acoustic velocity such as the HNLF because of its highly doped GeO_2 core. The spatial resolution is 30 cm and the frequency resolution is 1 MHz. The reason for the lower quality of the mapping Fig.(3.29 c) for the HNLF is probably the splic-

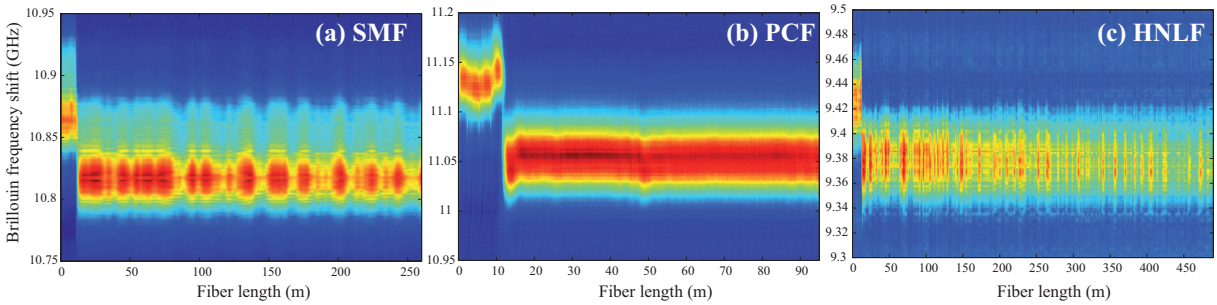

Figure 3.29: Brillouin frequency shift versus the fiber length for three different elongations applied to a 5-cm fiber section.

ing losses of the fiber or the pulses (intensity and phase pulse) are not adjusted accurately enough. However, the data were all exploitable and we obtain the following strain coefficients: 4.78 MHz/100 $\mu\varepsilon$ (SMF), 4.70 MHz/100 $\mu\varepsilon$ (PCF) and 3.69 MHz/100 $\mu\varepsilon$ (HNLF) which is comparable to values obtained in SMF and PCF in literature [37,38]. The similar value for the SMF and the PCF is not really astonishing because it depends mainly on the material, in this case pure silica.
However, it could have been possible that the value for PCFs and SMFs are different because of the air-hole micro-structure. Our recent results [39] for forward Brillouin scattering have shown a higher temperature sensitivity for PCFs. The temperature coefficient in the forward Brillouin scattering spectrum is about 10 times higher than for a SMF [39]. We can say that this is not the case for backward scattering. The micro-structure has apparently no influence on the strain coefficient unlike the material or the doping level.

3.4 Effect of structural irregularities in photonic crystal fibers

In this paragraph we investigate the effect of microstructure irregularities and applied strain on backward Brillouin scattering by comparing two PCFs drawn with different parameters in order to minimize diameter and microstructure fluctuations. We fully characterize two PCFs with the nearly same air-hole microstructure but drawn with different parameters in order to minimize diameter fluctuations. The experiments are twofold: we first perform a measurement of the Brillouin gain spectrum (BGS) and the critical power for the Brillouin threshold and then a Brillouin-echoes distributed sensing (BEDS) measurement with a high spatial resolution of 30 cm. These experiments have been performed with the Group for Fiber optics at the EPFL in Lausanne within a research stay supported by the COST 299 action. Our results show that these two fibers exhibit a single peak in the gain spectrum like an SMF and that their critical powers of stimulated

scattering are in good agreement with theory. The impact of structural irregularities and strain on the BFS is also clearly evidenced. We observe in particular long- and short-scale fluctuations in the BFS. Although short-scale longitudinal fluctuations were theoretically studied in Ref. [40], it is the first time, to our knowledge, that the short-scale fluctuations are observed in optical fibers using the BEDS technique. We further show that it is possible to extract the effective refractive index all along the fiber from the distributed BFS measurements, which allows a quantitative estimation of fiber irregularities. With these measurements we are able to draw conclusions about the fiber inhomogeneity induced by the drawing process because the results reveal a clear-cut difference of longitudinal homogeneity between the two fibers.

The Brillouin gain and Brillouin frequency shift (BFS) depend on the overlap of light and acoustic waves in the fiber core and on the material. Temperature and strain influence the velocity of the acoustic wave and thus the BFS. Since the acoustic modes are sensitive to temperature and strain, Brillouin backscattering has widely been studied for distributed sensing in single mode fibers (SMF) [4, 26] as well as in PCFs [41]. Due to their high nonlinear efficiency, PCFs have received particular attention for temperature and strain sensing. It has recently been reported that PCFs with small core exhibit in most cases a multi-peak Brillouin spectrum due to the periodic air-hole microstructure [7, 42, 43]. This aspect could be advantageously used for simultaneous strain and temperature distributed measurements. However, when multi peaks overlap, the spectrum broadens and the data analysis becomes more difficult. Another aspect that limits distributed measurements is the inhomogeneity of opto-geometrical parameters along the fiber. This is even more crucial in PCFs since their fabrication requires an accurate control of more parameters than for SMF during the drawing process. Fiber manufacturers are interested in controlling the fiber homogeneity and are looking for an adequate method. This was one of the motivations for the following experiments with two PCFs with different drawing processes provided by IRCICA institute in Lille.

The two PCFs under test have a hexagonal holy structure and their cross-sections are shown in the insets of Fig.(3.30). They originate from the same stack, but from different intermediate canes. The cane used to manufacture fiber #1 was 3.8 mm in outer diameter and drawn at a relatively high temperature (low tension). For fiber #2 the cane was drawn with the same parameters, except for the temperature that was much lower than for fiber #1, leading to a much higher tension during the drawing process. At this stage, the outer diameter fluctuations of both canes were comparable, but the air holes were slightly smaller in cane #1 than in cane #2. The canes were then inserted into jacketing tubes, and drawn down into fibers. Both fibers were drawn with comparable parameters, although a slightly higher pressure was used for fiber #1 to inflate air holes. The outer diameter fluctuations measured during the drawing process were about 2% for fiber #1 and less than 1% for fiber #2. Both of the fibers are designed to get a zero-dispersion-wavelength around 1060 nm and have an attenuation of 5 dB/km (#1) and 8.6 dB/km (#2) at 1.55 μm. Their effective mode area (EMA) is about 15 μm^2 (#1)

and 16 μm^2 (#2) at 1.55 µm found by calculation based on scanning electron microscopy (SEM) images. The core, hole diameter, pitch, and length can be found in table (3.1).

Table 3.1: Details of PCF microstructure

	#1	#2
Core diameter	5.5 µm	5.5 µm
Hole diameter	2.7 µm	2.3 µm
Pitch	4.1 µm	3.9 µm
Fiber length	100 m	400 m
Effective mode area	15 μm^2	16 μm^2

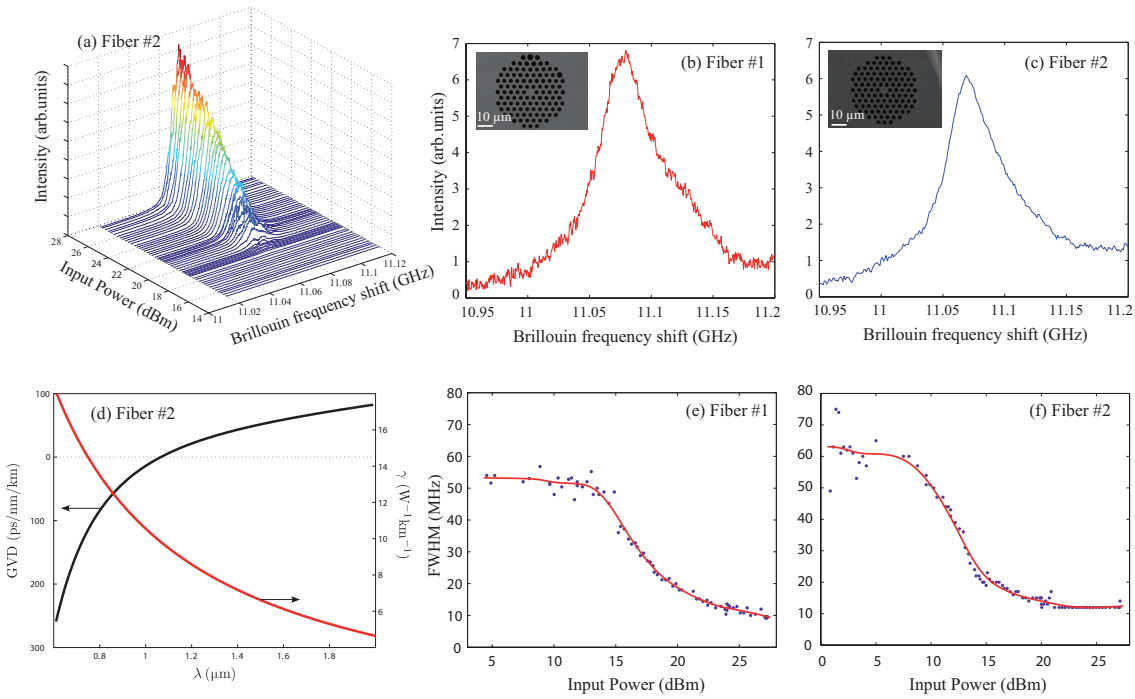

Figure 3.30: (a) Brillouin gain spectrum for fiber #2 with increasing input power. Brillouin spectrum for an input pump power of 11 dBm, which is under the critical power, for (b) fiber #1 and (c) fiber #2. The PCF cross-sections are shown in the insets. (d) Simulated group velocity dispersion and nonlinear coefficient γ here for fiber #2 (comparable to fiber #1). FWHM of the Brillouin gain depending on the input power (e) fiber #1 (f) fiber #2.

3.4.1 Brillouin gain spectrum

Before the distributed analysis of the BFS along the fibers we have first performed a direct measurement of the gain spectrum and the critical power using the experimental setup of the heterodyne measurement (Fig.(3.1)). Since in the latter case the scattered light is affected by strain, differences of temperature and air-hole microstructure fluctuations along the fiber, it is called integrated measurement. As an example, the Brillouin spectrum dynamics in function of the pump power obtained from fiber #2 is shown in Fig.(3.30 a). In Fig.(3.30 e,f) we can see the FWHM depending on the input power in dBm. As reported in previous work [7], there is a plateau in the low power regime. In the stimulated regime the Brillouin spectrum narrows as expected and tends to 10 MHz [44]. For spontaneous scattering we assume the FWHM to be about 60 MHz for fiber #2 and 55 MHz for fiber #1 keeping in mind that the measurement is rather noisy in this part. In a SMF the FWHM is about 27 MHz which is lower as our measured ones [2, 45]. This Brillouin linewidth broadening is due to fiber inhomogeneities and to the photonic crystal cladding that allows the simultaneous generation of several longitudinal acoustic modes, as previously demonstrated [7].
The FWHM in the spontaneous regime of Brillouin scattering is inversely proportional to the acoustic decay time of the material according to Eq.(2.37). With a FWHM of 27 MHz the natural phonon lifetime in silica is 11.7 ns which means that the amplitude of the acoustic wave decreases to 1/e in this time. Our measurements of the FWHM reveal an acoustic decay time of 5.3 ns for fiber #2 and 5.8 ns for fiber #1. Although our PCFs are made of silica, their phonon lifetimes are lower than that in silica. The reason for a lower value can be the interaction of several acoustic modes at the same time which causes a faster damping than with a single acoustic wave, reducing the coherence of SBS process. This will further be discussed in the next chapter.
To get better insight, Fig.(3.30 b,c) show the Brillouin spectra at 11 dBm which is below the critical power of stimulated scattering. One can see that there exists a single peak as in an SMF and an asymmetry in the spectra can be noticed, particularly for fiber #1. This asymmetry suggests the presence of two or more acoustic modes with close Brillouin frequency shift and thus overlapping gain spectra.

3.4.2 Critical power of stimulated Brillouin scattering

The critical power of the Brillouin threshold is also measured for the two fibers. The estimated value for the critical power for homogeneous fibers is given by Eq.(2.38) and the Brillouin gain can be determined by measuring the FWHM in the spontaneous Brillouin regime according to Eq.(2.36). For fiber #1 the Brillouin gain is $g_B = 1.25 \cdot 10^{-11}\ mW^{-1}$ and for fiber #2 we obtain $g_B = 1.15 \cdot 10^{-11}\ mW^{-1}$. In literature a value of $1.685 \cdot 10^{-11}$

m/W for g_B in SMF can be found, as recently reported by Lanticq *et al.* [8]. The higher g_B for SMF compared to our measured one in PCFs is not contradictive with the higher PCF nonlinear Kerr coefficient γ according to Eq.(1.23). Indeed g_B does not benefit from the smaller PCF effective mode area contrary to the nonlinear Kerr coefficient γ. To get a deeper insight to the definition and the theoretical threshold the reader is refered to chapter 4. With help of this theory the numerical factor C which depends amongst others on fiber length, attenuation, BFS and the threshold definition can be calculated as 14.4 for fiber #1 and 14.0 for fiber #2. With the measured and calculated values the theoretical critical power can be estimated as 24.28 dBm for fiber #1 and 20.16 dBm for fiber #2. The critical power for stimulated scattering is measured with the same setup as for the Brillouin spectrum without the heterodyne detection (Fig.(3.5)). The results for the backscattered and transmitted power depending on the input power for both fibers are shown in Fig.(3.31). The experimental value of the critical power is obtained as 26.7 dBm for fiber #1 and 20.2 dBm for fiber #2 taking into account splicing losses of about 1.5 dB. Comparing the theoretical values with the experimental ones we found them in good agreement for both fibers. Assuming the fairly high birefringence in those fibers, the factor 3/2 is probably too large, Fiber #1 being shorter. This may be a tentative explanation of the discrepancy with Fiber #1. Another possible reason may be the higher inhomogeneity of the fiber that will be shown in the next paragraph.

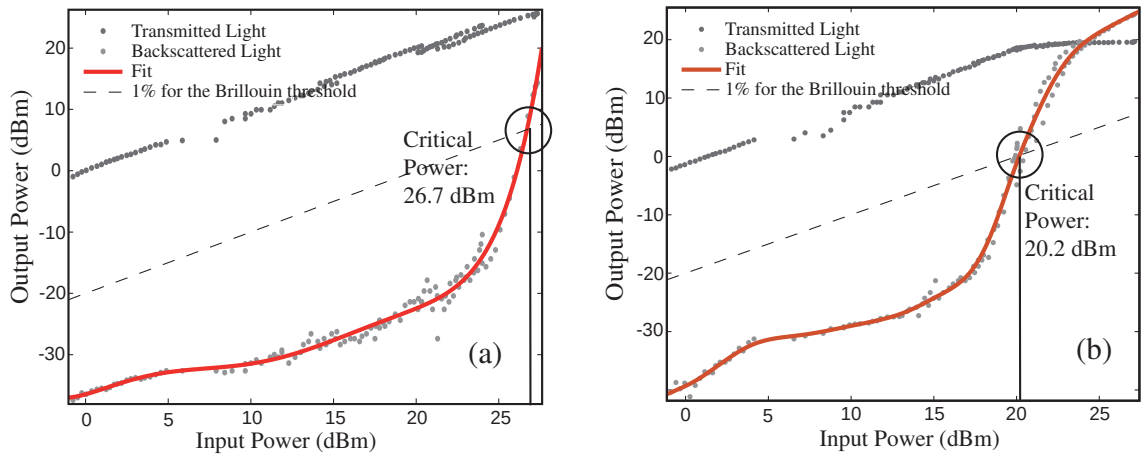

Figure 3.31: Backscattered and transmitted power versus input power of (a) fiber #1 and (b) fiber #2

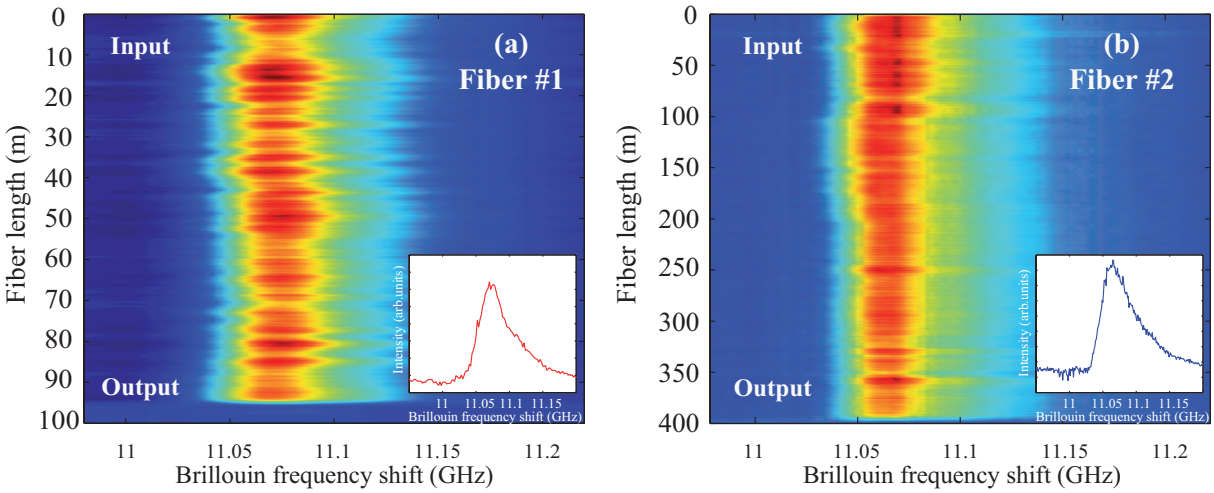

Figure 3.32: Mapping of the Brillouin gain for (a) fiber #1 and (b) fiber #2. The Brillouin gain spectrum at 50 m of the fiber is shown in the insets.

3.4.3 Distributed Sensing using Brillouin Echoes

In order to study longitudinal fluctuations in PCF we performed a classical BEDS measurement which has been carried out during a research stay at the EPFL in the fiber optics group. Besides the integrated measurement of the Brillouin spectrum the distributed one provides further informations concerning inhomogeneities and strain on the fiber. The setup has been explained in paragraph 3.2.2. We use the enhanced BEDS setup to avoid the second echo in Fig.(3.16). Taking into account the fiber losses a measurement with 30 cm spatial resolution and 2 MHz frequency resolution was possible. Fig.(3.32) illustrates the result of the BEDS measurement for fiber #1 (a) and fiber #2 (b) while the probe modulation frequency is swept around the BFS. The data were averaged and fitted by using a convolution with a rectangle to reduce noise. Then the spectra were fitted at each measuring point along the fiber to extract the BFS. The used fit for the FWHM is a Lorentzian profile; for the BFS a parabolic fit was used to obtain a higher precision.

In order to highlight shortly the difference between the parabolic fit and the Lorentzian fit, the analysis of the BFS of fiber #2 is presented in Fig.(3.33). The first image (a) is the result of fitting the distributed BGS with a parabolic fit of only the top points of the spectrum, the second one (b) with a Lorentzian fit of the whole data row. It can be observed that the parabolic fit leads to a more precise and distinct distributed BFS (Fig.(3.33 c)) than the Lorentzian fit. Here (Fig.(3.33 d)), the graph seems to be smoothed along the fiber. The reason is clearly remarkable in the fit of the BGS because the Lorentzian fit takes into account the whole measurement row whereas the parabolic fit uses only the top points of the data. This means that the Lorentzian fit is also influenced by asymmetry as it is the case here. The maximum of the Lorentzian curve is slightly

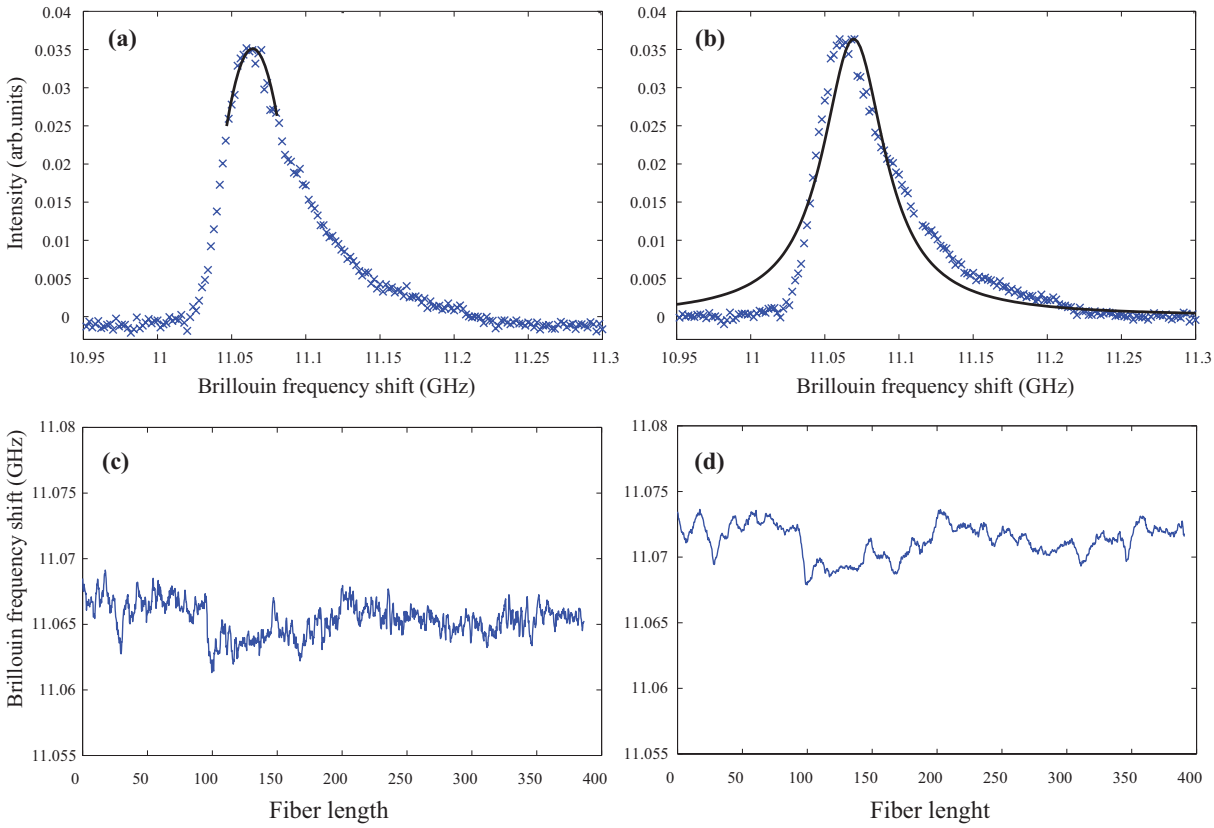

Figure 3.33: Brillouin gain spectrum at 50 m of fiber #2 with (a) parabolic fit and (b) Lorentzian fit. The resulting distributed BFS is shown in (c) and (d), respectively.

shifted to the real maximum which can also be observed in the two insets of Fig.(3.33). To find a more appropriate fitting curve for the whole measuring row we will use a multi-Lorentzian model in paragraph 3.5.

Fig.(3.34) gets further insight into the longitudinal fluctuations of the BFS. As it can be seen, the distributed BFS exhibit both long- and short scale longitudinal fluctuations that are due to diameter fluctuations. Particularly for fiber #1 we can identify a long-scale sinusoidal variation of about 8 MHz with a half-period of approximatively 50 m that corresponds to the middle of the fiber. This BFS variation is due to the strain induced by the fiber coiling as a half of the fiber length is coiled on the other half. This was easily confirmed by inverting the PCF in the setup. On the other hand, the short-scale longitudinal fluctuation (about 5±1 MHz every 2 m) seen in Fig.(3.34 a) indicates a random geometric variation of the air-hole microstructure. Note that this cannot be attributed to the influence of birefringence in the PCF since the variation on the refractive index can be estimated to $7 \cdot 10^{-4}$ using Eq. (2.18) which is well above the birefringence of the PCF (estimated phase birefringence by simulation: $\approx 1.5 \cdot 10^{-5}$, measured group birefringence: $\approx 5 \cdot 10^{-6}$). Fig. 3.34(b) shows a 5 MHz shift in BFS for fiber #2 between 80 m and 180 m which corresponds to one layer of the fiber coil. In this way we are able to detect the strain

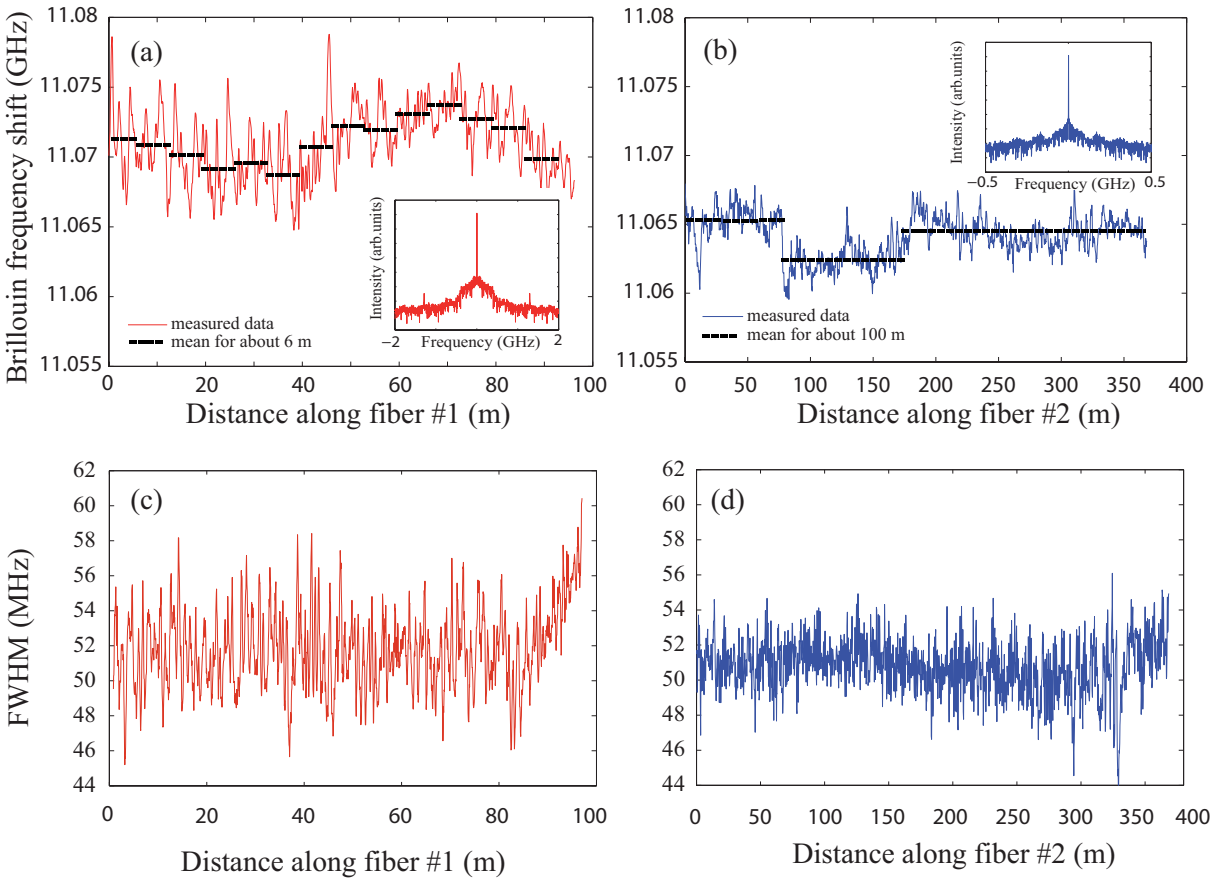

Figure 3.34: Brillouin frequency shift along (a) fiber #1 and (b) fiber #2 showing the effect of inhomogeneities and strain. The insets show the Fourier transforms. Distributed FWHM of the BGS for (c) fiber #1 and (d) fiber #2

applied to one layer. The short scale fluctuation is smaller (3±1 MHz, every 2-3 m of the fiber) and can be attributed to geometrical fluctuations of the air-hole microstructure. The mean power of the pump pulse in the distributed measurement for both fibers was 13 dBm. Taking into account the splicing losses the pump power is assumed to be well below the Brillouin threshold. Comparing our previous measurements of the Brillouin gain spectrum at this power level (about 11.5 dBm) and the spectrum of the distributed measurement at 50 m we find a good agreement for fiber #1 (Fig.(3.30 b) and Fig.(3.32 a)). Both spectra are asymmetric which may be explained by several frequency shifted acoustic modes. The peak frequency of the self-heterodyne Brillouin spectrum measurement amounts to 11.078 GHz (mean value in the power range 5-28 dBm). The distributed frequency along the fiber is 11.071±0.003 GHz. The same comparison for fiber #2 reveals a discrepancy between the self-heterodyne and the distributed measurements (Fig.(3.30 c) and Fig.(3.32 b)). The Brillouin gain spectrum in self-heterodyne measurement has a single mode shape but a little bump on the right side can be seen. However the distributed Brillouin spectrum in Fig.(3.32 b) appears more asymmetric than in the self-heterodyne measurement. In the distributed measurement the BFS varies around 11.064±0.002 GHz.

The self-heterodyne measurement reveals a mean BFS of 11.069 GHz over a power range 3-27 dBm.

The FWHM of the Brillouin gain spectrum has been extracted by help of a Lorentzian fit (because it is not possible to extract the FWHM with the parabolic fit) and is depicted in Fig.(3.34 c,d). For fiber #1 the distributed FWHM is about 52±2 MHz, compared to 51.5 MHz at 11.5 dBm in the integrated measurement (Fig.(3.30)). The FWHM for fiber #2 is 50±1 MHz (distributed) and 45.4 MHz (integrated). Hence the Brillouin gain broadening for PCF in the spontaneous regime is also noticed in this experiment. Concerning the inhomogeneity we can observe lower fluctuations for fiber #2. In this way the distributed measurement shows the effect of the different drawing process, in terms of the BFS and the FWHM of the Brillouin gain spectrum. Fluctuations in fiber #2 are clearly less pronounced than in fiber #1, as expected. The increase in FWHM at the end of the fiber may be due to pump depletion.

It is clear from Fig.(3.34 a,b) that the longitudinal fluctuations in BFS are less significant for fiber #2 than fiber #1 as the drawing process was better controlled. This is verified by studying the fast Fourier transform of the BFS trace shown in the insets of Fig.(3.34 a,b). We notice that for fiber #1 the frequencies pedestal around the main peak is wider than for fiber #2. In order to obtain an estimation of the diameter or microstructure fluctuations along the fibers, we have derived the distributed effective refractive index n_{eff} from the distributed BFS as they are proportionately linked by Eq. (2.18) (V_L and λ_P are known).

In the following, we assume that the main contributions to these fluctuations are due to homothetic variations of the microstructure, i.e. to fluctuations of the outer diameter only. We neglect here possible longitudinal inhomogeneities of individual air holes or pitch, as well as possible twists induced during the drawing process because of several reasons. The variation of the effective refractive index can derive from different origins: applied strain, temperature variation, longitudinal variations of the microstructure, individual air holes inhomogeneities or variation of the pitch. We assume that the temperature does not influence the experiment because of the short experiment duration. The impact of strain is observed in long scale fluctuations which indicates the effect of the fiber coiling. Moreover the variation of the pitch has an important impact on the effective refractive index, which can be found in Ref. [46]. However several SEM-images at different sections of the fibers show that there is no measurable variation of the pitch and singular air-holes. From our numerical simulation using Comsol it is found that the variation of the microstructure scale is the main cause of the variation of the effective refractive index. So we decided to vary the scale of the microstructure since this seemed to be the most general variation. To relate geometrical variations to n_{eff} the dependency of n_{eff} on the microstructure scale has been computed by using the PCF cross-section of the two fibers

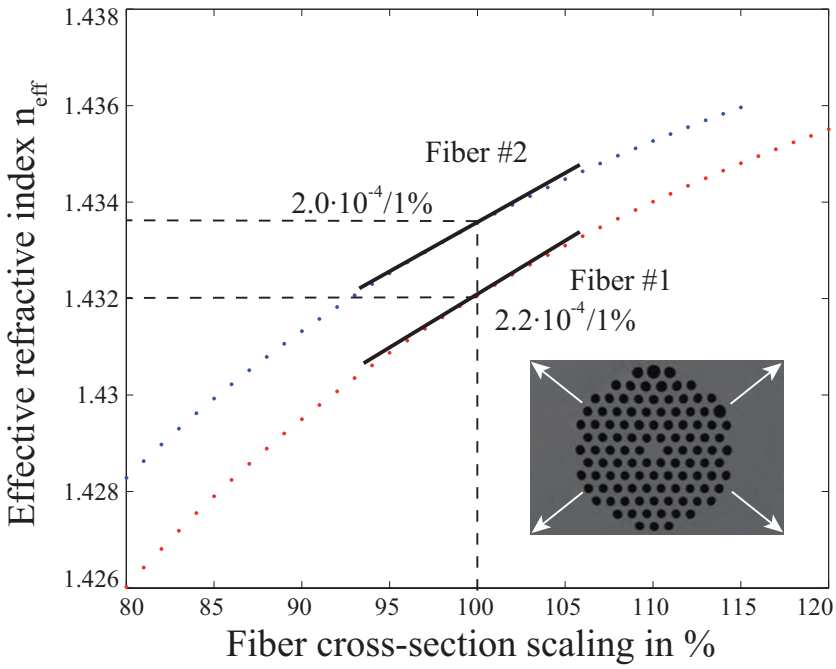

Figure 3.35: Variation of the effective refractive index while tuning the scale of the SEM-image

via Comsol software (Fig.(3.35)). A simulation based on the original image (corresponding to 100% in Fig.(3.35)) yields a certain amount of n_{eff} (1.434 for #2 and 1.432 for #1). By varying the scale of the original SEM-image different values of n_{eff} are obtained and depicted in Fig.(3.35) for the two fibers.

We have computed the local derivation of the obtained relation between n_{eff} and the geometrical scale around 100% as indicted by the tilt solid lines in Fig.(3.35). The effective refractive index changes by $2.2 \cdot 10^{-4}$ (#1) and $2.0 \cdot 10^{-4}$ (#2) for 1%. This is compared to the fluctuations of the effective refractive index in the fibers under test by using Eq. (2.18). The variation of the short scale fluctuations (5±1 MHz for fiber #1 and 3±1 MHz for fiber #2) corresponds to 2.9±0.6% and 1.9±0.6% of scale or diameter fluctuations, respectively. The large scale variation is 4.7% (8 MHz for #1) and 3.2% (5 MHz for #2). This means that the maximum core diameter fluctuation is 5.5±0.3 µm (fiber #1) and 5.5±0.2 µm (fiber #2). Since polarization and strain can influence the variation of the effective refractive index the contribution of the structure size is expected to be below these values. This estimation confirms the higher quality of the drawing process obtained for fiber #2. Note that the fluctuations measured in the present work are in good agreement with the specifications from state-of-the-art PCF manufacturers [47], [48].
To conclude this paragraph, the homogeneity of these two photonic crystal fibers drawn from the same preform but with a different drawing process has been investigated and

the fluctuations were logically found less important in the case of a fiber fabricated with a better process control. We have been able to identify and quantify both long- and short-scale longitudinal fluctuations in the Brillouin frequency shift resulting from residual strain due to fiber coiling and air-hole microstructure or diameter fluctuations, respectively. Our results finally demonstrate the great potential of the Brillouin echoes distributed sensing technique for small scale optical fiber characterization. Moreover, these results show the need for characterization of structural irregularities in fibers before they can be used for distributed sensing.
In the next chapter another performance of the BEDS technique will be presented. Due to the high spatial resolution it is possible to estimate the acoustic decay time in fibers. Besides a multi-Lorentzian model will be applied to get a better fitting of the row measured data and to understand the asymmetry in Brillouin gain spectra.

3.5 Observation of the acoustic decay time

In this paragraph we report the observation of the acoustic decay time in both, PCF and SMF, using the BEDS technique. As we have seen before, the BEDS technique basically differs from BOTDA since the BEDS technique enhances the spatial resolution. Not only a precise BGS distributed measurement can be performed but also a measurement of the decay time of acoustic waves gets possible. The BEDS technique has to be used without the second intensity modulator, as introduced in chapter 3.2.2, because this time we will make use of the second echo [49] to obtain the Brillouin response and the decay of the acoustic wave [20, 21].
To investigate the decay time of acoustic waves we used the distributed measurements that have been carried out in the 100-m long PCF from the previous chapter, another 15m-long PCF with multi-scale structure as well as in a short length of an SMF. Our results show in particular an asymmetrically-broadened Brillouin gain spectrum all along the PCF due to the presence of several acoustic modes. The Brillouin linewidth broadening for PCF is interpreted in term of a multiple-Lorentzian model. The BEDS technique leads to the observation of the apparent acoustic exponential decay time which agrees very well with the Brillouin linewidth for both fibers. Unlike SMF, the decay time indicates that the Brillouin linewidth of the PCF is not strictly related to the fundamental acoustic phonon lifetime. For the sake of comparison, the results obtained in a 10 m SMF are summarized in Fig.(3.36 a,b,c)[13]. The mapping of the 10m-long SMF is shown in (a) where we observe a homogeneous BFS and the slowly decaying Brillouin response at the end of the fiber. The BGS at one position of the fiber can be fitted by a Lorentzian graph with FWHM 26 MHz as presented in Fig.(3.36 b). Then we investigated the decay of the Brillouin sig-

[13]The measurement of the SMF is kindly provided by the group for Fiber optics at the EPFL

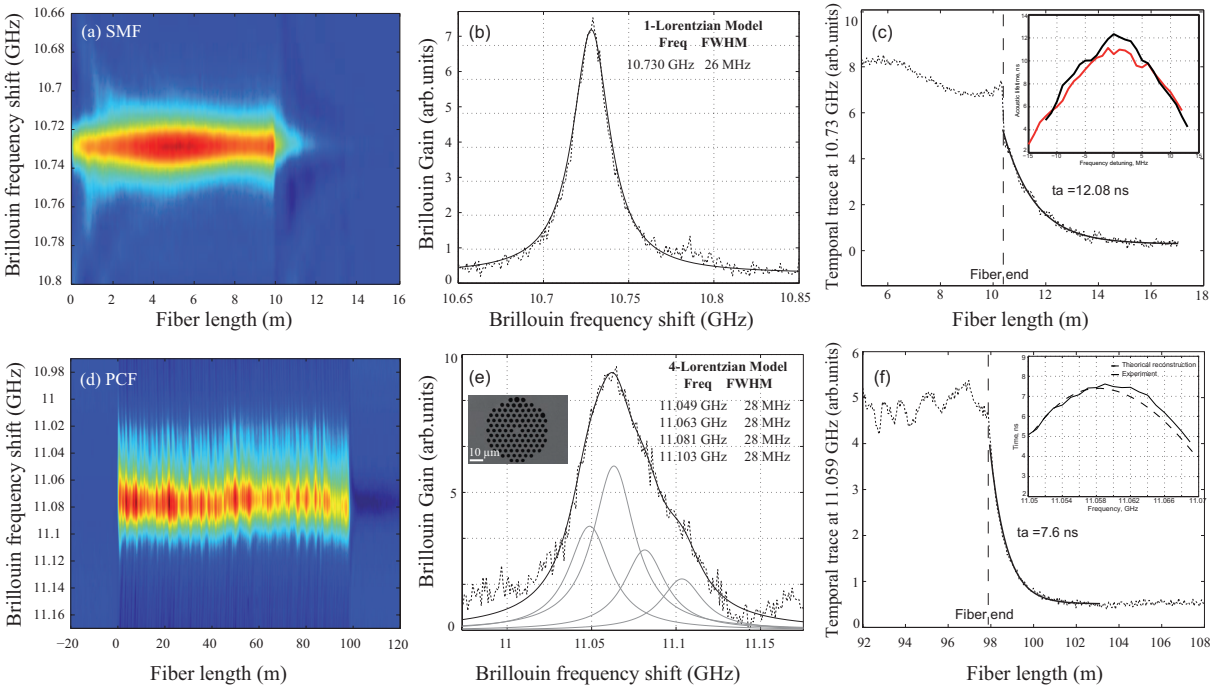

Figure 3.36: Mapping of the BGS in a 10m-long SMF (a) and a 100m long PCF (d), (b,e) Brillouin gain spectrum at a distance of 10m in SMF and 97m in PCF respectively. Grey curves are four single Lorentzian fit of the gain spectrum. (c,f) Brillouin gain at the peak frequency in the time domain at the end of the PCF and the SMF. The black curves show exponential fit curves to estimate the acoustic decay time. In the insets of (c,f) the decay time of the Brillouin response at the fiber end for different frequencies around BFS is shown. The maximal decay time is found at the maximum of BFS spectrum.

nal at the fiber end for each frequency shift (inset of Fig.(3.36 c)) which was confirmed by the same measurement at the fiber input. The maximal decay time is observed at the maximum of the BGS. For this frequency shift we analyzed the time trace as presented in Fig.(3.36 c). When the pulse leaves the fiber a linear decay can be observed first (to get better insight this is presented in Fig.(3.38) in detail). Then the Brillouin response decays exponentially as confirmed by the fitting curve. The resulting decay time of the acoustic wave is 12.08 ns in good agreement with the Brillouin linewidth measurement of Fig.(3.36 b) according to Eq.(2.37) and the value found in literature [10].

Now it is interesting to carry out the same measurement in PCF. The inset of Fig.(3.36 e) shows the cross-section of the PCF under test. It consists of a standard triangular lattice of air holes and its characteristics can be found in table (3.1). In Fig.(3.36 d) the BEDS measurement that maps the Brillouin gain along the PCF as a function of frequency and position is presented. It has been discussed in detail in the previous chapter. Fig.(3.36 e) presents the BGS at a propagation distance of 97 m where one can clearly observe an asymmetric and broadened Brillouin spectrum with a linewidth of 52 MHz

(FWHM) which is definitely larger than the Brillouin linewidth commonly observed in SMF (about 26 MHz, see Fig.3.36(b) for comparison). These features are mainly due to the air-hole periodic microstructure which alters the acoustic modal distribution and leads to a strong coupling between the longitudinal and transverse acoustic modes. Note that such novel characteristics are difficult to model numerically because each PCF exhibits completely different BGS [7, 42, 50]. Nevertheless, by expanding the gain spectrum as a superposition of multiple Lorentzian lines showing a linewidth identical to a SMF, we found that the BGS can be made of four main incoherently-coupled acoustic modes with slightly different central frequencies as show in Fig.(3.36 e). The fitting curves in Fig.(3.36 e) are plotted in grey and the resulting BGS in black. The distributed frequency of four Lorentzian shapes fitting the experimental Brillouin spectrum in PCF is shown in Fig.(3.37 a). A variation in the air-hole microstructure induces an identical variation for the estimated four frequencies fitting the Brillouin spectrum in PCF. Hence, the four acoustic modes are influenced in the same manner along the fiber length. For comparison, we also performed a fit with only two Lorentzian curves (Fig.(3.37 b)) but with variable FWHM which can be found in Fig.(3.37 c,d). The BFS of the two Lorentzian fits are not fluctuating in the same way. The higher Lorentzian fit even shows rather large fluctuations compared to the lower one. For the FWHM it is the same case, the two graphs are not comparable. This fact convinced us that the four Lorentzian model fits better for our measurement. Moreover, from a physical point of view it is more persuasive that different acoustic modes with the natural linewidth of pure silica (28 MHz) are propagating in the fiber than several modes with varying FWHM. The nature of these acoustic modes, e.g. if they are longitudinal or hybrid modes, has still to be investigated by a well-founded model, taking into account the effect of electrostriction.

Using the BEDS technique, we are also able to observe the slow exponential decay time of the acoustic wave in a PCF which is directly scaled by the acoustic phonon lifetime. Fig.(3.36 c) shows, similar to the SMF measurement, the decay time depending on the frequency shift. The black line in Fig.(3.36 c) is an exponential fit on the decay of the maximum BFS and we find a value t_A of 7.6 ns in the PCF. Unlike SMF, the Brillouin linewidth in PCF is not uniquely defined by the damping of the phonon wave. The superposition of multiple acoustic modes actually modifies the measured acoustic lifetime at the Brillouin resonance. The distribution of these acoustic modes is related to the waveguide characteristics for the hyper sound propagation which is influenced by the air-hole micro structure. The experimental value of 7.6 ns is confirmed by calculation (7.4 ns). Therefore the four Lorentzian curves are composed to one spectrum and then the Fourier transform leads to an exponential decay with constant $\tau = 7.4\,ns$. This calculation leads also to the theoretical graph in the inset of Fig.(3.36 c). A comparison to a second PCF has been realized to confirm the result of the shorter acoustic decay time. This PCF has a multi-scale microstructure with three different sizes of air holes (inset of Fig.(3.38 b)) and was provided by Draka, Marcoussis. The first two inner rows with 800 nm holes are based

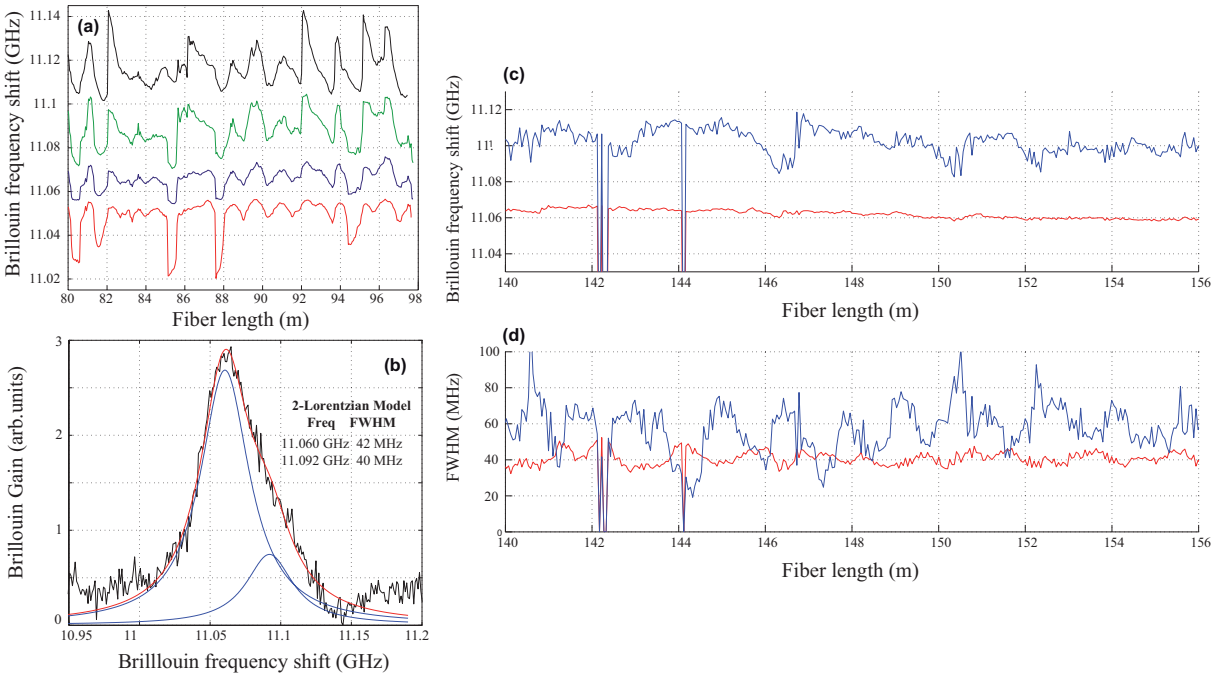

Figure 3.37: (a) Frequency of four-Lorentzian fit based on the SMF linewidth (28 MHz) of the BGS in PCF as a function of position. (b) two-Lorentzian fit of the BGS with variable linewidth, (c) BFS and (d) FWHM for a part of the fiber for the two-Lorentzian fit.

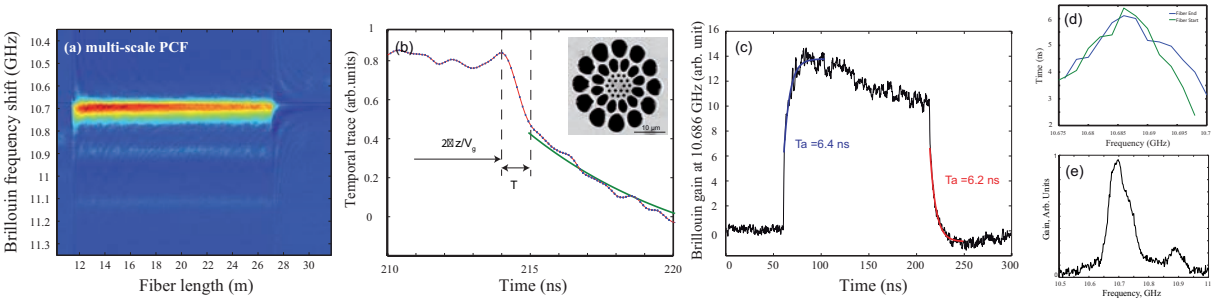

Figure 3.38: (a) Mapping of the BGS in a 15m-long PCF with multiscale structure, (b) zoom on the Brillouin gain at the peak frequency in the time domain at the end of the PCF, (c) Brillouin gain at the peak frequency in the time domain. The black curves show exponential fit curves to estimate the acoustic lifetime at both the input and output of the fiber: 6.4 ns and 6.2 ns, (d) decay time of the Brillouin response at the fiber end for different frequencies around BFS, (f) Brillouin gain spectrum.

on a triangular lattice and the fiber core measures 2.4 µm. This fiber will be studied in detail for it unique forward Brillouin scattering in chapter 5. In Fig.(3.38) we find the same order of measurements as explained before: the fiber mapping, the BGS at one position in the fiber, the decay time depending on the frequency shift and the measured decay time for the maximum of the BGS. For this multi-scale fiber a damping time of 6.3 ns can be

found which is as well significantly shorter than for SMF. Considering the broadened and asymmetric spectrum of this fiber we find five Lorentzian graphs with 28 MHz FWHM that fit into the measured data. Hence, the fitting model has to be carefully chosen for each PCF in order to find the number of Lorentzian fits and thus the acoustic modes. This topic needs further investigation because it has to be understood how the different incoherent acoustic modes interact with the optical mode. This also leads to the question if the shorter decay time signifies that the acoustic wave resulting from different acoustic modes is attenuated faster or if only the optical answer, the Brillouin response, decays faster and this effect can be observed in our BEDS measurement. For this purpose a distributed measurement of the phase should be carried out. Then the coherence of the acoustic waves has to be verified and this can be introduced into the theoretical model. Additionally an interesting theoretical approach for the full vectorial analysis of Brillouin gain has been developed in [51], that can help to get better insight to understand the shorter decay time of the Brillouin response in PCF.

3.6 Conclusion

In this chapter about Brillouin backscattering in photonic crystal fibers several topics have been presented. First techniques of Brillouin gain, Brillouin threshold and distributed Brillouin measurement have been explained in detail and results in different SMF and PCF were analyzed and interpreted. The different distributed techniques have been presented: Brillouin Optical Time Domain Analysis (BOTDA), Brillouin Echoes Distributed Sensing (BEDS), Differential Phase Shift Keying - BEDS (DPSK-BEDS) and finally with the use of a Single-Sideband-Modulator. The use of BEDS and DPSK-BEDS measurement permitted the characterization of all in this manuscript used fibers with high spatial resolution. A distributed strain measurement in SMF, HNLF and PCF was performed and the results were compared. Another application of the BEDS-system is monitoring fiber inhomogeneities in PCF. We identified and quantified both long- and short-scale longitudinal fluctuations in the BFS resulting from residual strain due to fiber coiling and air-hole microstructure or diameter fluctuations. The experimental results were confirmed by simulation based on the SEM image of the fibers. From a fundamental view point it was possible to observe Brillouin linewidth broadening in PCF and for the first time to the best of our knowledge the indirect observation of the acoustic decay time in PCF and SMF which turned out to be shorter in PCF than in conventional SMF.

Bibliography

[1] E. P. Ippen and R. H. Stolen, "Stimulated Brillouin scattering in optical fibers", *Applied Physics Letters*, vol. 21, no. 11, pp. 539–541, 1972.

[2] A. L. Gaeta and R.W. Boyd, "Stochastic dynamics of stimulated Brillouin scattering in an optical fibers", *Physical Review A*, vol. 44, no. 5, pp. 3205–3208, 1991.

[3] N. Shibata, R. G. Waarts, and R. P. Braun, "Brillouin-gain spectra for single-mode fibers having pure-silica G_eO_2-doped, and P_2O_5-doped cores", *Optics Letters*, vol. 12, no. 4, pp. 269–271, 1987.

[4] M. Niklès, L. Thévenaz, and P. A. Robert, "Simple distributed fiber sensor based on Brillouin gain spectrum analysis", *Optics Letters*, vol. 21, no. 10, pp. 758–760, 1996.

[5] R. W. Tkach, A. R. Chraplyw, and R. M. Derosier, "Spontaneous Brillouin scattering for single-mode optical-fibre characterization", *Electronics Letters*, vol. 22, no. 19, pp. 1011 – 1013, 1986.

[6] R. Billington, "Measurement methods for stimulated Raman and Brillouin scattering in optical fibres", Tech. Rep., NPL, 1999.

[7] J. C. Beugnot, T. Sylvestre, D. Alasia, H. Maillotte, V. Laude, A. Monteville, L. Provino, N. Traynor, S. Foaleng Mafang, and L. Thévenaz, "Complete experimental characterization of stimulated Brillouin scattering in photonic crystal fiber", *Optics Express*, vol. 15, no. 23, pp. 15517–15522, 2007.

[8] V. Lanticq, S. Jiang, R. Gabet, Y. Jaouën, F. Taillade, G. Moreau, and G. P. Agrawal, "Self-referenced and single-ended method to measure Brillouin gain in monomode optical fibers", *Optics Letters*, vol. 34, no. 7, pp. 1018–1020, 2009.

[9] S. M. Foaleng, *Brillouin Echoes for Advanced Distributed Sensing in Optical Fibres*, PhD thesis, Ecole Polytechnique Fédérale de Lausanne, 2011.

[10] G. P. Agrawal, *NonLinear Fiber Optics*, Academic Press, third edition, 2001.

[11] A. Kobyakov, M. Sauer, and D. Chowdhury, "Stimulated Brillouin scattering in optical fibers", *Advances in Optics and Photonics*, vol. 2, no. 1, pp. 1–59, 2010.

[12] A. Yeniay, J. M. Delavaux, and J. Toulouse, "Spontaneous and stimulated Brillouin scattering gain spectra in optical fibers", *Journal of Lightwave Technology*, vol. 20, no. 8, pp. 1425, 2002.

[13] A. Boucon, D. Alasia, J. Beugnot, G. Mélin, S. Lempereur, A. Fleureau, H. Maillotte, J. M. Dudley, and T. Sylvestre, "Supercontinuum generation from 1.35 to 1.7 μm by nanosecond pumping near the second zerodispersion wavelength of a microstructured fiber", *IEEE Photonics Technology Letters*, vol. 20, no. 10, pp. 842 – 844, 2008.

[14] J.-C. Beugnot, *La diffusion Brillouin dans les fibres optiques microstructurées*, PhD thesis, Université de Franche-Comté, 2007.

[15] R. W. Boyd, K. Rzazewski, and P. Narum, "Noise initiation of stimulated Brillouin scattering", *Physical Review A*, vol. 42, no. 9, pp. 5514–5521, 1990.

[16] R. G. Smith, "Optical power handling capacity of low loss optical fibers as determined by stimulated Raman and Brillouin scattering", *Applied Optics*, vol. 11, no. 11, pp. 2489–2494, 1972.

[17] I. H. Malitson, "Interspecimen comparison of the refractive index of fused silica", *J. Opt. Soc. Am.*, vol. 55, no. 11, pp. 1205–1208, 1965.

[18] S. Foaleng Mafang, F. Rodriguez-Barrios, S. Martin-Lopez, M. Gonzalez-Herraez, and L. Thévenaz, "Detrimental effect of self-phase modulation on the performance of Brillouin distributed fiber sensors", *Optics Letters*, vol. 36, no. 2, pp. 97, 2011.

[19] L. Thévenaz, S. M. Foaleng, and M. Niklès, "Fast measurement of local PMD with high spatial resolution using stimulated Brillouin scattering", in *Proceedings of the 33rd European Conference on Optical Communication ECOC'2007, Berlin, Germany*, 2007.

[20] J. C. Beugnot, B. Stiller, S. Foaleng Mafang, M. W. Lee, M. Delqué, A. Kudlinski, H. Maillotte, V. Laude, L. Thévenaz, and T. Sylvestre, "Experimental observation of Brillouin linewidth broadening and decay time in photonic crystal fiber", in *European Conference on Optical Communications ECOC, September 21-25, Torino, Italy*, 2010, Tu.4.D.S.

[21] B. Stiller, J. C. Beugnot, S. Foaleng Mafang, M. W. Lee, M. Delqué, A. Kudlinski, H. Maillotte, V. Laude, L. Thévenaz, and T.Sylvestre, "Observation of Brillouin linewidth broadening and decay time in photonic crystal fiber", in *Proceedings IEEE Photonics Society Summer Topical Meeting Series,*, 2010, pp. 168–169.

[22] L. Thévénaz, Ed., *Advanced Fiber Optics, Concepts and Technology*, EPFL Press, 2011.

[23] X. Bao, A. Brown, M. DeMerchant, and J. Smith, "Characterization of the Brillouin loss spectrum of single-mode fibres by use of very short (10-ns) pulses", *Optics Letters*, vol. 24, no. 8, pp. 510–512, 1999.

[24] L. Zou, X. Bao, Y. Wan, and L. Chen, "Coherent probe-pump-based Brillouin sensor for centimeter-crack detection", *Optics Letters*, vol. 30, no. 4, pp. 370–372, 2005.

[25] A. W. Brown and B. G. Colpitts, "Dark-pulse Brillouin optical time-domain sensor with 20-mm spatial resolution", *Journal of Lightwave Technology*, vol. 25, no. 1, pp. 381–386, 2007.

[26] L. Thévenaz, "Brillouin distributed time-domain sensing in optical fibers: state of the art and perspectives", *Frontiers in Optoelectronics China*, vol. 3, no. 1, pp. 13–21, 2010.

[27] S. Foaleng Mafang, J.-C. Beugnot, and L. Thévenaz, "Optimized configurarion for high resolution distributed sensing using Brillouin echoes", in *Proceedings SPIE, UK, Edinburgh*, 2009, p. 75032C.

[28] M. W. Lee, B. Stiller, J. Hauden, H. Maillotte, C. Roch, L. Thévenaz, and T. Sylvestre, "Differential phase-shift keying technique-based Brillouin echo-distributed sensing", *IEEE Photonics Technology Letters*, vol. 24, no. 1, pp. 79–81, 2012.

[29] G. Charlet, "Progress in optical modulation formats for high-bit rate wdm transmissions", *IEEE J. Quantum Electron.*, vol. 12, pp. 469–483, 2006.

[30] Y. J. Wen, A. Nirmalathas, and D.-S. Lee, "RZ/CSRZ-DPSK and chirped NRZ signal generation using a single-stage dual-electrode Mach-Zehnder modulator", *IEEE Photonics Technology Letters*, vol. 16, no. 11, pp. 2466–2468, 2004.

[31] T. Kurashima, T. Horiguchi, and M. Tateda, "Distributed-temperature sensing using stimulated Brillouin scattering in optical silica fibers", *Optics Letters*, vol. 15, no. 18, pp. 1038–1040, 1990.

[32] X. Bao, D. J. Webb, and D. A. Jackson, "22-km distributed temperature sensor using Brillouin gain in an optical fiber", *Optics Letters*, vol. 18, no. 7, pp. 552–554, 1993.

[33] A. Loayssa, R. Hernández, D. Benito, and S. Galech, "Characterization of stimulated Brillouin scattering spectra by use of optical single-sideband modulation", *Optics Letters*, vol. 29, no. 6, pp. 638–640, 2004.

[34] K.-Y. Song and K. Hotate, "Enlargement of measurement range in a Brillouin optical correlation domain analysis system using double lock-in amplifiers and a single-sideband modulator", *IEEE Photonics Technology Letters*, vol. 18, no. 3, pp. 499–501, 2006.

[35] K. Y. Song and H. J. Yoon, "High-resolution Brillouin optical time domain analysis based on brillouin dynamic grating", *Optics Letters*, vol. 35, no. 1, pp. 52–54, 2010.

[36] L. Zou, X. Bao, S. Yang, L. Chen, and F. Ravet, "Effect of Brillouin slow light on distributed Brillouin fiber sensors", *Optics Letters*, vol. 31, no. 18, pp. 2698–2700, 2006.

[37] J. M. S. Domingo, J. Pelayo, F. Villuendas, C. D. Heras, and E. Pellejer, "Very high resolution optical spectrometry by stimulated brillouin scattering", *IEEE Photonics Technology Letters*, vol. 17, no. 4, pp. 855 – 857, 2005.

[38] L. Zou, X. Bao, S. Afshar V., and L. Chen, "Dependence of the Brillouin frequency shift on strain and temperature in photonic crystal fiber", *Optics Letters*, vol. 29, no. 13, pp. 1485, 2004.

[39] E. Carry, J.-C. Beugnot, B. Stiller, M. W. Lee, H. Maillotte, and T. Sylvestre, "Temperature coefficient of the high-frequency guided acoustic mode in a photonic crystal fiber", *Applied Optics*, 2011, accepted.

[40] M. Karlsson, "Four-wave mixing in fibers with randomly varying zero-dispersion wavelength", *J. Opt. Soc. Am. B*, vol. 15, no. 8, pp. 2269–2275, 1998.

[41] L. Zou, X. Bao, and L. Chen, "Distributed Brillouin temperature sensing in photonic crystal fiber", *Smart Materials and Structures*, vol. 14, no. 3, pp. S8, 2005.

[42] P. Dainese, P. St. J. Russell, N. Joly, J. C. Knight, G. S. Wiederhecker, H. L. Fragnito, V. Laude, and A. Khelif, "Stimulated Brillouin scattering from multi-GHz-guided acoustic phonons in nanostructured photonic crystal fibres", *Nature Physics*, vol. 2, no. 6, pp. 388–392, 2006.

[43] A. Minardo, R. Bernini, W. Urbanczyk, J. Wojcik, N. Gorbatov, M. Tur, and L. Zeni, "Stimulated Brillouin scattering in highly birefringent microstructure fiber: experimental analysis", *Optics Letters*, vol. 33, no. 20, pp. 2329–2331, 2008.

[44] A. Yeniay, J. M. Delavaux, and J. Toulouse, "Spontaneous and Stimulated Brillouin Scattering Gain Spectra in Optical Fibers", *Journal of Lightwave Technology*, vol. 20, no. 8, pp. 1425, 2002.

[45] S. Le Floch and P. Cambon, "Study of Brillouin gain spectrum in standard single-mode optical fiber at low temperatures (1.4-370 K) and high hydrostatic pressures (1-250 bars)", *Optics Communications*, vol. 219, pp. 395–410, 2003.

[46] F. Poletti, K. Furusawa, Z. Yusoff, N. G. Broderick, and D. J. Richardson, "Non-linear tapered holey fibers with high stimulated Brillouin scattering threshold and controlled dispersion", *J. Opt. Soc. Am. B*, vol. 24, no. 9, pp. 2185–2194, 2007.

[47] *Crystal Fibres*, Characteristics of product, http://www.nktphotonics.com/files/files/NL-24-800.pdf.

[48] T. G. Euser, J. S. Y. Chen, M. Scharrer, P. St. J. Russell, N. J. Farrer, and P. J. Sadler, "Quantitative broadband chemical sensing in air-suspended solid-core fibers", *Journal of Applied Physics*, vol. 103, pp. 103108, 2008.

[49] L. Thevenaz and J.-C. Beugnot, "General analytical model for distributed Brillouin sensors with sub-meter spatial resolution", in *20th International Conference on Optical Fibre Sensors, Edinburgh, United Kingdom*, 2009.

[50] J. E. McElhenny, R. K. Pattnaik, J. Toulouse, K. Saitoh, and M. Koshiba, "Unique characteristic features of stimulated Brillouin scattering in small-core photonic crystal fibers", *J. Opt. Soc. Am. B*, vol. 25, no. 4, pp. 582–593, 2008.

[51] C. G. Carlson, R. B. Ross, J. M. Schafer, J. B. Spring, and B. G. Ward, "Full vectorial analysis of Brillouin gain in random acoustically microstructured photonic crystal fibers", *Phys. Rev. B*, vol. 83, pp. 235110, 2011.

Chapter 4

SBS mitigation in PCF with periodically varying micro-structure

In recent years, there have been active efforts to suppress stimulated Brillouin scattering (SBS) in optical fibers as it is detrimental to nonlinear optical processing fiber technologies and high-power narrow-linewidth fiber lasers. In order to increase the Brillouin threshold several passive and active methods have been demonstrated. Among active methods phase-modulation with different profiles have been shown, for example pseudo-random or duobinary phase pulse orders [1], which leads to spectral broadening of the pump wave. A method called frequency dithering is also supposed to enlarge the Brillouin gain spectrum by changing very fast the pump frequency [2]. A. Mussot *et al.* [3] proposed to use XPM for the phase modulation of a CW pump avoiding the use of electro-optical modulators. The advantage of active methods is the efficiency of Brillouin suppression but on the other hand it modifies the coherence of the pump wave and leads to a spectral broadening. To avoid changing the optical properties of the pump wave several passive methods have been proposed. Recently it has been reported about reducing the opto-acoustic overlap [4,5] by doping the fiber core or using multi-core fibers [6]. The use of hollow optical fiber helps for controlling the Brillouin frequency shift (BFS) [7] and a special photonic-phononic bandgap structure inhibits acoustic modes in the optical core [8]. SBS mitigation has also been proposed using photonic crystal fibers (PCFs) due to their ability to reduce the acousto-optic overlap or widen the Brillouin gain spectrum [9]. Nevertheless many methods are based on varying the Brillouin frequency shift along the fiber. This can be achieved by applying a strain or temperature distribution along the fiber length [10–12] as well as continuously changing properties of the micro-structure like the core diameter [13] or random distributed acoustic indices by varying parts of the air-hole-structure [9]. Shiraki *et al.* also studied the effect of longitudinal variation of the Brillouin frequency shift (BFS) [14] which has more recently also suggested by Poletti *et al.* [15] to increase the

SBS threshold through longitudinal variations of the structural parameters of a PCF.

In this chapter, PCFs with periodically-varied core diameter are studied experimentally and theoretically in view of suppressing SBS. These fibers have been designed and fabricated at the institute IRCICA, Université Lille 1. First an enhanced theoretical approach to calculate the critical pump power for the Brillouin threshold is introduced, based on Ref. [16]. In a theoretical parameter study the dependence on fiber length, linear loss, EMA and other used variables for a uniform fiber are studied and later different BFS variation profiles are investigated to increase the Brillouin threshold theoretically. In a second part the fibers under test are presented and then investigated in chapter 4.3 in terms of Brillouin gain, Brillouin threshold and distributed Brillouin measurement. By varying sinusoidally 7-14 % of the air-hole micro-structure over a period of 30 m, the Brillouin frequency shift (BFS) changes significantly and the Brillouin gain spectrum (BGS) broadens, which has been proposed in [13, 15]. This results in increasing the SBS threshold, compared to uniform fibers with an invariant core. The properties of these core-diameter varied PCFs are described and characterized by measuring the SBS threshold and the BGS linewidth. We performed a distributed measurement of the oscillating BFS using BEDS-technique and estimated the corresponding effective refractive index variations from scanning electron microscopy (SEM) images, which is in very good agreement with outer diameter variations. The measured SBS threshold is compared to theoretical and experimental results for uniform PCFs with the same air-hole structure but with no periodical variation of the structure dimension.

4.1 Theoretical approach

As we have introduced in paragraph 2.2.1.4, a critical pump power for the Brillouin threshold can be defined where the power of the backscattered wave begins to grow exponentially and is no more only due to noise. The critical power P_{Cr} for the Brillouin threshold is commonly defined as the input power where the power of the backscattered Stokes waves equals a certain fraction μ of the input power [16]: $P_{\mathrm{Cr}} = P_{\mathrm{in}}$ if

$$P_{\mathrm{Stokes}} = \mu \cdot P_{\mathrm{in}}. \tag{4.1}$$

Different values for μ are used, for example μ=1 [17,18] and μ=0.01 [19,20]. Hereafter, we will use μ=0.01. Per definition, for μ=1 the threshold is later reached and the backscattered power is already significant. The critical power for the Brillouin threshold can be solved by using the coupled differential equations, as derived in chapter 2.2.1, which results in Eq.(2.38) that is repeated here for completeness:

$$P_{\mathrm{cr}} = \frac{C \cdot K \cdot A_{\mathrm{eff}}}{g_B \cdot L_{\mathrm{eff}}}. \tag{4.2}$$

A_{eff} is the effective mode area (EMA), L_{eff} the effective length, C a constant and g_B the Brillouin gain, which can be determined by measuring the full width at half maximum (FWHM) in the spontaneous Brillouin regime and formula (2.36). K=3/2 is a factor that accounts for random polarization evolution in the PCF. C can be derived by approximating the SBS gain with asymptotic expansions of the modified Bessel functions [16] and depends amongst others on the fiber parameters, the BFS, the BGS and the 1% pump power fraction. Within a certain fiber length limit ($L \approx 40\,\text{km}$, $\alpha \approx 0.2\,\text{dB/km}$) the numerical factor can be calculated as [16]:

$$C = \psi \left(1 + \frac{3/2 \cdot ln(\psi)}{\psi - 3/2}\right), \tag{4.3}$$

where

$$\psi = -\ln\left[\frac{2\sqrt{\pi}\gamma\theta}{\mu\alpha} \cdot \exp^{-\alpha L}(1 - \exp^{-\alpha L})\right], \tag{4.4}$$

with

$$\theta = \frac{kT\Delta\nu_B c}{2\lambda_P \nu_B} \tag{4.5}$$

and

$$\gamma = \frac{g_B}{A_{\text{eff}} \cdot K}. \tag{4.6}$$

The Boltzmann constant k is $1.3806503 \cdot 10^{-23}\,JK^{-1}$ and T is the temperature, thus T=293.15 K. For a silica PCF with a Brillouin linewidth $\Delta\nu_B = 54\,\text{MHz}$, we have calculated $g_B = 1.30 \cdot 10^{-11}\,mW^{-1}$. With $L_{\text{eff}} = 244.2\,\text{m}$, $A_{\text{eff}} = 22.63\,\mu\text{m}^2$ and the other values for the variable constants that are listed in table (4.1), we obtain $C = 14.3$, which is different from the often used constant 21 as in [18]. This factor can be found in many publications and was firstly derived by Smith in 1972 [17]. This approximative factor considers high fiber loss (20 dB/km) and uses the definition μ=1. Calculating C with $L = 200\,\text{m}$, α =20 dB/km, $A_{\text{eff}} = 50\,\mu\text{m}^2$, $\Delta\nu_B = 28\,\text{MHz}$, $\nu_B = 10.85\,\text{GHz}$ and μ=1 leads to $C = 21.2$ which is close to 21. Other authors [20–22] also suggest smaller numerical values, depending on the effective fiber length.

Eq.(4.2) for the Brillouin threshold is valid for uniform fibers having a constant BFS. Taking into account the varying BFS, Eq.(4.2) must be modified. The term $g_B L_{\text{eff}}$ in Eq.(4.2) is then replaced by the following integral [14, 15]:

$$G(\nu) = \int_0^L g_B(\nu, z) \exp^{-\alpha z}\, dz, \tag{4.7}$$

where

$$g_B(\nu, z) = g_B \frac{(\Delta\nu_B/2)^2}{(\nu - \nu_B(z))^2 + (\Delta\nu_B/2)^2}. \tag{4.8}$$

If ν_B is constant along the fiber, we retrieve:

$$G(\nu) = g_B L_{\text{eff}} \tag{4.9}$$

With varying BFS along the fiber the critical input power can be rewritten as:

$$P_{\mathrm{cr}} = \frac{C \cdot K \cdot A_{\mathrm{eff}}}{G(\nu_{max})}, \tag{4.10}$$

where ν_{max} is the maximum of the resulting along the fiber integrated Brillouin gain spectrum.
From former equations we can clearly draw the conclusion, that the critical pump power P_{cr} rises with a higher EMA A_{eff}, a broader BGS (because this results in a lower Brillouin gain g_B) and a shorter effective fiber length. Moreover a varying BFS leads to a higher Brillouin threshold considering Eq.(4.7). A deeper insight about the dependence on the different parameters will be studied in the next paragraph.

4.1.1 Variation of several fiber characteristics

In this paragraph the effect of several fiber characteristics on the numerical factor C and the critical pump power P_{cr} is studied. The initial values are listed in table (4.1) and they originate from a PCF (see table (4.3), fiber V3) that will be discussed later.

Table 4.1: Parameters used in Eq.(4.3) and (4.2)

Parameter	**Value**
Temperature T	293.15 K
Boltzmann constant k	$1.3806503 \cdot 10^{-23} \frac{m^2 \cdot kg}{s^2 \cdot K}$
Density ρ	$2.21 \cdot 10^3 kg/m^2$
Acoustic velocity V_A	5960 m/s
Electrostrictive constant p_{12}	0.285
Pump wavelength λ_P	1.55 µm
Birefringence factor K	3/2
BFS ν_B	11.0882 GHz
FWHM of BGS $\Delta\nu_B$	54 MHz
Eff. refr. index n_{eff}	1.444
EMA A_{eff}	22.63 µm^2
Fiber loss α	7.7 dB/km
Fiber length L	320 m
Resulting L_{eff}	244.5 m

Using Eq.(4.3) and Eq.(2.38) P_{cr} and C are plotted in Fig.(4.1) for variable values of the effective mode area A_{eff} , the Brillouin frequency shift *BFS*, the FWHM of the Brillouin gain spectrum, the pump wavelength λ_P, the fiber length L , the fiber loss α,

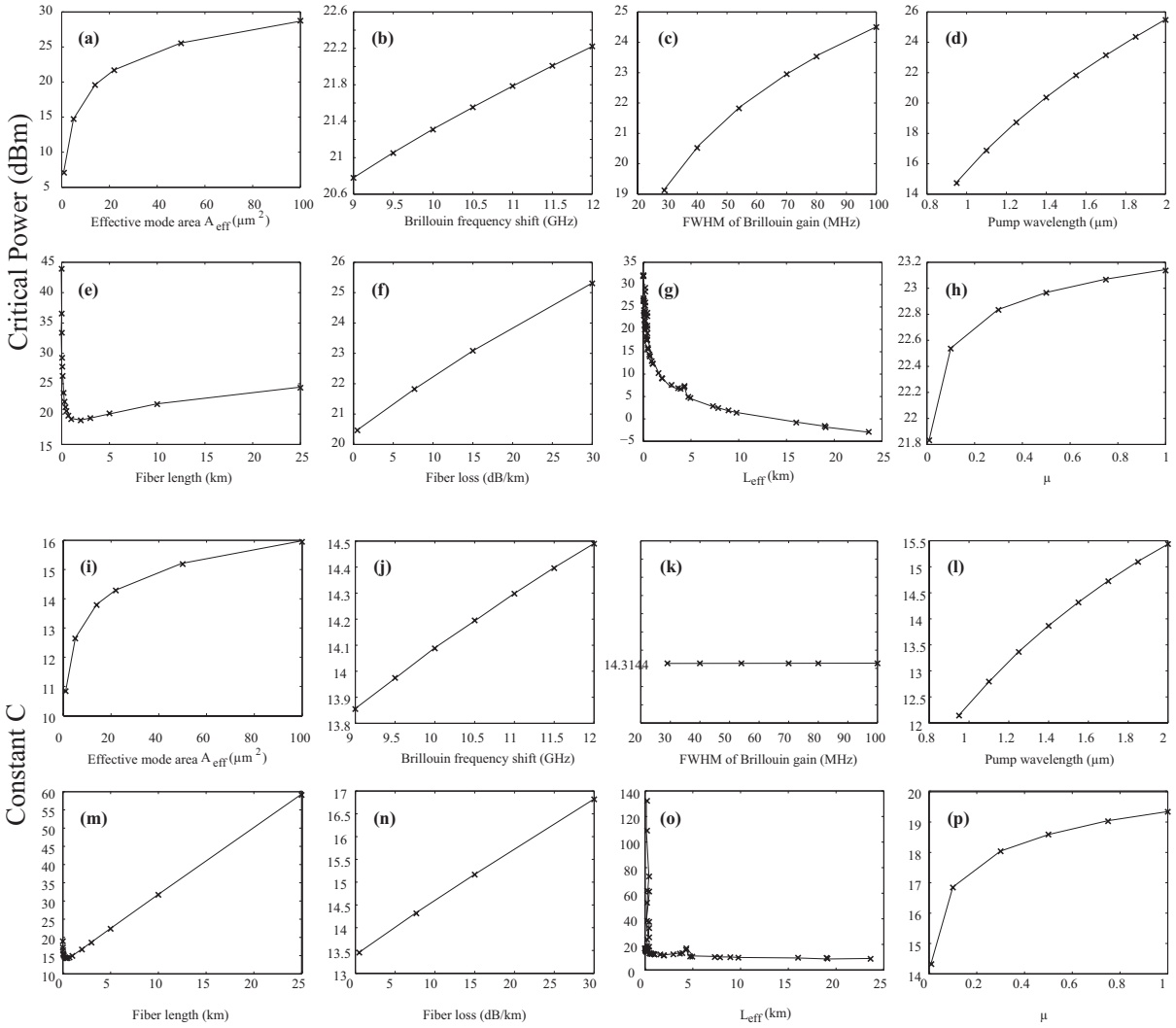

Figure 4.1: Critical pump power P_{cr} and Numerical factor C, versus (a,i) effective mode area, (b,j) Brillouin frequency shift, (c,k) FWHM of the Brillouin gain, (d,l) pump wavelength, (e,m) fiber length, (f,n) fiber loss, (g,o) effective length, (h,p) threshold definition.

the effective length L_{eff} and the threshold definition μ. As mentioned in the previous paragraph, Eq.(4.3) is valuable within a certain limit of the effective fiber length. As it can be seen in Fig.(4.1 g,o), C and P_{cr} exhibit a change at about 5 km which can be interpreted as a limit as the effective length tends to $1/\alpha_{\text{lin}}$ for long fiber lengths but the values for P_{cr} are still physically reasonable. This is no more the case for the dependence on the fiber length, seen in Fig.(4.1 e,m). Normally with increasing fiber length, the Brillouin threshold has to decrease according to Eq.(4.2). However, we see that above 5 km the Brillouin threshold starts to rise again which is unphysical. This is due to the estimation of the numerical factor Eq.(4.3). It must be noticed that the linear loss was fixed at 7 dB/km for a PCF, which is rather high. Hence, the 5 km limit is not generally valuable, especially not for SMF which have a linear attenuation of about 0.2 dB/km.

From Fig.(4.1), we can see that the Brillouin threshold can be increased with a higher pump wavelength and BFS. Besides it is well known, that the broadening of the BGS leads to an increase in Brillouin threshold. The numerical factor does not depend on the Brillouin linewidth. In this paragraph the material parameters of a fiber have been changed theoretically but the BFS was kept constant along the fiber. Based on Eq.(4.7) this will be the topic of the next paragraph.

4.1.2 Longitudinal variation of the Brillouin frequency shift

The previous numerical study has been carried out for uniform fibers. Now we fix the values as in table (4.1) and analyze the critical pump power for different distributions of the BFS. The numerical factor C is not shown because it almost does not change dependant on the different BFS profiles. Five BFS profiles have been tested: an linear increase of the BFS and ramp, triangle, sine and square BFS distributions with variable periods and amplitude of the BFS variation. The profiles of the BFS and the distributed BGS along the fiber is depicted in Fig.(4.2) according to Ref. [14]. For the latter the attenuation has been taken into account. First we set the period to 30 m and have a look on the amplitude of the periodic BFS variation (Fig.(4.3)). The amplitude is varied from 0 to 700 MHz and a zoom on 0-100 MHz is shown in Fig.(4.3 a). For high variation amplitudes we observe a saturation for the square-distribution. The saturation begins where both Lorentzian curves have less and less overlap, thus two times the Brillouin linewidth, $2 \cdot 54\,\mathrm{MHz} = 108\,\mathrm{MHz}$. The other curves increase square-root-like and reache saturation for higher values, for example the sinusoidal distribution upon 3 GHz variation at about 33 dBm and the triangle and linear distribution upon 5 GHz at about 40 dBm. The critical pump power rises the most for the triangular and ramp distribution, thus for high BFS variations, these shapes should be used. Since BFS variation are normally in shorter scale we have to focus on the first picture, the zoom to 0-100 MHz, Fig.(4.3 a). In this plot we observe that the square shaped distribution has a higher influence on the increasing Brillouin threshold at the same variation amplitude than the other distributions. But also the sinusoidal one sets itself apart from the linear, ramp and triangle distribution. In the low amplitude region, it seems to be crucial that the BFS changes abruptly and stays as long as possible at the minimum and maximum of the BFS distribution as it is the case for the squared distribution. The gradient of the increasing BFS does not play a decisive role because the difference between the linear, the triangle and the ramp distribution is very small. In a second step the amplitude of the periodic variation is fixed at 20 MHz and the period is varied from 0 to 100 m (Fig.(4.4)). We observe again that the square-shaped distribution has the most influence since we fixed the amplitude to 20 MHz which is in the low region of Fig.(4.3). The same observation as previously can be done for the other distributions: the triangular, ramp and linear distribution have almost the same and less

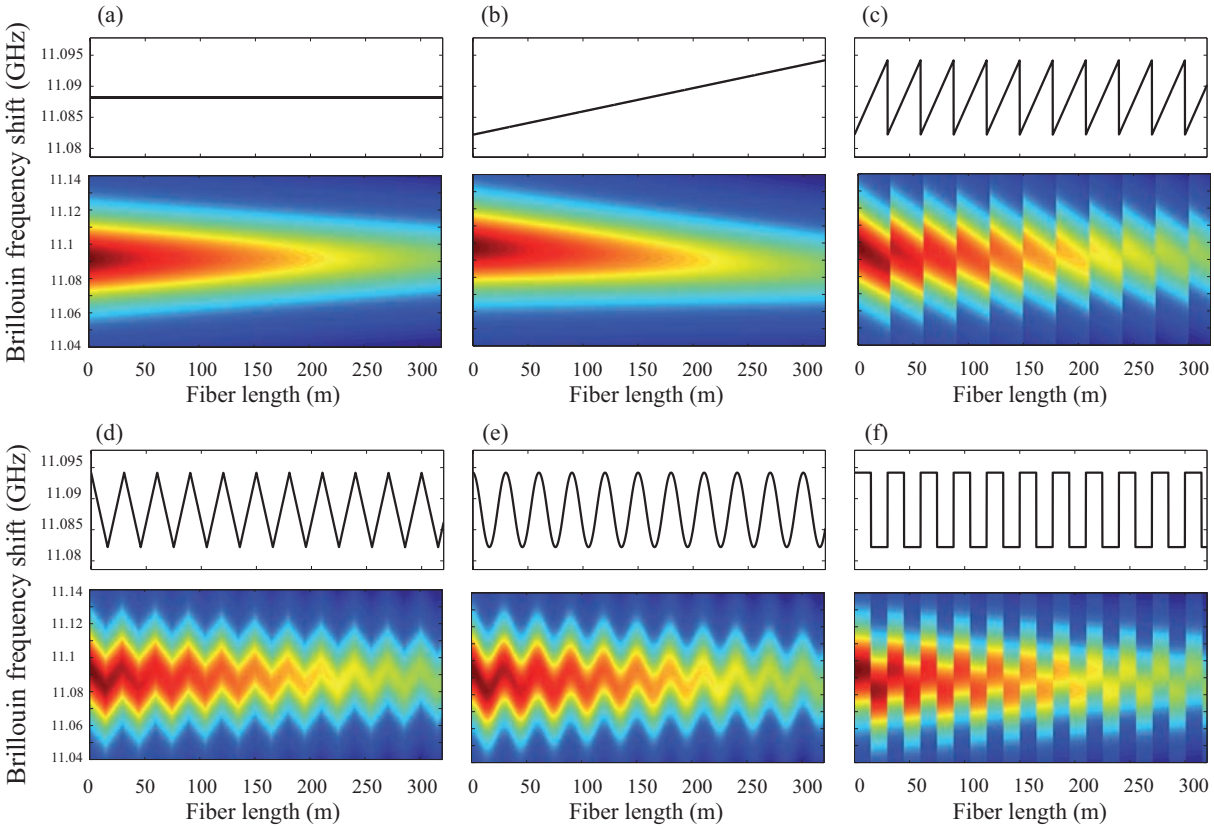

Figure 4.2: Different Brillouin frequency shift distributions and mappings of the Brillouin gain spectrum with 54 MHz FWHM: (a) uniform, (b) linear increase, (c) ramps, (d) triangle shape, (e) sine shape, (f) square shape with 30 m period and 12 MHz amplitude, respectively.

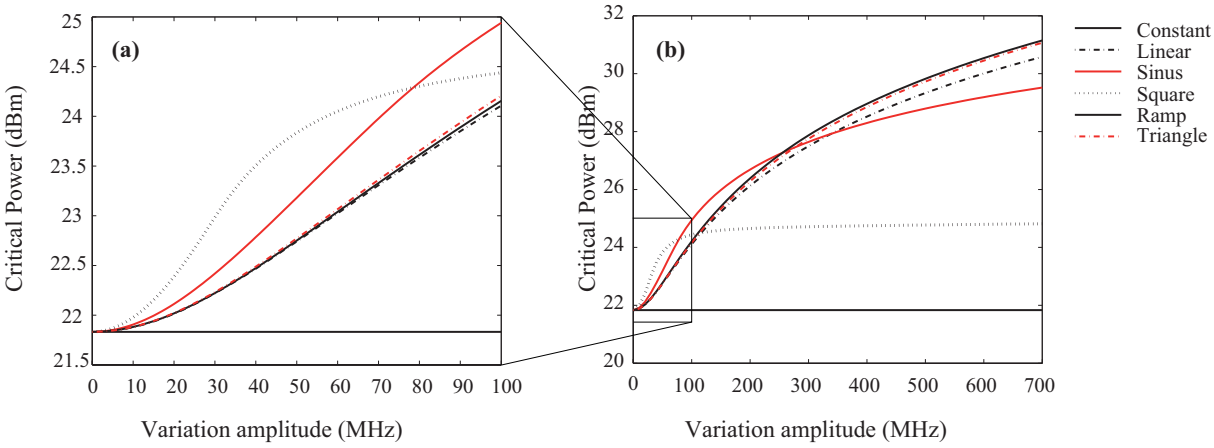

Figure 4.3: Critical pump power in function of the variation amplitude (a) 0 to 100 MHz, (b) 0 to 700 MHz, for different distributions of the Brillouin frequency shift. The period is fixed at 30 m.

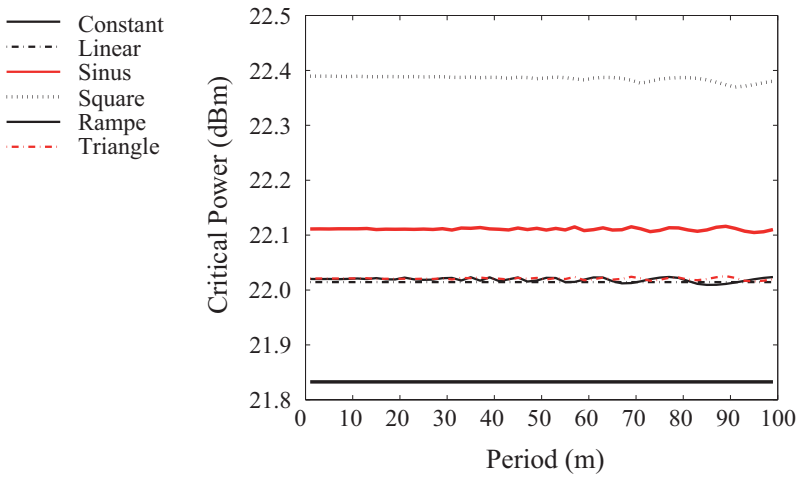

Figure 4.4: Critical pump power as a function of the variation period (0 to 100 m) for different distributions of the Brillouin frequency shift. The variation amplitude is fixed to 20 MHz

effect on the threshold increase as the sinusoidal one. But we focus on the dependency of the variation period. Except for slight fluctuation that are more pronounced for larger periods, no significant dependence of the variation period on the Brillouin threshold can be found. The reason for the randomly varying values is probably the fact that in Eq.(4.3) θ and γ depend on the BFS ν_B (Eq.(4.5) and Eq.(4.6)). This is taken into account in the numerical calculation and C was obtained by taking the mean value. This may induce numerical noise which is in a negligible order of magnitude.
To conclude it would be interesting to study PCFs with periodically varying micro structure with a sine or squared profile with an as high as possible variation amplitude. The influence of the period on the threshold increase should not be that significant, it induces more linear losses. In the following paragraphs, several fibers with a sine BFS distribution will be investigated by Brillouin gain, threshold and distributed BGS measurement.

4.2 The micro-structured optical fibers under test

For the sake of comparison five different PCFs have been investigated. Two of them have an uniform structure along the fiber, whereas the other three fibers are drawn by inducing a periodical varying outer diameter which induces size variation of the micro-structure. The uniform fibers are called U1 and U2, as indicated in table (4.2), and the other three fibers with periodic variation of 7% and 14% are named with V1, V2 and V3 respectively (table (4.3)). The difference in longitudinal size variation was induced

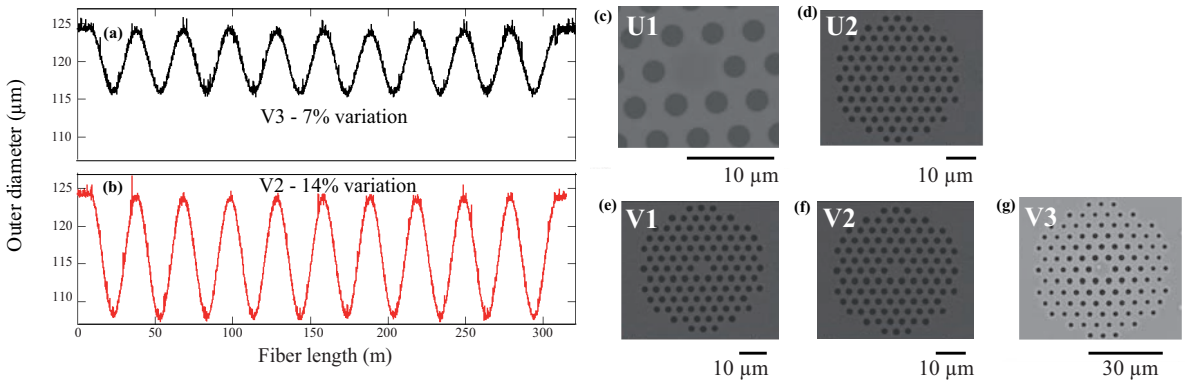

Figure 4.5: (a,b) Outer diameter along the fiber length for the PCFs with varying structure size: 7% varying (a) and 14% (b), (c-d) SEM image at the maximum outer diameter (125 µm) of the uniform PCFs, (e-g) SEM image at the maximum outer diameter (125 µm) of the PCFs with varying structure size.

during the fiber drawing process. The PCFs with the periodically varying micro-structure have been drawn directly on a fiber tower by varying velocity and pressure during the drawing process. Fig.(4.5 a) shows the evolution of their outer diameters as a function of length, measured during the drawing stage. It closely follows a sine evolution over 320 m and 325 m with a period of 30 m and a modulation amplitude rate of 7 % and 14 %(outer diameter variations from 116 to 125 µm (V1 and V3) and 107 to 125 µm (V2)). For the uniform fibers U1 and U2 the outer diameter is constantly 125 µm. Figs.(4.5 c-g) show the scanning electron microscope (SEM) images of the input cross-section for the largest outer diameter (125 µm) for all fibers. They all exhibit nearly the same hexagonal air-hole micro-structure and core diameters, varying from 5.6 to 6.4µm. For fiber V3 the holes of the two first rows around the core have a diameter of 1.8 µm which becomes smaller for the outer rows due to deformations during the cane drawing process. The lattice pitch Λ is nearly constant across the whole structure for all fibers and equal to 3.9 µm(U2, V1 and V2) 4.1 µm (V3) and 4.4 µm (U1). For the varying fibers drawing parameters were adjusted so that outer diameter variations only modify the pitch Λ and keep the d/Λ ratio approximately constant all along the fiber length. The linear attenuation is different for each fibers which is due to fiber coiling and fluctuations during the drawing process. The fiber loss at 1.55 µm, estimated experimentally, varies from 7.7 dB/km (V3) to 14.2 dB/km (U2). All other parameters of all PCFs under test can be taken from tables (4.2) and (4.3).

Using the commercial finite element method solver COMSOL, we have calculated for one fiber, fiber V3, based on the SEM image zero-dispersion wavelength (ZDW) variations from 1.07 µm to 1.095 µm. The corresponding group-velocity dispersion (GVD) parameter D at the operating wavelength of 1.55 µm slightly shifts from 48.5 to 53.0 ps/nm/km, which is reasonable for practical applications.

Table 4.2: Fiber parameters for the uniform fibers

Parameter	**Fiber U1**	**Fiber U2**
Length L	350 m	314 m
Linear fiber loss α (1.55 µm)	14 dB/km	14.2 dB/km
Resulting L_{eff}	207.6 m	195.5 m
Description	uniform	uniform
Core diameter	6.2 µm	5.6 µm
Pitch Λ	4.4 µm	3.9 µm
Hole diameter d/Λ	0.54	0.51
EMA A_{eff}	22.3 µm^2	19.7 µm^2

Table 4.3: Fiber parameters for the fibers with varying micro-structure size

Parameter	**Fiber V1**	**Fiber V2**	**Fiber V3**
Length L	320 m	325 m	320 m
Linear fiber loss α (1.55 µm)	10.3 dB/km	9.3 dB/km	7.7 dB/km
Resulting L_{eff}	223.4 m	235.6 m	244.5 m
Description	7% variation	14% variation	7% variation
Core diameter	5.6 µm	5.6 µm	6.4 µm
Pitch Λ	3.9 µm	3.9 µm	4.1 µm
Hole diameter d/Λ	0.51	0.51	0.44
EMA A_{eff}	19.7 µm^2	19.7 µm^2	22.6 µm^2

4.3 Brillouin gain spectrum measurement

4.3.1 Self-heterodyne Brillouin measurement

First the measurement of the BGS has been performed to obtain the Brillouin linewidth FWHM and the BFS. A standard heterodyne detection technique has been used where the back-scattered Brillouin signal beats with the input one [23], as explained in chapter 3.1.1. Figs.(4.6 a-l) show the FWHM of the BGS with variable input power and the BGS at 9 dBm, 12 dBm, and 15 dBm. The different input power values have been taken because the spectrum was too noisy below these values. For fibers U2, V1, V2 and V3 the FWHM in the lower regime (5 dBm) reaches an average of 58 MHz, 58 MHz, 60 MHz and 54 MHz SBS linewidth. It might be surprising that the FWHM is about the same for the longitudinally varied and uniform fibers but the Brillouin power rises significantly just in the last 1/10 - part of the fiber length, as found in Ref. [24] (p.35). As the fibers under test have a length of about 300m, the Brillouin spectrum is mostly influenced by the last 30 m-part which represents only one variation period as the former is 30 m. This might

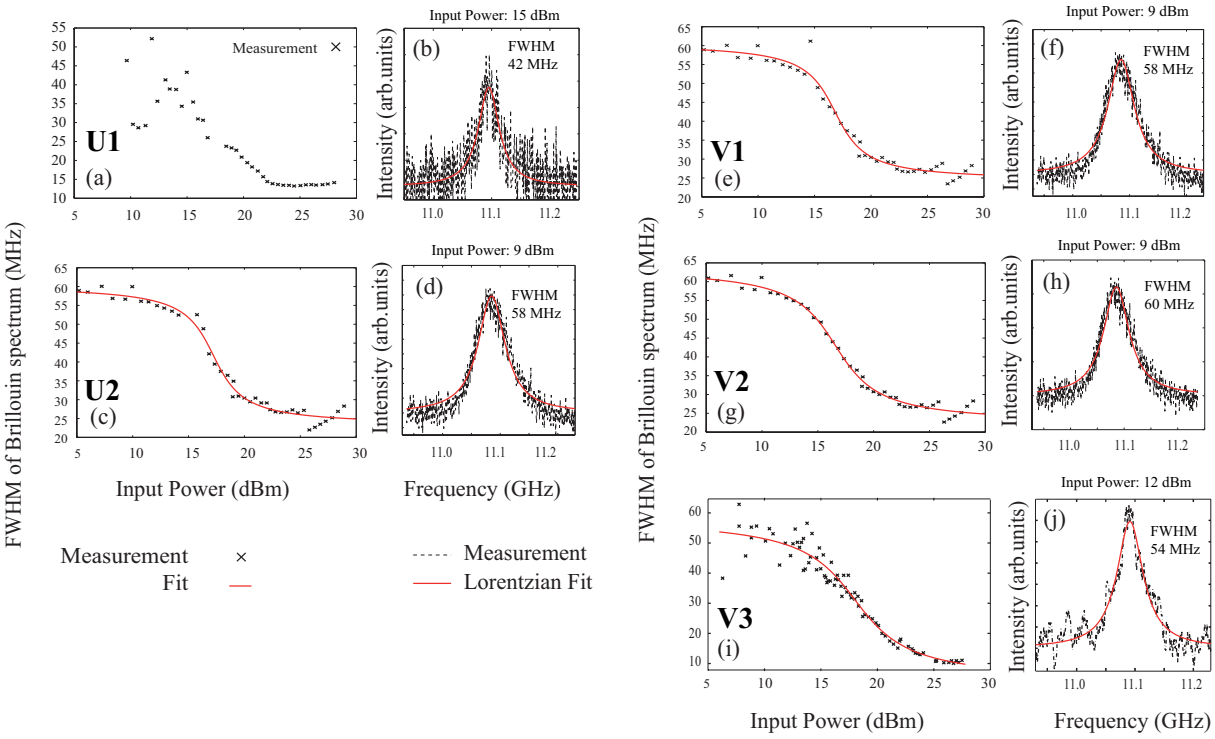

Figure 4.6: Brillouin gain spectrum (FWHM) with increasing input power for fibers (a) U1 (c) U2 (e) V1 (g) V2 (i) V3 , Brillouin gain spectrum below the critical pump power for fibers (b) U1 (d) U2 (f) V1 (h) V2 (j) V3

be the reason that the Brillouin spectrum is not broaden for the longitudinally varied fibers in comparison to the uniform fibers. For fiber U1 the spectra were noisy in the low power region (Fig.(4.6 c)), so that it was not possible to estimate properly the FWHM. Nevertheless, we can assume that the FWHM is about 60 MHz since the canes and the drawing process were identical with those from fiber U2, V1 and V2. The difficulties in measurement come probably from the splicing loss. As can be seen, the SBS linewidth in the stimulated regime narrows to 10-20 MHz near the threshold power. The FWHM in the low power regime indicates a strong spectral broadening of the BGS compared to the standard value for single-mode fiber (SMF) below threshold (FWHM $\Delta\nu_B = 29$ MHz, measured in an SMF). This effect has already been reported in other PCFs as resulting from the impact of air-hole micro-structure on the acoustic waves distribution [25]. It leads to a significant reduction of the Brillouin gain and to the inhomogeneous spectral broadening of the BGS.

Assuming the values for the FWHM $\Delta\nu_B$, we can estimate g_B by help of formula (2.36). The results for the different fibers have been listed in table (4.4) and (4.5) and can be used to calculate the theoretical threshold when we include the following distributed measurements.

Table 4.4: Measured Brillouin linewidth and calculated Brillouin gain g_B for the uniform fibers

Parameter	**Fiber U1**	**Fiber U2**
Brillouin linewidth $\Delta\nu_B$ (MHz)	60	58
Brillouin gain g_B (mW^{-1})	$1.17 \cdot 10^{-11}$	$1.22 \cdot 10^{-11}$

Table 4.5: Measured Brillouin linewidth and calculated Brillouin gain g_B for the fibers with varying micro-structure size

Parameter	**Fiber V1**	**Fiber V2**	**Fiber V3**
Brillouin linewidth $\Delta\nu_B(MHz)$	58	60	54
Brillouin gain g_B (mW^{-1})	$1.22 \cdot 10^{-11}$	$1.17 \cdot 10^{-11}$	$1.30 \cdot 10^{-11}$

4.3.2 Distributed BEDS measurement

The Brillouin threshold depends on different BFS distributions due to core diameter and effective refractive index variations as discussed in paragraph 4.1. In order to verify this fact we have performed a distributed measurement of the BFS by use of the BEDS technique that provides a high spatial resolution without spectral broadening. The experimental setup is sketched in Fig.(3.16) and a detailed description can be found in chapter 2 and Ref. [26, 27]. All measurements have been performed with a 3ns-long π-phase pulse which results in 30 cm spatial resolution. The Brillouin gain is scanned by the intensity modulator around the BFS with 1 MHz resolution so that all variations can be detected along the fiber. Fig.(4.7) shows the color plots of the fitted BEDS traces and the retrieved BFS along the propagation distance for each fiber. The fluctuations in BFS of fiber U1 are confirmed by inverting the fiber, as obvious in Fig.(4.7 b). Fiber U2 exhibit a hot spot caused by a failure which appears as a sharp intensity decrease at about 130 m in Fig.(4.7 c). It is not exactly in the middle of the fiber located, thus a different threshold value for the different fiber inputs is expected. This will be verified in the next paragraph. The periodic sinusoidal variations of the BFS can clearly be observed in Figs.(4.7 h,j,l). The comparison with the outer diameter variations previously shown in Figs.(4.5 a,b) is very good except in the beginning of fiber V3 where the first period cannot be observed. A probable explanation is the simple fact that 320 m of varied core diameter fiber were taken at the starting point of the drawn fibers whereas V1 and V2 are parts of the fiber middle where the sine variation is enough pronounced from the beginning on. In addition, one can also see short-scale fluctuations of meter scale that can be attributed to structural irregularities along the fiber. For fiber V1 and V2, where the inverted measurement has been plotted in Figs.(4.7 h,j), the fluctuations are less sinusoidal but even rather square shaped, especially for fiber V1. As investigated in the theoretical part (see paragraph 4.1), this should lead to a higher Brillouin threshold since the square distribution is the most

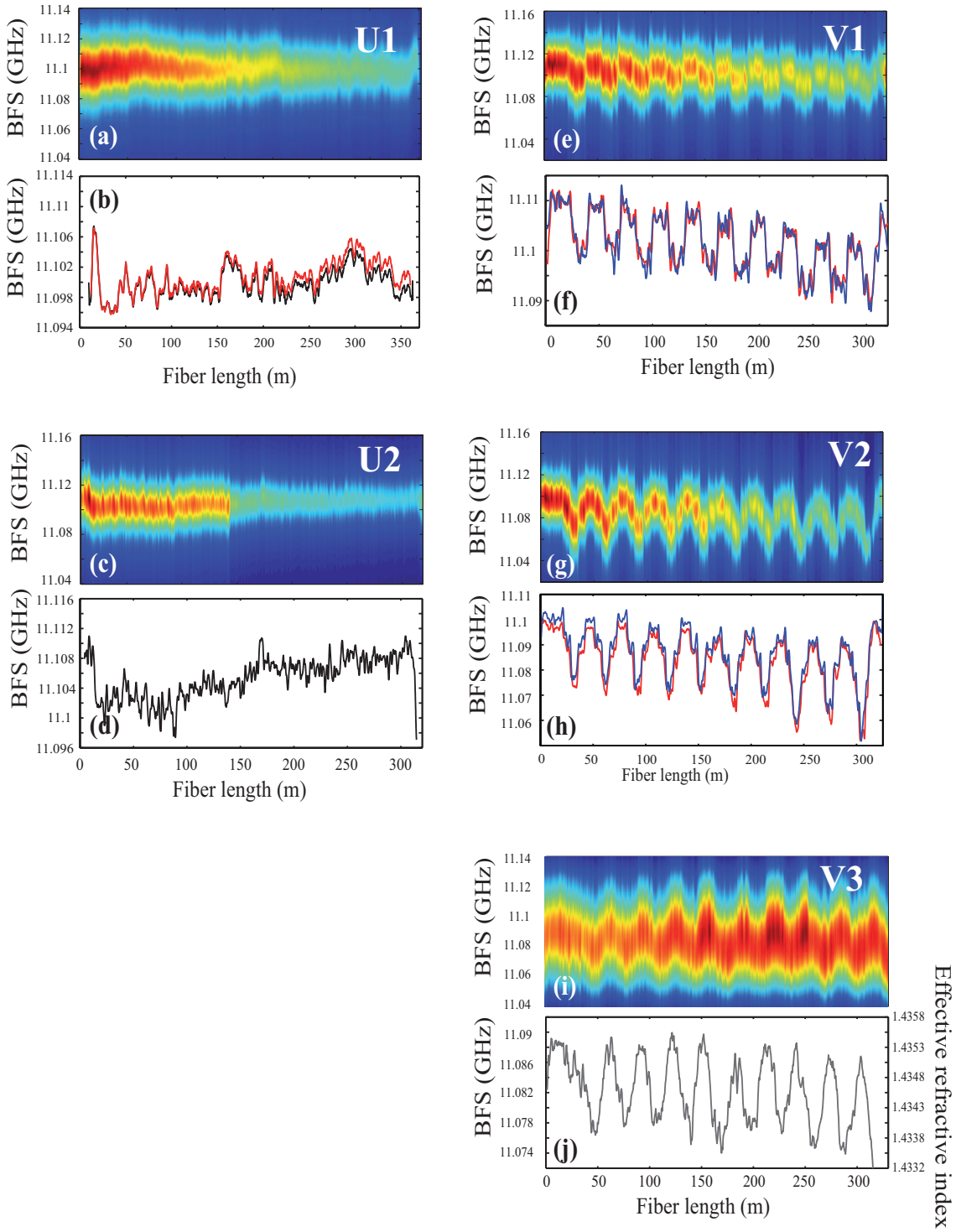

Figure 4.7: Color plot of the Brillouin gain spectrum along the fiber. The spatial resolution is 30 cm and the frequency resolution is 1 MHz for fibers (a) U1 (c) U2 (e) V1 (g) V2 (i) V3 ; retrieved Brillouin frequency shift variations along the fiber distance for fibers (b) U1 (d) U2 (f) V1 (h) V2 (j) V3. Second measurement is obtained by inverting the fiber.

effective distribution among the five tested ones. In addition to the periodic variations and the BGS broadening, the short scale variations also impact on the Brillouin threshold. For fiber V3 additional simulations based on the SEM image have been carried out. We can calculate the corresponding effective refractive index variations using a FEM method by scaling the fiber cross-section shown in Fig.(3.35) [28] as explained in paragraph 3.4.3. For the maximal and minimal sizes (corresponding to 125 and 116 µm in outer diameter) of the air-hole micro-structure they reveal a difference of 0.0013 in the effective refractive index. This value is consistent with the one retrieved from the distributed BFS measurement that varies from 1.4337 to 1.4353, calculated using n_{eff} and Eq.2.18. This confirms that our BEDS technique provide accurate measurement of the diameter or structural variations PCFs.

4.3.3 Brillouin threshold

Considering all measured data it is possible to calculate the theoretical Brillouin threshold power. Therefore we use the theory, presented in paragraph 4.1, where we need the distributed BFS, the FWHM of the Brillouin gain, fiber loss and the EMA A_{eff} which is all provided by previous experiments and the SEM image. The distributed BFS is directly inserted into Eq.(4.7) instead of the theoretical (sine, square, etc.) distribution as used in the parameter study. The results are summarized in tables (4.6) and (4.7).

Table 4.6: Theoretical Brillouin threshold for the uniform fibers

Parameter	**Fiber U1**	**Fiber U2**
Brillouin gain g_B (mW^{-1})	$1.17 \cdot 10^{-11}$	$1.22 \cdot 10^{-11}$
L_{eff}	207.6 m	195.5 m
EMA A_{eff}	22.3 µm^2	19.7 µm^2
C	15.1	15.1
P_{cr} (dBm) (theory)	23.1	22.7

Table 4.7: Theoretical Brillouin threshold for the size varying fibers

Parameter	**Fiber V1**	**Fiber V2**	**Fiber V3**
Brillouin gain g_B (mW^{-1})	$1.22 \cdot 10^{-11}$	$1.17 \cdot 10^{-11}$	$1.30 \cdot 10^{-11}$
L_{eff}	223.4 m	235.6 m	244.5 m
EMA A_{eff}	19.7 µm^2	19.7 µm^2	22.6 µm^2
C	14.6	14.5	14.3
P_{cr} (dBm) (theory)	22.1	22.3	21.9

We obtain a high threshold value for fiber U2 which is due to the high attenuation caused by the hot spot at 130 m of the fiber. The induced variation of 14 % causes a

slightly higher P_{cr} for fiber V2 in comparison to fiber V1. The small difference can also be attributed to the longer effective length of fiber V2.
Fiber V3 shows a lower threshold than V1 although they have the same BFS distribution and the same length. One reason is the shorter effective length based on the higher linear fiber loss. Besides g_B is slightly higher for V3 than for the other two varying fibers, which depends mostly on the different FWHM of the BGS.

The experimental Brillouin threshold has been graphically solved for all fibers from

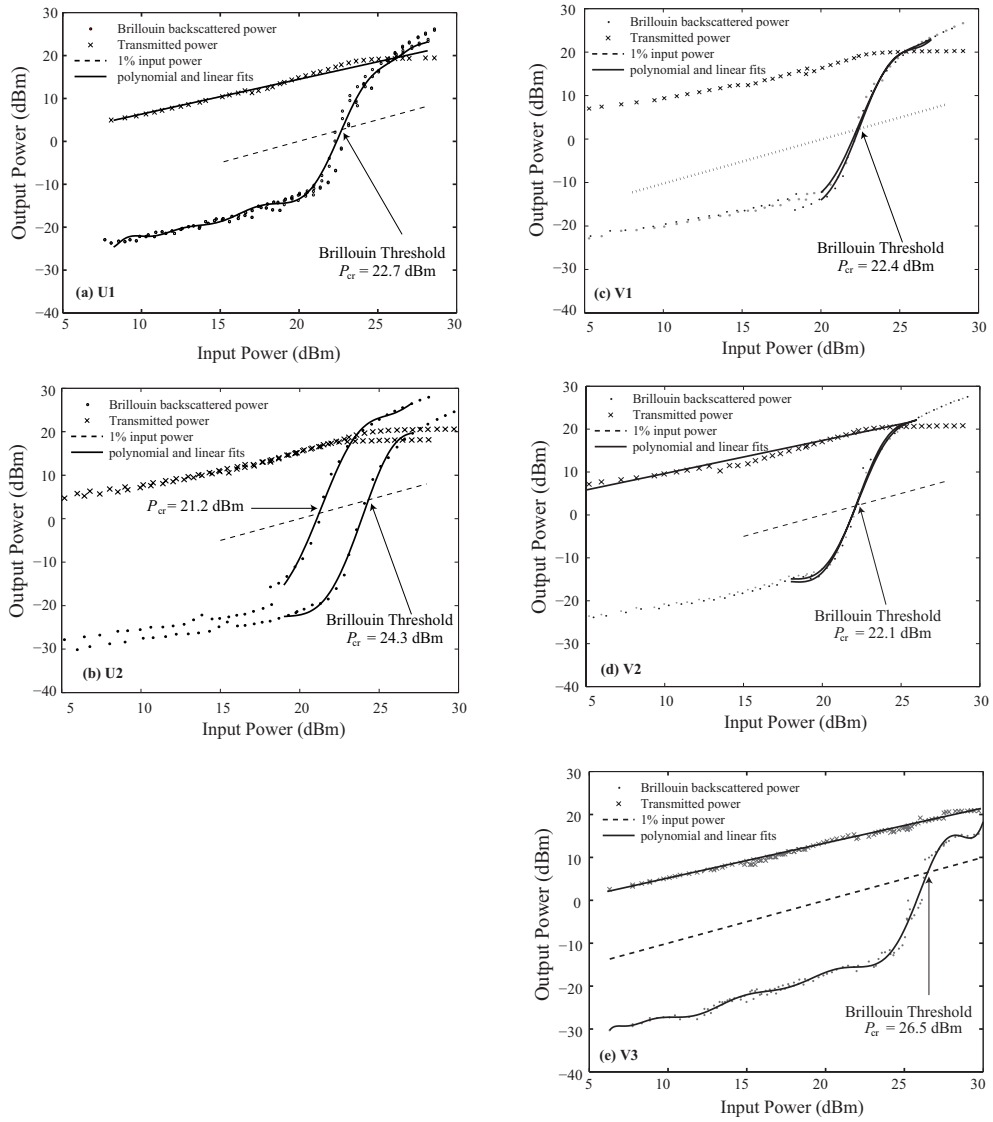

Figure 4.8: Experimental measurements of the Brillouin backscattered and transmitted powers through the periodically varying PCFs and the homogenous PCFs with similar micro-structure but without varying structure size. The Brillouin thresholds of the five PCFs are indicated by arrows for 1% fraction of the input power.

Figs.(4.8) that show the transmitted and backscattered powers as a function of the input power. The experimental setup has been already introduced in chapter 3.1.2 where we used as a pump laser a 1550 nm DFB laser with a 45 kHz linewidth amplified by an EDFA. We define here as mentioned before the Brillouin threshold as the input power whereby the reflected power is 1% of the injected one. A polynomial fit of our experimental measurements yields the Brillouin threshold power. The experimental values for the Brillouin threshold can be found in table (4.8) and (4.9).

Table 4.8: Experimental Brillouin threshold for the uniform fibers

Parameter	**Fiber U1**	**Fiber U2**
P_{cr} (dBm) (experiment)	22.7	21.2 / 24.3 (inverting fiber)

Table 4.9: Experimental Brillouin threshold for the size varying fibers

Parameter	**Fiber V1**	**Fiber V2**	**Fiber V3**
P_{cr} (dBm) (experiment)	22.4	22.1	26.5

The measurement uncertainty for the SBS threshold is about ±0.5 dB taking into account the uncertainty of the splicing loss and measurement accuracy. For fiber U1 the experimental value is lower than exspected which is within the measurement uncertainty. The threshold measurement of fiber U2 reveals clearly two different values when the fiber is inverted. This has been predicted by help of the BEDS measurement where a hot spot at 130 m has been observed. For fiber U2, 130 m fiber length contributes most effectively to Brillouin backscattering, resulting in 24.3 dBm critical pump power. For the other side, the "effective" part of the fiber measures 184 m which leads to a lower value: 21.2 dBm. These values are close to the theoretical ones. Theory and experiment for fiber V1 fortunately agree very well which seem to confirm our theoretical approach. For fiber V2 the threshold should be higher than for fiber V1 since the variation amplitude is 14 % compared to 7 %, which is not the case. Firstly it should be mentioned that the difference is still in the measurement uncertainty. Another argument is the higher effective length for fiber V2 which decreases the critical power. It appears that the lower fiber loss has a higher influence on the experiment than predicted by calculation. The measuring data for fiber V3 reveal a still more unexpected value for the experimental critical pump power that rises up to 26.5 dBm, as shown in Fig.(4.8). Since this does not match with the theoretical value, wherefore some further theoretical investigations have been carried out. In table (4.10) we can find theoretical results for 29 MHz and 54 MHz FWHM of the BGS and for different BFS distributions: sinusoidal function with 30 m period and 16 MHz and 170 MHz variation amplitude and the real BFS extracted from the BEDS measurement. As it can be seen the experimental value (26.5 dBm) shows 7 dB increase to a conventional silica fiber with 29 MHz FWHM and uniform BFS. A periodical variation of the BFS with 16 MHz (difference of minimum to maximum BFS) reveal 0.6 dB threshold elevation whereas a spectral broadening from 29 MHz to 54 MHz leads to 21.83 dBm, so a

2.7 dB higher critical pump power. Correspondingly, the spectral broadening has a higher influence on the threshold increase than the periodic BFS variation alone. But it should be noticed that the varying BFS also influences the FWHM of the BGS because the backscattered light is integrated along the fiber, according to Eq.(4.7). For the broader spectrum with 54 MHz FWHM the increase due to the periodic variation with 16 MHz is 0.2 dB, thus less than for the 29 MHz broad spectrum. Calculating the threshold with real data reveals 21.93 dBm. In order to reach the same result as for the experiment a BFS variation with 170 MHz is needed which is actually not the case for this fiber.

Table 4.10: Theoretical Brillouin threshold of fiber V3, for different parameters

FWHM $\Delta\nu$	**BFS**	**Threshold P_{cr}**
29 MHz	uniform	19.13 dBm
29 MHz	16 MHz variation	19.71 dBm
54 MHz	uniform	21.83 dBm
54 MHz	16 MHz variation	22.01 dBm
54 MHz	real BFS, BEDS measurement	21.93 dBm
54 MHz	170 MHz variation	26.5 dBm

The reason for the exceptionally high Brillouin threshold might be the different structure for this PCF since the hole diameter is not constant. Another explanation could simply be a problem in terms of splicing losses but taking into account the way how splicing loss is estimated this reason should be excluded. For each splice we connected one fiber input and measured the power out coming from the PCF. Then the fiber was spliced and the power leaving the fiber pigtail was measured. The only problem can be the fluctuating power of the laser. Linear loss or a hot spot cannot be a potential explanation because this would have been seen on the fiber mapping by help of BEDS technique as it was observed for fiber U2 in Fig.(4.7 e).
From an experimental point of view we can compare V3 with the uniform fiber U1. U2 is less adequate for a comparison because U2 has the previously shown diffusion spot at 130 m. One can see in Fig.(4.8 b) that the critical power for the Brillouin threshold (red curve) is reached at 22.7 dBm which is almost 4 dB below the value for the periodically varying PCF. Since the effective length of the uniform fiber is shorter than for the periodically varying PCF, the Brillouin threshold can be expected to be even lower than 22.7 dBm and the impact of the BFS variation higher than 4 dB. Thus the experimental threshold increases by more than 4 dB by comparing the modulated and the uniform fiber. Note that this increase can be seen as a higher limit since we assumed in our calculation a uniform PCF without any structural irregularities that increase the Brillouin threshold.

4.4 Conclusion

Photonic crystal fibers with a periodically-varying core diameter have been investigated in order to mitigate the detrimental effect of stimulated Brillouin scattering. Only 7% and 14% of outer variation enables an increase of the Brillouin threshold power up to 4 dB compared to a homogeneous micro-structured optical fiber, which is a promising result for further investigations with higher amplitude variations.
The theoretical model has been explained and the different fiber parameters have been studied theoretically first to estimate the impact on the increase of the Brillouin threshold. We focused especially on different Brillouin frequency shift distributions along the fiber length. In the experimental part, five different uniform and structure varied photonic crystal fibers have been presented and investigated in terms of Brillouin gain spectrum, distributed Brillouin measurement and Brillouin threshold. The periodic oscillations of the Brillouin frequency shift has been checked by an accurate distributed measurement based on Brillouin echoes distributed sensing. The broadened Brillouin gain and the longitudinal variations in PCF lead to an increase in Brillouin threshold. Due to their ability to design custom-fit micro-structures, adapted to the respective need, PCFs are ideal for further studies on passive Brillouin mitigation. Additionally they can doped or taper can be drawn to enhance the suppression effect.
To get further insight to this topic it may be interesting to study other Brillouin frequency shift distribution as proposed theoretically in paragraph 4.1, especially a pure square shaped BFS progression. Besides higher variation amplitudes should impact highly on the Brillouin threshold. On the other hand this will induce more linear fiber loss. Nevertheless, it should be clear after the last paragraph of this chapter that an experimental comparison for different fibers is rather difficult because fiber length, loss, effective area, micro-structure, etc. have an influence as well as the splicing loss contributes to different experimental values. However, PCFs with varying BFS are expected to help for suppressing Brillouin backscattering. This can also be combined with other active and passive suppressing techniques.

Bibliography

[1] Y. Aoki, K. Tajima, and I. Mito, "Input power limits of single mode optical fibers due to stimulated Brillouin scattering in optical communication systems", *Journal of Lightwave Technology*, vol. 6, no. 5, pp. 710–719, 1988.

[2] Y. K. Park, O. Mizuhara, L. D. Tzeng, J.-M. P. Delavaux, T. V. Nguyen, M.-L. Kao, P. D. Yeates, and J. Stone, "A 5 Gb/s repeaterless transmission system using erbium-doped fiber amplifiers", *IEEE Photonics Technology Letters*, vol. 5, no. 1, pp. 79–82, 1993.

[3] A. Mussot, M. Le Parquier, B. Berrier, M. Perard, and P. Szriftgiser, "All-optical sbs reduction in fiber optic parametric amplifiers", *Optics Communication*, vol. 282, no. 5, pp. 988–991, 2009.

[4] T. Sakamoto, T. Matsui, K. Shiraki, and T. Kurashima, "SBS suppressed fiber with hole-assisted structure", *Journal of Lightwave Technology*, vol. 27, pp. 4401–4406, 2009.

[5] L. Grüner-Nielsen, S. Dasgupta, M. D. Mermelstein, D. Jakobsen, S. Herstrøm, M. E. V. Pedersen, E. L. Lim, S. Alam, F. Parmigiani, D. Richardson, and B. Pálsdóttir, "A silica based highly nonlinear fibre with improved threshold for stimulated Brillouin scattering", in *European Conference of Optical Communication 2010, Torino, Italy*, 2010, p. Tu.4.D.3.

[6] C. Wang, F. Zhanga, Z. Tonga, T. Ninga, and S. Jian, "Suppression of stimulated Brillouin scattering in high-power single-frequency multicore fiber amplifiers", *Optical Fiber Technology*, vol. 14, no. 4, pp. 328–338, 2008.

[7] Y. Jeong, K.-Y. Song, K. Hotate, and K. Oh, "Analysis of Brillouin frequency shift and acoustic waves in a hollow optical fiber", *Optics Letters*, vol. 34, no. 20, pp. 3217–3219, 2009.

[8] V. Laude, A. Khelif, S. Benchabane, M. Wilm, T. Sylvestre, B. Kibler, A. Mussot, J. M. Dudley, and H. Maillotte, "Phononic band-gap guidance of acoustic modes in photonic crystal fibers", *Physical Review B*, vol. 71, no. 4, pp. 045107, 2005.

[9] J. Spring and B. Ward, "Brillouin gain suppression in photonic crystal fibers with random acoustically microstructured cores", *Optics Letters*, vol. 35, no. 1, pp. 31–33, 2010.

[10] N. Yoshizawa and T. Imai, "Stimulated Brillouin scattering suppression by means of applying strain distribution to fiber with cabling", *Journal of Lightwave Technology*, vol. 11, no. 10, pp. 1518–1522, 1993.

[11] J. Hansryd, F. Dross, M. Westlund, P. A. Andrekson, and S. N. Knudsen, "Increase of the SBS threshold in a short highly nonlinear fiber by applying a temperature distribution", *Journal of Lightwave Technology*, vol. 19, no. 11, pp. 1691–1697, 2001.

[12] J. M. Chavez Boggio, J. D. Marconi, and H. L. Fragnito, "Experimental and numerical investigation of the SBS-threshold increase in an optical fiber by applying strain distributions", *Journal of Lightwave Technology*, vol. 23, no. 11, pp. 3808–3814, 2005.

[13] K. Shiraki, M. Ohashi, and M. Tateda, "Suppression of stimulated Brillouin scattering in a fibre by changing the core radius", *Electronics Letters*, vol. 31, no. 8, pp. 668–669, 1995.

[14] K. Shiraki, M. Ohashi, and M. Tateda, "SBS threshold of a fiber with a Brillouin frequency shift distribution", *Journal of Lightwave Technology*, vol. 14, no. 1, pp. 50, 1996.

[15] F. Poletti, K. Furusawa, Z. Yusoff, N. G. Broderick, and D. J. Richardson, "Nonlinear tapered holey fibers with high stimulated Brillouin scattering threshold and controlled dispersion", *J. Opt. Soc. Am. B*, vol. 24, no. 9, pp. 2185–2194, 2007.

[16] A. Kobyakov, M. Sauer, and D. Chowdhury, "Stimulated Brillouin scattering in optical fibers", *Advances in Optics and Photonics*, vol. 2, no. 1, pp. 1–59, 2010.

[17] R. G. Smith, "Optical power handling capacity of low loss optical fibers as determined by stimulated Raman and Brillouin scattering", *Applied Optics*, vol. 11, no. 11, pp. 2489–2494, 1972.

[18] G. P. Agrawal, *NonLinear Fiber Optics*, Academic Press, third edition, 2001.

[19] R. W. Boyd, K. Rzazewski, and P. Narum, "Noise initiation of stimulated Brillouin scattering", *Physical Review A*, vol. 42, no. 9, pp. 5514–5521, 1990.

[20] V. I. Kovalev and R. G. Harrison, "Threshold for stimulated Brillouin scattering in optical fiber", *Optics Express*, vol. 15, no. 26, pp. 17625–17630, 2007.

[21] S. Le Floch and P. Cambon, "Theoretical evaluation of the Brillouin threshold and steady-state Brillouin equations in standard single-mode optical fibers", *J. Opt. Soc. Am. A*, vol. 20, no. 6, pp. 1132–1137, 2003.

[22] D. Cotter, "Stimulated Brillouin scattering in monomode optical fiber", *J. Opt. Commun.*, vol. 4, pp. 10–19, 1983.

[23] J-C Beugnot, T. Sylvestre, H. Maillotte, G. Mélin, and V. Lande, "Guided acoustic wave Brillouin scattering in photonic crystal fibers", *Optics Letters*, vol. 32, no. 1, pp. 17–19, 2007.

[24] M. Niklès, *La Diffusion Brillouin dans les fibres optiques : étude et application aux capteurs distribués*, PhD thesis, Ecole Polytechnique Fédérale de Lausanne, 1997.

[25] J.-C. Beugnot, *La diffusion Brillouin dans les fibres optiques microstructurées*, PhD thesis, Université de Franche-Comté, 2007.

[26] S. M. Foaleng, M. Tur, J.-C. Beugnot, and L. Thévenaz, "High spatial and spectral resolution long-range sensing using Brillouin echoes", *Journal of Lightwave Technology*, vol. 28, no. 20, pp. 2993–3003, 2010.

[27] S. M. Foaleng, *Brillouin Echoes for Advanced Distributed Sensing in Optical Fibres*, PhD thesis, Ecole Polytechnique Fédérale de Lausanne, 2011.

[28] B. Stiller, S. M. Foaleng, J.-C. Beugnot, M. W. Lee, M. Delqué, G. Bouwmans, A. Kudlinski, L. Thévenaz, H. Maillotte, and T. Sylvestre, "Photonic crystal fiber mapping using Brillouin echoes distributed sensing", *Optics Express*, vol. 18, no. 19, pp. 20136–20142, 2010.

Chapter 5

Guided acoustic wave Brillouin scattering

When a coherent optical wave propagates through an optical fiber, it suffers from phase noise due to the interaction with transverse acoustic waves that modulate the refractive index of the fiber. This effect, called guided acoustic wave Brillouin scattering (GAWBS) or forward Brillouin scattering, has been known since 1985 and considered for many years as detrimental to fiber-based standard and quantum communication systems [1]. In recent years there has been a renewed interest in the effect of GAWBS in photonic crystal fibers (PCFs) due to their remarkable ability to either suppress or enhance acoustic resonances, with the aim of using PCFs for quantum optics or developing new efficient acousto-optic devices [2–4]. Recent works have indeed shown that GAWBS in PCF is radically different from GAWBS in conventional fibers and cannot only be considered as a noise source any more. Instead, it leads to efficient phase modulation in the GHz range through the generation of high-frequency transverse acoustic waves trapped by the air-hole microstructure [2,5–7]. It has also been reported that these ultra high-frequency acoustic resonances can be coherently controlled in PCF using laser pulses [8] or be turned into highly nonlinear artificial Raman oscillators [9].

In this chapter, we investigate both theoretically and experimentally GAWBS in various PCFs including modulated and multiscale structure. We report the generation of single and multiple high-frequency guided acoustic modes up to 2 GHz. Based on a full vector finite-element model (FEM), we show that these guided acoustic modes result from elastic radial vibrations selected by the wavelength-scale air-silica microstructure.

First the numerical calculation of GAWBS based on the FEM is derived from basic differential equations and the used parameters are shown. The relationship between core diameter and main GAWBS peak is examined numerically and analytically and the effect of the air-filling fraction of the micro-structure is studied. Then the experimental setup is

explained and measurements in different PCFs are analyzed and compared to simulations. In the last part we investigate GAWBS in a PCF with a multi-scale structure design and report the frequency-selective excitation of multiple high-frequency guided acoustic modes up to 2 GHz. We further show the strong impact of structural irregularities of the fiber on these transverse acoustic modes by numerically studying a perfectly symmetric air-hole structure designed from the real cross section of the PCF. Our results suggest that PCFs can be advantageously used to enhance and control guided acousto-optic interactions at ultra-high frequency by fiber design in view of potential applications for fiber-optic sensors or efficient acousto-optic devices.

5.1 Theoretical model and numerical simulation

As mentioned in chapter 2.3, for a conventional SMF the theoretical GAWBS spectrum can be calculated by solving Eq.(2.42) for the R_{0m}-modes and Eq.(2.43) for the T_{2m}-modes. They are derived analytically for simple all-silica glass rods without micro structure. For PCF with an air-silica micro-structure a numerical model is needed to include the real structure of the fiber taking into account boundary conditions between air and silica. For the acoustic modes we start with the equation for the conservation of momentum [10, 11]:

$$\rho \frac{\partial^2 u_i}{\partial t^2} = \frac{\partial T_{ij}}{\partial x_j} + F_i \tag{5.1}$$

where u_i, $i = x, y, z$ are the position vectors, F_i external forces and T_{ij} the strain tensor:

$$T_{ij} = \sum_{k,l} c_{ijkl} S_{kl} \tag{5.2}$$

and the displacement:

$$S_{kl} = \frac{1}{2}\left(\frac{\partial u_k}{\partial x_l} + \frac{\partial u_l}{\partial x_k}\right). \tag{5.3}$$

c_{ijkl} is the elastic coefficient matrix that depends on the material. For silica we will find the coefficients in matrix 5.16. In order to solve Eq. 5.2 we use a test function v_i (weak formulation of FEM)[1] and integrate:

$$\int \rho v_i^\star \frac{\partial^2 u_i}{\partial t^2} d\Omega = \int v_i^\star \frac{\partial T_{ij}}{\partial x_j} d\Omega \tag{5.4}$$

which is by partial integration:

$$\int \rho v_i^\star \frac{\partial^2 u_i}{\partial t^2} d\Omega = \underbrace{\int d\Sigma v_i^\star T_{ij}.\vec{n}}_{\text{Boundary condition : } = 0} - \int d\Omega \frac{\partial v_i^\star}{\partial x_j} T_{ij}. \tag{5.5}$$

[1] The complex conjugate $v_i^\star$ has to be used because we have to define a finite element space, equipped with a scalar product, before we can construct a variational formulation of a partial differential equation.

This gives:

$$\int \rho v_i^\star \frac{\partial^2 u_i}{\partial t^2} d\Omega = -\int d\Omega \frac{\partial v_i^\star}{\partial x_j} T_{ij} \tag{5.6}$$

Taking into account that u_x, u_y, u_z, $v_i \propto e^{ik_z}$ we can calculate partially [11]:

$$\begin{aligned} \frac{\partial v_i^\star}{\partial x_j} T_{ij} &= \sum_j \frac{\partial v_i^\star}{\partial x_j} \sum_{kl} c_{ijkl} S_{kl} = \sum_j \frac{\partial v_i^\star}{\partial x_j} \sum_{kl} c_{ijkl} \frac{\partial u_k}{\partial x_l} \qquad (5.7) \\ &= \underbrace{-ik_z v_i^\star \sum_{kl} c_{izkl} \frac{\partial u_k}{\partial x_l}}_{j=z, l\neq z\text{: the sign "-" comes from } \star} + \underbrace{\sum_j \frac{\partial v_i^\star}{\partial x_j} ik_z \sum_k c_{ijkz} u_k}_{j\neq z, l=z} \\ & \underbrace{-ik_z v_i^\star \sum_k ik_z c_{izkz} u_k}_{j=z,l=z} + \underbrace{\sum_j \frac{\partial v_i^\star}{\partial x_j} \sum_{kl} c_{ijkl} \frac{\partial u_k}{\partial x_l}}_{j\neq z, l\neq z} \qquad (5.8) \end{aligned}$$

and can rewrite Eq. 5.6 as:

$$\begin{aligned} 0 = & -\int d\Omega \rho v_i^\star \tfrac{\partial^2 u_i}{\partial t^2} - \int d\Omega i k_z v_i^\star \textstyle\sum_{kl} c_{izkl} \frac{\partial u_k}{\partial x_l} + \int d\Omega \sum_j \frac{\partial v_i^\star}{\partial x_j} ik_z \sum_k c_{ijkz} u_k \\ & - \int d\Omega i k_z v_i^\star \textstyle\sum_k ik_z c_{izkz} u_k + \int d\Omega \sum_j \frac{\partial v_i^\star}{\partial x_j} \sum_{kl} c_{ijkl} \frac{\partial u_k}{\partial x_l}. \end{aligned} \tag{5.9}$$

This equation has to be solved in order to find all types of acoustic modes for any design of microstructure. For this purpose we extract the micro-structure from a scanning electron microscope (SEM) image. Then a mesh with a finite number of nodes and their connecting segments is built as used in FEM and shown in Fig.(5.1 a), Fig.(5.2 c) and Fig.(5.16 e) using Comsol software [12]. For the acoustic modes the PDE-mode solver fits the best to analytical and experimental results. The following equation is solved in the PDE-mode:

$$e_a \frac{\partial^2 u}{\partial t^2} + d_a \frac{\partial u}{\partial t} + \nabla.(-c\nabla u - \alpha u + \gamma) + \beta.\nabla u + au = f \tag{5.10}$$

In the Comsol [12] handbook the coefficients are described as follows: Mass term e_a, damping term d_a, diffusive flux c, conservative flux term α, conservative flux source γ, convection term β, absorption term a and source term f.
Then we have to find the corresponding counterparts to Eq.(5.9), which we would like to solve for the acoustic modes. Taking into account the different derivations, we can find the following correspondents [11]:

$$e_a = -\rho \tag{5.11}$$

$$\beta.\nabla u = -ik_z \sum_{kl} c_{izkl} \frac{\partial u_k}{\partial x_l} \tag{5.12}$$

$$\nabla.(-\alpha u) = ik_z \sum_{jk} \frac{\partial v_i^\star}{\partial x_j} c_{ijkz} u_k \tag{5.13}$$

$$au = k_z^2 v_i^\star \sum_k c_{izkz} u_k \tag{5.14}$$

$$\nabla.(-c\nabla u) = \sum_{jkl} \frac{\partial}{\partial x_j} c_{ijkl} \frac{\partial u_k}{\partial x_l} \tag{5.15}$$

and d_a, γ, $f = 0$. Let us now focus on the elastic coefficient matrix c_{ijkl}. In silica the matrix is rather symmetric and most of the elements are zero. Actually, only three different elements remain: c_{11}, c_{12} and c_{44} and they are located as follows [13]:

$$c = \begin{bmatrix} c_{11} & c_{12} & c_{12} & 0 & 0 & 0 \\ c_{12} & c_{11} & c_{12} & 0 & 0 & 0 \\ c_{12} & c_{12} & c_{11} & 0 & 0 & 0 \\ 0 & 0 & 0 & c_{44} & 0 & 0 \\ 0 & 0 & 0 & 0 & c_{44} & 0 \\ 0 & 0 & 0 & 0 & 0 & c_{44} \end{bmatrix} \tag{5.16}$$

c_{11}, c_{12} and c_{44} depend on the Lamé coefficients λ and μ as [13],

$$c_{11} = \lambda + 2\mu,\ c_{12} = \lambda,\ c_{44} = \mu \tag{5.17}$$

with

$$\lambda = \frac{E\nu}{(1+\nu)(1-2\nu)} \tag{5.18}$$

$$\mu = \frac{E}{2(1+\nu)} \tag{5.19}$$

and the Young's Modulus $E = 73.1 \cdot 10^9\,\mathrm{Pa}$ and Poisson's coefficient $\nu = 0.17$. The density value $\rho = 2203\,\mathrm{kg\,m^{-3}}$ is used. With these elements it is also possible to express the longitudinal and transverse acoustic velocities as [13]:

$$V_L = \sqrt{\frac{c_{11}}{\rho}} \tag{5.20}$$

$$V_T = \sqrt{\frac{c_{44}}{\rho}} \tag{5.21}$$

The values for e_a, d_a, c, α, γ, β, a and f have been integrated in the PDE-mode in Comsol. Using Comsol, the solutions for the acoustic modes in form of u_x, u_y, u_z and their derivations, e.g. $\partial u_x/\partial x$, $\partial u_x/\partial y$, $\partial u_y/\partial x$, $\partial u_y/\partial y$, are obtained. To visualize them it is either useful to plot the kinetic energy E_{kin} [13]:

$$E_{kin} = \frac{1}{2}\rho\omega^2(u_x^2 + u_y^2), \tag{5.22}$$

with ω the angular frequency of the acoustic mode and ρ the density, or the strain energy density SED [13]:

$$W_s = \frac{1}{2}\left(\frac{\partial u_x}{\partial x}T_{xx} + \frac{\partial u_y}{\partial y}T_{yy} + (\frac{\partial u_x}{\partial y} + \frac{\partial u_y}{\partial x})T_{xy}\right), \tag{5.23}$$

where (u, v, w) and T_{kl} are the displacements and stresses of the FEM solution, respectively.
As GAWBS is an acousto-optical interaction, we also need to solve the optical mode which is calculated by Comsol software [12] by resolving Maxwell equations with the RF module. As expected the light is guided in the fiber core which is presented in Fig.(5.1 d). The refractive index of silica was obtained by the Sellmeier equation [14]:

$$n(\lambda) = \sqrt{1 + \frac{P_1\lambda^2}{\lambda^2 - P_2} + \frac{P_3\lambda^2}{\lambda^2 - P_4} + \frac{P_5\lambda^2}{\lambda^2 - P_6}} \tag{5.24}$$

with λ in microns and

$$P_1 = 0.6961663 \tag{5.25a}$$
$$P_2 = 0.0684043^2 \tag{5.25b}$$
$$P_3 = 0.4079426 \tag{5.25c}$$
$$P_4 = 0.1162414^2 \tag{5.25d}$$
$$P_5 = 0.8974794 \tag{5.25e}$$
$$P_6 = 9.896161^2. \tag{5.25f}$$

We now need a parameter that links the acoustic and optical modes to compute the overlap of both modes. This is given by the elasto-optic coefficient [3]:

$$\kappa = \int_\sigma \mathrm{d}x\mathrm{d}y E_i E_j p_{ijkl} S_{kl}. \tag{5.26}$$

In this expression, σ is the transverse section of the fiber, E_i and E_j are the pump and scattered optical modes, respectively, p_{ijkl} is the strain-optical tensor, and S_{kl} is the displacement tensor. Because of symmetry reasons, in silica p_{ijkl} can be readily obtained as only the elements p_{11} and p_{12} are non-zero:

$$p_{11} = 0.125,\ p_{12} = 0.27,\ p_{44} = \frac{p_{11} - p_{12}}{2} = -0.0725 \tag{5.27}$$

The elasto-optic coefficient is obtained by integrating the strain and optical energy directly in Comsol as follows:

$$\kappa = \sum_{\text{surface}} (p_{11}\frac{\partial u}{\partial x} + p_{12}\frac{\partial v}{\partial y})|E_x|^2 + (p_{12}\frac{\partial u}{\partial x} + p_{11}\frac{\partial v}{\partial y})|E_y|^2 + 2p_{44}(\frac{\partial u}{\partial y} + \frac{\partial v}{\partial x})|E_x E_y| \tag{5.28}$$

κ^2 is proportional to the scattering efficiency and thus models correctly the GAWBS spectrum. To illustrate our theory, we tested a PCF with d_c=2.7 µm core diameter and hexagonal structure. The results are presented in Fig.(5.1) and this fiber has been used for investigating the temperature coefficient of GAWBS in PCF [15]. The SEM image is depicted in Fig.(5.1 b) and the micro-structure was meshed as shown in Fig.(5.1 a). With

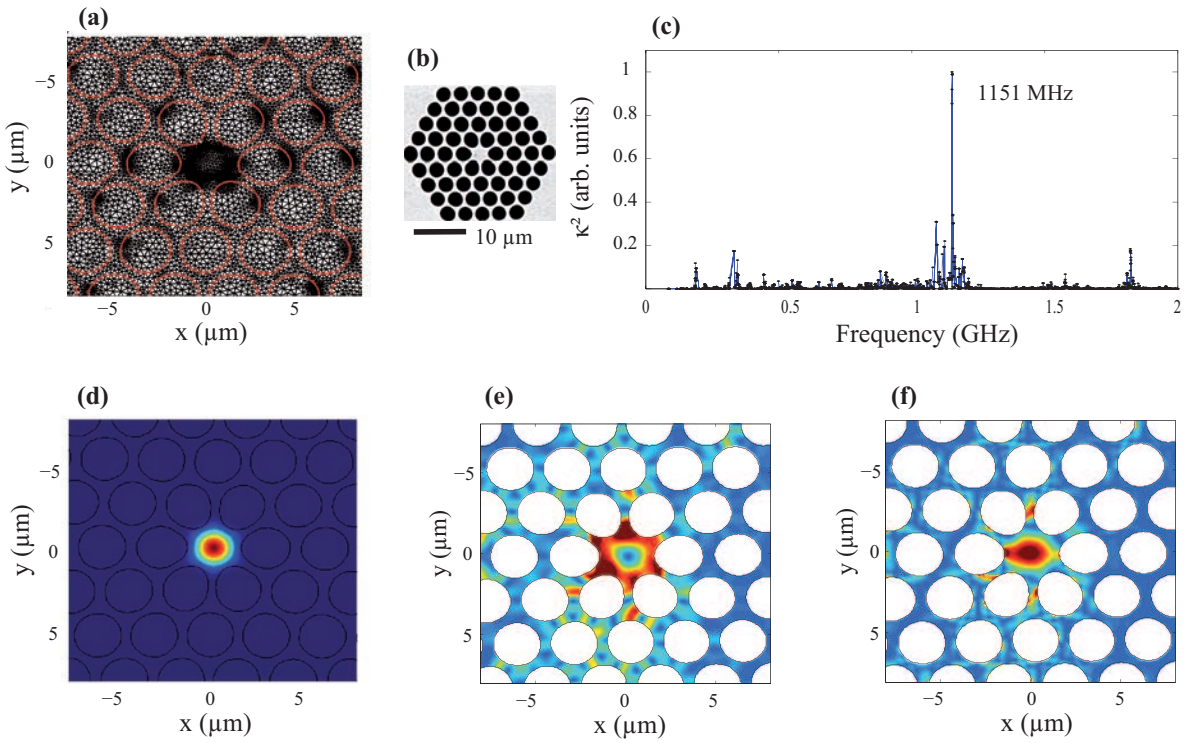

Figure 5.1: PCF with core diameter d_c=2.7 µm, hole diameter d=2.55 µm and pitch Λ=2.9 µm (d/Λ=0.88): (a) Micro-structure with mesh, (b) SEM image, (c) elasto-optic coefficient, (d) optical mode, (e) kinetic energy Eq.(5.22) and (f) strain energy density Eq.(5.23) of the acoustic mode of the main GAWBS peak.

help of Comsol and the RF-module, the optical mode has been calculated and it is confined in the fiber core, as can be seen in Fig.(5.1 d). With the PDE-mode solver the acoustic modes have also been calculated for this structure. Combining both, the elasto-optic coefficient is achieved and plotted in Fig.(5.1 c). For the main peak, the acoustic mode have been investigated in more detail and the kinetic energy (Fig.(5.1 e)) and strain energy density (Fig.(5.1 f)) are visualized for this in the fiber core confined mode. The kinetic energy (Fig.(5.1 e)) highlights the parts of the microstructure that are moving the most. As shown in this figure the ring in red presents the parts where the structure is moving a lot in comparison to the blue parts. It is a radial symmetric mode. The strain energy density (Fig.(5.1 f)) shows the region where the micro structure is stressed the most. Since it is a radial symmetric mode the center of the fiber is indeed under pressure because the region around the fiber core is moving in radial direction. The strain energy density is also crucial for the overlap with the optical mode. If there is a good overlap between the maximum of the strain energy density and the optical mode, then forward scattering is efficient and a high peak in the GAWBS spectrum will appear, such as in Fig.(5.1 c). Looking at this figure, one can already imagine that forward Brillouin scattering behaves in a different way in a PCF as in a conventional single-mode fiber (SMF). It is demonstrative that in

a PCF a main peak appears whereas the low frequency modes are mostly suppressed. Reasons for this behavior are manifold. The air-hole structure acts like a filter of acoustic modes because the fiber core is acoustically isolated from the cladding around the air-hole structure. Besides the optical mode is confined in a smaller effective area, which turns the overlap more effective. The other acoustic modes around the fiber core are not crucial for GAWBS because there is no overlap between optical and acoustic mode. This leads to the efficient generation of a fundamental acoustic mode trapped in the PCF solid core. Thus the fiber behaves like an efficient passive phase modulator. These findings will be checked in paragraph 5.3 against experimental observation. In the next paragraph we will first study the relationship between the frequency of the single peak, as observed in PCF, as in Fig.(5.1 c), and the fiber geometry, especially the fiber core diameter.

5.2 Acoustic modes in homogeneous silica rods

In this paragraph the dependence between the frequency of the main peak and the diameter of the fiber core in PCF is investigated in more detail. In several publications it has been reported that the smaller the fiber core the higher the frequency of the acoustic resonance frequency [7, 16, 17]. Ref. [18] introduced the formula

$$\nu = \frac{V_T}{D}, \tag{5.29}$$

with V_T=3740 m s^{-1} and D the core diameter. This simple expression was confirmed by measurement in several fibers. In [16] simulations for a taper with variable diameter have been performed to show the dependency between frequency and taper thickness. We will show and compare here some experimental results in various PCFs. Besides simulations of acoustic modes in silica glass rods have been carried out to corroborate the experiments. A study about the influence of the fiber hole over the pitch d/Λ on the frequency of GAWBS helps us to understand better why experiments do not agree with Eq.(5.29) for all PCFs. Finally the relation between frequency and core diameter is derived analytically by resolving the Pochhammer-Cree-Equation [13].

Four PCFs with different EMA have been tested in terms of forward Brillouin scattering and the results are shown in table (5.1). The core diameter has been extracted from SEM-images and the mode diameter is taken from simulations of the EMA based on the SEM-images. The measured GAWBS spectra can be found in [18] and the frequency of the main peaks is listed in table (5.1). We clearly see that the frequency of the main peak rises when the core diameter or the mode field diameter decreases. In order to find an exact relation between the structure and the frequency the products $\nu \cdot d_{EMA}$ and $\nu \cdot d_{SEM}$ were calculated. Taking into account V_T=3740 m s^{-1}, it can be seen in table (5.1) that

Table 5.1: Comparison of mode diameter, core diameter and main GAWBS peak frequency

EMA A_{eff} (μm^2)	3.19	4.0	6.0	8.8
Mode diameter d_{EMA} (μm)	2.02	2.26	2.77	3.34
Core diameter (SEM image) d_{SEM} (μm)	2.09	2.43	3.22	3.94
Acoustic frequency (experiment) ν (MHz$\pm$10 MHz)	1545	1281	1154	812
$\nu \cdot d_{EMA}$ ($m\,s^{-1}$)	3121	2895	3196	2712
$\nu \cdot d_{SEM}$ ($m\,s^{-1}$)	3229	3113	3716	3120

Eq.(5.29) is satisfied for the fiber with A_{eff}=6.0 μm^2 only. Nevertheless, the values for the core diameters measured with help of the SEM image fit a bit better than the mode diameter. For that reason a more rigorous numerical and analytical investigation seemed to be appropriate and is presented in the following paragraphs.

5.2.1 Numerical model

First a numerical approach based on FEM with Comsol-software has been undertaken. To this end, we use the acoustic model of paragraph 5.1 to simulate the fundamental R_{01}-mode and the first torsional T_{21}-mode. For a rod diameter d=1 μm the kinetic energy and the strain energy density are shown in Fig.(5.2). For V_T=3740 $m\,s^{-1}$ and V_L=5996 $m\,s^{-1}$ the following dependencies have been found by varying the diameter of the silica rod:

$$\nu = \frac{3.82 \cdot 10^3}{D}, \text{ for } R_{01}\text{-modes} \tag{5.30}$$

$$\nu = \frac{2.79 \cdot 10^3}{D}, \text{ for } T_{21}\text{-modes} \tag{5.31}$$

in exact agreement with results of Ref. [16]. Additionally, the dependence of V_T and V_L on the numerical factor in Eq.(5.30) for the fundamental mode has been studied to compare silica to other materials. Let us call the numerical factor q_{R01} as proposed in Ref. [16]. The results are presented in Fig.(5.3 a,b). V_T in Fig.(5.3 a) is fixed to 3740 $m\,s^{-1}$ whereas V_L varies from about 3750 $m\,s^{-1}$ to 7000 $m\,s^{-1}$. The fit reveals a square root shape and a cut-off frequency at V_T=V_L.
The same results can be found in Fig.(5.3 b) where V_L=5996 $m\,s^{-1}$ is fixed: the factor q_{R01} turns to 0 if V_T becomes equal to V_L. Here, the fit shows a polynomial shape with exponent 0.14. For the sake of completeness the dependence of the taper thickness on q_{R01} has been shown for several values of V_T and V_L. The standard values are plotted in green and the case V_T=V_L in red, respectively.

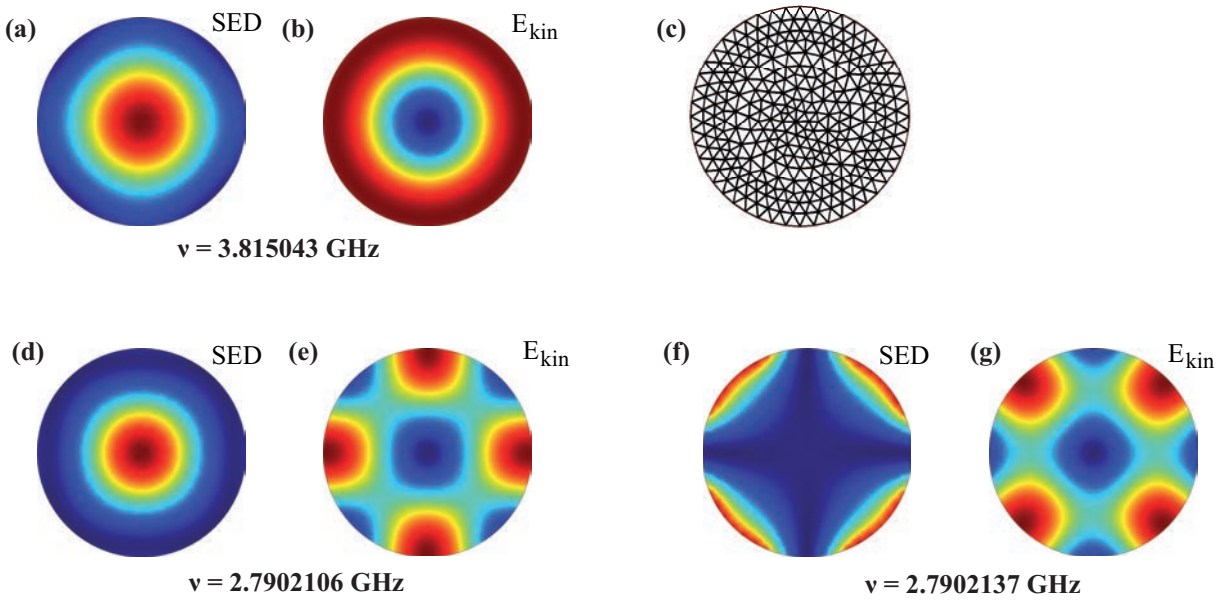

Figure 5.2: Simulation of acoustic modes in a silica rod with diameter d=1 µm: (a,b) fundamental mode R_{01}-mode, (c) mesh of the silica rod, (d-g) torso-radial modes T_{21}, kinetic Energy E_{kin} Eq.(5.22) (red = large displacement, blue = low displacement) and strain energy density SED Eq.(5.23) (red = large density, blue = low density).

5.2.2 Analytical model

Now it is interesting to find the same numerical factor q_{R01} by an analytical approach. The starting point is the Pochhammer-Cree-Equation, written as [19]:

$$\frac{2p}{a}\left(q^2+k^2\right)J_1(pa)J_1(qa)-\left(q^2-k^2\right)^2J_0(pa)J_1(qa)-4k^2pqJ_1(pa)J_0(qa)=0 \qquad (5.32)$$

with $p^2=\omega^2/V_L^2-k^2$ et $q^2=\omega^2/V_T^2-k^2$, ω the angular frequency of the elastic mode, J_i, $i=0.1$ the i-th Bessel function, a the rod diameter, so $a=D/2$. Eq.(5.32) is a dispersion equation derived from the potential for two independent displacement components u_r and u_z [13]:

$$\Psi = AJ_0(pr)e^{i(\omega t-kz)} \qquad (5.33)$$

$$\Phi_\theta = -CJ_1(qr)e^{i(\omega t-kz)} \text{ with } \Phi_r=\Phi_z=0 \qquad (5.34)$$

In Ref. [19] the same approach based on the solution of a boundary value problem has been presented. Their considerations leads them to the following equation, written as the

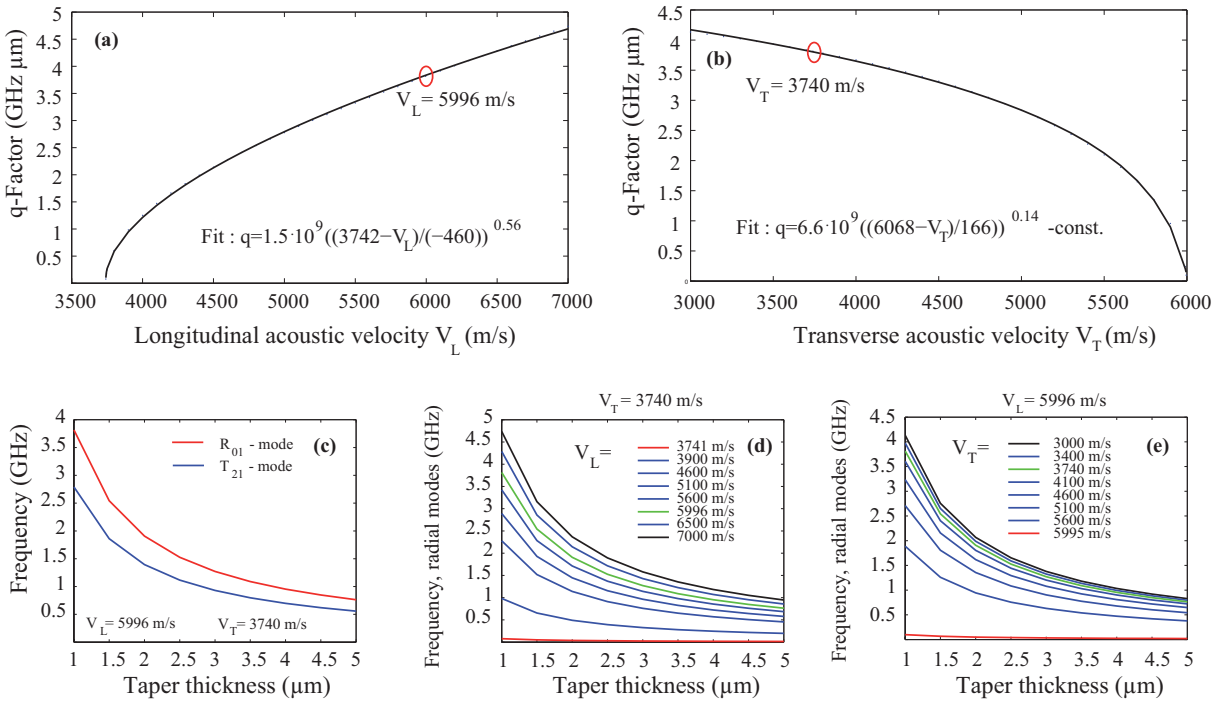

Figure 5.3: (a) Dependence of the numerical factor q_{R01} on the longitudinal acoustic velocity V_L, (b) dependence of the numerical factor q_{R01} on the transversal acoustic velocity V_T, dependence of the taper thickness on q_{R01} for (c) V_T=3740 m s^{-1} and V_L=5996 m s^{-1}, (d) several values of V_L and (e) several values of V_T. The standard values are plotted in green and the case V_T=V_L in red, respectively

determinant of the following matrix:

$$\begin{vmatrix} \rho^2-1-\tau^2(x-1) & \rho^2-1-\tau^2(2x-1) & 2(\rho^2-1)[\mathscr{J}_p(ka)-p]-\tau^2(2x-1) \\ \mathscr{J}_p(ha)-p-1 & \mathscr{J}_p(ka)-p-1 & 2\rho^2-2[\mathscr{J}_p(ka)-p]-\tau^2(2x-1) \\ \mathscr{J}_p(ha)-p & -(x-1)[\mathscr{J}_p(ka)-p] & \rho^2 \end{vmatrix} = 0. \tag{5.35}$$

where

$$\begin{aligned} a &= D/2 \\ h^2 &= \frac{\omega^2}{V_L^2} - k_z \\ k^2 &= \frac{\omega^2}{V_T^2} - k_z \\ \tau &= k_z a = \omega a/V \\ x &= V^2/2V_T^2 \\ \mathscr{J}_p(y) &= yJ_{p-1}(y)/J_p(y) \end{aligned}$$

and p mode number (fundamental mode: p=0). J_p is the pth Bessel function. Resolving this equation under the conditions p=0 (fundamental modes) and $k_z \approx 0$ (transverse

acoustic modes[2]) leads to:

$$0 = \left(-2\,\mathscr{J}_0(ka) - \tau^2(2x-1)\right) \;\cdot\; \mathscr{J}_0(ka) \;\cdot\; \left(-\frac{\omega^2 a^2}{2V_T^2} - \mathscr{J}_0(ha)\right) \tag{5.36}$$

Previous equation has three possible solutions [11]:

$$-2\,\mathscr{J}_0(ka) - \tau^2(2x-1) = 0 \tag{5.37a}$$
$$\mathscr{J}_0(ka) = 0 \tag{5.37b}$$
$$-\frac{\omega^2 a^2}{2V_T^2} - \mathscr{J}_0(ha) = 0 \tag{5.37c}$$

Let us focus on the last solution that can be rewritten as [11]:

$$-\frac{\omega^2 a^2}{2V_T^2} = \mathscr{J}_0(ha) \tag{5.38a}$$
$$\frac{\omega^2 a^2}{2V_T^2} = -ha\frac{J_1(ha)}{J_0(ha)} \tag{5.38b}$$

with

$$J_1(x) = 1/4 \cdot \left[\sin(x) + \sqrt{2}\sin(x/\sqrt{2})\right] \tag{5.39a}$$
$$J_0(x) = 1/4 \cdot \left[1 + \cos(x) + 2\cos(x/\sqrt{2})\right] \tag{5.39b}$$

Considering $h^2 = \frac{\omega^2}{V_L^2} - k_z^2$, $\omega = 2\pi\nu$, $k_z = 0$ and a=D/2, we can further provide:

$$\frac{2\pi\nu\frac{D}{2}V_L}{2V_T^2} = \frac{J_1(\frac{2\pi\nu}{V_L}\cdot\frac{D}{2})}{J_0(\frac{2\pi\nu}{V_L}\cdot\frac{D}{2})} \tag{5.40a}$$
$$\frac{\pi\nu D}{V_T} = 2\cdot\frac{J_1(\frac{\pi\nu D}{V_L})}{J_0(\frac{\pi\nu D}{V_L})}\cdot\frac{V_T}{V_L}. \tag{5.40b}$$

For V_T=3740 m s^{-1} and V_L=5996 m s^{-1} in silica equation (5.40) can be solved graphically as shown in Fig.(5.4):

$$\nu = \frac{V_T}{D}\cdot\frac{3.205}{\pi} = \frac{3.82\cdot 10^3 \mathrm{m\,s^{-1}}}{D} \tag{5.41}$$

which confirms the simulations in the previous chapter and in Ref. [16]. Additionally it can be approximatively written:

$$\nu = \frac{V_T}{D}\cdot\frac{3.205}{\pi} \approx \frac{V_T}{D}, \tag{5.42}$$

which is the experimentally found Eq.(5.29) in Ref. [18]. Nevertheless, formula (5.29) is not in full agreement with all results in table (5.1). The most evident reason is that fiber

[2] k_z=0 would mathematically lead to $V = \infty$ in previous equation (5.36), which is not physical.

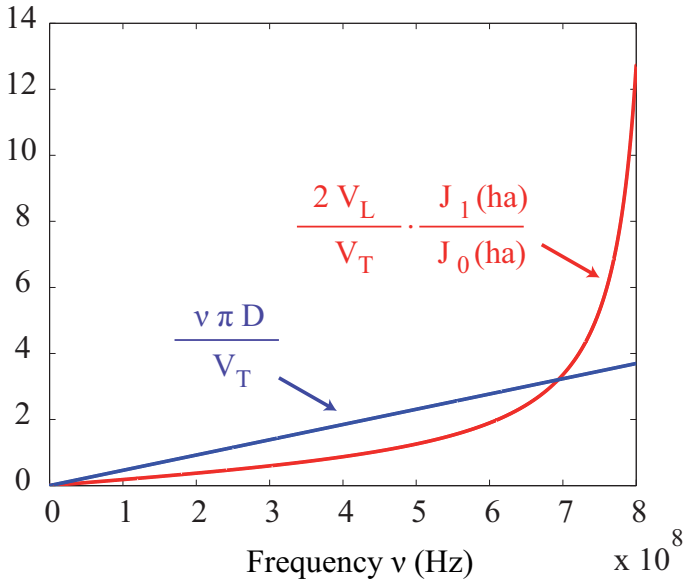

Figure 5.4: Graphical solution of Eq.(5.40).

cores of PCFs are not perfect glass rods. The optical and acoustic modes do not depend only on the fiber core diameter but also on the other parts of the fiber structure, more precisely on the air hole diameter and the pitch. In order to get more into detail into this question it is interesting to study numerically the influence of d/Λ, with d the air hole diameter and Λ the pitch, on the GAWBS spectrum which will lead us to the next paragraph.

5.2.3 Effect of air-filling fraction on GAWBS

The effect of the air-filling fraction in birefringent silica-air PCFs has been studied in Ref. [17]. They found that with increasing air-filling fraction the number of acoustic modes originating from the cladding decreases and the efficiency of core-confined acoustic mode rises. Besides they observed phononic band-gaps at higher air-filling fractions which leads to additional peaks in the GAWBS spectrum.
In this paragraph, we study a sixfold symmetric non-birefringent PCF with perfect structure where the impact of d/Λ, with d the air hole diameter and Λ the pitch (the air-filling fraction), on the GAWBS-spectrum has been investigated[3]. All over the study the core diameter has been fixed to 4 µm whereas the diameter of the air holes d and the pitch Λ changed which leads to a varying d/Λ from d/Λ=0.2 to d/Λ=0.95. The air hole structure for d/Λ=0.4, 0.6 and 0.9 are shown in Fig.(5.5 d). The optical and acoustic modes have been modeled and some of the acoustic modes can also be found in Fig.(5.5 d). From the

[3]Simulations kindly provided by Dr. Michaël Delqué

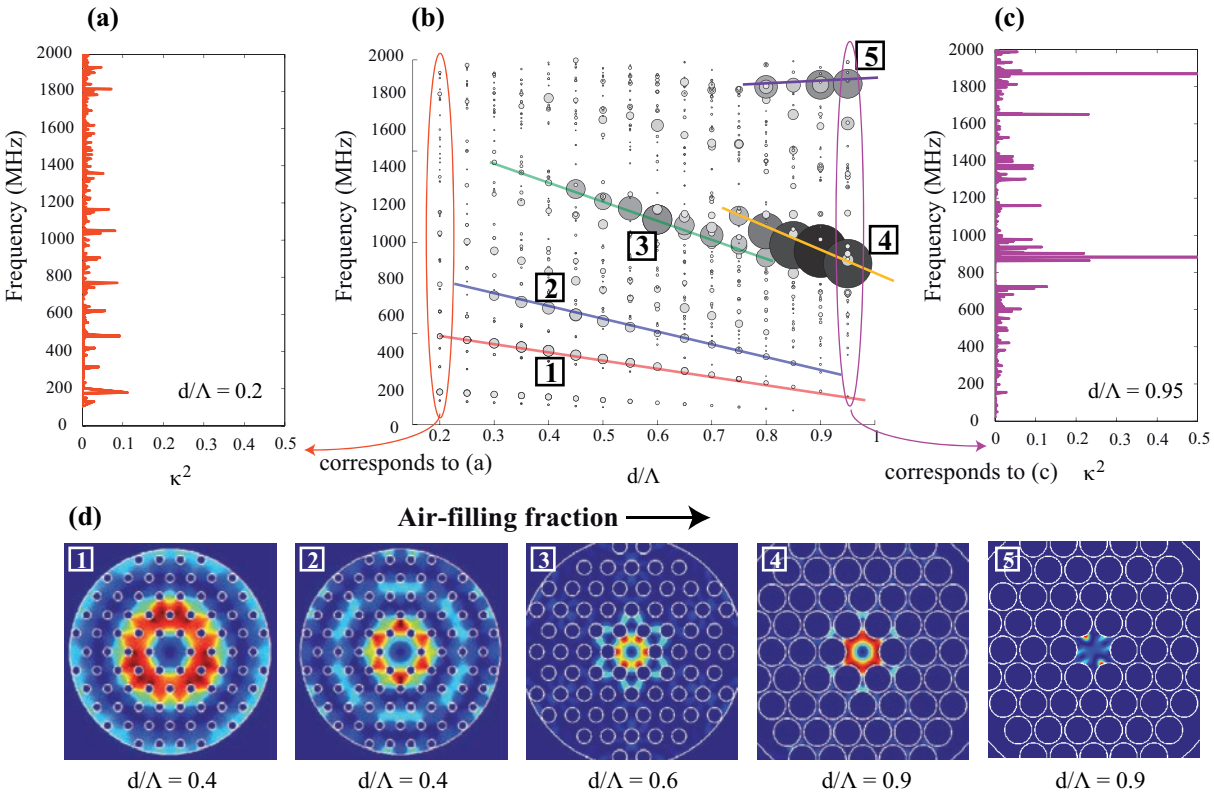

Figure 5.5: Elasto-optic coefficient for (a) $d/\Lambda = 0.2$, (b) evolution from $d/\Lambda = 0.2$ to $d/\Lambda = 0.95$, (c) $d/\Lambda = 0.95$, (d) air hole structure for d/Λ=0.4, 0.6 and 0.9, the numbers corresponds to the acoustic modes indicated in (b), shown is the kinetic energy Eq.(5.22) (red = large displacement, blue = low displacement)

acoustic and optical modes the elasto-optical coefficient of Eq.(5.28) is calculated and the overlap of both modes is visualized in Fig.(5.5 a,c) as a theoretical GAWBS-spectrum. These two spectra were calculated for d/Λ=0.2 (Fig.(5.5 a)) and d/Λ=0.95 (Fig.(5.5 c)). In the middle (Fig.(5.5 b)) the development of the elasto-optical coefficient from d/Λ=0.2 to d/Λ=0.95 is shown by demonstrating the intensity by the size of bubbles. The bigger the circle, the higher the intensity at some point in the frequency range. For d/Λ=0.95 we can see a big bubble at about 900 MHz on Fig.(5.5 b) which corresponds to the high peak at 900 MHz on Fig.(5.5 c). In Fig.(5.5 a) the peaks are all rather small wherefore the bubbles for d/Λ=0.2 in Fig.(5.5 b) also have a small diameter. Some interesting observations can be made based on this diagram. As indicated by the colored lines several intensity peaks are observed while increasing d/Λ. The frequency decreases with higher d/Λ and the higher the frequency, the steeper is the gradient of the decrease which, for instance, can be seen for the rows 1-4. Only the frequency of row 5 for the highest peak seems to rise with increasing d/Λ. For small values of d/Λ the most efficient modes are in the low frequency range up to 1 GHz, similar to the GAWBS spectrum in an SMF. Indeed, looking at the acoustic modes (Fig.(5.5 d)) that are corresponding to line 1 and 2,

we observe similar modes as in a glass rod limited by the boundary, shown in Fig.(5.2 a). The air hole structure below d/Λ=0.45 seems not to be pronounced enough to suppress the acoustic modes of the fiber cladding. At d/Λ=0.45 a stronger peak appears and its intensity rises until d/Λ=0.6, for which value the acoustic mode is depicted in Fig.(5.5 d). The mode is mostly present in the fiber core and has a $2\pi/6$-symmetry. The frequency decreases with increasing d/Λ as mentioned before. At d/Λ=0.75 a second high frequency peak comes along at about 1.2 GHz. This acoustic mode, depicted at d/Λ=0.9, is more circular as the previous one but still mostly concentrated in the fiber core. The acoustic modes for higher values of d/Λ seem to act more like silica rods limited by the air-hole structure than rods limited by the fiber boundary [11].
This study leads to the conclusion that the frequency of the main peaks in a GAWBS-spectrum also depends on the air-hole-fraction d/Λ, not only on the core diameter as seen in [17]. The higher d/Λ the more the fiber core acts like a small silica rod isolated from the cladding. The acoustic modes are circular and appear at high frequency. The lower d/Λ the more we observe peaks in the lower frequency range, the cladding modes, and the structure acts like a big silica rod. In the middle range we observe sixfold symmetric acoustic modes because of the hexagonal structure of the PCF. This gives us a wider comprehension for the limits of Eq.(5.29).

5.3 Experimental investigation of forward Brillouin scattering

5.3.1 Experimental setup

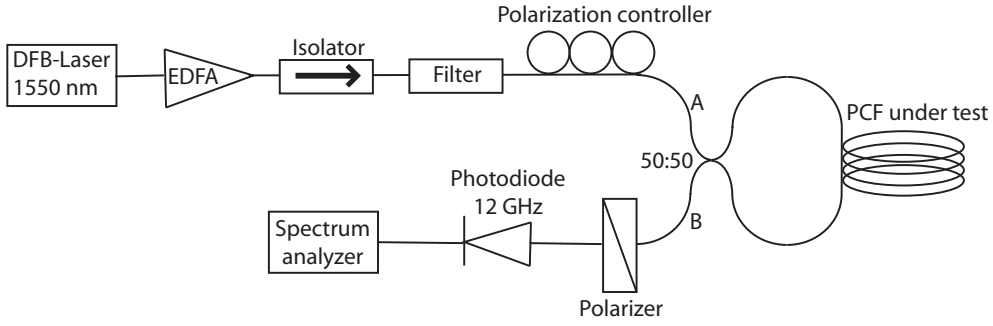

Figure 5.6: Experimental setup for observing GAWBS.

Polarized and depolarized GAWBS in an optical fiber originates from radial and torso-radial elastic modes and leads to phase modulation and the appearance of a set of new frequencies in the wave spectrum [1]. As briefly explained in chapter 2.3 forward Brillouin scattering can be observed by measuring the depolarized acoustic modes varied

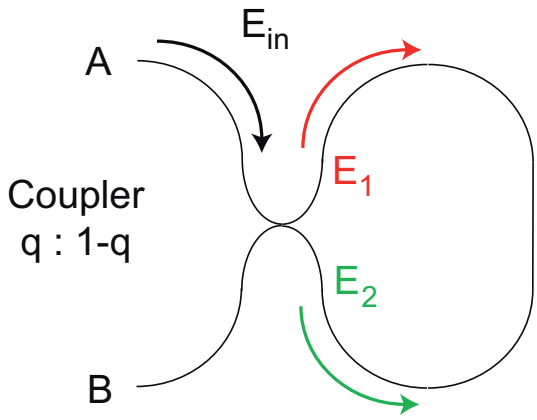

Figure 5.7: Fiber loop mirror.

in another polarization as the pump wave or by measuring the phase modulation since both R_{01} and Tr_{21} induce phase shifts on the pump wave. The setup to measure depolarized GAWBS contains a polarization controller with which the polarization is set. A polarization analyzer is placed on the fiber output in order to obtain the spectrum in another polarization state as injected into the fiber. This setup is not further presented here. To detect the phase shift induced by polarized and depolarized GAWBS, we set up the fiber loop mirror depicted in Fig.(5.6) [20, 21], which is a Sagnac interferometer. A CW distributed-feedback (DFB) Erbium-doped fiber laser[4] at 1550 nm is amplified by an Erbium-doped fiber amplifier (EDFA). Amplified spontaneous emission (ASE) is removed by use of a 5 nm bandpass filter because it prevents the measurement of GAWBS. The output is then split into two counter-propagating beams and launched in the fiber loop mirror via a 50/50 fiber coupler [21]. This loop mirror acts as a Sagnac-interferometer such that the two counterpropagating waves interfere destructively at the 50/50 fiber coupler and power is reflected to the port A. However, the two counterpropagating waves suffer phase modulation due to GAWBS and this small signal is retrieved in port B. The polarization controller and the polarizer are used to suppress the carrier wave as much as possible at port B and to maximize the GAWBS signal in the RF spectrum. Finally the GAWBS spectrum is recorded by using a fast photodiode (band width up to 12 GHz) followed by an RF spectrum analyzer (Anritsu[5]).

5.3.1.1 Fiber loop mirror

Let us now go further into detail to explain the operation mode of the fiber loop mirror [20–22]. A directional coupler with a fixed ratio q : 1-q is used where the two outputs are

[4]RIO 0194-1-34-1, linewidth 20 kHz at 1.55 nm
[5]Anritsu MS2667C Spectrum Analzer 9 kHz-30 GHz

connected (Fig.(5.7)). The electrical field E_{in} is injected in input A. It is imperative:

$$|E_{\text{in}}|^2 = |E_1|^2 + |E_2|^2 + 2\,\text{Re}(E_1 E_2^\star \cos\theta) \tag{5.43}$$

where θ is the relative phase and E_1, E_2 are the coupling and the transmission fields. Energy conservation:

$$|E_{\text{in}}|^2 = |E_1|^2 + |E_2|^2 \tag{5.44}$$

leads to $cos\theta = 0$ between the coupling and the transmission fields. Energy conservation in Eq.(5.44) also requires that the two mode fields, E_1 and E_2, are in quadrature, in other words the modes are orthogonal or phase-shifted by $\pi/2$. For a complete mathematical derivation of the $\pi/2$-shift the reader is referred to Ref. [23].
We can now calculate the transmitted electrical field at output B. The used variables are: L the length of the fiber loop, α the fiber attenuation, β the propagation constant, ϵ the coupler loss and q : 1-q the coupling ratio. Then the electrical field E_B can be expressed as follows [22]:

$$\begin{aligned} E_B = E_{in} \cdot \big(&\left[q^{1/2}(1-\epsilon)^{1/2}\right] \cdot \left[q^{1/2}(1-\epsilon)^{1/2}\right] e^{(-\alpha+i\beta)L} + \\ &+ \left[(1-q)^{1/2}(1-\epsilon)^{1/2}\right] e^{(-\alpha+i\beta)L} e^{-i\pi/2} \cdot \left[(1-q)^{1/2}(1-\epsilon)^{1/2}\right] e^{-i\pi/2}\big) \end{aligned} \tag{5.45}$$

where $E_{in} \cdot q^{1/2}$ and $E_{in} \cdot (1-q)^{1/2}$ are propagating clockwise and counter-clockwise fields, respectively. The phase quadrature is added by $e^{-i\pi/2}$.
The ratio E_B/E_{in} reveals:

$$\frac{E_B}{E_{in}} = (2q-1) \cdot e^{(-\alpha+i\beta)L} \tag{5.46}$$

It is obvious that for q=0.5 no light is transmitted to output B. This is valid for perfect fibers where no additional phase shifts are added while the light is propagating in the fiber loop. This calculation is visualized in Fig.(5.8 a). The electrical field E_1 does not cross the fiber coupler and hence does not receive a phase shift whereas E_2 crosses two times the couplers and has a phase shift of π at the end. Thus, there is destructive interference at output B. The same calculation can be made for input A:

$$\begin{aligned} E_A = E_{in} \cdot \big(&\left[q^{1/2}(1-\epsilon)^{1/2}\right] \cdot \left[(1-q)^{1/2}(1-\epsilon)^{1/2}\right] e^{(-\alpha+i\beta)L} e^{-i\pi/2} + \\ &+ \left[q^{1/2}(1-\epsilon)^{1/2}\right] e^{(-\alpha+i\beta)L} \cdot \left[(1-q)^{1/2}(1-\epsilon)^{1/2}\right] e^{-i\pi/2}\big) \end{aligned} \tag{5.47}$$

which leads to the ratio:

$$\frac{E_A}{E_{in}} = -2iq^{1/2}(1-q)^{1/2}(1-\epsilon)e^{(-\alpha+i\beta)L} \tag{5.48}$$

For q=0.5 we see:

$$\frac{E_A}{E_{in}} = -i(1-\epsilon)e^{(-\alpha+i\beta)L} = -e^{i\cdot\pi/2}(1-\epsilon)e^{(-\alpha+i\beta)L} \tag{5.49}$$

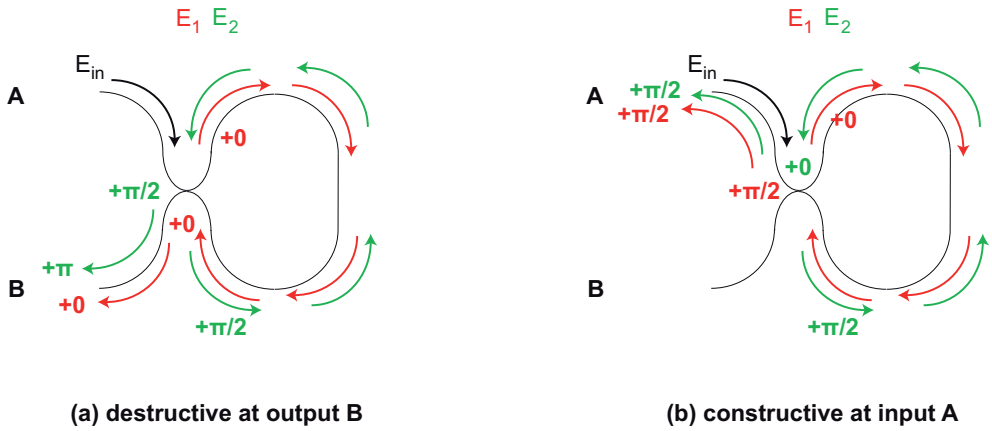

Figure 5.8: Fiber loop mirror: (a) destructive interference at input B, (b) constructive interference at input A.

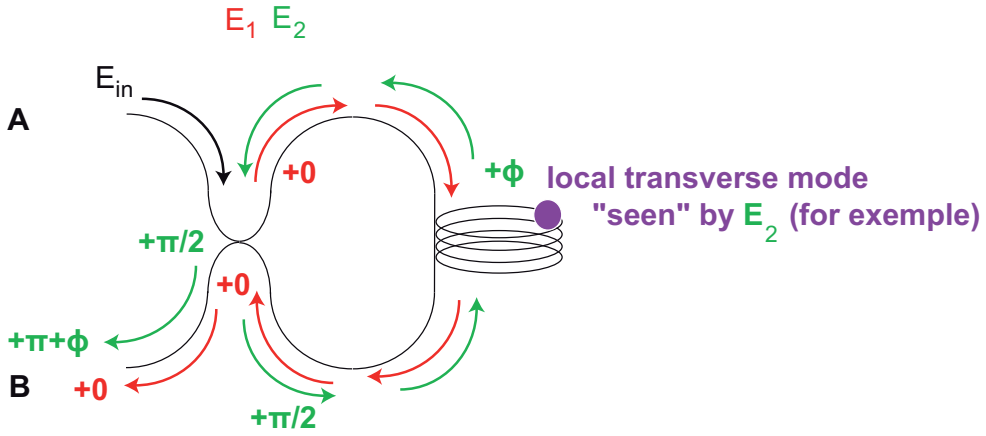

Figure 5.9: Fiber loop mirror: the two counterpropagating waves suffer phase modulation due to GAWBS and this small signal goes to the port B

and that the optical wave gets a $\pi/2$-shift at every reflexion. This is also depicted in Fig.(5.8 b) where both electrical fields E_1 and E_2 crosses one time the coupler and get one $\pi/2$-shift. Thus we find constructive interference at the input A. In other words, the fiber loop acts as a perfect mirror.

This conclusion is of course valid when no phase modulation occurs along the way through fiber loop. However, both fields, E_1 and E_2, suffer from GAWBS effect and phase noise. Since the acoustic modes have a finite lifetime and both counter-propagating wave do not get the same phase-shift all along the fiber, the destructive interference at output B is not achieved anymore. Instead the small signal of GAWBS exists through output B and can be measured by a photodiode and an electrical spectrum analyzer. In Fig.(5.9) this effect is illustrated for E_2 which gets an additional Φ-shift caused by a local acoustic mode. It should just be emphasized on the fact that the two optical waves do not necessarily receive the same phase shift which leads to a small non-destructive part at output B.

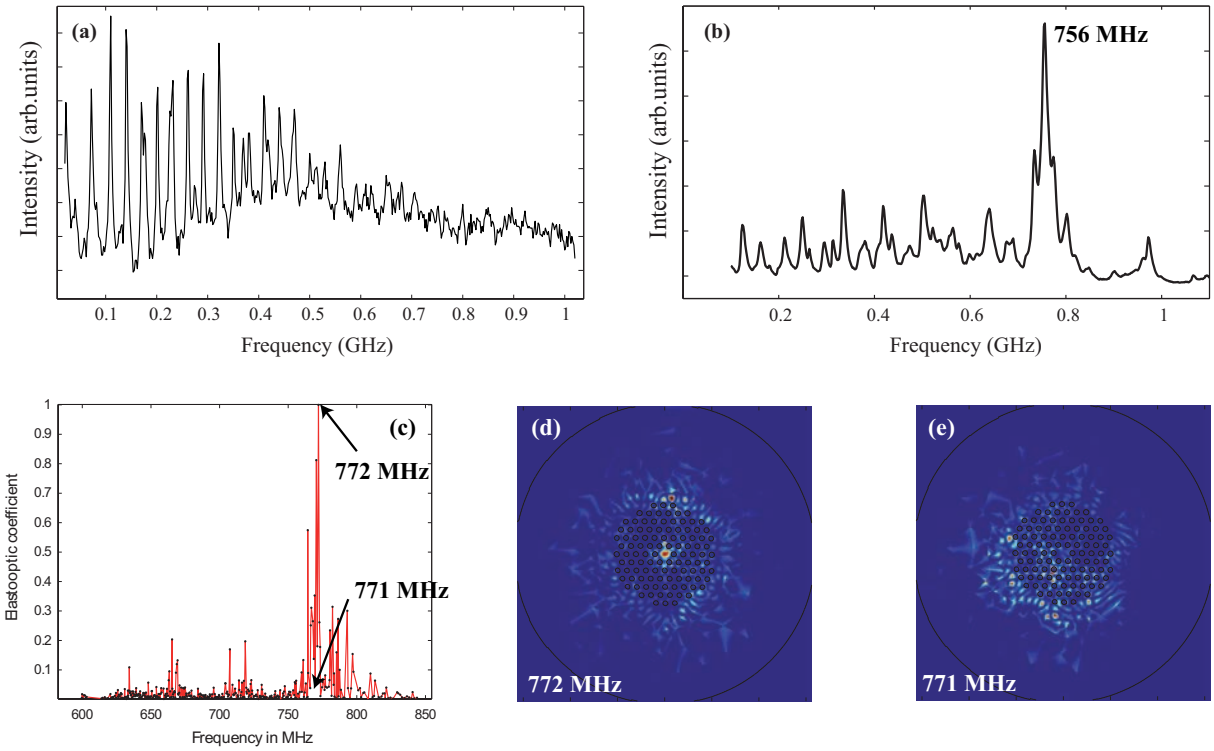

Figure 5.10: Experimental results of GAWBS measurement. (a) GAWBS in a conventional SMF, (b) GAWBS in a PCF with 5.5 µm fiber core, (c) elasto-optic coefficient in the same PCF, (d,e) strain energy density Eq.(5.23) for the acoustic mode at 772 MHz and 771 MHz (red = large density, blue = low density)

5.3.2 Experimental Results

5.3.2.1 Conventional single-mode fiber versus photonic crystal fiber

Fig.(5.10) shows a comparison of forward Brillouin scattering in a conventional SMF and a PCF with hexagonal structure. As introduced in paragraph 2.3, we retrieve again the numerous frequency peaks of a conventional SMF in Fig.(5.10 a). It can be seen in that the peaks are well distinct and narrow with a FWHM of about several MHz. Note that they are not equidistant. In comparison, the GAWBS spectrum of a PCF is shown in Fig.(5.10 b). This PCF has been presented in chapter 3.4 with a 5.5 µm fiber core and a hexagonal structure. As predicted by our acoustic model in the previous paragraph, we mainly observe one main peak at 756 MHz in the GAWBS spectrum which has been measured for the first time in [2, 7]. The experiment in Fig.(5.10 b) in PCF has been confirmed by simulation, depicted in Fig.(5.10 c) where we find a main mode at 772 MHz. The frequency difference can be explained by the uncertainty in structure size in the SEM-image. Interested in the behaviour of the acoustic modes, we plotted the strain energy

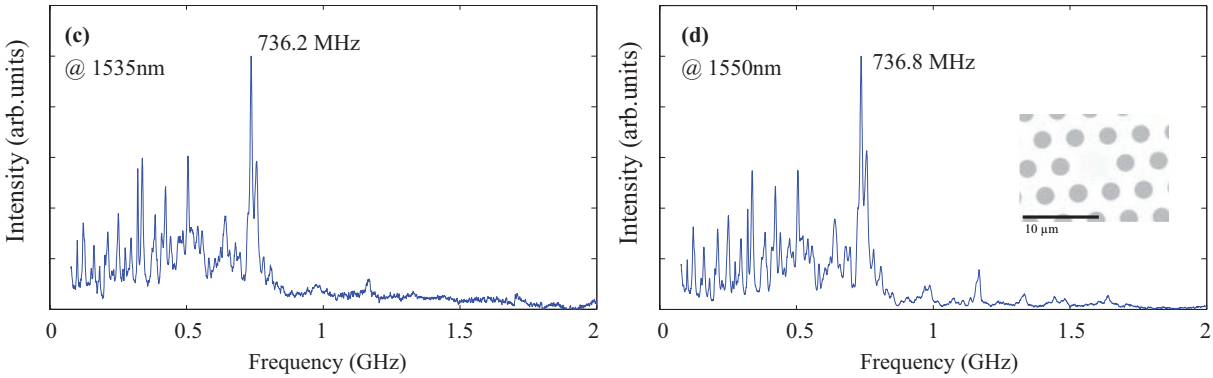

Figure 5.11: Experimental results of GAWBS measurement in PCF with 6.2 µm fiber core at two different pump wavelengths: (a) 1535 µm and (b) 1550 µm.

density in Fig.(5.10 d,e) for two different frequencies. As it can be seen, the acoustic mode which is responsible for the highest GAWBS peak (772 MHz) is confined in the fiber core whereas the other ones (for example at 771 MHz) are distributed around the core between the air holes, even with very close frequencies.
Another PCF with 6.2 µm core diameter (fiber TH in chapter 4) was investigated in terms of GAWBS in Fig.(5.11 a,b). These two measurements have been performed for two different pump wavelengths: 1550 µm and 1535 µm. The frequency of the main peak do not change with the pump wavelength. The small difference of 736.2-736.8 MHz can be due to measurement uncertainty because we should always keep in mind that even if we obtain quite clear results, we are still measuring phase noise. Consequently, this spectrum clearly shows that the GAWBS frequency does not depend on the pump wavelength. This is also the reason for which Dainese *et al.* [6] choose to call forward Brillouin scattering Raman-*like* scattering because the Raman frequency shift does not depend on the pump wavelength either.

5.3.2.2 Effect of longitudinal structural irregularities

Since forward Brillouin scattering is based on transverse modes which depend highly on the fiber structure, GAWBS are very sensitive to fiber irregularities. In paragraph 3.4 two PCFs have been presented that originate from the same stack but were drawn in different drawing processes. This resulted in a higher homogeneity for fiber #2 (see table (3.1)). The distributed measurement revealed clearly the difference between the two fibers but also forward Brillouin scattering indicates a difference. As shown in Fig.(5.12) the main peak is much narrower for fiber #2 (22 MHz) compared to fiber #1 (60 MHz). Since the spectrum is averaged we see the instability of the GAWBS peak as a broadening in frequency. Thus, GAWBS measurement can be used as one indicator for monitoring fiber uniformity.

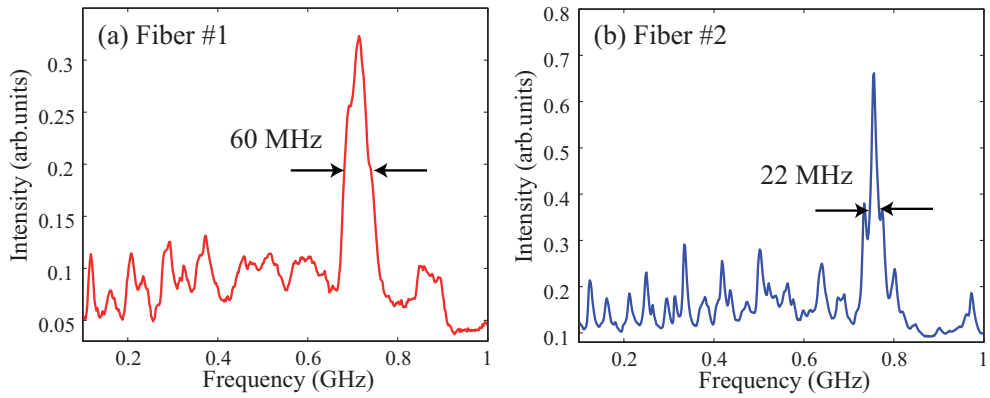

Figure 5.12: Effect of fiber inhomogeneities on GAWBS measurement. Fiber #1 (a) and fiber #2 (b) originate from the same stack but were drawn with different fiber drawing processes. Fiber #2 shows less irregularities in distributed Brillouin measurement. See chapter 3.4

5.3.2.3 PCF with varying microstructure

Another interesting observation can be made for the PCFs with varying core size which have been investigated in chapter 4.2 for increasing the Brillouin threshold. In Fig.(5.13 a-c) we see the serial of three fibers: a uniform PCF (called U2 in chapter 4.2), a PCF with 7%-varying structure size (V1) and 14%-varying structure size (V2). As it is obvious in Fig.(5.13 a) the main peak is narrow and the lower frequency peaks are mostly suppressed. For the 7%-varying structure the GAWBS peak splits into a two-maxima-peak (Fig.(5.13 b)) and the lower frequency peaks get noisy. In the third case (Fig.(5.13 c)) with the result for the 14%-varying structure we finally observe that the distance of the maxima are still larger as for (b) which is expected so because the variation of the structure size is higher. The frequency for the main peak is related to the fiber core diameter, as discussed in paragraph 5.2 with Eq.(5.30) and Eq.(5.29). Thus the varying fiber core diameter of V1 and V2 causes the spectral broadening. To verify this assumption, we have

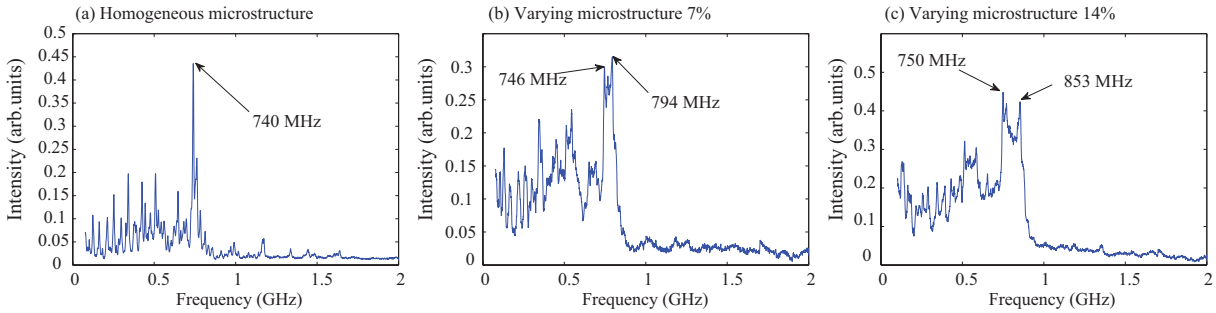

Figure 5.13: Experimental GAWBS spectrum for fibers with varying microstructure size: (a) unifrom, (b) 7% variation, (c) 14% variation. See chapter 4.2

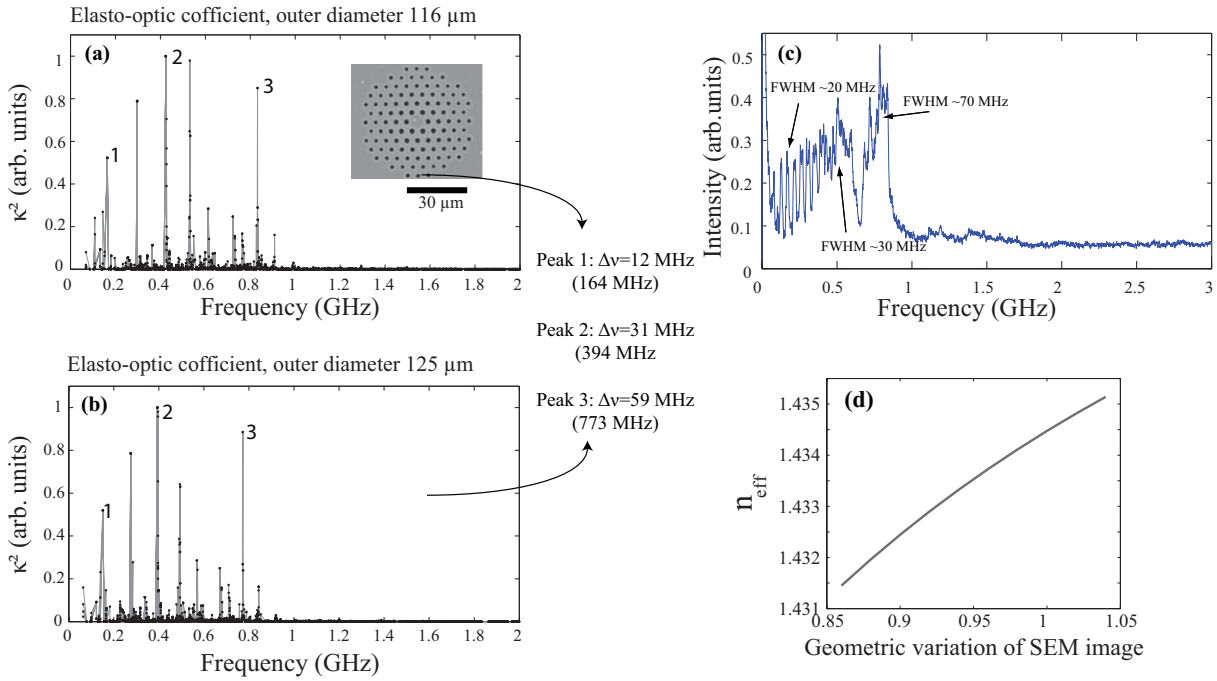

Figure 5.14: GAWBS measurement and simulation for a fiber with varying microstructure size (7% variation, fiber V3, table (4.3): (a,b) Elasto-optic coefficient for minimal and maximal outer diameter, (c) experimental GAWBS spectrum, (d) effective refractive index while varying the microstructure size.

performed some numerical simulations. Fiber V3 with also 7%-varying structure (parameters see table (4.3) has been investigated and the peak broadening has been verified by simulation. In Fig.(5.14 c) we first show the experimental results. Several peaks can be observed and above 800 MHz GAWBS are mostly suppressed. The multi-peak structure can be due to the relatively big core diameter or to the fiber structure where the air holes becomes smaller in the outer rows (SEM-image as inset in Fig.(5.14 a)). For some peaks the FWHM has been measured as seen in Fig.(5.14 c): 20 MHz at about 160 MHz, 30 MHz at about 500 MHz and 70 MHz at about 800 MHz. To support the claim that the broadening is due to the varying fiber structure the theoretical GAWBS spectrum has been computed, once for the original SEM-image with 125 µm outer diameter and a second simulation for the by 7% smaller structure with 116 µm outer diameter. The results are depicted in Fig.(5.14 a,b). For three peaks the difference is noted down next to the figures: 12 MHz at 164 MHz, 30 MHz at 394 MHz and 59 MHz at 773 MHz. They correspond almost to the experimental values but are rather smaller. This is due to the fact that the FWHM of GAWBS also depends on the life time of the acoustic modes which leads to an additional broadening [8]. The higher the frequency of the GAWBS peak, the broader its FWHM [24]. For completeness the effective refractive index of the optical mode depending on the structure size is also shown in Fig.(5.14 d). It has been compared to the distributed frequency shift in chapter 4.3 and was in very good accordance to the

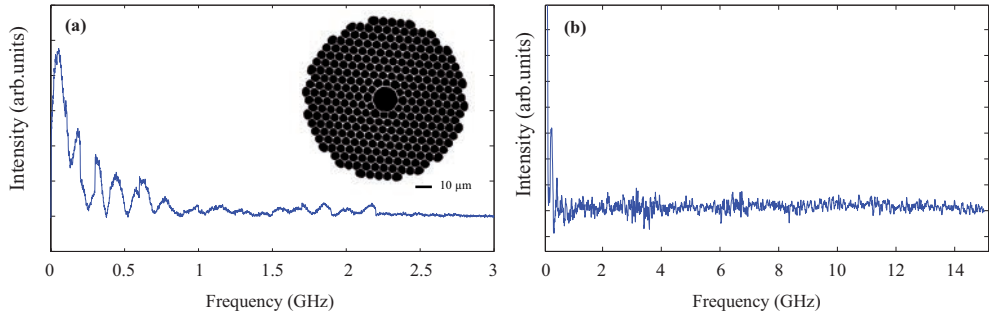

Figure 5.15: GAWBS in a hollow core fiber (d_c=10 µm): (a) up to 3 GHz, (b) up to 15 GHz.

experimental results.

5.3.2.4 GAWBS in hollow core fibers

In Ref. [25, 26], GAWBS in a hollow core fiber are presented. Light is here guided in air by photonic band gap guiding [3, 27]. Zhong *et al.* [26] report on polarization noise at sideband frequencies in the MHz range up to 35 MHz and they identify by simulation torsional-radial modes and acoustic modes trapped in the air-silica structure.
We also measured a 5m-long hollow core PCF since we wondered if the acousto-optic interaction would be efficient enough in a hollow core PCF. Since the optical mode is mainly propagating in air, where the acoustic modes do not exist, the GAWBS signal should be much lower than in full-silica fibers. Besides the fiber is rather short, so we did not expect high GAWBS peaks. We can also expect that the GAWBS frequency must be very high due to the small silica bridges (about 400 nm) of the air-silica structure around the air-core. Thus measurement up to 15 GHz has been performed. The results of the GAWBS measurement in the hollow core PCF are presented in Fig.(5.15). The cross section is shown in the inset of Fig.(5.15 a) and the core diameter ia about 10 µm. We observe several peaks in the lower frequency region (Fig.(5.15 a)) up 600 MHz. The peaks are not very distinct and have a FWHM of about 50-100 MHz. At about 2.2 GHz in Fig.(5.15 a) a cut-off frequency can be observed. For the frequency range up to 15 GHz no more peaks were observed. The question is weather the sensitivity of the setup was not high enough to detect peaks at high frequencies. Moreover it would be interesting to know if the observed peaks up to 600 MHz are really classical GAWBS peaks, resulting from an acousto-optical interaction, or another phenomena based on the light being reflected on the vibrating structure or if it results from any measurement errors due to laser noise. A numerical investigation including the calculation of the elasto-optic coefficient is needed and is under investigation.

5.4 Study of a multi-scale photonic crystal fiber

In this paragraph, we investigate GAWBS in a PCF with a multi-scale structure design and report the frequency-selective excitation of multiple high-frequency guided acoustic modes up to 2 GHz. The multi-scale fiber has been provided by Draka, Marcoussis. Based on a full vector finite-element model (FEM), we show that these guided acoustic modes result from elastic radial vibrations selected by the wavelength-scale air-silica microstructure. The elasto-optic coefficient is calculated and is found to be in good agreement with the experimental GAWBS spectrum. We further show the strong impact of structural irregularities of the fiber on these transverse acoustic modes by numerically studying a perfectly symmetric air-hole structure designed from the real cross section of the PCF. Our results suggest that PCFs can be advantageously used to enhance and control guided acousto-optic interactions at ultra-high frequency by fiber design in view of potential applications for fiber-optic sensors or efficient acousto-optic devices.

5.4.1 Experiments

The PCF under test, illustrated in Fig.(5.16 c), consists of a multiscale microstructure with three different sizes of air holes and has a length of 106 m. The first two inner rows with 800 nm holes are based on a triangular lattice and define the fiber core and the single-mode propagation at 1550 nm, as confirmed by numerical simulations shown in Fig.(5.16 d). The two external rows consist of 12 larger elliptical holes and are intended to isolate the fiber core from the cladding to lower the intrinsic confinement losses [28]. This fiber actually exhibits two zero-dispersion wavelengths and a high nonlinear coefficient ($25\,\mathrm{W^{-1}km^{-1}}$) and has been used for supercontinuum generation [29]. Fig.(5.16 a) shows the GAWBS spectrum. Several sideband frequency peaks are observed from 200 MHz to 2 GHz and, in particular, three dominant acoustic modes at 410 MHz, 915 MHz and 1940 MHz. Above 2 GHz no other acoustic modes appear. This multi-frequency spectrum is different from the single-mode spectrum previously observed in standard triangular-lattice PCF [6, 7].

5.4.2 GAWBS model

To identify guided acoustic modes in the PCF, we have performed FEM-based numerical simulations of the optical and acoustic modes using the COMSOL Multiphysics software as explained in chapter 5.1. For this purpose, the PCF cross-section has been imported from a SEM image and transformed to a finite element mesh. We have used the RF

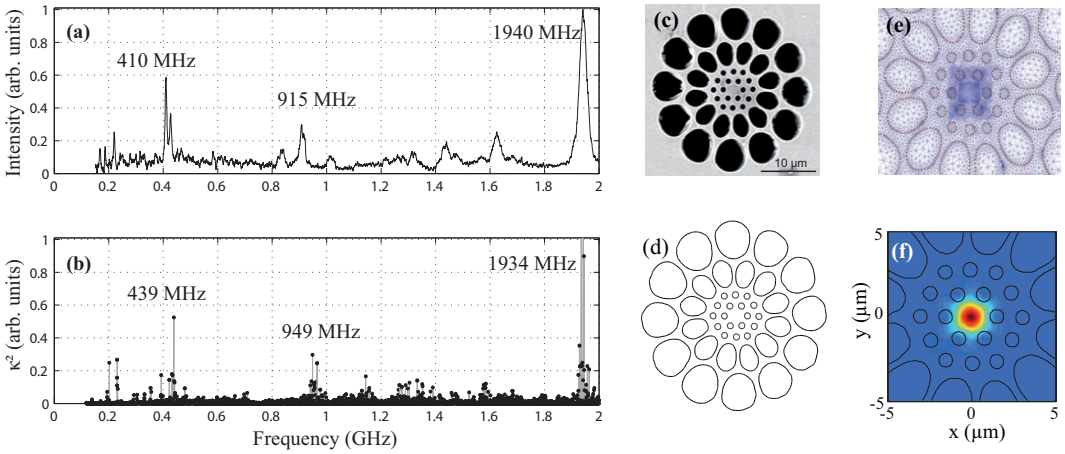

Figure 5.16: (a) Experimental RF spectrum showing the guided acoustic modes of the photonic crystal fiber shown in (c). (b) FEM-based numerical simulation of the elasto-optic coefficient κ^2 as a function of the acoustic frequency. (c) scanning electron microscope (SEM) image of the PCF cross-section: core diameter 2.4 µm, diameter of small holes 820 nm, diameter of middle holes 3.6 µm, diameter of big holes 5.1 µm. (d) extracted boundaries of the micro-structure, (e) meshing the micro-structure, (f) fundamental optical mode solved at 1550 nm using FEM simulation. Air-holes contour lines are depicted in black.

module to solve the optical mode and PDE-mode for full-vector 3D acoustic modeling. As acoustic constants, we used silica density $\rho = 2203\,\mathrm{kg.m^{-3}}$, Young's modulus $E_Y = 73.1\ 10^9\,\mathrm{Pa}$, and Poisson ratio $\nu_P = 0.17$. The optical refractive index of silica is $n = 1.444$. Single-mode optical propagation was found at 1550 nm, with an effective refractive index $n_{\mathrm{eff}}(1550\ nm) = 1.392$. The fundamental optical mode is shown as a color plot in Fig.(5.16 d). Both the optical and acoustic modal shapes are then combined to estimate the elasto-optic diffraction coefficient κ that is written as [3] (see also chapter 5.1):

$$\kappa = \int_{\sigma} \mathrm{d}x\mathrm{d}y E_i E_j p_{ijkl} S_{kl}. \tag{5.50}$$

In this expression, σ is the transverse section of the fiber, E_i and E_j are the pump and scattered optical modes, respectively, p_{ijkl} is the strain-optical tensor, and S_{kl} is the acoustic displacement tensor. The Einstein summation convention on repeated indices is employed. κ^2 is proportional to the scattering efficiency and thus models the GAWBS spectrum. The result is depicted in Fig.(5.16 b). Three main peaks are found, in good agreement with Fig.(5.16 a), both with respect to modal frequencies and relative scattering efficiencies. The small discrepancy of acoustic frequencies can be attributed to scaling errors on the SEM image. In order to investigate more clearly the acoustic modes trapped by the air-hole microstructure, we compute the strain energy density (SED) from Eq.(5.23) and the kinetic energy density ($\mathrm{E_{kin}}$) from Eq.(5.22)(see chapter 5.1). The SED and $\mathrm{E_{kin}}$ of the three main acoustic modes are plotted in Figs.5.17(a-c) and (d-f), respectively. It is

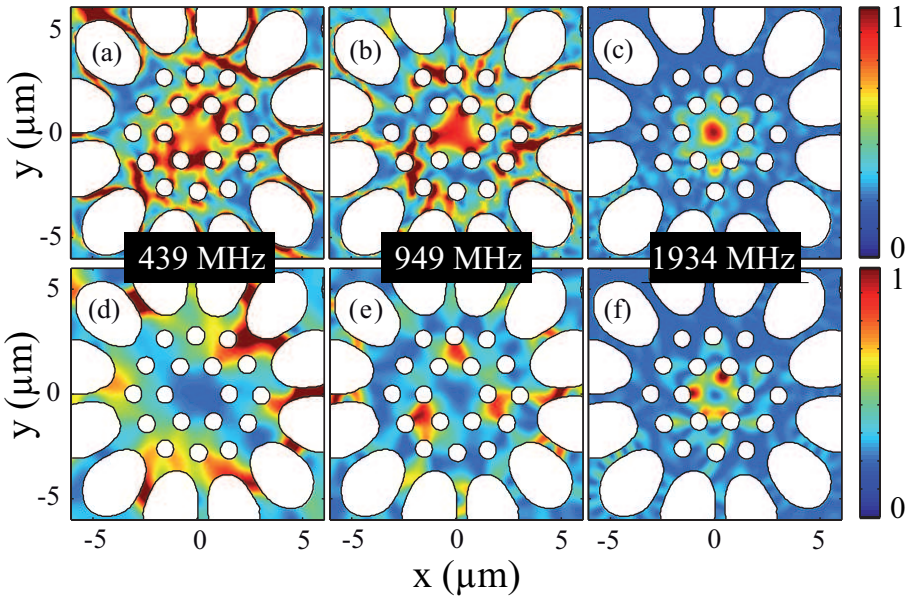

Figure 5.17: Numerical calculation (color plot) of the strain energy density distribution (a-c) and the kinetic energy density (d-f) of the 439, 949 and 1934 MHz acoustic modes.

clearly seen that the three acoustic modes are spatially confined within the first external row of the fiber (the big core), the second internal row, and the fiber core (small core), respectively. As GAWBS is the signature of the scattering of the incident optical mode by acoustically-induced strain, the scattering efficiency κ is expected to be higher for a strong overlap between the SED and the optical mode. This is clearly apparent for the highest frequency mode at 1934 MHz in Fig.(5.17 c). Note that the small peaks around 200 MHz seen in both Figs.5.16 (a) and (b) were also analyzed and were attributed to the modes confined to the second (outermost) external row. It is seen from Figs.5.17(a-f) that both the SED and E_{kin} are not symmetrically distributed due to structural irregularities of the PCF. To get further insight, we have performed numerical simulations for a model PCF without any structural irregularity. For this purpose, we have designed a fiber cross-section representing the same microstructure as in Fig.(5.16 c) but with defect-less holes, pitches and angles. The resulting scattering efficiency is plotted in Fig.(5.18 a) and is similar to that of Fig.(5.16 b). Of particular interest are the three main acoustic resonance peaks now appearing at unique frequencies, whereas those computed for the real structure degenerate in several peaks with close frequencies (see, *e.g.*, the 950 MHz peak in Fig.(5.16 b) which is composed of five adjacent modes). The structural irregularities of the fiber actually remove the degeneracy of acoustic modes and the multimodal nature of the real structure originates from an energy splitting (or frequency splitting) of the acoustic modes. In this way, we can interpret the spectral width of GAWBS peaks as resulting not only from the acoustic lifetime (related to acoustic propagation losses) but also from transverse structural irregularities of the fiber cross-section. The SED and E_{kin} of the three main acoustic modes of the model PCF are shown in Fig.(5.19 a-c)

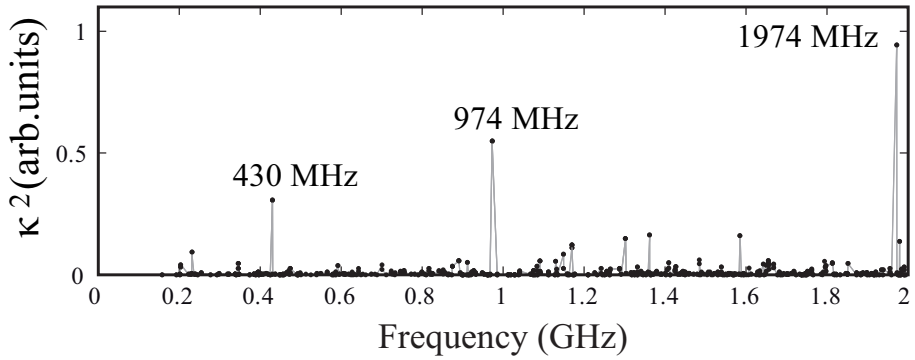

Figure 5.18: Elasto-optic coefficient as a function of the acoustic frequency for the perfect microstructure.

and (d-f), respectively. In contrast to Fig.(5.17), both energy density distributions are now symmetric. This clearly demonstrates the strong impact of structural irregularities of the PCF on guided acoustic modes and their frequencies. The SED in Fig.(5.19 a-c) confirms the efficient overlap between the strain field and the optical mode. The low-frequency mode in Fig.(5.19 a) can be understood as a circularly symmetric mode of the big core, whereas the middle- and high-frequency modes in Fig.(5.19 b,c) can be identified as $2\pi/6$-symmetric modes limited to the second internal row and the optical core, respectively. The fact that the structure in the middle is triangular enhances these $2\pi/6$-symmetric modes contrary to the quasi-circular distribution of the first large holes surrounding the big core (see chapter 5.2). In this way, the big core nearly behaves like a silica rod. This can be quantitatively verified by the relation $\nu = c_{R01} \cdot V_T/D$ which links the frequency ν of the fundamental elastic mode to the rod diameter D by a constant $c_{R01} \cdot V_T$, where $V_T = 3740\,\mathrm{m\,s^{-1}}$ is the transverse acoustic velocity and c_{R01} is a factor which depends on the acoustic mode, in this case the fundamental R_{01}-mode. The product $c_{R01} \cdot V_T$ is equal to $3.82 \cdot 10^3\,\mathrm{m\,s^{-1}}$ (equivalent to the factor q in [16], see derivation see chapter 5.2) and was obtained from simulation but also by solving the Pochhammer-Chree relations [19] that depend on both the transverse acoustic velocity $V_T = 3740\,\mathrm{m\,s^{-1}}$ and the longitudinal acoustic velocity $V_L = 5996\,\mathrm{m\,s^{-1}}$. The latter analytic solution leads to $\nu = c_{R01} \cdot V_T/D \approx 3.205/\pi \cdot V_T/D = 3.82 \cdot 10^3/D$, in good agreement with the numerical simulation. Consequently, the constant $c_{R01} \cdot V_T$ can be seen as an effective acoustic velocity that depends on both the transverse and longitudinal acoustic velocities. For the radial mode with the lowest frequency, at 410 MHz, the rod diameter can be estimated from the above expression to 8.7 µm, in excellent agreement with the diameter measured on the SEM image. This suggests that the GAWBS spectrum can be used to provide an accurate measurement of the dimensions of the PCF core. However, this conclusion is not valid for the middle- and the high-frequency modes at 915 MHz and 1940 MHz, because these exhibit $2\pi/6$-symmetry and thus cannot be identified as fundamental rod modes.

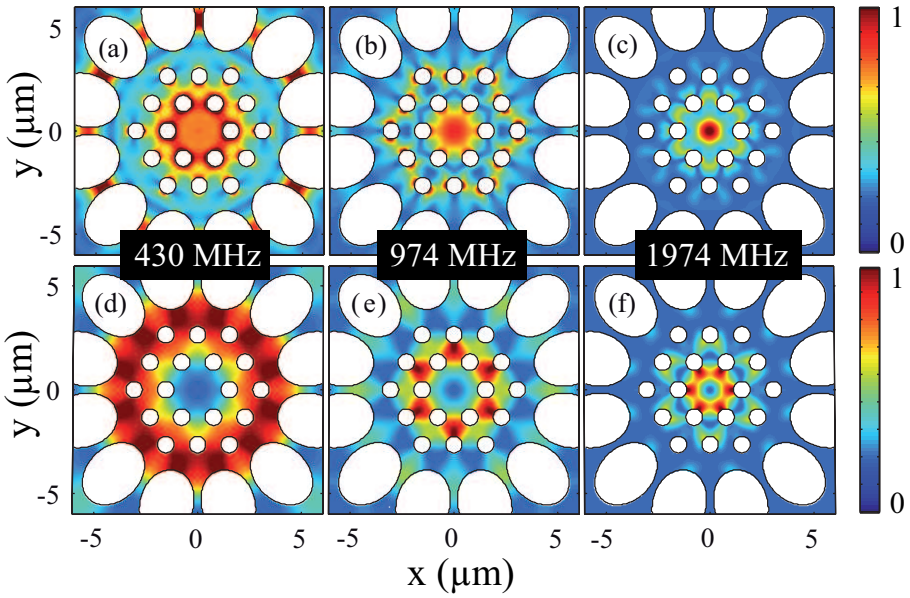

Figure 5.19: Numerical simulations (color plot) of a perfect PCF design without any structural irregularity. (a-c) strain energy density distribution and (d-f) elastic energy distribution of the 430, 974 and 1974 MHz acoustic modes confined to the microstructure, respectively

5.5 Conclusion

Guided acoustic wave Brillouin scattering has been investigated both theoretically and experimentally. An acoustic model for the transverse acoustic modes is presented with its application to numerical simulations with FEM in Comsol. With help of this model the theoretical GAWBS spectrum for PCF based on SEM-images is extracted and compared to experimental results. The experimental setup to measure forward Brillouin scattering was shown and results for PCF with manifold microstructures are investigated. A special photonic crystal fiber with a multiscale structure has been shown then which revealed both experimentally and numerically that such air-silica microstructure supports the simultaneous frequency-selective excitation of several transverse guided acoustic modes with frequencies up to 2 GHz. The continuous comparison between experimental and theoretical results provides us with a rather global understanding of GAWBS phenomena in PCF. It is now quite clear how size, geometry and air-silica fraction in a PCF simultaneously participate in the composition of its GAWBS spectrum. This is not only of high interest for PCF characterization but also for promising use to enhance and control guided acousto-optic applications at ultra-high frequencies for fiber-optic sensors [15] or acousto-optic fiber devices. In addition, at low frequencies the acoustic modes being almost suppressed, PCF can be employed for quantum optics experiments [2].

Bibliography

[1] R. M. Shelby, M.D. Levenson, and P.W. Bayer, "Guided acoustic-wave Brillouin scattering", *Physical Review B*, vol. 31, pp. 5244–5252, April 1985.

[2] D. Elser, U. L. Andersen, A. Korn, O. Glockl, S. Lorenz, Ch. Marquardt, and G. Leuchs, "Reduction of guided acoustic wave Brillouin scattering in photonic crystal fibers", *Physical Review Letters*, vol. 97, pp. 133901, 2006.

[3] V. Laude, A. Khelif, S. Benchabane, M. Wilm, T. Sylvestre, B. Kibler, A. Mussot, J. M. Dudley, and H. Maillotte, "Phononic band-gap guidance of acoustic modes in photonic crystal fibers", *Physical Review B*, vol. 71, no. 4, pp. 045107, 2005.

[4] P. Dainese, P. St. J. Russell, N. Joly, J. C. Knight, G. S. Wiederhecker, H. L. Fragnito, V. Laude, and A. Khelif, "Stimulated Brillouin scattering from multi-GHz-guided acoustic phonons in nanostructured photonic crystal fibres", *Nature Physics*, vol. 2, no. 6, pp. 388–392, 2006.

[5] N. Shibata, A. Nakazono, N. Taguchi, and S. Tanaka, "Forward Brillouin scattering in holey fibers", *IEEE Photonics Technology Letters*, vol. 18, no. 2, pp. 412–414, January 2006.

[6] P. Dainese, P. St. J. Russell, G. S. Wiederhecker, N. Joly, H. L. Fragnito, V. Laude, and A. Khelif, "Raman-like light scattering from acoustic phonons in photonic crystal fiber", *Optics Express*, vol. 14, no. 9, pp. 4141–4150, 2006.

[7] J-C Beugnot, T. Sylvestre, H. Maillotte, G. Mélin, and V. Lande, "Guided acoustic wave Brillouin scattering in photonic crystal fibers", *Optics Letters*, vol. 32, no. 1, pp. 17–19, 2007.

[8] G. S. Wiederhecker, A. Brenn, H. L. Fragnito, and P. St. J. Russell, "Coherent control of ultrahigh-frequency acoustic resonances in photonic crystal fibers", *Physical Review Letters*, vol. 100, pp. 203903, 2008.

[9] M. S. Kang, A. Nazarkin, A. Brenn, and P. St. J. Russell, "Tightly trapped acoustic phonons in photonic crystal fibres as highly nonlinear artificial Raman oscillators", *Nature Physics*, vol. 5, pp. 276–280, 2009.

[10] S. Benchabane, *Guidage et filtrage des ondes dans les cristaux phononiques*, PhD thesis, Université de Franche-Comté, 2006.

[11] Michaël Delqué, *Private communication*, 2010.

[12] *Comsol*, http://www.comsol.com/.

[13] D. Royer and E. Dieulesaint, *Ondes Élastiques Dans Les Solides*, Dunod, Paris, 1997.

[14] I. H. Malitson, "Interspecimen comparison of the refractive index of fused silica", *J. Opt. Soc. Am.*, vol. 55, no. 11, pp. 1205–1208, 1965.

[15] E. Carry, J.-C. Beugnot, B. Stiller, M. W. Lee, H. Maillotte, and T. Sylvestre, "Temperature coefficient of the high-frequency guided acoustic mode in a photonic crystal fiber", *Applied Optics*, 2011, accepted.

[16] M. S. Kang, A. Brenn, G. S. Wiederhecker, and P. St. J. Russell, "Optical excitation and characterization of gigahertz acoustic resonances in optical fiber tapers", *Applied Physics Letters*, vol. 93, no. 13, pp. 131110, 2008.

[17] A. Brenn, G. S. Wiederhecker, M. S. Kang, H. Hundertmark, N. Joly, and P. St.J. Russell, "Influence of air-filling fraction on forward Raman-like scattering by transversely trapped acoustic resonances in photonic crystal fibers", *J. Opt. Soc. Am. B*, vol. 26, no. 8, pp. 1641–1648, 2009.

[18] J.-C. Beugnot, *La diffusion Brillouin dans les fibres optiques microstructurées*, PhD thesis, Université de Franche-Comté, 2007.

[19] R. N. Thurston, "Elastic waves in rods and clad rods", *J. Acoust. Soc. Am.*, vol. 64, no. 1, pp. 1–37, 1978.

[20] N. Nishizawa, S. Kume, M. Mori, T. Goto, and A. Miyauchi, "Symmetric and asymmetric fiber loop mirrors for observing guided-acoustic-wave Brillouin scattering in polarization-maintaining fibers", *Optics Letters*, vol. 19, pp. 1424–1426, 1994.

[21] D. B. Mortimore, "Fiber loop reflectors", *Journal of Lightwave Technology*, vol. 6, no. 7, pp. 1217–1224, 1988.

[22] M. Dossou, *Les modes de résonance acoustique dans les fibres optiques microstructurées - Applications aux capteurs répartis*, PhD thesis, Université Lille 1, 2011.

[23] X. Fang, R. O. Claus, and G. Indebetouw, "Interferometric model for phase analysis in fiber couplers", *Applied Optics*, vol. 35, no. 22, pp. 4510–4515, 1996.

[24] T. C. Zhu, H. J. Maris, and J. Tauc, "Attenuation of longitudinal-acoustic phonons in amorphous SiO_2 at frequencies up to 440 GHz", *Phys. Rev. B*, vol. 44, pp. 4281–4289, 1991.

[25] W. Zhong, B. Heim, D. Elser, C. Marquardt, and G. Leuchs, "Photon-phonon interaction in hollow-core photonic crystal fibers", in *Deutsche Physikalische Gesellschaft - Tagung, Dresden 2011*, 2011.

[26] W. Zhong, B. Heim, D. Elser, Ch. Marquart, and G. Leuchs, "Polarization noise induced by photon-phonon interaction in hollow-core photonic crystal fibres", in *CLEO*, 2011, CE4.3.

[27] Y. Jeong, K.-Y. Song, K. Hotate, and K. Oh, "Analysis of Brillouin frequency shift and acoustic waves in a hollow optical fiber", *Optics Letters*, vol. 34, no. 20, pp. 3217–3219, 2009.

[28] G. Mélin, L. Provost, A. Fleureau, S. Lempereur, X. Rejeaunier, E. Bourova, and L. Gasca, "Innovative design for highly non-linear microstructured fibers", in *European Conference of Optical Communication 2004*, 2004, p. Tu4.3.2.

[29] A. Boucon, D. Alasia, J. Beugnot, G. Mélin, S. Lempereur, A. Fleureau, H. Maillotte, J. M. Dudley, and T. Sylvestre, "Supercontinuum generation from 1.35 to 1.7 μm by nanosecond pumping near the second zerodispersion wavelength of a microstructured fiber", *IEEE Photonics Technology Letters*, vol. 20, no. 10, pp. 842 – 844, 2008.

Conclusion and perspectives

The aim of this thesis was to investigate Brillouin scattering in photonic crystal fibers (PCFs) from fundamental viewpoint to applied aspects. We have concentrated on the two aspects of this opto-acoustic interaction present in fiber optics, i.e., forward and backward Brillouin scattering. We have shown in both cases that the periodic wavelength-scale air-silica microstructure of photonic crystal fibers fundamentally changes the acoustic waves spatial distribution, leading to new characteristics for Brillouin scattering. Our investigations ranged from the fundamentals such as the observations of Brillouin linewidth broadening or of high-frequency guided acoustic modes trapped by the air-silica microstructure, to more applied topics, as the Brillouin passive suppression and the development of distributed Brillouin sensors. In the following we will give a brief overview of the key results for each of these topics treated in this thesis. Furthermore we will identify directions of interests as well as open questions for future research efforts.

In chapter 3 we conducted many experiments to fully characterize backward stimulated Brillouin scattering in various photonic crystal fibers and compared the observed behaviours to those occurring in conventional all-silica fibers. This encompassed Brillouin gain spectrum and threshold measurements as well as distributed Brillouin frequency shift measurements, respectively. For this purpose, we first introduced the Brillouin optical time domain analysis (BOTDA) and then successfully demonstrated a new distributed differential measurement technique using Brillouin echoes (BEDS) with π-phase-shift pulses. It is based on differential phase-shift keying (DPSK) using a single Mach-Zehnder modulator to generate a pump pulse and a short π-phase-shifted pulse with an easy and accurate adjustment of delay. With this simplified technique, we achieved centimeter spatial resolution when measuring a splice segment between two different fibers while reducing the optical loss for the pump pulse. A quadrature-phase shift keying (QPSK) modulator for the Brillouin probe has also been investigated as a single-sideband modulator in the BOTDA system and compared to the previous dual-sideband case. Further improvements of our distributed Brillouin sensing systems will be considered to increase the sensing range by using bidirectional erbium-doped fiber amplifiers as in fiber-based communication systems.

Using the BEDS technique, we further performed distributed mappings in photonic crystal fibers that show both short-scale and long-scale longitudinal fluctuations of the periodic wavelength-scale air-hole microstructure. Our technique is very sensitive to structural irregularities and thus interesting for fiber manufacturers to characterize and improve the fiber uniformity during the drawing process.
From a fundamental viewpoint, we also reported the observation of Brillouin linewidth broadening and, for the first time to our knowledge, the acoustic decay time in photonic crystal fibers. Interestingly, our measurements have revealed an unexpected faster decay for photonic crystal fibers than in a standard single-mode fiber. A multi-Lorentzian shape model of the Brillouin gain, assuming a rich acoustic mode distribution within the fiber core, has been used to explain the linewidth broadening. This is an interesting topic that should be deepened in theory and experiment. A further understanding of how the different coherent or incoherent acoustic modes interact together and how this yields to a shorter decay time in photonic crystal fibers should be pursued. A new theoretical approach based on Laude *et al.* [1] and Carlson *et al.* [2] could be helpful for this purpose. Another idea is to get access to the phase of the Brillouin gain spectrum that would help for confirming our theoretical assumption of the linewidth broadening in photonic crystal fiber.

In chapter 4, photonic crystal fibers with periodically-varied core diameter have been investigated both theoretically and experimentally. This work was motivated by application to Brillouin suppression in fiber optic technologies. We experimentally tested several fibers and demonstrated a 4 dB increase of the Brillouin threshold in a photonic crystal fiber by varying periodically the core diameter by only 7%. The efficiency of this passive technique has been verified by comparing with a uniform PCF and by use of our distributed sensing technique where the oscillating Brillouin frequency shift is clearly observed. Brillouin suppression was however not achieved for all modulated fibers due to different fiber parameters, as splicing losses, linear loss, measurement uncertainties. Nevertheless, we believe that such varying-core photonic crystal fibers may find potential applications in all-optical processing and fiber lasers where Brillouin backscattering is detrimental. For completeness, PCFs with higher amplitude variations and other variation profiles would be interesting to investigate. Unexpected effects in modulation instability and soliton propagation may also be observed by exploiting the periodically-varying zero-dispersion wavelength of these fibers.

In the last chapter of this doctoral thesis we studied guided acoustic wave Brillouin scattering (GAWBS) both numerically and experimentally in several photonic crystal fibers. Of particular interest, we demonstrated the simultaneous frequency-selective excitation of several guided transverse acoustic Brillouin modes up to 2 GHz in a photonic crystal fiber with a multi-scale structure design. These guided acoustic modes have been clearly identified by using a full vector finite-element model as resulting from elastic radial vi-

brations trapped by the air-silica microstructure. A clear formula of the relationship between core diameter of glass rods and acoustic resonance frequencies was then derived. We further showed the strong impact of structural irregularities of the fiber on the frequency and modal shape of these acoustic resonances by numerical comparison with a perfect symmetric fiber model. Our results suggest that PCFs can be advantageously used to enhance and control guided opto-acoustic interactions at ultra-high frequency in view of potential applications for fiber-optic sensors, acousto-optic devices and quantum communication experiments. Further experimental studies can include a distributed measurement of GAWBS in PCFs with help of the setup proposed by Kang *et al.* [3]. This can be interesting for sensor applications since the GAWBS peaks are highly sensitive to strain and temperature [4]. Another interesting study would be a GAWBS measurement in an ultra-cold PCF. Would the main mode still be present or suppressed because the acoustic phonon number is reduced? Moreover, the influence of GAWBS in a PCF-based Brillouin fiber ring laser is another focus for further research on forward Brillouin scattering.

Let us conclude this dissertation by saying that this work on the boundary of fundamental research and development has improved our understanding of Brillouin scattering in photonic crystal fibers. These fibers will continue to attract much attention because of their remarkable and unique acoustic properties that are essential for Brillouin scattering and its application to fiber optic technologies and distributed sensors.

Bibliography

[1] V. Laude, J.-C. Beugnot, S. Benchabane, Y. Pennec, B. Djafari-Rouhani, N. Papanikolaou, J. M. Escalante, and A. Martinez, "Simultaneous guidance of slow photons and slow acoustic phonons in silicon phoxonic crystal slabs", *Optics Express*, vol. 19, no. 10, pp. 9690–9698, 2011.

[2] C. G. Carlson, R. B. Ross, J. M. Schafer, J. B. Spring, and B. G. Ward, "Full vectorial analysis of Brillouin gain in random acoustically microstructured photonic crystal fibers", *Phys. Rev. B*, vol. 83, pp. 235110, 2011.

[3] M. S. Kang, A. Nazarkin, A. Brenn, and P. St. J. Russell, "Tightly trapped acoustic phonons in photonic crystal fibres as highly nonlinear artificial Raman oscillators", *Nature Physics*, vol. 5, pp. 276–280, 2009.

[4] E. Carry, J.-C. Beugnot, B. Stiller, M. W. Lee, H. Maillotte, and T. Sylvestre, "Temperature coefficient of the high-frequency guided acoustic mode in a photonic crystal fiber", *Applied Optics*, 2011, accepted.

Nomenclature

List of acronyms

BDG-DS	Brillouin dynamic grating distributed sensing
BEDS	Brillouin echoes distributed sensing
BFS	Brillouin frequency shift
BGS	Brillouin gain spectrum
BOCDA	Brillouin optical correlation-domain analysis
BOFDA	Brillouin optical frequency-domain analysis
BOTDA	Brillouin optical time-domain analysis
BOTDR	Brillouin optical time-domain reflectometry
CW	continuous wave
DCF	Dispersion compensation fiber
DFB	Distributed feedback (laser)
DFG	Difference frequency generation
DPSK	Distributed phase shift keying
DSF	Dispersion shifted fiber
EDFA	Erbium doped fiber amplifier
EMA	Effective modal area
FBG	Fiber Bragg grating
FEM	Finite elements method
FWHM	Full width at half maximum
FWM	Four wave mixing
GAWBS	Guided acoustics wave Brillouin scattering
GVD	Group velocity dispersion
HiBi fiber	Highly birefringent fiber
HNA	High numerical aperture

HNLF	Highly non-linear fiber
MI	Modulation instability
MOF	Micro-structured fiber
MZI	Mach-Zehnder interferometer modulator
NA	Numerical aperture
OFC	Optical fiber communciation (conference)
OPA	Optical parametric amplifier
OTDR	Optical time-domain reflectometry
PCF	Photonic crysal fiber
PD	Photo diode
POF	Polymer optical fiber
PMF	Polarization maintaining fiber
RF	Radio frequency
SBS	Stimulated Brillouin scattering
SRS	Stimulated Raman scattering
SED	Strain energy density
SEM	Scanning electron microscopy
SFG	Sum frequency generation
SHG	Second harmonic generation
SIPS	Forward stimulated inter-polarization scattering
SPM	Self phase modulation
THG	Third harmonic generation
XPM	Cross phase modulation
ZDW	Zero dispersion wavelength

List of often used symbols

A_{eff}	Effective mode area
$\mathbf{d}$	Air hole diameter
$\mathbf{d}_c$	Fiber core diameter
$\Delta\nu_B$	Linewidth of Brillouin gain spectrum
$\mathbf{E}_{\text{kin}}$	Kinetic energy
g_B	Brillouin gain
γ_e	Electro-strictive constant
J_i	Bessel-function of order i
κ	Elasto-optic coefficient
L_{eff}	Effective length
λ_P	Pump wavelength
Λ	Pitch, distance between two air hole centers
$\mathbf{n}$	Refractive index
$\mathbf{n}_{\text{eff}}$	Effective refractive index
ν_B	Brillouin frequency shift
P_{cr}	Critical power for the Brillouin threshold
ρ	Density
S_{kl}	Displacement
T_{ij}	Strain tensor
τ	Acoustic decay time
V_L	Longitudinal acoustic velocity
V_T	Transverse acoustic velocity
V_π	Bias point in a modulator
W_S	Strain energy density

Abstract Brillouin scattering is a fundamental nonlinear opto-acoustic interaction present in optical fibers with important implications in fields ranging from modern telecommunication networks to smart optical fiber sensors. This thesis is aimed at providing a comprehensive theoretical and experimental investigation of both forward and backward Brillouin scattering in next generation photonic crystal fibers in view of potential applications to above mentioned fields. We show in particular that these micro-structured optical fibers have the remarkable ability to either suppress or enhance photon-phonon interactions compared to what is commonly observed in conventional fibers. Firstly, this thesis provides a complete experimental characterization of several photonic crystal fibers using a novel highly-resolved distributed sensing technique based on Brillouin echoes. We perform distributed measurements that show both short-scale and long-scale longitudinal fluctuations of the periodic wavelength-scale air-hole microstructure along the fibers. Our mapping technique is very sensitive to structural irregularities and thus interesting for fiber manufacturers to characterize and improve the fiber uniformity during the drawing process. With this technique, we also report the first experimental observation of the acoustic decay time and the Brillouin linewidth broadening in both standard and photonic crystal fibers. Furthermore, we experimentally demonstrate a simplified architecture of our Brillouin echoes-based distributed optical fiber sensor with centimeter spatial resolution. It is based on differential phase-shift keying technique using a single Mach-Zehnder modulator to generate a pump pulse and a π-phase-shifted pulse with an easy and accurate adjustment of delay. These sensing techniques are also applied to distributed strain measurement. Another aspect of this thesis is the investigation of a novel method for suppressing stimulated Brillouin scattering that is detrimental to optical fiber transmissions and fiber lasers. We experimentally study several fibers and a demonstrate 4 dB increase of the Brillouin threshold in a photonic crystal fiber by varying periodically the core diameter by only 7%. The efficiency of this passive technique is verified by use of our distributed sensing technique where the oscillating Brillouin frequency shift is clearly observed. Lastly, we present experimental and numerical results demonstrating the simultaneous frequency-selective excitation of several guided acoustic Brillouin modes in a photonic crystal fiber with a multi-scale structure design. These guided acoustic modes are identified by using a full vector finite-element model to result from elastic radial vibrations confined by the air-silica microstructure. We further show the strong impact of structural irregularities of the fiber on the frequency and modal shape of these acoustic resonances.

Keywords : Nonlinear optics, stimulated Brillouin scattering, guided acoustic wave Brillouin scattering, photonic crystal fiber, Brillouin threshold, optical fiber sensors.

Résumé Le cadre général dans lequel s'insère ce travail de thèse est celui de l'étude de la diffusion Brillouin dans une nouvelle génération de fibres optiques à cristaux photoniques (PCFs). Ces fibres, qui présentent un arrangement périodique de micro-canaux d'air parallèles le long de la fibre, possèdent en effet des propriétés optiques et acoustiques remarquables et inédites par rapport aux fibres conventionnelles. De façon plus précise, nous montrons dans ce travail, par le biais de simulations numériques et de données expérimentales, que les fibres à cristaux photoniques offrent la possibilité de supprimer ou, à contrario, augmenter les interactions entre les photons et les phonons. Dans une première partie, nous présentons une méthode de cartographie des fluctuations longitudinales de la microstructure des fibres PCFs à l'aide d'un capteur distribué basé sur une méthode innovante d'écho Brillouin. Cette méthode, très sensible et à haute résolution, est directement intéressante pour caractériser et améliorer l'uniformité des PCFs lors de leur fabrication et également pour la détection des différentes contraintes de témperature et étirement induites le long des fibres. Sur le plan fondamental, notre système de mesure distribuée à haute résolution nous a également permis d'observer, pour la première fois à notre connaissance, le temps de vie des ondes acoustiques dans les fibres à cristaux photoniques et les fibres standard. Par ailleurs, sur le plan technique, nous avons développé une architecture simplifiée de capteur distribué combinant la technique des échos Brillouin et celle de la modulation différentielle par déplacement de phase avec un seul modulateur d'intensité. Nos résultats montrent une résolution centimétrique dans la zone de soudure entre deux fibres optiques à l'aide d'une impulsion de phase de 500 ps. Nous démontrons dans une deuxième partie la suppression directe et passive de la rétro-diffusion Brillouin stimulée dans une fibre optique microstructurée en faisant varier pério-diquement le diamètre de la microstructure. Une augmentation de 4 dB du seuil de puissance Brillouin a été obtenue avec une variation de seulement 7 % sur une période de 30 m. Ce résultat est très intéressant car la diffusion Brillouin est un facteur limitant dans les systèmes de télécommunications par fibre optique et les laser à fibre. La troisième et dernière partie est consacrée à l'étude numérique et expérimentale de la diffusion Brillouin en avant dans les fibres à cristaux photoniques. En plus de la suppression de la plupart des modes acoustiques transverses, nous montrons que cette diffusion Brillouin est fortement augmentée pour certains modes acoustiques à haute fréquence qui sont piégés au coeur de la microstructure. Nous avons également étudié une fibre à structure multi-échelle qui révèle l'excitation sélective de plusieurs phonons acoustiques à des fréquences allant jusqu'a 2 GHz. Ces mesures ont étés confirmées par des simulations numériques basées sur une méthode vectorielle aux éléments finis. L'impact des irrégularitées de la microstructure a aussi été mise en évidence.

Mots clés : optique non linéaire, diffusion Brillouin, fibres optiques microstructurées, seuil Brillouin, capteurs Brillouin distribués.